Implications of Self-Assembly and Metal Binding on the Bactericidal Potential of Synthetic Amphiphiles

A Thesis

Submitted in Partial Fulfillment of the Requirements for the Degree of

DOCTOR OF PHILOSOPHY

by

POULOMI DEY

Department of Biosciences and Bioengineering
Indian Institute of Technology Guwahati
Guwahati-781039, Assam, India

September 2019

Implications of Self-Assembly and Metal Binding on the Bactericidal Potential of Synthetic Amphiphiles

A Thesis

Submitted in Partial Fulfillment of the Requirements for the Degree of

DOCTOR OF PHILOSOPHY

by

POULOMI DEY

Department of Biosciences and Bioengineering
Indian Institute of Technology Guwahati
Guwahati-781039, Assam, India

September 2019

Curiosity is the Fuel for Discovery,

Inquiry and Learning

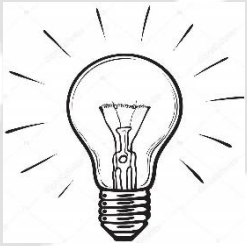

INDIAN INSTITUTE OF TECHNOLOGY GUWAHATI

DEPARTMENT OF BIOSCIENCES AND BIOENGINEERING

STATEMENT

I do hereby declare that the research findings of this thesis is the result of research work carried out by me in the Department of Biosciences and Bioengineering, Indian Institute of Technology Guwahati, Guwahati, India, under the supervision of Professor Aiyagari Ramesh.

As per the general norms of reporting research findings, due acknowledgements have been made, wherever the research findings of other researchers have been cited in this thesis.

Date: **Poulomi Dey**

INDIAN INSTITUTE OF TECHNOLOGY GUWAHATI

DEPARTMENT OF BIOSCIENCES AND BIOENGINEERING

CERTIFICATE

It is certified that the work described in this thesis entitled " ***Implications of Self-Assembly and Metal Binding on the Bactericidal Potential of Synthetic Amphiphiles***" by Ms. Poulomi Dey for the award of degree of Doctor of Philosophy is an authentic record of the results obtained from the research work carried out under my supervision in the Department of Biosciences and Bioengineering, Indian Institute of Technology Guwahati, India, and this work has not been submitted elsewhere for the award of any other degree.

CERTIFIED

Poulomi Dey

(Candidate)

Roll No: 146106018

Aiyagari Ramesh, Ph.D.

(Thesis Supervisor)

Date:

ACKNOWLEDGEMENT

I would like to take this opportunity to express my heartfelt gratitude to my family, friends and teachers who have made my learning experience so wonderful.

First and foremost, I would like to acknowledge the pivotal role played by Professor Aiyagari Ramesh, who is not only my PhD thesis supervisor but also a father figure to me. I am really grateful to God for giving me the opportunity to be his student and to learn so much from him. During my PhD tenure, Prof. Ramesh not only taught me the basics of research but also inculcated in me a yearning for science and the philosophy of life. The association with Prof. Ramesh has been extremely inspiring and motivating for me. He is the best teacher anyone can get who makes studying and working so interesting that it triggers intrigue and the leaning process becomes fun. Even if a small portion of his virtues of dedication, determination and unquenchable thirst for knowledge rub on, on me, I will consider myself blessed. Furthermore, his rock-solid guidance and fatherly support during the course of my PhD work has helped me learn to face hardships head on and pull through rough patches with patience and positivity. Most importantly, Prof. Ramesh's jovial nature, compassion and empathy has taught me that humanity comes first, professionalism later. Acquaintance with him has polished me, not only as a student of science but also as a person, for which I am forever grateful.

I am grateful to my doctoral committee members, Professor Kannan Pakshirajan, Professor Gurvinder Kaur Saini and Dr. Lal Mohan Kundu for their insightful suggestions, support and constant motivation, which has led to an improvement in the quality of my research work.

I would like to acknowledge Professor Gopal Das, Department of Chemistry, for giving me an opportunity to learn new aspects of supramolecular and surface chemistry along with the fundamentals of sensing. Under his kind guidance, I could learn a lot and acquire some confidence in the subject which I have dreaded since my school days. I owe him my sincere gratitude for his insights, patience and never-ending kindness, which has made my stay at IIT Guwahati all the more meaningful.

My sincere gratitude goes towards Dr. V.G.M. Naidu, Department of Pharmacology and Toxicology, NIPER Guwahati, for guiding me through the animal model studies. Dr. Naidu's overflowing energy, positivity and enthusiasm guided and

fueled my baby steps into a completely unknown field of research. He threw light on a completely new perspective pertaining to my PhD work. My tenure working in NIPER was extremely enjoyable, all thanks to Eswara Rao Puppala. He is such a fun colleague and teacher that I would look forward to the *in vivo* experimental sessions. I will take this opportunity to mourn the souls of the cute and innocent mice, who had to be sacrificed for science. Their contribution to the scientific community will be remembered in high regard. My heartfelt gratitude goes to Dr. U.S.N. Murty, Director, NIPER Guwahati, for permitting us to carry out the animal model experiments in the institute.

I sincerely express my gratitude and thanks to Professor Benu Dhawan, All India Institute of Medical Sciences (AIIMS), New Delhi and Professor Kasturi Mukhopadhyay, Jawaharlal Nehru University (JNU), New Delhi for kindly providing the MRSA strain for my work.

I am grateful to Professor Latha Rangan, Head of the Department of Biosciences and Bioengineering, IIT Guwahati, Professor Kannan Pakshirajan and Professor V.V. Dasu Former Heads of the Department Biosciences and Bioengineering, IIT Guwahati for providing me the necessary facilities that helped me to pursue my research at IIT Guwahati.

I am also grateful to all faculty members and staff of the Department of Biosciences and Bioengineering for supporting me throughout the Ph.D. tenure. I would like to thank Department of Biosciences and Bioengineering for providing infrastructural facility for my research work. I would also like to thank Central Instruments Facility (CIF) of IIT Guwahati for providing ambient atmosphere of research and high-end equipments to execute my experiments. I would also like to acknowledge Department of Chemistry and Centre of Environment, IIT Guwahati for providing high-end equipment for my experiments.

I am grateful to Professor Siddhartha Sankar Ghosh, Professor Pranab Goswami, Professor Lingaraj Sahoo and Dr. Biplab Bose for providing a state-of-the-art facility and an academic environment which enabled me to develop my skills and complete my Ph.D. work.

I acknowledge the state-of-art facility at the Center for Excellence under the aegis of Program Support Grant provided by Department of Biotechnology (DBT),

Government of India. I am grateful to Department of Biotechnology (DBT) and Science and Engineering Board (SERB), Department of Science & Technology (DST) for supporting my research through grants. I am also grateful to Ministry of Human Resource Department (MHRD) and IIT Guwahati for providing research fellowship.

I would like to extend sincere gratitude to Dr. Soham Samanta, Ms. Senjuti Halder and Ms. Madhurima Boral, Department of Chemistry, IIT Guwahati for the scientific collaboration.

I am indebted to my lab seniors Dr. Sudeep Goswami and Dr. Thiyagarajan Durairaj and Dr. Sandipan Mukherjee, for being my first teachers here at IIT Guwahati. They welcomed me with open arms into the lab and guided this novice through every basic experiment like a pampered little sister. I owe all my experimental skills to them. Without their contribution and motivation, the realization of this thesis would not have been possible. It has been my privilege to have worked with them. It is also my pleasure to thank my current lab members Priya Mullick, Basu Bhattacharjee and Barlina Konwar. A special mention would go to Rajanikant, Preeti, Tabassum, Narahari and Dipanjali who were not only my former labmates but also very dear friends.

I also wish to thank my departmental seniors, Dr. Asif Raza, Dr. Mahesh Agarwal and Dr. Mohitosh Dey for all the elevating discussions and knowledge they have passed on to me during the initial years of my Ph.D.

I wish to thank my friends Suvo, Suvro, Satendra, Bapi, KK, Bandhan, Anil, Mayur, Shreya, Sangjukta, Arithra, Jhuma, Anwesha, Shrutika, Srirupa, and Harsita for supporting me through thick and thin. I would also like to thank all my batchmates and my dance team for making my life in IIT Guwahati so enjoyable.

Lastly, and also most importantly, I am extremely grateful to my parents, Mrs. Ranjana Dey and Mr. Dilip Kumar Dey who have taught me the virtues which make me who I am . They have filled my life with their unconditional love and blessings. I am thankful for the freedom, support and guidance they have given me at every step of my life.

Poulomi Dey

CONTENTS

CHAPTER 2: Bactericidal Activity of a Salicaldehyde-based Synthetic Amphiphile (C1)

ABBREVIATIONS

Π–A	Surface pressure–mean molecular area
μ	Specific Growth Rate
μg	Microgram
μL	Microliter
μM	Micromolar
Å	Armstrong
A_{600}	Absorbance at 600 nm
AFM	Atomic Force Microscope
AMPs	Antimicrobial peptides
ANS	8-Anilino-1-naphthalenesulfonic acid
ATR-FTIR	Attenuated total reflectance Fourier-transform infrared spectroscopy
BALB/c	Bagg and Albino laboratory-bred strain of the house mouse
BHI	Brain-heart infusion broth
BLAST	Basic local alignment search tool
bp	Base pair
cFDA-SE	5(and 6)-carboxyfluorescein diacetate succinimidyl ester
CFU	Colony forming unit
cps	Counts per second
CR	Congo red
CV	Crystal violet
C1	Compound 1
C2	Compound 2
$C1_M$	C1 Micelle
$C1_M$-A	Antibiotic Loaded C1 Micelle
$C1_M$-R	rifampicin-loaded C1 Micelle
$C1_M$-V	vancomycin-loaded C1 Micelle
CMC	Critical Micellar Concentration
cntA	Carnitine monooxygenase oxygenase subunit gene
cntL	L-histidine 2-aminobutanoyltransferase gene
C_T	cycle threshold
$DiSC_35$	3,3′-dipropylthiadicarbocyanine iodide
DLS	Dynamic light scattering
DMEM	Dulbecco's modified eagles medium
DMSO	Dimethyl sulfoxide

Abbreviations

DNA	Deoxyribonucleic Acid
D.P.X	Dibutylphthalate Polystyrene Xylene
ECM	extracellular matrix
EDTA	Ethylenediaminetetraacetic acid
EDX	energy-dispersive X-ray
EE	Encapsulation Efficiency
EPR	Enhanced permeability and retention
ESI-MS	Electrospray Ionisation Mass Spectrometry
FBS	Fetal bovine serum
FESEM	Field emission scanning electron microscope
FETEM	Field-Emission Transmission Electron Microscope
FIC	Fractional inhibitory concentration
fnbA	Fibronectin-binding protein A gene
FTIR	Fourier-transform infrared spectroscopy
G	Group
HEK	Human embryonic Kidney
HEPES	N-2-Hydroxyethyl Piperazine N-2 Ethane Sulphonic acid
HeLa	cervical cancer cells cultured from Henrietta Lacks
H&E	hematoxylin and eosin
HLB	Hydrophilic-lipophilic balance
hld	Delta-hemolysin gene
HT-29	Human Colorectal Adenocarcinoma Cell Line
IC_{50}	half maximal inhibitory concentration
ITC	Isothermal Titration Calorimetry
K_a	Association constant
k_d	Dissociation constant
kDa	Kilo Dalton
Kg	Kilogram
LB-Trough	Langmuir Blodgett Trough
LC	Loading Content
LE	Loading Efficiency
logP	Partition coefficient
LTA	Lipoteichoic acid
MBEC	Minimum Biofilm Eradication Concentration
MBIC	Minimum Biofilm Inhibitory Concentration
mg	Milli grams
MIC	Minimum inhibitory concentration

Abbreviations

MKC	Minimum killing concentration
mL	Milliliter
mM	Millimolar
MRSA	Methicillin resistant *Staphylococcus aureus*
MSSA	methicillin-susceptible Staphylococcus aureus
MSCRAMMs	Microbial surface component recognizing adhesive matrix molecules
MT	Mason's Trichrome
MTCC	Microbial Type Culture Collection, Institute of Microbial Technology (IMTECH), Chandigarh, India
MTD	Maximum Tolerated Dose
MTT	3-(4,5-Dimethylthylthiazol-2-yl)-2,5-diphenyltetrazolium bromide
MW	Molecular weight
MWCO	Molecular weight cut-off
NB	Nutrient Broth
NCIM	National Collection of Industrial Microorganism, National Chemical Laboratory (NCL), Pune, India
nm	Nanometer
NMR	Nuclear magnetic resonance
NPN	1-N-phenyl naphthylamine
OD_{600}	Optical density at 600 nm
OECD	Organization for Economic Co-operation and Development
o/w	oil in water
PBS	Phosphate buffered saline
PCR	polymerase chain reaction
p-DMAB	para-Dimethylaminobenzaldehyde
PI	Propidium iodide
PSM	phenol-soluble modulin
qRT-PCR	Real-Time Quantitative Reverse Transcription PCR
RBC	red blood corpuscle
RNA	Ribonucleic acid
rRNA	Ribosomal RNA
rpm	Revolutions per minute
RT	Room Temperature
SBF	Simulated body fluid
SD	Standard deviation
SGF	Simulated gastric fluid
SIF	Simulated intestinal fluid
S.S.	Stainless Steel

Abbreviations

stp	Staphylopine
SWF	Simulated Wound Fluid
TI	Therapeutic index
WBC	White Blood Cells
λ_{Em}	Emission wavelength
λ_{Ex}	Excitation wavelength

LIST OF TABLES

CHAPTER 5

CHAPTER 6

LIST OF SCHEMES AND FIGURES

Chapter 1

Introduction and Literature Review

Introduction

The emergence of antibiotic-resistant pathogenic bacteria is a global healthcare concern, which demands the development of a radical therapeutic approach. This impending crisis in conjunction with the sluggish pace of discovery of novel drugs has bolstered the need for the discovery of potent bactericidal agents that can act on profound cellular targets and are counterproductive to resistance development. In this regard, membrane-targeting antibacterials such as antimicrobial peptides (AMPs) hold special interest as the likelihood of developing resistance against them demands extensive renovation of membrane components, which can be a daunting challenge for the target bacteria. However, in the context of their therapeutic application, the high production cost, poor pharmacokinetics and protease sensitivity are serious bottlenecks. Under these circumstances, AMP-mimicking synthetic amphiphiles offer a promising therapeutic paradigm against drug-resistant pathogenic bacteria owing to their facile synthesis, possibility of generating structural variants in order to maximize their bactericidal potency, resistance to proteolysis and their potent membrane directed activity.

An archetypical feature of synthetic amphiphiles is their proclivity to self-assemble. Hence a membrane-targeting amphiphile can be rationally designed to self-assemble and yield a biocompatible micellar vehicle for delivery of therapeutic antibiotics. Such self-assembly driven composite synthetic antibacterial can conceivably breach the resistance and render synergy of two warheads by harnessing their activity in tandem, which may lead to a more efficient annihilation of the target pathogen. Metals play a pivotal role in the cellular physiology including growth and biofilm formation, virulence and manifestation of resistance during the infection process by pathogenic bacteria. Conceivably, membrane acting synthetic amphiphiles tethered with metal coordinating groups can be leveraged for disruption of metal acquisition and hinder infection by pathogenic bacteria. In the backdrop of seemingly continuous development of resistance against antibiotics, exploration of synthetic amphiphiles that can interfere with metal uptake emerges as a promising approach towards antibacterial drug development.

Based on the aforementioned premise, the present investigation ascertains the potential of a membrane-targeting synthetic amphiphile to self-assemble and yield antibiotic-replete micelles as a therapeutic platform against drug-resistant pathogenic bacteria. As metal binding synthetic amphiphiles offer new opportunities for therapeutic

intervention, the study also unravels a fundamental understanding of the impact of supramolecular interaction of synthetic amphiphiles with cell surface ligands vis-a-vis metal binding in the context of their bactericidal potential. The following section provides a detailed literature review pertinent to the research area of the present investigation.

Literature Review

1.1. An Overview of Antibiotic-Resistance in Pathogenic Bacteria

The emergence of antibiotic-resistant pathogenic bacteria is a burgeoning issue in contemporary healthcare. Pathogenic bacteria are empowered by a gamut of adaptations, which have rendered them highly resistant to prevalent therapeutic antibiotics. Further, an indiscriminate use of antibiotics in the therapeutic regime has induced the emergence of drug-resistant traits in pathogenic bacteria and this predicament has exacerbated the problem. Recognizing the need to highlight these grave concerns, the emergence and healthcare implications of antibiotic-resistant pathogenic bacteria has been articulated in a series of review articles (Peterson and Kaur, 2018; Petchiappan and Chatterjee, 2017; de Kracker *et al*., 2016; Fair and Tor, 2014, Wright, 2011; Davies and Davies, 2010; Fischbach and Walsh, 2009, Gootz, 2010, Nikaido, 2009; Alekshun and Levy, 2007).

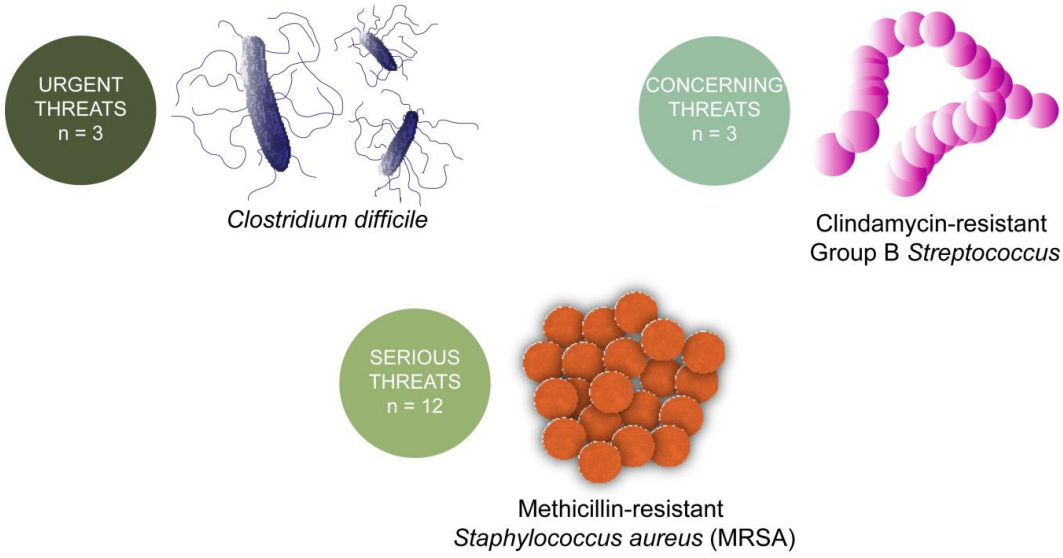

Figure 1.1. Antibiotic-resistant pathogenic bacteria categorized under various threat levels and a representative pathogen belonging to each of the categories. The threat levels are based on CDC report (2013).

Literature reports indicate that the principal clinically relevant drug-resistant pathogens include β-lactam resistant Pneumococci, penicillin and chloramphenicol-resistant *Neisseria meningitides*, vancomycin-resistant enterococci (VRE), vancomycin- resistant *Staphylococcus aureus* (VRSA) (Kaye and Kaye, 2000), methicillin-resistant *Staphylococcus aureus* (MRSA), penicillin-resistant *Streptococcus pneumoniae* (Lee *et al*., 2018; Tong *et al*., 2015; Lowy, 2003), multidrug-resistant *Salmonella typhimurium* (MRST) (Mather *et al*., 2013), multidrug-resistant *Acinetobacter*, carbapenem-resistant Enterobacteriaceae (CRE) and several others (Fair and Tor, 2014). The emergence of *Klebsiella pneumonia* NDM-1 has drawn lot of attention in recent times. This pathogen is potentially life-threatening and highly resistant to penicillin, cephalosporins and other lactam-based antibiotics owing to the presence of a metallo-β-lactamase-resistance gene (blaNDM.1) (Hawkey and Jones, 2009; Nordmann *et al*., 2011; Barantsevich *et al*., 2013; Brink *et al*., 2012; Jin *et al*., 2015; Arpin *et al*., 2012).

Global organizations such as the Centers for Disease Control (CDC) in the USA and the World Health Organization (WHO) have also highlighted the concerns regarding antibiotic-resistant pathogens in their published reports. For instance, it was stressed in a report published by the Centers for Disease Control (CDC) in the USA in 2013 that the human race is now in the "post-antibiotic" era (CDC Report, 2013). Based on the perceived threat levels, the pathogenic bacteria have been grouped under various categories by CDC (CDC Report, 2013). A schematic representation of the threat level and the representative pathogen belonging to a particular category is indicated in Figure 1.1. The World Health Organization (WHO) has opined that the antimicrobial resistance (AMR) crisis is becoming ominous and that the risk of mortality associated with infections caused by drug resistant-bacteria is twice in comparison to a non-resistant pathogen (WHO Report, 2014). In 2017, apart from multidrug-resistant and extensively-resistant *Mycobacterium* tuberculosis, WHO created a priority list of antibiotic-resistant bacteria to support research and development of antibacterial drugs (Tacconelli *et al*., 2017). The priority list was based on three tiers (critical, high, and medium priority) and is indicated in Table 1.1. In terms of statistics, the consequences and healthcare burden imposed by antibiotic-resistant pathogenic bacteria is quite ominous. For instance, as per the CDC report of 2013, of nearly 2.0 million people infected by pathogenic bacteria in United States, the number of annual deaths caused by antibiotic-resistant bacteria is 23,000 (CDC Report, 2013). A schematic illustrating the implications of antibiotic-resistant pathogenic bacteria is indicated in Figure 1.2.

Table 1.1. Priority list and representative antibiotic-resistant pathogenic bacteria proposed by WHO for research and development of new antibiotics.

Priority	Pathogenic Bacteria/ Family	Antibiotic-resistant Trait
Priority 1: Critical	*Acinetobacter baumannii*	Carbapenem-resistant
	Pseudomonas aeruginosa	Carbapenem-resistant
	Enterobacteriaceae	Carbapenem resistant, third generation cephalosporin resistant
Priority 2: High	*Staphylococcus aureus*	Methicillin-resistant, Vancomycin-resistant
	Helicobacter pylori	Clarithromycin-resistant
	Campylobacter spp.	Fluoroquinolone-resistant
	Salmonella spp.	Fluoroquinolone-resistant
	Neisseria gonorrhoeae	Third-generation cephalosporin-resistant, Fluoroquinolone-resistant
Priority 3: Medium	*Streptococcus pneumoniae*	Penicillin non-susceptible
	Haemophilus influenzae	Ampicillin-resistant
	Shigella spp.	Fluoroquinolone-resistant

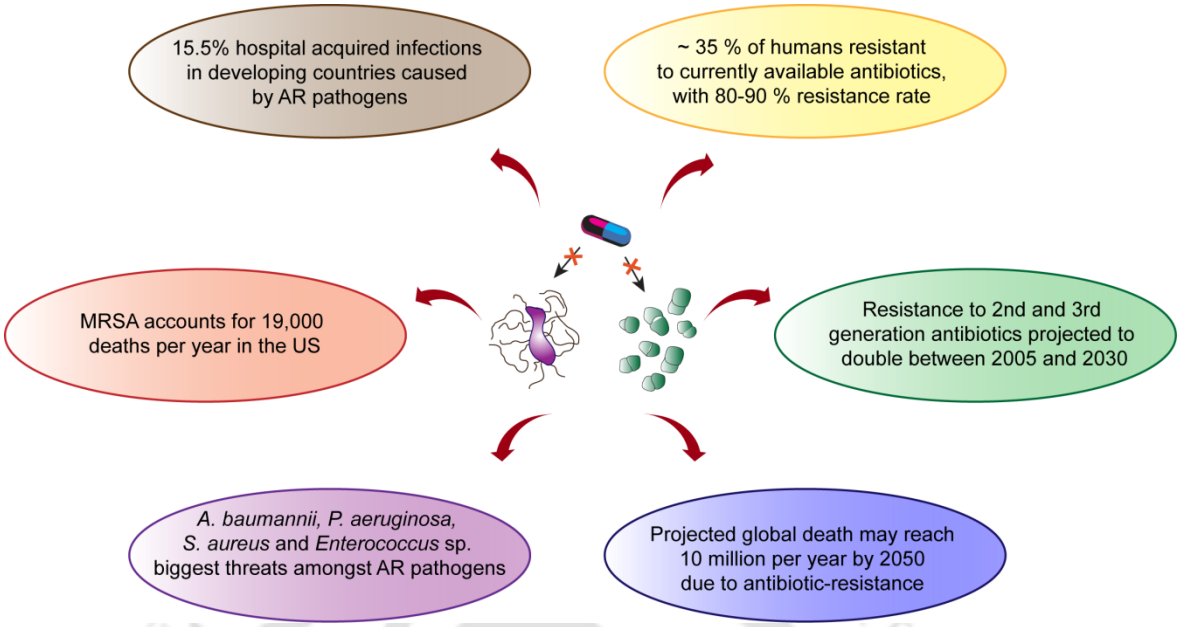

Figure 1.2. Significant clinical implications of antibiotic-resistant (AR) pathogenic bacteria. The statistics shown in the figure is obtained from CDC Report, 2013, WHO Report 2014 and Fair and Tor, 2014.

The timeline of the discovery of antibiotic classes seem to suggest that majority of them were discovered between 1930s-1960s. Since the 1960s, only six novel scaffolds have been approved following a nearly thirty-year innovation gap and a sluggish drug discovery research (Fair and Tor 2014; Silver, 2011; Fischbach and Walsh, 2009). Another model of the timeline of antibiotic discovery spanning 100 years from 1925-2025 proposes four major periods namely: (a) the golden era, (b) medicinal chemistry era, (c) resistance era and (d) narrow-spectrum era (Brown and Wright, 2016).

1.2. Antibiotic-Resistance Mechanism in Pathogenic Bacteria

Antibiotic-resistant pathogenic bacteria are empowered with complex and potent countermeasures that enable the bacteria to evade the action of most therapeutic antibiotics (Blair *et al*., 2015; Wright, 2011). The prevalent therapeutic antibiotics basically target essential physiological processes in cells such as DNA synthesis (Collin *et al*., 2011; Kohanski *et al*., 2010), cell wall synthesis (Hurdle *et al*., 2011; Lewis, 2013), protein synthesis (McCoy *et al*., 2011; Wilson, 2014) and folate synthesis (Lange *et al*., 2007; Palmer and Kishony, 2014). However, in pathogenic bacteria a number of attributes are present in order to evade the host defense mechanism and defy the action

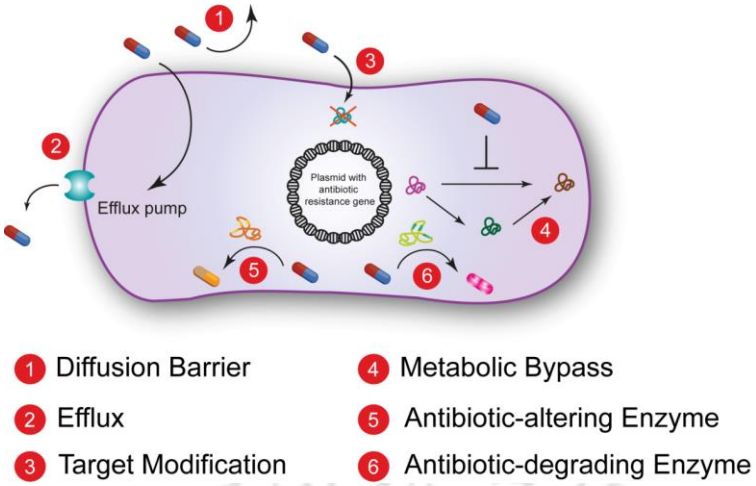

Figure 1.3. Schematic representation of various mechanisms of antibiotic-resistance prevalent in pathogenic bacteria

Table 1.2. Characteristic machinery of antibiotic-resistance in pathogenic bacteria.

Resistance Mechanism	Consequence	Reference
Lipopolysaccharide (LPS) barrier	Antibiotic-resistance in Gram-negative bacteria	Delcour, 2009
Peptidoglycan and wall teichoic acid (WTA) barrier	Antibiotic-resistance in Gram-positive bacteria	Weidenmaier and Peschel, 2008
Modified porin proteins	Reduced entry of antibiotic	Fernandez and Hancock, 2012
Efflux pump	Antibiotic expelled from cell	Li and Nikaido, 2009; Chambers and DeLeo, 2009
Antibiotic modifying and hydrolyzing enzymes	Inactivation of β-lactams, macrolides, aminoglycosides and choramphenicol	Gootz, 2010; Kumar and Varela, 2013; Wright, 2005
Target modification	Resistance against cationic antibiotics, quinolones, rifamycin, macrolides and β-lactam resistance	Gutsmann and Seydel, 2010; Kaye and Kaye, 2000; Wright, 2011

of antibiotics. Some of these features include (i) the presence of a permeability barrier that hinders diffusion of drugs, (ii) presence of an efflux pump that can export certain antibiotics and thereby reduce its effective concentration at target sites, (iii) alterations

in molecular targets, (iv) existence of a metabolic bypass reducing the sensitivity of the cell to the drug, (v) prevalence of enzymes that can either alter or degrade antibiotics (Nikaido, 2009, Wright, 2011). Moreover, indiscriminate and excessive use of antibiotics may lead to favorable selection of resistant cells and dissemination of the resistance trait from these cells through horizontal gene transfer can exacerbate the problem further (Davies and Davies 2010; Fair and Tor 2014, Toprak *et al*., 2012). A schematic representation of the various mechanism by which pathogenic bacteria can develop antibiotic-resistance is shown in Figure 1.3 and a summary of the essential features and consequences of the development of antibiotic-resistance in pathogenic bacteria is illustrated in Table 1.2.

1.3. Bacterial Biofilms

In the present study, the potential of synthetic amphiphile as an antibiofilm agent was investigated. Hence, in the following section, an overview of the essential features of biofilm, their role in causing infections and the challenges associated with antibiofilm therapy are outlined.

1.3.1. Characteristic Features of Biofilm

Bacterial biofilms are organized clusters of cells that have an inherent ability to adhere to a substratum and secrete an extracellular polymeric substance, known as matrix that promotes cell attachment and shields the cell (Flemming and Wingender, 2010; Archer *et al*., 2011; Kostakioti *et al*., 2013). Bacterial biofilms are largely involved in causing infections in humans such as periodontitis, chronic lung infection in cystic fibrosis patients and implant-associated infections and it has been estimated that treatment of these biofilm-based infections may amount to a staggering cost exceeding $1.0 billion annually (Parsek and Singh, 2003; Stewart and Costerton, 2001; Davies, 2003; Singh *et al*., 2000; Arciola *et al*., 2012; Worthington *et al*., 2013). The clinically relevant bacteria that form biofilms include *Staphylococcus aureus*, *Staphylococcus epidermidis* and *Pseudomonas aeruginosa*. As a consequence of the grave healthcare concerns of biofilms and their profound resistance towards antibiotics, development of antibiofilm agents has come to the limelight (Bordi and Bentzmann, 2011; Thompson *et al*., 2012; Piletska *et al*., 2011; Mintzer *et al*., 2012).

Bacterial biofilm formation is perceived as an alternative lifestyle wherein the switch from planktonic mode of growth to biofilm is a response to environmental signals,

leading to spatial and temporal restructuring of cells prior to biofilm formation under the control of regulatory networks (Lenz *et al*., 2008; Monds and O'Toole, 2009; O'Toole *et al*., 2000). The typical stages of biofilm formation constitute the following:

(a) At the onset, a reversible interaction of planktonic cells with the substratum is promoted by hydrophobic, van der Waals and electrostatic interactions (Aricola *et al*., 2012). Further, a stronger adhesion of cells to the substratum is mediated by proteinaceous ligands such as autolysins and adhesions (Heilmann *et al*., 1997).

(b) In the second step, biofilm establishment is mediated by Microbial Surface Components Recognizing Adhesive Matrix Molecules (MSCRAMMs) and intercellular adhesion (Patti *et al*., 1994; Speziale *et al*., 2009).

(c) Subsequently, biofilm maturation is accomplished.

(d) Finally, by cell dispersion the planktonic cells are set free to initiate a fresh cycle of invasion and colonization.

1.3.2. Challenges in Eradication of Biofilm

Bacterial biofilms display remarkable resistance towards therapeutic antibiotics as compared to the planktonic cells (Kostakioti *et al*., 2013; Hoiby *et al*., 2010). The extracellular polymeric matrix of biofilms constitutes a formidable barrier for diffusion of antibiotics (Flemming and Wingender, 2010; Kostakioti *et al*., 2013; Bordi and Bentzmann, 2011; Otto, 2008). Presence of high levels of metal ions and a low pH associated with the biofilm matrix may inactivate antibiotics (Kostakioti *et al*., 2013; Costerton *et al*., 2007). In biofilms, metabolically inactive persister cells can emerge, which display resistance towards antibiotics known to act on growing cells (Lewis, 2008;

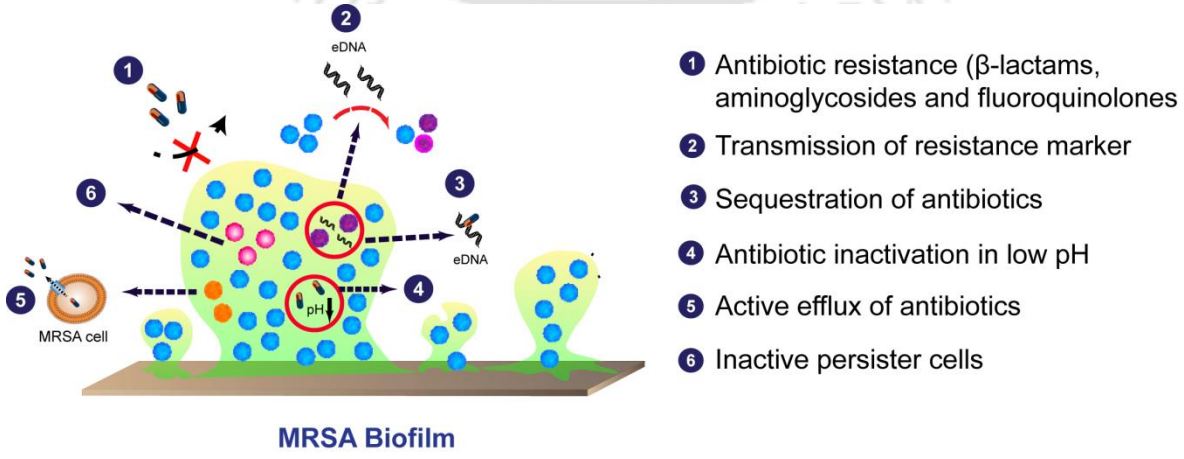

Figure 1.4. Principle therapeutic challenges associated with a bacterial biofilm.

Fux *et al*., 2005; Stewart and Costerton, 2001). In some cases, the released extracellular DNA (eDNA) from biofilm has been shown to chelate cations and sequester antibiotics. The essential challenges associated with the treatment of biofilms is indicated in the cartoon shown in Figure 1.4.

1.3.3. Methicillin-Resistant Staphylococcus aureus (MRSA) Biofilm

In the present investigation, the potential of the generated amphiphile as a bactericidal and antibiofilm agent against a clinical strain of MRSA was also tested. Hence in the following section, a brief overview on the antibiotic-resistance and the problems and pointers in anti-MRSA therapy is discussed. MRSA is not only prevalent in hospital-acquired infections, but is also implicated in community-acquired infections (Lee *et al*., 2018, Tong *et al*., 2015; Deresinki, 2005; Stryjewski and Corey, 2014). MRSA has evolved as multi-drug resistant strain and resistance to a prevalent therapeutic antibiotic such as vancomycin have been reported (Deresinski, 2009; Rehm and Tice, 2010). Similarly, daptomycin-resistant MRSA strains have also been reported (Hayden *et al*., 2005; Marty *et al*., 2006). A plethora of efflux pumps are involved in rendering resistance against biocides and therapeutic antibiotics in MRSA (Kaatz *et al*., 1993; Floyd *et al*.,

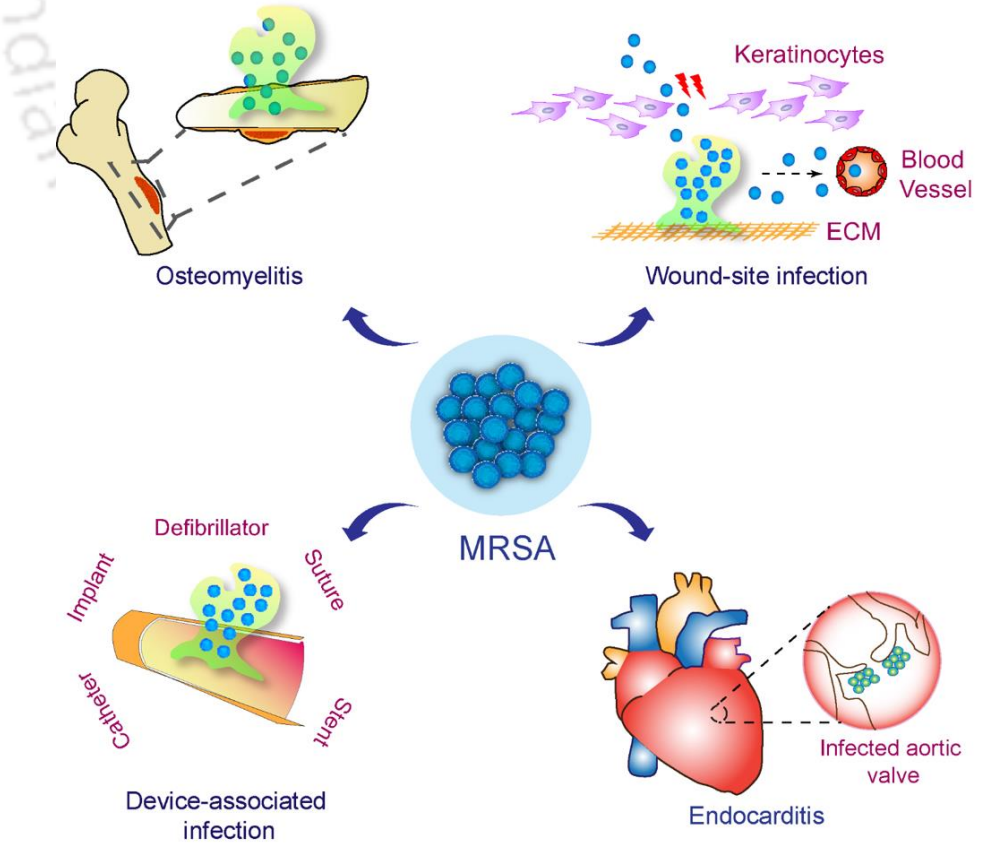

Figure 1.5. Representative healthcare implications of MRSA biofilm.

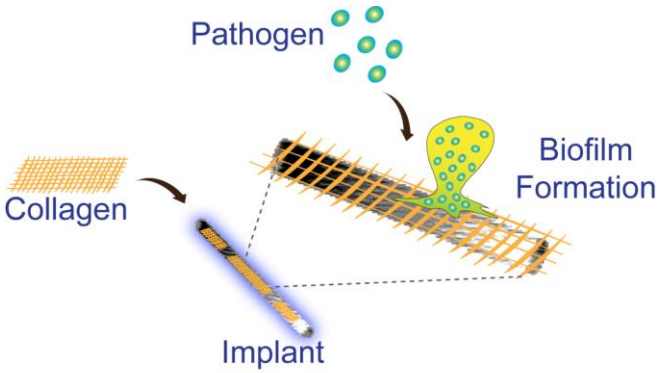

Figure 1.6. Cartoon illustrating collagen deposition on medical implant leading to biofilm formation.

2010; Kaatz *et al*., 2005). MRSA biofilm is implicated in a large number of infections in both tissues as well as implants (Stoodley *et al*., 2011; Oliveira *et al*., 2018; Shah *et al*., 2013; Darouiche, 2004; Ribeiro *et al*., 2012). A schematic representation of the major infections caused by MRSA biofilm is indicated in Figure 1.5. A significant number of hospital-acquired infections are caused by biofilm formation on medical devices, resulting in tissue destruction, systemic dissemination of the pathogen and malfunctioning of the device, which can result in fatality (Hall-Stoodley *et al*., 2004; Bryers, 2008; Darouiche, 2001). In the context of colonization of implantable medical devices by MRSA biofilm, human matrix proteins such as collagen, which are known to deposit on the device's surface can promote the initial attachment of MRSA cells and thereby trigger biofilm formation as indicated in the cartoon shown in Figure 1.6.

1.3.4. Genetic Basis of Biofilm Formation

Literature has provided evidence that the development of staphylococcal biofilm is controlled by an intricate network of signal molecules, which either activate or inhibit the expression of key biofilm components (Aricola *et al*., 2012). Expression of the *ica* operon genes and biofilm production in *S. aureus* has been shown to be dependent on environmental factors (Baldassarri *et al*., 2001; Cramton *et al*., 2002). In *S. aureus*, a matrix-associated adhesin known as a biofilm-associated protein (Bap) has been shown to influence biofilm formation (Cucarella *et al*., 2001). Other adhesins such as the fibronectin-binding proteins (FnBPA and FnBPB) were characterized and these adhesins are integral components of a proteinaceous biofilm in *S. aureus* (O'Neill *et al*., 2008;

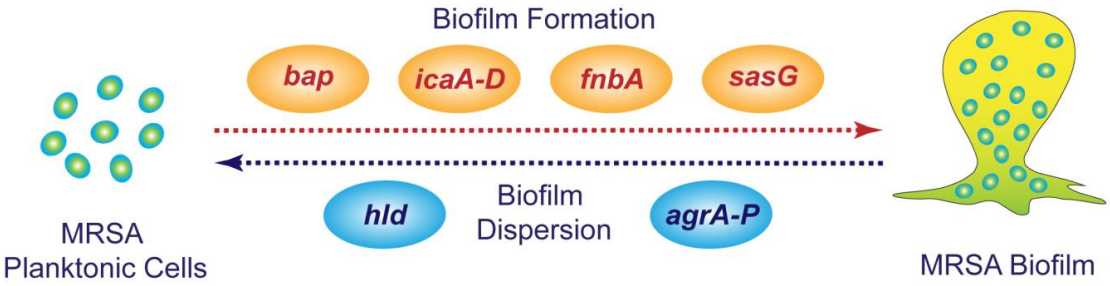

Figure 1.7. Key genes involved in *S. aureus* biofilm formation and dispersion.

Vergara-Irigaray *et al*., 2009). In *S. aureus*, quorum sensing is also involved in biofilm formation and in this context, the role of the accessory gene regulator (*agr)* system in *S. aureus* biofilm formation has been demonstrated (Vuong *et al*., 2000). The polysaccharide intercellular adhesin poly-N-acetyl-1-6-glucosamine (PNAG) encoded by *ica* operon (*icaADBC*), which enables *S. epidermidis* and *S. aureus* to form biofilm is controlled by the regulatory locus *sarA* (Diemond-Hernandez *et al*., 2010; Trotonda *et al*., 2005). In *S. aureus*, SasG is a surface protein that is implicated in biofilm formation. In presence of physiological levels of Zn^{2+}, SasG can dimerize and promote cell-cell adhesion (Geoghegan *et al*., 2010). The autolysins encoded by set of *atl* genes in *S. epidermidis* and *S. aureus* facilitate primary substratum attachment of cells in the process of biofilm development (Molin and Tolker-Nielsen, 2003). The effector molecule of the *agr* system is RNAIII, a regulatory RNA, which also codes for the 26 amino acid δ-toxin (*hld*) and is involved in *S. aureus* biofilm dispersion (Aricola *et al*., 2012). A schematic representation of the key genes involved in biofilm formation and dispersion in *S. aureus* is indicated in Figure 1.7.

1.4. Rational in Target Selection and Drug Design against Antibiotic-Resistant Pathogens In the context of drug discovery against antibiotic-resistant bacterial strains, the following rational can be considered to be key factors:

(a) Selection of vital cellular targets, which are germane to the survival and virulence of the target strain (Johnston *et al*., 2016)

(b) Selection of targets that lack structural homologs in the mammalian host

(c) Develop candidate antibacterials having optimum pharmacodynamic and pharmacokinetic attribute (Mueller *et al*., 2004; Silver, 2011; Onufrak *et al*., 2016).

(d) Develop antibacterials which are non-toxic to host cells, even at concentrations higher than their MIC (Wispelwey, 2005).

(e) Develop antibacterials which are less likely to induce resistance development.

1.4.1. Membrane as a Target

Considering the above criteria, membrane-targeting agents hold considerable therapeutic potential against antibiotic-resistant pathogens. Unlike antibiotics that are known to target specific biochemical and physiological processes and are thus liable to resistance development, the chances of resistance development against membrane-targeting agents is less as it entails major restoration of membrane components, which is challenging for the target bacteria (van Bambeke *et al*., 2008; Hurdle *et al*., 2011).

1.4.2. Targeting Metal Acquisition

Besides developing membrane-targeting agents, hindering the process of metal acquisition may offer interesting opportunities for therapeutic intervention against MRSA given that metals are critical to establishment of virulence and the infection process of staphylococci (Corbin *et al*., 2008; Remy *et al*., 2013; Hood and Skaar, 2012; Kehl-Fie, *et al*., 2011). In this context, Schiff bases and their complexes with Cu and Fe have been explored as antibacterial agents against *S. aureus* (Negm and Zaki, 2008). Studies have also shown that biologically active compounds and a pyridinium-based amphiphile displayed higher antibacterial activity upon chelation with metal ions (Chohan *et al*., 2002; Goswami et al., 2015). In pathogenic bacteria, metal transporters are frequently implicated in cellular acquisition of metals needed for critical physiological processes. In *S. aureus*, such a transporter is the staphylopine, which plays

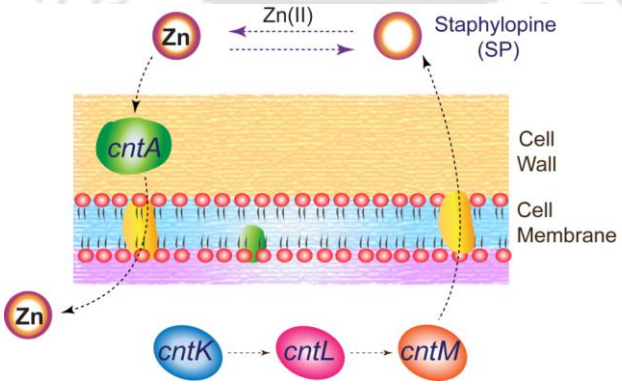

Figure 1.8. Cartoon indicating the genes *cntKLM* involved in staphylopine synthesis and the gene *cntA* involved in the transport of zinc by complexation with staphylopine in *S. aureus*.

a vital role in zinc acquisition (Grim *et al.*, 2017; Capdevila *et al*., 2016; Ghssein *et al*., 2016). A cartoon depicting the role of the essential genes *cntKLM* involved in staphylopine synthesis and the gene *cntA* implicated in the transport of zinc by complexation with staphylopine is shown in Figure 1.8. It would thus be appealing to decipher the effect of metal complexing ligands on the expression levels of these genes.

1.5. Potential of Membrane-Targeting Antimicrobial Peptides (AMPs)

Antimicrobial peptides (AMPs) are prototype membrane acting agents, which are ubiquitous in all organisms and possess a broad-spectrum antibacterial activity (Hancock and Sahl, 2006; Shai, 2002, Zasloff, 2002). It is well recognized that the cationic charge of AMPs interacts with anionic bacterial cells, while the hydrophobic scaffold of AMPs penetrates and disrupt membrane integrity (Wimley, 2011; Brogden, 2005; Yeaman and Yount, 2003; Chen *et al*., 2010). The models that provide explanations for AMP-mediated membrane permeabilization are the barrel-stave, toroidal pore and carpet model (Hurdle *et al*., 2011; Wimley, 2011). Despite their potent activity, the therapeutic potential of AMPs is hampered by several factors such as: (a) prohibitive manufacturing cost (Marr *et al*., 2006), (b) Challenges in drug formulations (Findlay *et al*., 2010), (c) loss of *in vivo* activity in presence of mono and divalent cations (Bowdish *et al*., 2005) and (d) proteolytic inactivation (Marr *et al*., 2006, Yeaman and Yount, 2003).

1.6. Synthetic Amphiphiles as AMP-Mimicking Antibacterials

Extensive research in the area of medicinal chemistry has led to the generation of AMP-mimicking synthetic amphiphiles. As opposed to AMPs, synthetic amphiphiles offer several advantages such as (a) Structural variability introduced through synthesis, which allows a library of scaffolds to be generated, with varying head groups, varying length of hydrophobic tail, metal binding attributes, etc., (b) Membrane-directed activity to counter antibiotic-resistant pathogens, (c) Functionalization with a fluorophore for sensing applications, (d) Resistance to proteolysis, (e) High antibacterial selectivity accomplished by prudent choice of functional groups, (f) Leveraging the self-assembly attribute of amphiphile to generate a micellar carrier for antibiotic delivery. A schematic illustrating the aforementioned traits of synthetic amphiphiles is shown in Figure 1.9. Conventionally synthetic amphiphiles essentially consist of a hydrophilic/polar head group e.g. phosphates, heterocyclic aromatic/non-aromatic rings, amines, hydroxyl or

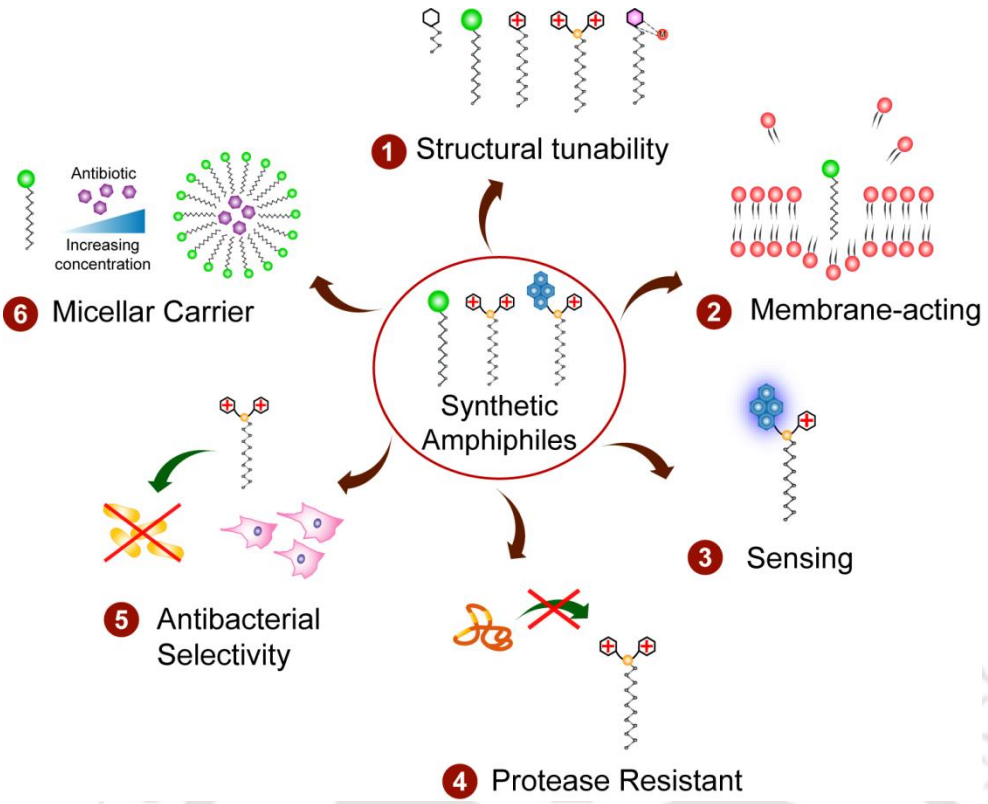

Figure 1.9. Cartoon illustrating various attributes of synthetic amphiphiles.

acidic groups and a hydrophobic moiety, which is typically a long hydrocarbon chain. Based on the nature of the charge on the head group, amphiphiles can be categorized as cationic, anionic, zwitterionic or nonionic (Ramanathan *et al*., 2013). On the basis of the number and type of connection of polar head(s)/hydrophobic tail(s) amphiphiles can be categorized as: single head/single tail amphiphiles, bolaamphiphiles having two hydrophilic heads, gemini amphiphiles consisting of two hydrocarbon tails and two ionic groups linked by a spacer, a double or triple chain amphiphiles and catanionic amphiphiles, which encompasses oppositely charged surfactants (Sorrenti *et al*., 2013). Apart from the conventional amphiphiles, an up-and-coming research area is on supra-amphiphiles, which are essentially based on noncovalent interactions (Kang *et al*., 2014).

1.7. Self-Assembly of Amphiphiles and Drug Delivery Applications

Synthetic amphiphiles are surface-active molecules and hence display the characteristics attributes of surfactants. One such archetypical feature of synthetic amphiphiles is their proclivity to self-assemble. This phenomenon is basically driven by non-covalent interactions and the medium that can trigger the formation of various levels of complex

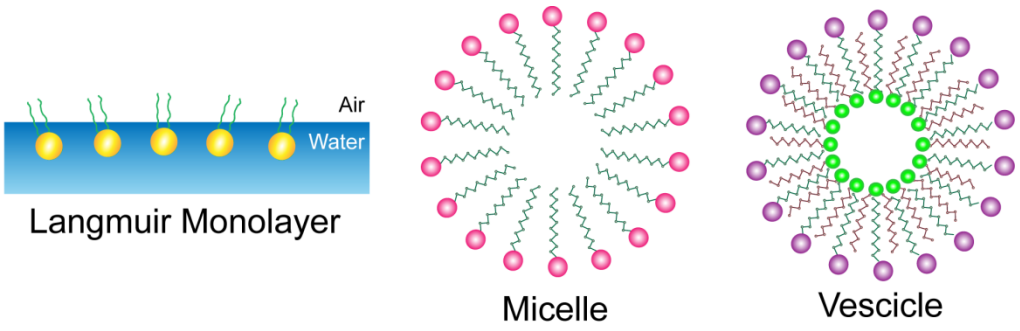

Figure 1.10. Formation of representative molecular aggregates by synthetic amphiphiles.

molecular aggregates as indicated in Figure 1.10. The origin of self-aggregated supramolecular assemblies stems from the ratio between the size of the hydrophilic and the hydrophobic moiety as well as the nature of the solvent. While micelles and vesicles are common self-assemblies of amphiphiles formed in water, scanning electron microscope and other powerful techniques have revealed a gamut of structural variations for these aggregates such as micellar rods, bilayers, helical and tubular aggregates (Sorrenti *et al*., 2013; Ramanathan *et al*., 2013).

The self-assembly of synthetic amphiphiles can be modulated through metal coordination. Complexation with metals may result in a change in the ionic charge or molecular geometry of an amphiphile, which in turn, may trigger a prominent morphological change of the aggregate (Owen *et al*., 2007). Literature reports indicate metal-dependent phase changes, from planar lamellae to a reversed hexagonal phase for the natural surfactant cardiolipin (Vasilenko *et al*., 1982; Vail *et al*., 1979; Rand and Sengupta, 1972). In case of marinobactins it has been demonstrated that coordination with Fe (III) can lead to structural changes from micelles to large vesicles Owen *et al*., 2007. Owen *et al*., 2005. Martinez *et al*., 2003). Transition of synthetic single-tailed amphiphiles into vesicles upon coordination of transition-metals has also been reported (Luo *et al.*, 2002; Apostol *et al.*, 2005).

A large number of studies have also revealed the potential of self-assembling amphiphiles in drug encapsulation and its delivery for various therapeutic applications (Gaucher *et al*., 2005; Puri *et al*., 2009; Bartolami *et al*., 2016; Zheng *et al*., 2011; Zhang *et al*., 2009). Bactericidal activity of self-assembling amphiphiles have been reported in the literature. For instance, self-assembling palmitic (C16) and stearic (C18) fatty acid microcrystallite interfaces were observed to be efficient antibacterial nanocoatings (Ivanova *et al*., 2017). In another work, a self-assembling polymer block-chitosan based

cationic micelles loaded with triclosan was interacted with poly-acrylic acid to generate a multilayer film, which emerged as a self-protective antibacterial coating (Wang *et al*., 2017). Surface tethering of vesicular structures self-assembled from oligonucleotide-polymer hybrids was accomplished by hybridization and the resulting soft surface could hinder bacterial colonization (Cottenye *et al*., 2012). Self-assembled nanoparticles have also been employed to encapsulate rifampicin and produce an aerosol (Ishikawa *et al*., 2016). pH-responsive chitosan nanoparticles containing an anionic gemini surfactant were used for loading vancomycin and were shown to exhibit anti-MRSA activity (Kalhapure *et al*., 2017).

1.8. Bactericidal Activity of Synthetic Amphiphiles: Structure-Function Relationship

Membrane-targeting synthetic amphiphiles have emerged as promising lead molecules to generate effective therapeutic agents against antibiotic-resistant pathogenic bacteria (Findlay *et al*., 2010; Gokel and Negin, 2012; Thiyagarajan *et al*., 2014). Evidence from literature reports seem to unequivocally converge on the notion that the design and structure of amphiphiles are critical determinants of their bactericidal potential. In one of the early studies, it was observed that synthetic di- and trimethyl-substituted phosphonium salts containing alkyl chains of varying lengths exhibited higher bactericidal activity than polymeric quaternary ammonium salts with the same hydrophobic structure (Kanazawa *et al*., 1994). With regard to structure-function relationship, it has been shown that the bactericidal activity of cationic amphiphilic polymethacrylate derivatives can be heightened by modulating the charge, hydrophobicity and molecular weight (Kuroda and DeGrado, 2005). An increase in the length of the alkyl side chain of low molecular weight random methacrylamide copolymers translated into higher antimicrobial activity (Palermo *et al*., 2009). In another study, amphiphilic aminoglycoside antibiotics were generated wherein neomycin B-derived heptaphenyl carbamate exhibited superior potency against MRSA in comparison to the parental neomycin B scaffold (Bera *et al*., 2010). A large number of studies have indicated that multiplicity of cationic head groups, position of the head group and alkyl chain length of amphiphiles can influence their bactericidal activity (Haldar *et al*., 2005; Jiang *et al*., 2008; Mitra *et al*., 2009; LaDow *et al*., 2011). In a comprehensive study, the balance of spacer distance, hydrophobicity, and charge was investigated and their roles were deciphered in the context of the bactericidal activity of amphiphilic polymers (Song *et al*., 2011).

In case of quinoline-based synthetic amphiphiles, the antimicrobial activity was enhanced by imparting a cationic charge and increasing the alkyl chain length (Vudumula *et al*., 2012). For pyridinium amphiphiles, double cationic heads and a 12 carbon chain length tail yielded the best antibacterial activity (Goswami *et al*., 2013). A similar observation was noted for gemini surfactants, whose activity was higher with the increase of alkyl chain length (Zhang *et al*., 2015). The antibacterial activity of tris-cationic, triple-headed, double-tailed amphiphiles were evaluated wherein the bactericidal activity was increased with tail length, with the best activity obtained when the derivatives had two 12 carbon chains (Marafino *et al*., 2015). Quaternary ammonium compound-based amphiphilic scaffolds have been shown to be promising antibacterials (Jennings *et al*., 2015). Amphiphilic neamine conjugates bearing a metal binding motif have been shown to be potent antibacterials that can permeabilize the membrane and also inhibit efflux pump activity (Allam *et al*., 2017). AMP-mimicking xanthone-based amphiphiles were generated that displayed high membrane-directed activity and antibacterial selectivity and were also efficient in mitigating corneal infection in a mice model (Lin *et al*., 2017). In case of dialkyl cationic amphiphiles, the amphiphilic balance, length of the alkyl chain and types of amino acids tethered to the compounds were critical in the context of their antibacterial activity (Zhang *et al*., 2018). Cationic amphiphilic polyproline helices (CAPHs) were synthesized, which displayed cell penetrating attributes and could thus be employed for elimination of intracellular bacterial pathogens (Nepal *et al*., 2018). Cationic antibacterial polymers have been synthesized that exhibit local facial amphiphilicity. Amongst these amphiphiles, cholic acid derivatives with three charged head groups were more effective than lithocholic and deoxycholic counterparts (Rahman *et al*., 2018). In case of bis quarternary ammonium amphiphiles (bisQAC), a strong anti-MRSA activity could be related with the length of nonpolar side chains and amide containing side chains (Kontos *et al*., 2019). In a recent study, it was demonstrated that supramolecular self-associating amphiphiles (SSAs) can be engaged to bring about a synergy and effectively target MRSA (Tyuleva *et al*., 2019). Based on recent available literature reports, an overview of bactericidal synthetic amphiphiles is presented in Table 1.2.

Table 1.3. Overview of bactericidal synthetic amphiphiles.

Sl. No.	Amphiphile	Target Bacteria	MIC Range	Reference
1.	Biscationic Tartaric Acid-based Amphiphiles	*S. aureus, L. monocytogenes, E. coli, P. aeruginosa*	12.5-125 µM	Faig *et al*., 2015
2.	Lysine Norspermidine Conjugates	*S. aureus, E. faecium, MRSA, VREF, K. pneumoniae*	1.2 -250 µM	Konai and Halder, 2015
3.	Quartenary Ammonium Compound-based Amphiphile	MRSA and MSSA	1.2 -250 µM	Jennings *et al*., 2015
4.	Amphiphilic Neomycin and Neosamine Derivatives	*S. aureus, P. aeruginosa*	0.5-8 µM	Zimmermann *et al*., 2016
5.	Amphiphilic Helical Peptides	*E. coli, MRSA, Salmonella, L. monocytogenes, M. luteus, Bacillus, Shigella, P. fluorescens*	0.21-142.3 µM	Ma *et al*., 2016
6.	Cationic Amphiphiles	*S. aureus, L. monocytogenes E. coli, S. typhimurium P. aeruginosa*	1.9 - > 250 µg/mL	Zhang *et al*., 2017
7.	Amphiphilic Neamine Conjugate	*E. coli, E. erogenes*	2.0 - 128 µM	Allam *et al*., 2017
8.	Xanthone Amphiphile	*S. aureus, MRSA, B. Cereus*	0.78 - > 50 µg/mL	Lin *et al*., 2017
9.	Dialkyl Cationic amphiphiles	*S. aureus, E. faecalis, E. coli, S. enterica, MRSA, Carbapenem-resistant Enterobacteriaceae (CRE)*	<0.125 - >128 µg/mL	Zhang *et al*., 2018
10.	Amphiphilic Nanodots	*E. coli, S. aureus, P. aeruginosa*	125 - 250 µg/mL	Xu *et al*., 2018
11.	Facial Amphiphile	*S. aureus, P. aeruginosa, E. coli*	3.0 - 56.8 µg/mL	Rahman *et al*., 2018

Table 1.3. Overview of bactericidal synthetic amphiphiles.

Sl. No.	Amphiphile	Target Bacteria	MIC Range	Reference
12.	Amphiphilic quaternary Ammonium Derivatives of Quinuclidine	*S. aureus, B. cereus, P. aeruginosa, E. coli*	0.4 - > 500 µg/mL	Burilova *et al*., 2018
13.	Amphiphilic Aminoglycoside	*S. aureus, P. Aeruginosa*	1.0 - > 128 µg/mL	Zimmermann *et al*., 2018
14.	Amphiphilic Polyproline	*Salmonella, Shigella, Listeria*	8.0 - 32 µM	Nepal *et al*., 2018
15.	Alkyl Rhamnosides	*S. aureus, P. aeruginosa*	39.1 - > 10 × 10^3 nM/mL	Peng *et al*., 2019
16.	Synthetic Ionophores (Hydraphiles)	*S. aureus, MRSA, E. faecalis, S. pneumoniae, K. pneumoniae, A. baumannii, P. aeruginosa, E. coli, S. enterica, MRSA, Carbapenem-resistant Enterobacteriaceae (CRE)*	1.5 - > 100 µM	Patel *et al*., 2019
17.	Self-associating Amphiphiles	*MRSA*	MIC_{50} = 0.46 mM	Tyuleva *et al*., 2019
18.	Biscationic Quaternary Ammonium Amphiphiles	*S. aureus, MRSA, E. faecalis, P. aeruginosa, E. coli*	0.25 - > 250 µM	Kontos *et al*., 2019
19.	Cationic Peptide Amphiphiles	*S. aureus, MRSA, P. aeruginosa, E. coli K. pneumoniae, A. Baumannii*	1.0 - 8.0 µg/mL	Almeida *et al*., 2019
20.	Cationic Amphiphiles	*L. monocytogenes, E. coli*	2.6 - > 250 µg/mL	Moretti *et al*., 2019

1.9. Cytotoxic Potential of Synthetic Amphiphiles

Literature reports suggest that to achieve optimum antimicrobial activity and avoid inadvertent cytotoxic effects, a judicious balance between hydrophilic and hydrophobic

moieties is critical as vindicated for pyridinium head group-based amphiphilic hydrogelators (Brahmachari *et al*., 2010) and quaternary ammonium head group based gemini amphiphile (Hoque *et al*., 2012). In case of synthetic dipeptide-based cationic amphiphiles, the charge and the number of hydrophobic amino acids present in the peptide chain were critical for biocompatibility and high antibacterial selectively high antimicrobial activity (Mitra *et al*., 2009). In case of low molecular weight random methacrylamide copolymers, the alkyl chain length and mole fraction of alkyl chain were important determinants of hemolytic and membrane-disrupting activity (Palermo *et al*., 2009). In another study it was deciphered that proper balance of spacer distance, hydrophobicity, and charge was critical to achieve high biocompatibility for hydrocarbon polymers (alternating copolymers, random copolymers, and homopolymers) with cationic and hydrophobic groups (Song *et al*., 2011). Further, for polymeric amphiphiles molecular weight, charge density, cationic functionalities, structure and sequence and conformational flexibility of the molecule were critical for reducing the cytotoxic effect (Fischer *et al*., 2003). In an interesting study, it was deciphered that the presence of block copolymers enhances the selectivity of macromolecular amphiphiles against bacteria over human cells (Oda *et al*., 2011).

1.10. Animal Models to Validate Therapeutic Potential of Antibacterials

A key aspect in the characterization of new antibacterials is the validation of their therapeutic potential. The initial tests can encompass *in vitro* cytotoxicity assays, which offer certain advantages such as the ease of the experimental protocol and rapid assay time. However, assessment of a holistic effect such as the adverse consequences on blood parameters or on certain vital organs cannot be accomplished. Hence, to strengthen the tests, animal models are proposed as they can serve as a reliable bridge between *in vitro* efficacy and initial clinical evaluation of antibacterials. Further, animal models allow to study the effect in the context of neighboring cells, complex environmental milieu consisting of body fluids as well as in the midst of host response. With regard to the choice of the animal model, mice are largely considered as suitable models to study infectious diseases as they are small, easy to maintain, thereby allowing experiments with large number of animals in order to obtain a statistically significant result. Moreover, in case of wound models, the process is facile, and reproducible for studying earlier phases of wound healing (Dai *et al*., 2011; Chen *et al*., 2015).

S. aureus is known to colonize human skin. In case of a skin injury, breakage of the skin may cause a wound infection, that can manifest as abscesses, carbuncles, and also disseminate into the blood stream (Archer, 1998; Watkins, *et al*., 2012; Tong *et al*., 2015). Staphylococcal infection of a skin wound can delay the wound healing process. In case of a skin wound mice model, the healing process of the wound is likely to proceed through various defined stages as depicted in Figure 1.11. The normal skin wound healing process has been elucidated (Delavary *et al*., 2011) and includes the following essential steps:

(a) Phase I: Hemostasis- herein, platelets aggregate and a blood clot is formed
(b) Phase II: Inflammation - herein, neutrophils populate the wound area and stimulate differentiation of monocytes to M1macrophages (Werner and Grose, 2003), which clear senescent cells and debris and help in stimulation of collagen production, angiogenesis and re-epithelialization (Baum and Arpey, 2005).
(c) Phase III: Proliferation - consists of granulation phase, and collagen production.
(d) Phase IIIa: Angiogenesis - encompasses the formation of new capillaries from pre-existing blood vessels
(e) Phase IIIb: Re-epithelialization - which forms an epidermis over the new tissue.
(f) Phase IV: Remodeling - herein essentially collagen is remodeled and fibrils are organized.

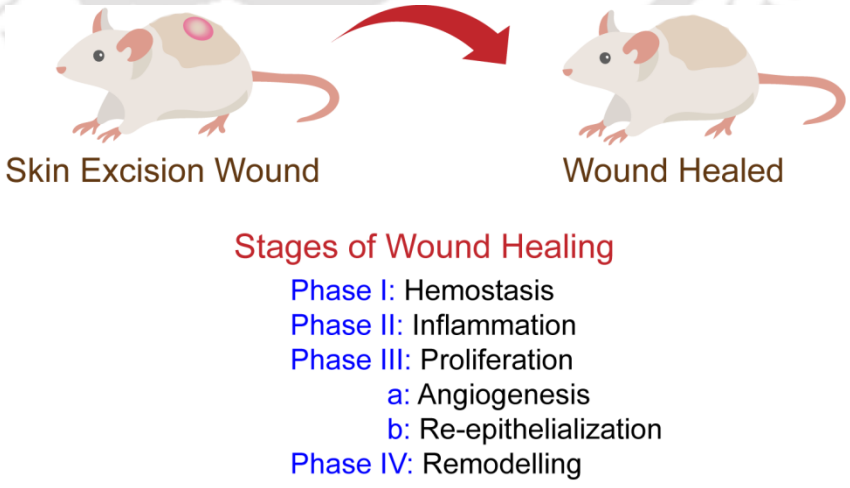

Figure 1.11. Various stages of the wound healing following an excision wound in a mice model.

Literature reports describe animal models for studying skin and soft tissue staphylococcal infection (Marra, 2014; Dai *et al*., 2011). In a study, the *in vivo* bactericidal potential of a synthetic antibacterial was evaluated against MRSA in the normal dorsal skin of mice (Inoue *et al*., 2015).

In another study, it was shown that topical application of mupirocin and retapamulin ointments could reduce MRSA counts in a wound infection model in mice (Guo *et al*., 2013). In another study, a tape stripping model in mice was developed to evaluate the potential of topical antibiotic applications in superficial skin infections caused by *S. aureus* (Kugelberg *et al*., 2005). In a burn wound infection model in mice, daptomycin application could promote wound healing (Simonetti *et al*., 2017).

MOTIVATION AND OBJECTIVES OF THE PRESENT INVESTIGATION

MOTIVATION AND OBJECTIVES OF THE PRESENT INVESTIGATION

The origin of the present research investigation and the principal motivating factors emerge from the following considerations:

(1) The high resistance of pathogenic bacteria towards frontline antibiotics is a serious healthcare concern. The bacterial membrane can be considered as an Achilles heel and thus membrane-targeting antibacterials are perceived to thwart resistance development.

(2) Membrane-targeting synthetic amphiphiles offer considerable promise as antibacterials owing to their facile synthesis, the potential to generate a large number of lead scaffolds through rational structural design and their resistance to proteolysis.

(3) The proclivity of synthetic amphiphiles to self-assemble in solution is a fundamental attribute that can have a significant bearing on its therapeutic potential. Hence, it is imperative to conduct a nuanced evaluation of how self-assembly influences the bactericidal and cytotoxic potential of amphiphiles.

(4) On the other hand, self-assembly of membrane-targeting synthetic amphiphiles can perhaps be leveraged to develop a nano-micellar carrier for delivery of therapeutic antibiotics. Assimilation of two warheads in a single entity could render significant benefit as the adjuvant activity of one warhead breaks the resistance and paves the way for the counterpart to exert a profound bactericidal effect.

(5) Given the integral role of metals in the physiology and infection process of pathogenic bacteria, the potential to engage membrane acting synthetic amphiphiles endowed with an additional attribute of metal binding augers well in the light of limited therapeutic options against infections caused by drug-resistant pathogenic bacteria.

(6) In order to explore metal-binding synthetic amphiphiles as emerging chemotherapeutics against antibiotic-resistant pathogenic bacteria, it is paramount to acquire a nuanced understanding of the effect of supramolecular interaction of synthetic amphiphiles with bacterial cell surface ligands as well as the impact of metal binding on

the bactericidal potential of the synthetic amphiphile. The outcome of the study is likely to provide a foundation and a guiding design principle for the development of pluri-active and potentially therapeutic synthetic antibacterials.

(7) It is imperative that the therapeutic potential of bactericidal synthetic amphiphiles is validated by using models, which can mimic clinical problems such as device- and extracellular matrix- associated biofilm infection and ascertain the in vivo toxicity and wound healing potential of the molecule in an appropriate animal model.

Design Principle of Synthetic Amphiphiles used in the Investigation:

Amphiphiles having either a salicaldehyde head group referred as compound 1 (C1) or a napthaldehyde head group referred as compound 2 (C2) were synthesized, each having a 12-carbon alkyl chain (Figure 1.12). The amphiphilic nature of C1 and C2 render a membrane-targeting ability to the molecules (Figure 1.12), whereas the self-assembly of amphiphiles supported by their hydrophobic tail, intermolecular hydrogen bonding and Π-stacking interactions of the head group, can perhaps be leveraged to form a micelle, encapsulate antibiotics and generate a composite antibacterial (Figure 1.12). The head groups of the amphiphiles can also participate in hydrogen bond interaction with

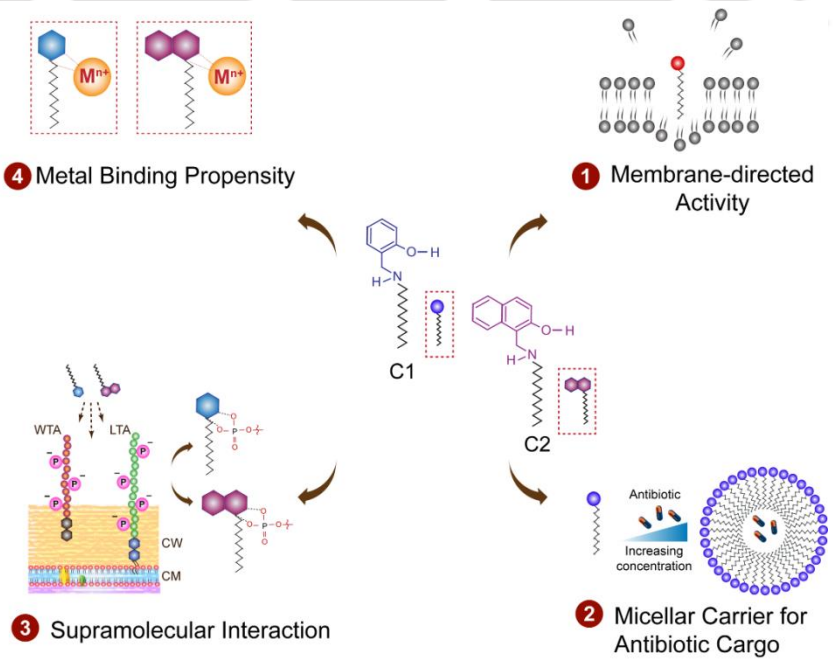

Figure 1.12. Design principle of the synthetic amphiphiles used in the present investigation.

phosphoryl groups of teichoic acid present in bacterial cell wall and thereby promote targeting of the amphiphile onto the cell surface (Figure 1). Further, the head groups of the amphiphiles can also bind metals and may have the potential to interfere with metal acquisition by the target pathogen and curb their growth and infection process.

Objectives:

Based on the prospect of leveraging the design-based self-assembly and metal binding attributes of synthetic amphiphiles, in generating potent antibacterials, the essential objectives of the Ph.D. thesis encompassed the following:

1. Evaluation of the bactericidal spectrum, membrane-directed activity, adjuvant potential, antibiofilm activity and in vitro cytotoxic effect of a salicaldehyde-based synthetic amphiphile referred as compound 1 (C1).

2. Investigations on the self-assembly of C1, bactericidal efficacy and antibiofilm potential of antibiotic-loaded micellar systems based on C1.

3. Evaluation of the bactericidal activity, aggregation propensity, potential in combinatorial therapy, antibiofilm activity and *in vitro* cytotoxicity of a napthaldehyde-based synthetic amphiphile referred as compound 2 (C2).

4. Studies on the impact of metal binding propensity and supramolecular interaction of C1 and C2 on their bactericidal activity and cytotoxic potential.

5. Investigations on device and extra-cellular matrix associated biofilm inhibition by C1 and C2 and determination of *in vivo* toxicity and wound healing potential of C1.

Chapter 2

Bactericidal Activity of a Salicaldehyde-based Synthetic Amphiphile (C1)

This chapter illustrates the bactericidal potential of a salicaldehyde-based amphiphile (C1). The membrane-directed activity of the amphiphile, its antibacterial activity in physiologically relevant fluids and its antibiofilm potential is also reported in this chapter.

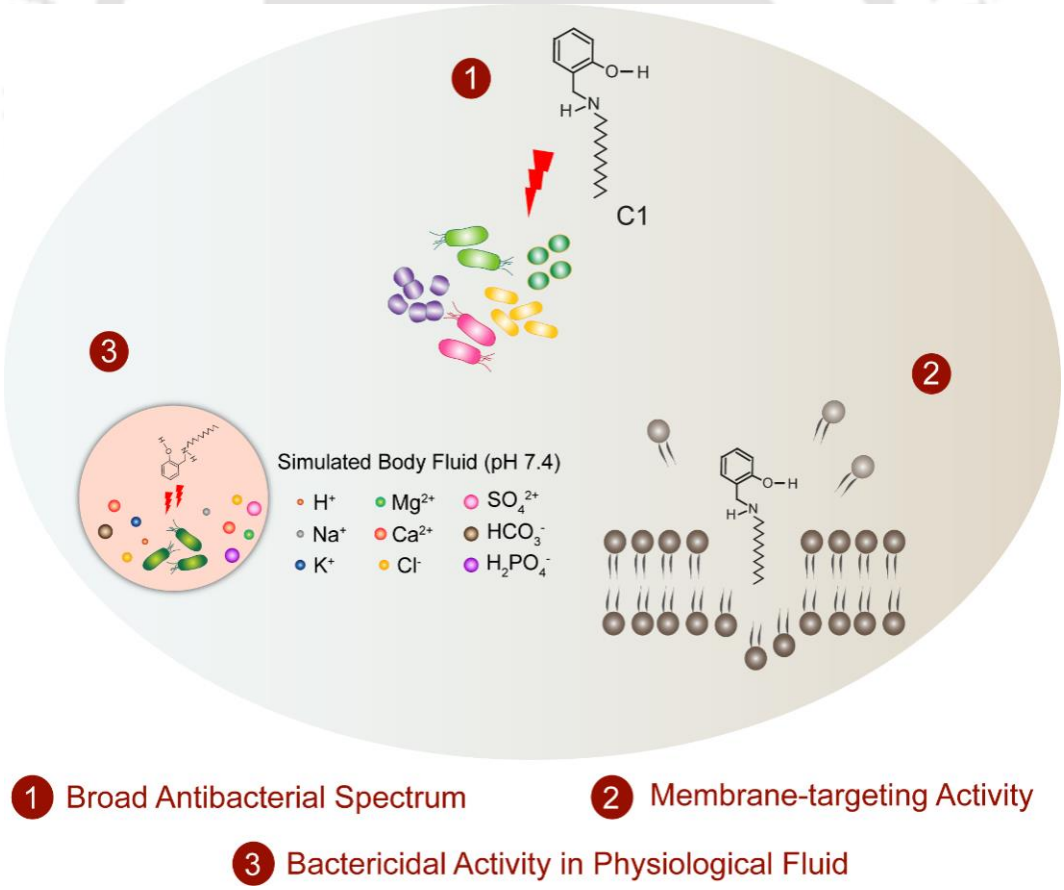

ABSTRACT

In this chapter, the antibacterial activity of a salicaldehyde-based synthetic amphiphile, which is referred as compound 1 (C1) is outlined. C1 was synthesized by forming a Schiff-base followed by reduction using sodium borohydride and its characterization was accomplished by ESI-MS and NMR. UV-visible absorption spectra of C1 revealed a peak at 290 nm, which perhaps originated from a n-π* transition, while a fluorescence emission peak could be observed at 350 nm, upon excitation of C1 at 290 nm. FTIR analysis of C1 indicated the stretching frequency of C-N bond at 1470 cm^{-1} and 1603 cm^{-1} and a broad peak centered around 2900 cm^{-1} corresponding to O-H stretching frequency. The amphiphile exhibited a broad-spectrum antibacterial activity with a superior potency against Gram-positive target bacteria. The minimum inhibitory concentration (MIC) and minimum killing concentration (MKC) of C1 against the clinical MRSA strain *S. aureus* MRSA 100 was 40 µM and 80 µM, respectively. FESEM analysis indicated prominent cellular damage in C1-treated cells of *S. aureus* and *E. coli*. The membrane-targeting activity of C1 was captured in a cFDA-SE leakage assay, which clearly indicated concentration-dependent membrane damage in *S. aureus* MRSA 100. The membrane-directed activity of C1 against the target bacteria was also corroborated by a PI uptake assay, fluorescence microscopy-based live/dead assay and $DiSC_3(5)$-based membrane depolarization assay. Interestingly C1 could also permeabilize the membrane of *E. coli* MTCC 433 cells. The antibacterial activity of the amphiphile was observed to be retained in physiologically relevant fluids highlighting its therapeutic prospect. With regard to the adjuvant potential of C1, a significant increase in the growth inhibition of target bacteria was observed when the cells were treated with the therapeutic antibiotics erythromycin and polymyxin B in combination with C1. A synergistic effect was evident in the presence of 10 µM C1 and 40 µM polymyxin B, whereas a similar effect was also observed in the presence of 5.0 µM C1 and 40 µM erythromycin. Inhibition of *S. aureus* MRSA 100 biofilm formation by C1 was evident in fluorescence microscopy, while an MTT assay suggested a dose-dependent eradication of MRSA biofilm by C1, with the $MBEC_{50}$ being 160 µM. An MTT-based assay suggested that C1 was non-toxic to cultured HEK 293 cells at 80 µM, which was equivalent to 2 x MIC against *S. aureus* MRSA 100.

2.1. Introduction

The menace of drug-resistant pathogenic bacteria is a burgeoning issue in contemporary healthcare owing to their remarkable ability to counter a majority of the clinically relevant antibiotics. (Liu *et al*., 2015) A gamut of resistance mechanisms are prevalent in these pathogenic bacteria, such as enzyme-catalyzed target modification, presence of outer membrane as a drug diffusion barrier, drug inactivation and others (Chambers and Deleo, 2010; Yeaman and Yount 2003; Culyba *et al*., 2015; Davies and Davies, 2010) enabling them to defy the action of conventional antibiotics, and thus exacerbating the crisis (Chambers and Deleo, 2010; Deresinski, 2005; Stryjewski and Corey, 2014; McCarthy *et al*., 2015; Hayden *et al*., 2005; Rehm and Tice, 2010). This quandary has kindled the need for a rational drug discovery program, which is focused towards the generation of potent antimicrobial agents (Alekshun and Levy, 2007; Fair and Tor, 2014). Amongst the clinically relevant pathogenic bacterial strains, methicillin-resistant *Staphylococcus aureus* (MRSA) is of particular concern as the bacteria is known to form resilient biofilms and has developed an inherent resistance towards therapeutic antibiotics such as vancomycin and daptomycin (Hayden *et al.,* 2005; Rehm and Tice, 2010; Deresinski, 2009; Marty *et al.,* 2006). Thus, there is a compelling need for a potent therapeutic strategy that can breach the resistance in MRSA cells and enhance the efficacy of antibiotics. Such an endeavor should essentially spur from judicious drug design and rational medicinal chemistry so as to generate antibacterial agents that act on profound cellular targets and are counterproductive to resistance development (Marty *et al*., 2006).

Antimicrobial agents that exhibit a membrane-directed activity hold significant therapeutic implications as the development of resistance against such molecules demands extensive repair of membrane components, which can be a severe physiological challenge for the target bacteria (Steinbuch and Fridman, 2016). Cationic antimicrobial peptides (AMPs) have been known to validate this premise (Wright 2011; Pages *et al.,* 2013; Wimley and Hristova, 2011). However, the therapeutic potential of AMPs is limited by their high manufacturing cost, complex formulation, inferior pharmacokinetics, proteolytic inactivation and lower *in vivo* efficacy (Chen *et al.,* 2012; Marr *et al.,* 2006). Under these circumstances, AMP-mimicking synthetic amphiphiles offer a unique therapeutic paradigm as antibacterial agents against drug-resistant pathogens owing to their facile synthesis, structural variations that can be exploited for activity, resistance to proteolysis and potent membrane-directed activity (Herzog and

Fridman, 2014; Findlay *et al*., 2010). The present investigation is an endeavor based on the aforementioned premise.

2.2. Materials and Methods

2.2.1. Growth Media and Chemicals

Nutrient Broth (NB), Brain-Heart Infusion (BHI) Broth and crystal violet (CV) dye were procured from HiMedia, Mumbai, India. Dimethyl sulfoxide (DMSO), chloroform, methanol and ethanol were obtained from Merck, India. 5(6)-carboxyfluorescein diacetate succinimidyl ester (cFDA-SE), propidium iodide (PI), congo red (CR), erythromycin, polymyxin B, 1-N-phenyl naphthylamine (NPN), 3,3'-dipropylthiadicarbocyanine iodide ($DiSC_3(5)$), 3-(4,5-dimethyl-2-thiazolyl)-2,5-diphenyl-2H-tetrazolium bromide (MTT), pepsin, pancreatin, Dulbecco's Modified Eagle Medium (DMEM) and trypsin–EDTA were obtained from Sigma-Aldrich (USA). Foetal bovine serum (FBS) was procured from Gibco^{TM}, Thermo Scientific.

2.2.2. Synthesis of Compound 1 (C1)

In a round bottom flask, 8.25 mM of dodecyl amine was taken and salicylaldehyde (9.0 mM) was added to it in excess in ethanol solution. The mixture was stirred for 6 h followed by solvent evaporation in a rotavapor. A precipitate (Schiff base) was obtained, which was then dissolved in ethanol. Sodium borohydride was then added pinch by pinch until the effervescence ceased. A colorless solution was obtained, which was then stirred for 12 h, followed by solvent evaporation. Using a separating funnel, the mixture was separated and the crude product was purified by column chromatography. The yield of the product was 66%. The synthesis route of C1 is indicated in Scheme 2.1.

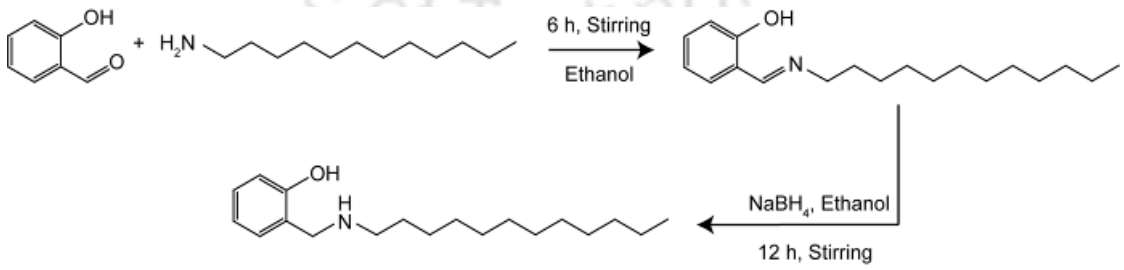

Scheme 2.1. Schematic representation of the synthesis route of C1.

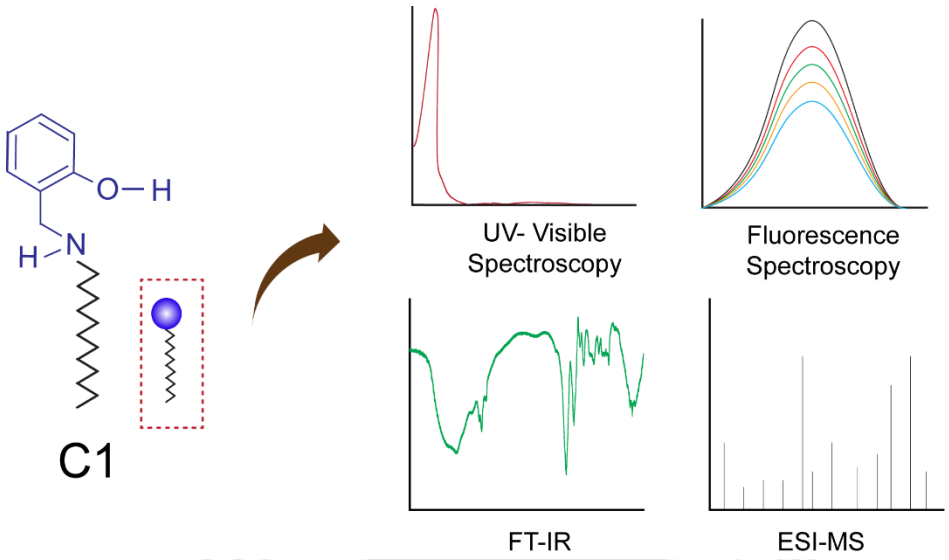

Scheme 2.2. Cartoon illustrating the techniques used to characterize C1.

2.2.3. Characterization of C1

A 20 mM stock solution of C1 was prepared in DMSO. The stock solution was diluted in water to obtain C1 in the concentration range of 20 µM - 320 µM. UV-vis absorption spectra of C1 was then measured in a spectrophotometer (Lambda 25, Perkin-Elmer). For recording the measurements, a scanning window from 200 nm to 500 nm was chosen. Absorption spectra was recorded for three independent experimental samples for every concentration of C1. In order to record the fluorescence emission spectra, the concentration of C1 was varied from 20 µM - 320 µM. The samples were excited at 290 nm and the emission of the samples was measured in a spectrofluorimeter (FluoroMax-4, HORIBA) in a range from 350 nm to 600 nm. Fluorescence spectra was also recorded for three independent experimental samples for every concentration of C1. For Fourier Transform Infrared (FTIR) spectroscopy, KBr pellets of C1 was prepared and FTIR spectra of the same was recorded at 4.0 cm^{-1} resolution in an infrared spectrometer (Spectrum One, Perkin-Elmer). The spectra was measured in the range of 4000 cm^{-1} to 400 cm^{-1} and eight scans were recorded for the sample. The spectrum for pure KBr was also measured. ESI-MS and NMR analysis of C1 was also conducted as indicated in Scheme 2.2.

2.2.4. Bacterial Strains and Growth Conditions

The Gram-positive strains consisted of *Staphylococcus aureus* MTCC 96 (*S. aureus*), methicillin-resistant *Staphylococcus aureus* (MRSA) MRSA 100, methicillin-

susceptible *Staphylococcus aureus* (MSSA) MSSA 104, *Listeria monocytogenes* Scott A (*L. monocytogenes*), *Bacillus subtilis* MTCC 441 (*B. subtilis*) and *Micrococcus luteus* NCIM 2379 (*M. luteus*). *Escherichia coli* MTCC 433 (*E. coli*), *Enterobacter aerogenes* MTCC 2822 (*E. aerogenes*), *Pseudomonas aeruginosa* MTCC 2488 (*P. aeruginosa*) and *Yersinia enterocolitica* MTCC 859 (*Y. enterocolitica*) were selected as Gram-negative target bacterial strains. The culture media and the growth conditions for bacterial strains is indicated in Table 2.1.

Table 2.1. Growth media and culture conditions for various target bacteria used in the present investigation.

Sl. No.	Target Bacteria	Growth Media	Culture Conditions
1.	*S. aureus* MTCC 96	Brain-Heart Infusion (BHI) Broth	37°C and 180 rpm for 12 h
2.	*S. aureus* MRSA 100*	Brain-Heart Infusion (BHI) Broth	37°C and 180 rpm for 12 h
3.	*S. aureus* MSSA 104*	Brain-Heart Infusion (BHI) Broth	37°C and 180 rpm for 12 h
4.	*L. monocytogenes* Scott A	Brain-Heart Infusion (BHI) Broth	37°C and 180 rpm for 12 h
5.	*B. subtilis* MTCC 441	Nutrient Broth (NB)	37°C and 180 rpm for 12 h
6.	*M. luteus* NCIM 2371	Brain-Heart Infusion (BHI) Broth	37°C and 180 rpm for 12 h
7.	*E. coli* MTCC 433	Nutrient Broth (NB)	37°C and 180 rpm for 12 h
8.	*E. aerogenes* MTCC 2822	Nutrient Broth (NB)	37°C and 180 rpm for 12 h
9.	*P. aeruginosa* MTCC 2488	Nutrient Broth (NB)	37°C and 180 rpm for 12 h
10.	*Y. enterocolitica* MTCC 859	Brain-Heart Infusion (BHI) Broth	37°C and 180 rpm for 12 h

* Strains were kindly provided by Prof. Benu Dhawan, All India Institute of Medical Sciences (AIIMS), New Delhi and Prof. Kasturi Mukhopadhyay, Jawaharlal Nehru University (JNU), New Delhi. MTCC: Microbial Type Culture Collection, Institute of Microbial Technology (IMTECH), Chandigarh, India. NCIM: National Collection of Industrial Microorganism, National Chemical Laboratory (NCL), Pune, India

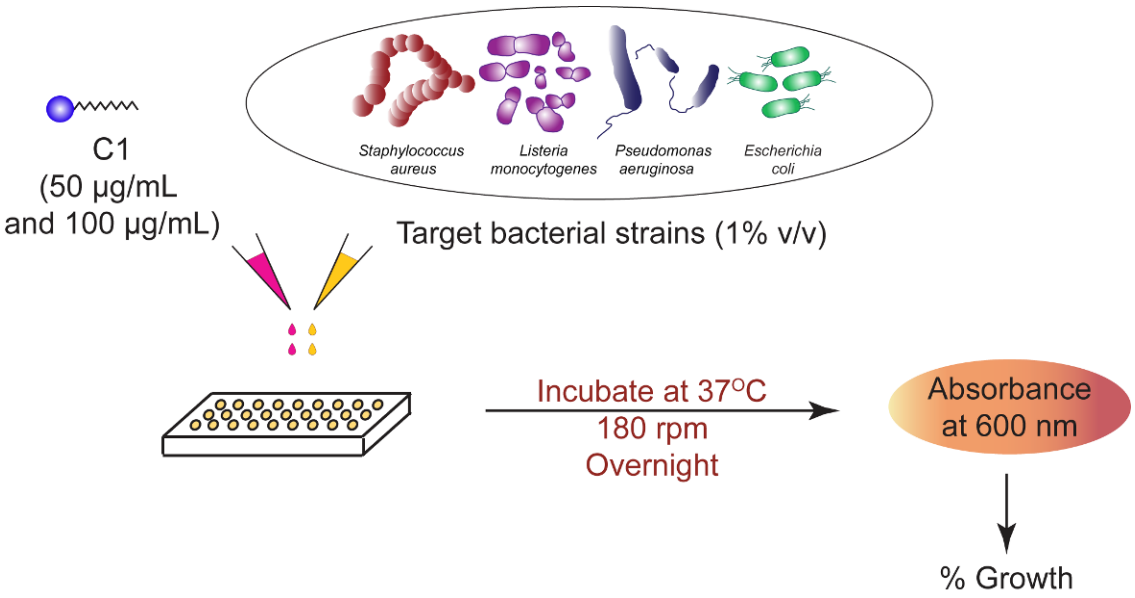

Scheme 2.3. Schematic representation of the protocol used for screening of the bactericidal activity of C1.

2.2.5. Screening of Antibacterial Activity of C1

Each of the target bacterial strains were grown in the specific growth media in separate sets in presence of either 50 µg/mL or 100 µg/mL C1 for 24 h. Following treatment, with the amphiphile, growth of the cells was assessed by recording the absorbance at 600 nm in a microtiter plate reader (Infinite M200, TECAN, Switzerland). The results were expressed as percentage growth compared to control (untreated cells). All the experiments were performed in triplicates. A schematic representation of the protocol for screening the antibacterial activity of C1 is depicted in Scheme 2.3.

2.2.6. Minimum Inhibitory Concentration (MIC) and Minimum Killing Concentration (MKC) of C1

The MIC and MKC of C1 against the specific bacterial strain was ascertained by a standard microtitre dilution method. The target bacterial cultures were inoculated at 1% level in microtitre wells (approximately 5×10^5 CFU/well) having 100 µL of the specific growth medium and propagated overnight at 37°C and 180 rpm in presence of varying concentrations of C1. The growth of the bacterial strains was verified by measuring absorbance at 600 nm in a microtitre plate reader (Infinite M200, TECAN, Switzerland). MIC of C1 was defined as the minimum amphiphile concentration that resulted in growth inhibition of the target bacteria (A_{600} <0.1). An aliquot (1% v/v) from all the wells that indicated a lack of cell growth (A_{600} <0.1) was re-inoculated into

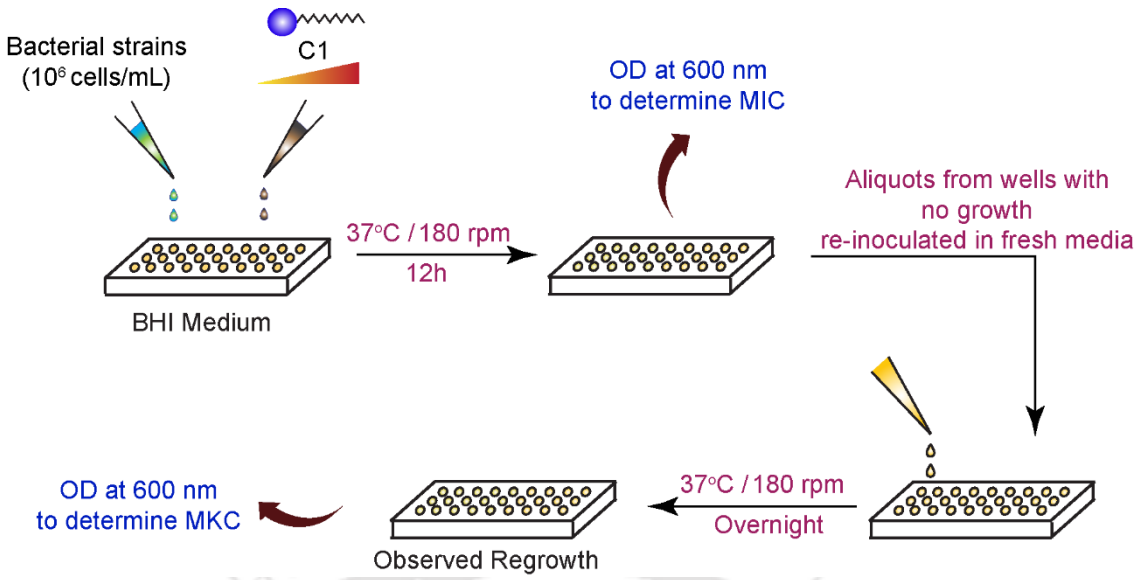

Scheme 2.4. Schematic representation of the protocol used for the determination of MIC and MKC of C1.

separate microtiter wells with fresh growth medium in the absence of amphiphile and incubated overnight at 37°C and 180 rpm. MKC of C1 was defined as the lowest concentration of amphiphile that inhibited the growth of the bacterial cells following re-inoculation (A_{600} <0.1). Six independent experiments were conducted to determine the MIC and MKC, which were expressed as average values. A schematic representation of the protocol used for the determination of MIC and MKC of C1 is indicated in Scheme 2.4.

2.2.7. Field Emission-Scanning Electron Microscope (FESEM) Analysis to Study the Antibacterial Activity of C1

S. aureus MTCC 96 and *E. coli* MTCC 433 cells were grown overnight and the cells were collected by centrifugation, washed with sterile PBS and resuspended in the same. Subsequently *S. aureus* MTCC 96 cells were treated with 40 µM C1, whereas *E. coli* MTCC 433 cells were treated with 80 µM C1 for 12 h at 37°C. Untreated cells (control samples) were also incubated in sterile PBS under the same conditions. Following incubation, untreated as well as treated cells were collected by centrifugation, washed with sterile PBS and sterile MilliQ water and finally suspended in sterile MilliQ water. A 10 µL aliquot of each sample was spotted on separate aluminum foil covered glass stub and air dried in the laminar hood. The samples were then mounted on a carbon tape

covered metal stub and gold (Au) coating was done twice. Finally, the samples were analyzed in a field emission scanning electron microscope (Zeiss Sigma, USA) at 2.0-3.0 Kv.

2.2.8. Membrane-Directed Bactericidal Activity of C1

The experiments conducted to determine the membrane-directed activity of C1 consisted of the following:

2.2.8.1. cFDA-SE Leakage Assay

A stock solution of cFDA-SE (500 µM) was prepared in DMSO and stored at -20°C. *S. aureus* MTCC 96, *S. aureus* MRSA 100 and *E. coli* MTCC 433 cells were grown overnight and harvested by centrifugation at 8000 rpm for 5 min. The cell pellet was washed with sterile phosphate buffer to remove media components and resuspended in the same buffer. For labelling, cFDA-SE was then added to the cells (final concentration of 50 µM) and the cells were incubated at 37°C for 30 min. The labelling reaction was terminated by pelleting the cells followed by washing with phosphate buffer to remove excess dye and resuspended in 1.0 mL of sterile PBS. To separate sets of cFDA-SE labelled cells, varying concentrations of C1 was then added (5.0 µM, 10 µM, 15 µM, 20 µM, 40 µM 80 µM and 160 µM) and the cells were incubated at 37°C and 180 rpm for

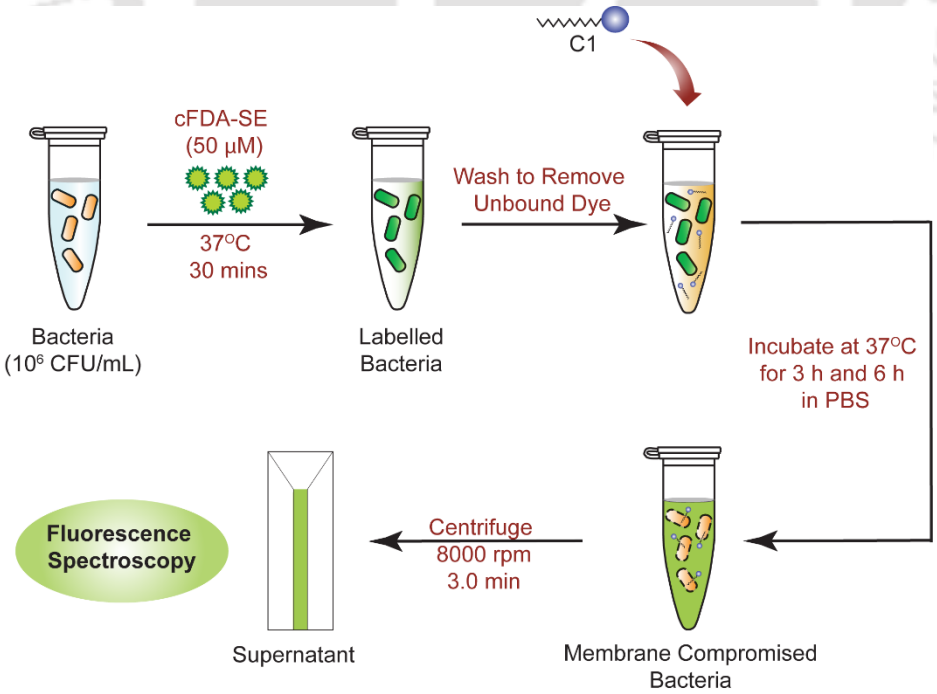

Scheme 2.5. Schematic representation of the protocol used to ascertain membrane damage by C1 using cFDA-SE leakage assay.

3 h and 6 h. As a control sample, cFDA-SE labelled cells devoid of C1 was also incubated under the same conditions. At intermittent periods of incubation (3 h and 6 h), cells were harvested by centrifugation. Leakage of carboxyfluorescein from the cells was ascertained by recording the fluorescence emission of the cell free supernatant at 518 nm upon excitation at 488 nm. For the amphiphile-treated samples, the fluorescence emission was recorded after subtracting the fluorescence of the dye effluxed from control samples. For every concentration of C1 and the control sample, fluorescence measurements were recorded from three independent experimental samples. A cartoon representing the salient steps of cFDA-SE leakage assay is shown in Scheme 2.5.

2.2.8.2. PI uptake assay

Propidium iodide stock solution (30 mM) was prepared in water and stored at -20°C. *S. aureus* MTCC 96 and *E. coli* MTCC 433 cells were grown overnight and harvested by centrifugation at 8000 rpm for 5 min. The cell pellet was washed with sterile phosphate buffer to remove media components and resuspended in the same buffer. To separate sets of the suspended cells, varying concentrations of C1 was then added (5.0 µM, 10 µM, 15 µM and 20 µM) and incubated at 37°C and 180 rpm for 3 h and 6 h. As a control sample, only cells devoid of C1 were incubated under the same conditions.

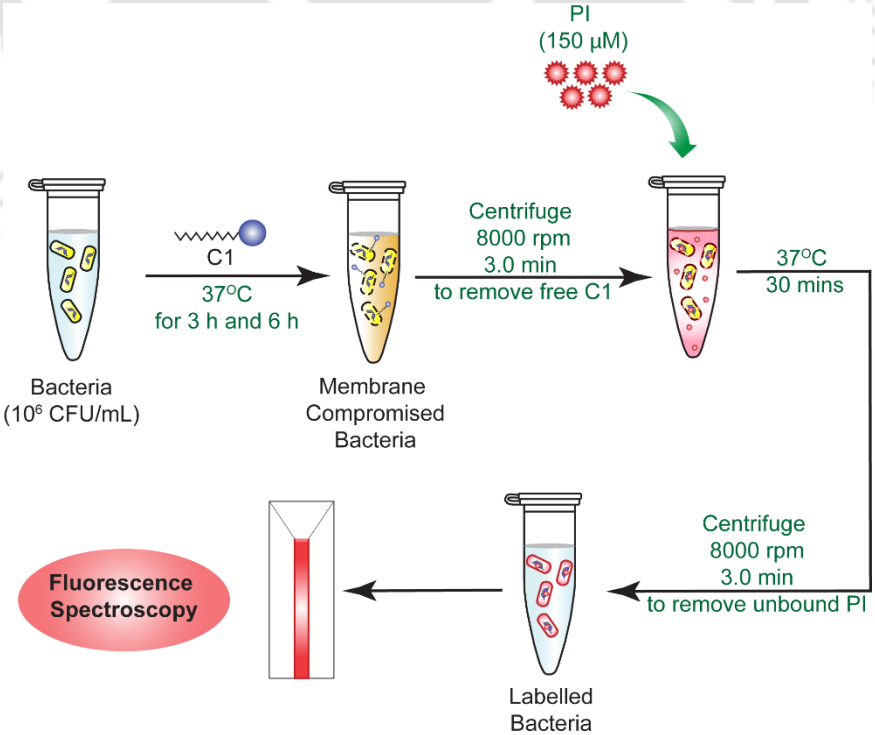

Scheme 2.6. Schematic representation of the protocol used to ascertain membrane damage by C1 using PI uptake assay

At intermittent periods of incubation (3 h and 6 h), PI was then added in separate sets to the treated and control cells at final concentration of 150 µM and kept at 37°C for 30 min. The labelling reaction was terminated by pelleting the cells followed by resuspension in 1.0 mL of sterile PBS. The fluorescence emission of the control as well as the treated cells was recorded at 618 nm upon excitation at 535 nm. For every concentration of C1 and the control sample, fluorescence measurements were recorded from three independent experimental samples. A cartoon representing the relevant steps of PI uptake assay is shown in Scheme 2.6.

2.2.8.3. Fluorescence Microscope Analysis

S. aureus MTCC 96 and *E. coli* MTCC 433 cells suspended in sterile PBS (approximately 10^6 CFU/mL) were labelled with cFDA-SE, followed by treatment in separate sets with varying concentrations of C1 (5.0 µM, 10 µM, 15 µM and 20 µM) at 37°C and 180 rpm for 6 h. Subsequently, cells were washed with sterile PBS to remove unbound amphiphile. A 10 µL aliquot of the stained sample was spotted on a clean glass slide, air dried and observed under fluorescence microscope (Eclipse Ti-U, Nikon, USA) with a filter that allowed blue light excitation at 445 nm - 495 nm. For PI staining, cells were treated with C1 (5.0 µM, 10 µM, 15 µM and 20 µM) at 37°C and incubated at 180 rpm for 6 h and subsequently exposed to PI for 30 min at 37°C. The stained cells were pelleted down and resuspended in PBS. A 10 µL aliquot was similarly spotted onto a glass slide and observed under an excitation filter of 495 nm - 570 nm. The images of the cells labelled with cFDA and PI in separate sets were recorded.

2.2.8.4. Membrane Depolarization Assay

Cells of *S. aureus* MTCC 96 were grown till mid-logarithmic phase (A_{600} = 0.4 - 0.5) at 37°C, 180 rpm. The cells were harvested by centrifugation, washed and resuspended in HEPES buffer (5.0 mM HEPES, 20 mM glucose, pH 7.2) to achieve A_{600} of 0.05. The cell suspensions were incubated with 0.4 µM $DiSC_3(5)$ for 1 h at 37°C followed by the addition of KCl (final concentration of 100 mM) and further incubated for 15 min. The cell suspension was then placed in a cuvette to which varying concentrations of C1 (5.0 M, 10 µM and 15 µM) was added and the fluorescence emission intensity (λ_{Ex} = 622 nm and λ_{Em} = 670 nm) was monitored in short time intervals in a spectrofluorimeter (FluoroMax-4, HORIBA) with excitation and emission slit width set at 5 nm each. Cells treated with valinomycin (30 µM) were used as positive control.

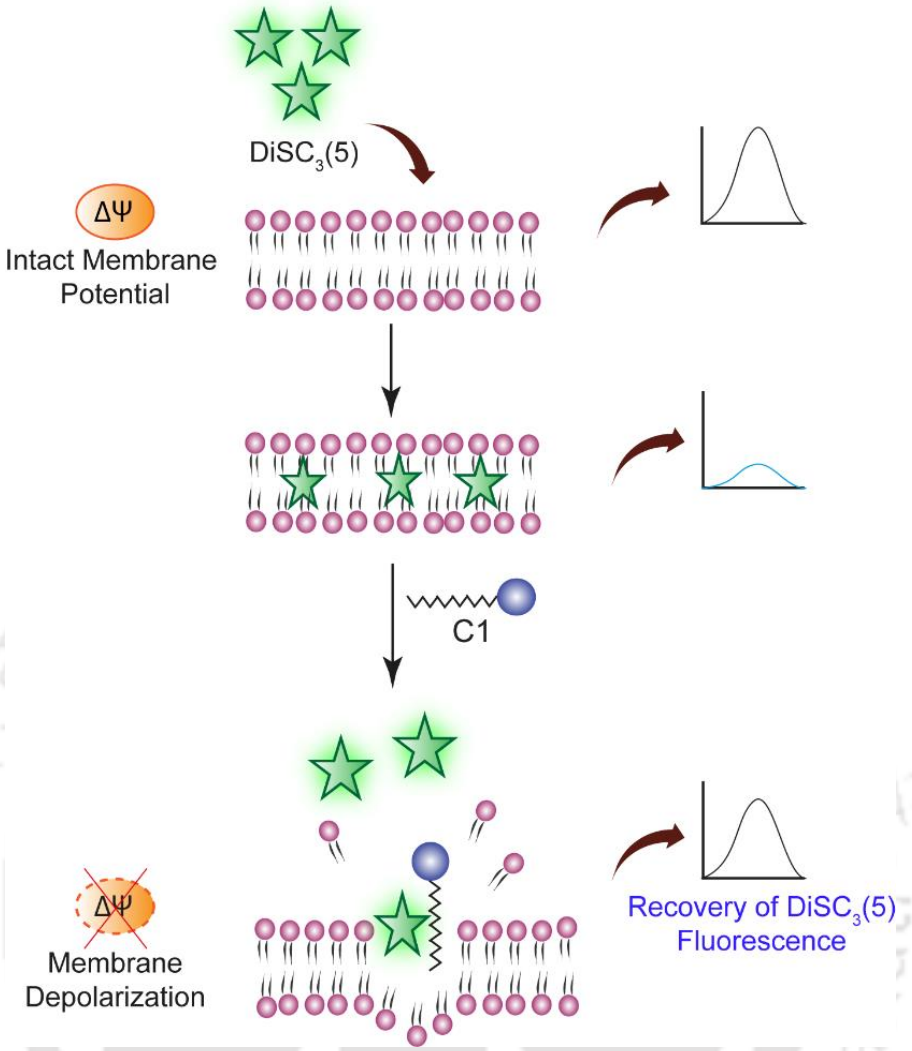

Scheme 2.7. Schematic representation of $DiSC_3(5)$ based membrane depolarization assay.

Fluorescence measurements were taken for three independent experimental samples. A cartoon representing the protocol used to measure membrane depolarization in cells treated with C1 is shown in Scheme 2.7.

2.2.8.5. Outer Membrane Permeabilization Assay

A stock solution of NPN (500 µM) was made in acetone. Target cells of *E. coli* MTCC 433 were grown in nutrient broth (NB) medium at 37°C in a shaker incubator till mid-logarithmic phase (A_{600} of 0.5). The cells were centrifuged, washed twice with 5.0 mM HEPES buffer (pH 7.4) and resuspended in the same buffer. A 1.0 ml aliquot of target cells was taken in a cuvette to which NPN (final concentration of 10 µM) was added. Following addition of varying concentrations of C1 (5.0 µM, 10 µM and 15 µM), enhancement in the fluorescence intensity of NPN was measured as a function of time.

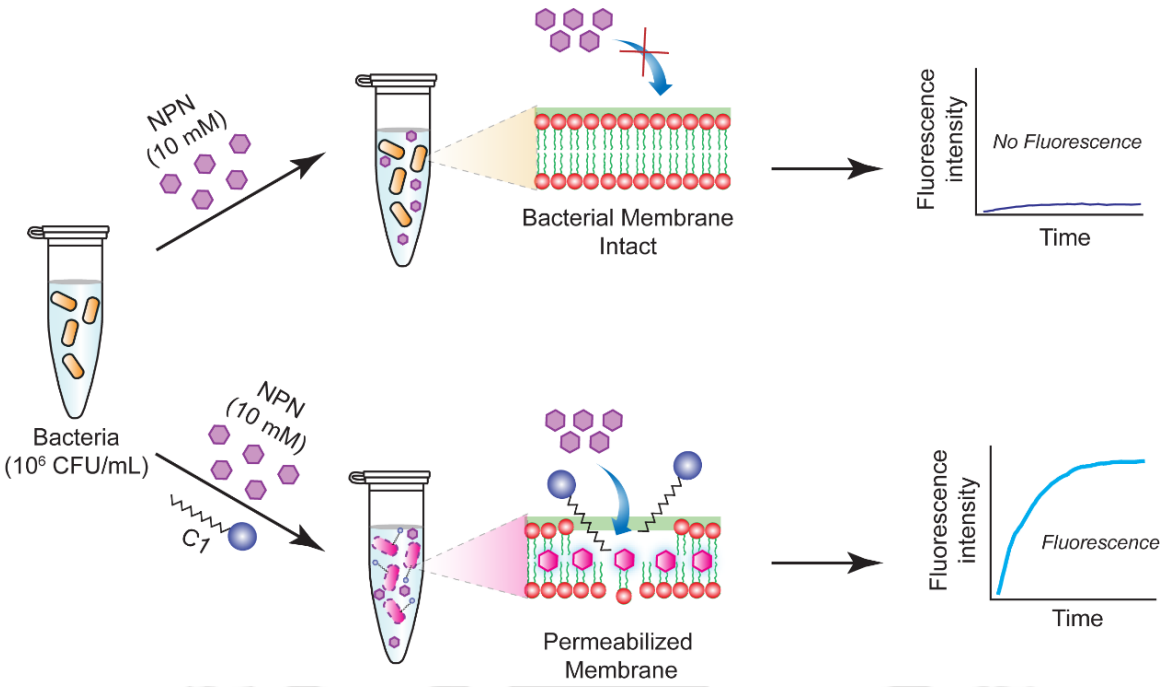

Scheme 2.8. Schematic representation of the NPN-based outer membrane permeabilization assay.

As a positive control sample, cells treated with polymyxin B (1.0 µg/mL) was included. Fluorescence measurements were taken for three independent samples at an excitation and emission wavelength of 350 nm and 420 nm, respectively. A cartoon representing the protocol used to determine the outer membrane permeabilization in cells treated with C1 is shown in Scheme 2.8.

2.2.9. Antibacterial Activity of C1 in Physiological Fluids

The bactericidal activity of C1 was ascertained in three physiologically relevant fluids in separate experiments as follows:

2.2.9.1. Activity in Simulated Intestinal Fluid (pH. 8.0)

L. monocytogenes Scott A cells (6.0 $\log_{10}$ CFU/mL) were suspended in simulated intestinal fluid (SIF) (0.5% saline pH 8.0 having 0.1% pancreatin) (Charteris *et al*., 1998) and subjected to treatment with variable concentrations of C1 (5.0 µM, 10 µM, 15 µM and 20 µM) at 37°C and 180 rpm. Samples were withdrawn at regular intervals of 3 h, 6 h, 12 h and 24 h and subjected to serial dilution and plating to ascertain the viable cell count ($\log_{10}$ CFU/mL).

Table 2.2. Composition of simulated body fluid (SBF).

Sl. No.	Component	Amount (g/L)
1.	Sodium chloride (NaCl)	8.035
2.	Sodium hydrogen carbonate ($NaHCO_3$)	0.355
3.	Potassium chloride (KCl)	0.225
4.	Di-potassium hydrogen phosphate trihydrate ($K_2HPO_4.3H_2O$)	0.231
5.	Magnesium chloride hexahydrate ($MgCl_2.6H_2O$)	0.311
6.	Calcium chloride ($CaCl_2$)	0.292
7.	Sodium sulfate (Na_2SO_4)	0.072
8.	Tris-hydroxymethyl aminomethane ($(HOCH_2)_3CNH_2$), Tris	6.110

2.2.9.2. Activity in Simulated Body Fluid (pH 7.4)

The composition of SBF was as described earlier (Marques *et. al*., 2011) and is indicated in Table 2.2. In order to prepare 1000 ml of SBF, 700 ml of distilled water was taken in a beaker and heated to 37°C under stirring. The reagents (listed in Table 2.2.) were dissolved sequentially into the solution. At the end, 1.0 M solution of hydrochloric acid was used to adjust the pH to 7.4 and then the volume was made up to 1000 ml by water. Varying concentrations of C1 (5.0 µM, 10 µM, 15 µM and 20 µM) were added separately to *S. aureus* MTCC 96 and *E. coli* MTCC 433 cells (6.0 $\log_{10}$ CFU/mL each) suspended in SBF and incubated at 37ºC and 180 rpm. Treated bacterial samples were withdrawn after 3 h, 6 h, 12 h and 24 h of incubation and subjected to serial dilution followed by plating to ascertain the viable cell number ($\log_{10}$ CFU/mL).

2.2.9.3. Activity in Simulated Gastric Fluid (pH 2.0)

L. monocytogenes Scott A cells (6.0 $\log_{10}$ CFU/mL) were taken in simulated gastric fluid (0.5% saline pH 2 having 0.3% pepsin) (Charteris *et al*., 1998) and subjected to treatment with varying concentrations of C1 (5.0 µM, 10 µM, 15 µM and 20 µM) at 37ºC and 180 rpm. Samples were withdrawn at regular intervals of 3 h, 6 h, 12 h and 24 h subjected to serial dilution and plating to ascertain the viable cell number ($\log_{10}$ CFU/mL).

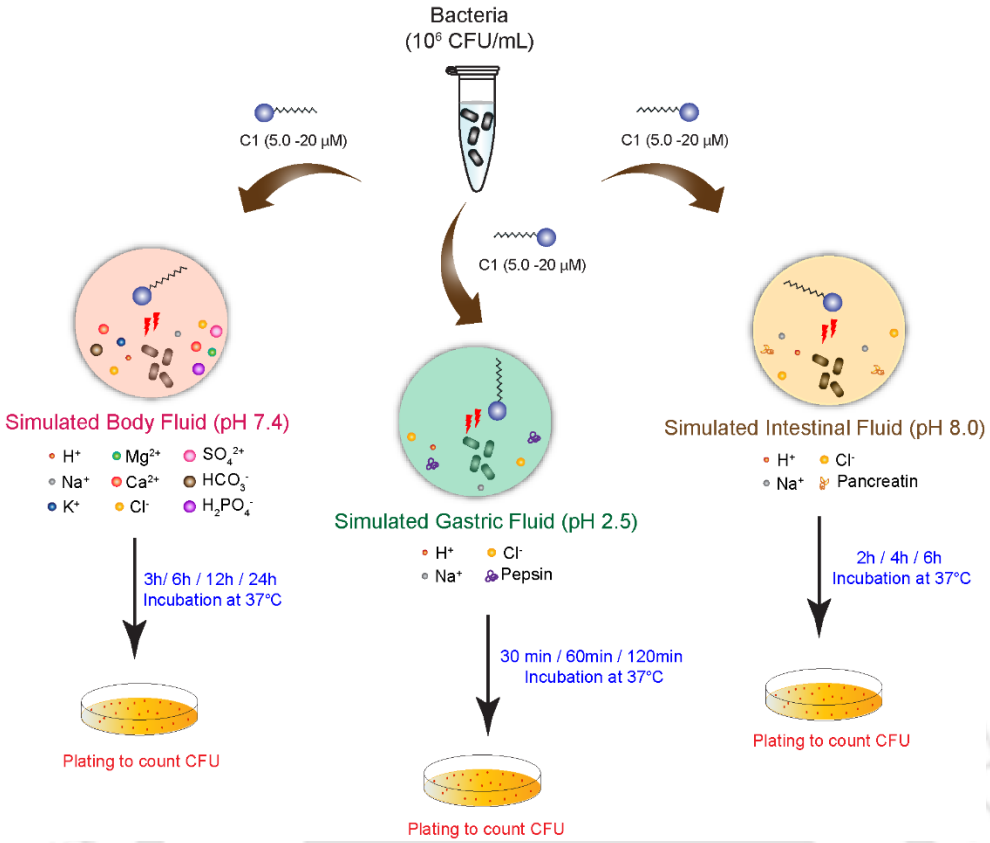

Scheme 2.9. Schematic representation of the protocol used to assess the bactericidal activity of C1 in various physiological fluids.

The viable cell count for untreated cells suspended in the respective physiological fluids alone was also determined at the specified intervals. A schematic representation of the protocol used to ascertain the bactericidal activity of C1 in various physiological fluids is illustrated in Scheme 2.9.

2.2.10. Bactericidal Activity of Polymyxin B and Erythromycin in Combination with C1

The adjuvant potential of C1, in combination with polymyxin B was ascertained against *S. aureus* MTCC 96 or *S. aureus* MRSA 100 and C1 in combination with erythromycin was ascertained against *E. coli* MTCC 433. Bacterial cell suspension (10^6 CFU/mL) was inoculated in separate sets into sterile microtitre plate wells filled with 100 µL growth media having either polymyxin B (10 µM - 80 µM for *S. aureus* MTCC 96 and 10 µM - 160 µM for *S. aureus* MRSA 100) or erythromycin (10 µM - 80 µM for *E. coli* MTCC 433) in combination with various concentrations of C1 depending on the MIC of C1 for the respective target bacterial strains. The antibiotics were used in these experiments at concentrations manifold below their MICs against the respective target

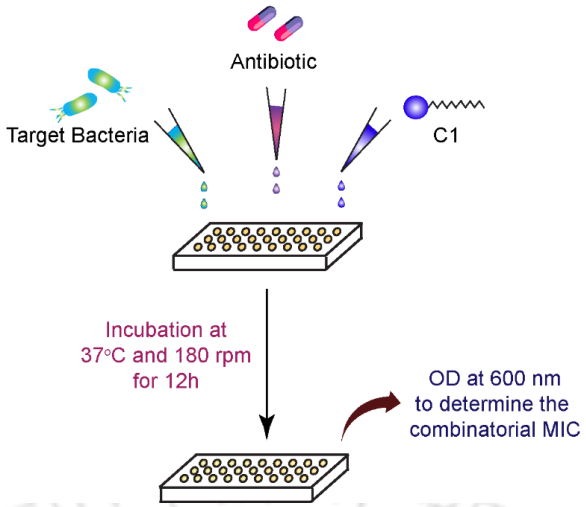

Scheme 2.10. Schematic representation of the experimental protocol used to determine the antibacterial activity of antibiotics in combination with C1.

bacteria. Following incubation at 37°C and 180 rpm for 12 h, the absorbance of the samples was recorded at 600 nm in a microtitre plate reader and the results were expressed as percentage growth in comparison to untreated cells (cells grown in the absence of antibiotics and C1). In separate sets, the effect of varying concentrations of the antibiotics or C1 alone on the growth of target bacteria was also ascertained. Three independent experiments, each having three replicas was conducted for every sample. A schematic representation of the experimental protocol used for the combinatorial assay is shown in Scheme 2.10. The interaction of C1 and the antibiotics was quantified and expressed as the fractional inhibitory concentration (FIC) index using the following expression:

$$FIC = \frac{[A]}{MIC_A} + \frac{[B]}{MIC_B}$$

where MIC_A and MIC_B indicate the MIC of drug A (polymyxin B or erythromycin) and drug B (C1), respectively. [A] and [B] are the MIC of drug A and drug B when used in combination. The nature of the combinatorial effect of antibiotics and C1 was interpreted following the method described earlier (Giacometti *et al*., 2000).

2.2.11. Antibiofilm Activity of C1

2.2.11.1. Solution-based Assay

S. aureus MTCC 96 and *S. aureus* MRSA 100 biofilm was grown in separate sets in sterile 96 well microtiter plate having BHI media incorporated with 0.25% glucose and

variable concentrations of C1 (5.0 μM - 320 μM for *S. aureus* MTCC 96 and 10 μM - 640 μM for *S. aureus* MRSA 100, respectively). Likewise, *P. aeruginosa* MTCC 2488 biofilm was grown in microtitre well having NB media with 0.25% glucose and C1 in the range of 20 μM - 640 μM. In both the cases, the biofilms were grown by incubating the microtitre plate for 24 h in a static and humid chamber at 37°C. Following incubation, the spent media from the wells was removed carefully along with the non-adherent bacterial cells. The effect of C1 on the metabolic activity of biofilm cells, biofilm biomass and the biofilm matrix was ascertained by an MTT assay, crystal violet assay and a congo red assay, respectively.

For an MTT assay, 5 mg/mL MTT stock solution was made in water. The spent media from the wells was removed carefully along with the non-adherent bacterial cells and 5 % (v/v) MTT solution was dissolved in fresh media and added to the wells and incubated for 2-3 h. Subsequently, MTT solution was aspirated followed by addition of DMSO to the wells. The absorbance of the solution was recorded at 570 nm, with a reference wavelength of 640 nm.

For the crystal violet assay, following aspiration of the spent media, 150 μL of a 0.1% (v/v) crystal violet solution in water was added to each well to stain the biofilm. Following an incubation period of 30 min, excess crystal violet stain was washed with water and the biofilm bound stain was solubilized with 200 μL of 95% ethanol. A 150 μL aliquot from this well was transferred to a new microtiter plate and the absorbance of the solution was measured at 590 nm.

In the congo red based assay, after aspiration of the spent media, 1% (v/v) congo red solution (100 μL) in water was added to each well and incubated for 10 mins. Following a washing step, the residual congo red stain incorporated into the biofilm matrix was solubilized in DMSO (100 μL), transferred into a fresh microtitre well and the absorbance of the solution was measured at 490 nm to estimate the effect of C1 on the formation of biofilm matrix.

The minimum biofilm inhibition concentration ($MBIC_{50}$) for C1 was calculated as the concentration, which resulted in 50% reduction in biofilm metabolic activity as compared to untreated control sample. For every experiment, three independent sets with three replicates each were included. Data analysis and assessment of standard deviation was accomplished with Microsoft Excel 2016 (Microsoft Corporation, USA). A schematic representation of the solution-based assays used to ascertain the antibiofilm activity of C1 is shown in Scheme 2.11.

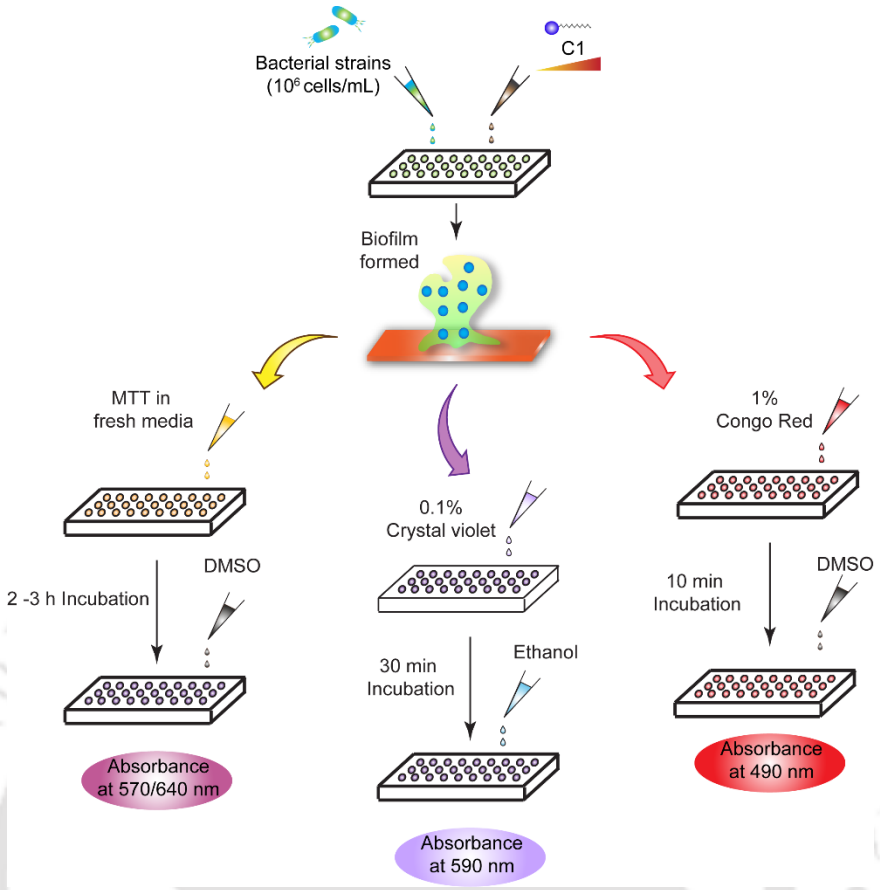

Scheme 2.11. Cartoon representing the solution-based assays used to ascertain the antibiofilm activity of C1.

For biofilm eradication studies, *S. aureus* MTCC 96 biofilm, *S. aureus* MRSA 100 biofilm and *P. aeruginosa* MTCC 2488 biofilm were grown in microtitre well in static and humid condition at 37°C in the respective media having 0.25% glucose. Following 24 h of incubation and biofilm growth, the media was removed and fresh growth media having various concentrations of C1 was added to the biofilms. The concentration of C1 was as follows: (a) 5.0 µM - 160 µM for *S. aureus* MTCC 96 biofilm, (b) 10 µM - 640 µM for *S. aureus* MRSA 100 biofilm and (c) 10 µM - 640 µM for *P. aeruginosa* MTCC 2488 biofilm. The biofilms were incubated for 24 h in a static and humid chamber at 37°C. Untreated biofilms were also incubated as control. Subsequently, MTT assay, crystal violet assay and congo red assay was performed to ascertain the antibiofilm activity of C1 as mentioned previously. The minimum biofilm eradication concentration ($MBEC_{50}$) for C1 was determined as the concentration, which led to 50% reduction in biofilm metabolic activity as compared to the control sample. For every experiment, three independent sets with three replicates each were included.

2.2.11.2. Fluorescence Microscopy

S. aureus MTCC 96, *S. aureus* MRSA 100 and *P. aeruginosa* MTCC 2488 biofilms were grown in sterile 96 well microtiter plate and treated with C1 as mentioned previously in both inhibition and eradication mode. Untreated (control) as well as C1-treated biofilm samples were stained separately with cFDA-SE and congo red (Thiyagarajan *et al*., 2016). The stained biofilms were then subjected to fluorescence microscopic analysis (Eclipse Ti-U, Nikon). Images of the biofilms were captured using a filter allowing blue light excitation (465 nm – 495 nm) for cFDA-SE and green light excitation (515 nm – 565 nm) for congo red stained biofilm. Images were captured from multiple fields for every sample.

2.2.12. In Vitro Cytotoxic Effect of C1

The cytotoxic effect of C1 was ascertained on HeLa, HEK and HT-29 cells by MTT assay. Growth of the cells in tissue culture flask and seeding of the cells onto 96-well tissue culture plates at a density of 10^4 cells per well was accomplished by following a previously described method (Goswami *et al*., 2013). The seeded cells were subjected to treatment with varying concentrations of C1(20 µM -320 µM for HEK 293 and 5.0 µM -160 µM for HeLa and HT-29 cells) in DMEM, for a period of 24 h. The concentration of C1 used in the experiment was equivalent to various multiples of the MIC of C1 against *S. aureus* MRSA 100. Following incubation for 24 h and removal of the media, fresh DMEM having MTT solution was added to the wells and further incubated for 4 h at 37°C. The media was removed and DMSO was added to solubilize

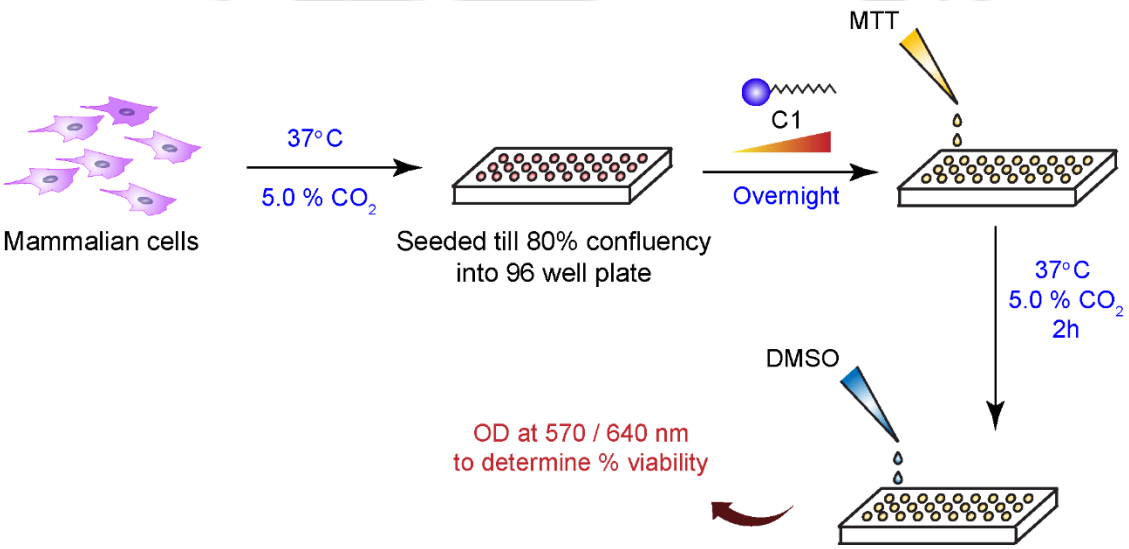

Scheme 2.12. Cartoon representing the MTT-based assay used to ascertain the cytotoxic potential of C1.

the insoluble formazan product. The absorbance of the solution was then measured in a microtiter plate reader at 570 nm against a reference of 640 nm. The MTT assay was conducted in four sets for every tested concentration of C1. Cells subjected to DMSO treatment were also analyzed. The absorbance obtained for the untreated control samples represented 100% cell viability. The absorbance obtained for C1-treated cells was compared to the control to ascertain the % cell viability. A schematic representation of the MTT-based assay used to ascertain the cytotoxic potential of C1 is shown in Scheme 2.12.

2.3. Results and Discussion

2.3.1. Design Rational and Characterization of C1

In the present investigation, the principal motivation driving the design of the bactericidal synthetic amphiphile is the choice of a biocompatible salicaldehyde group that would enable strong interaction with bacterial cells and a twelve-carbon chain

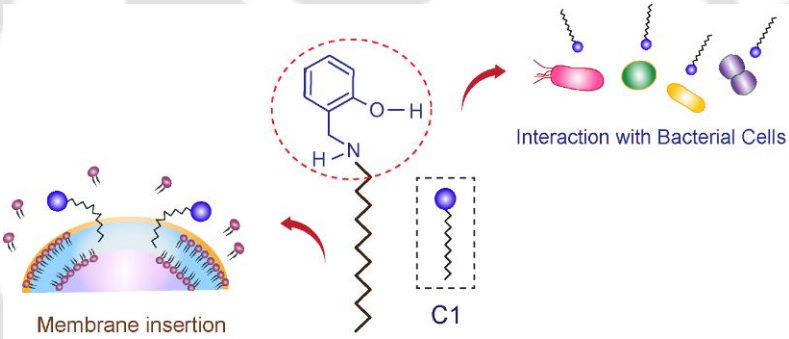

Figure 2.1. Cartoon indicating the design principle envisaging the head group based interaction with bacteria and a hydrophobic tail that influences membrane-directed activity of C1.

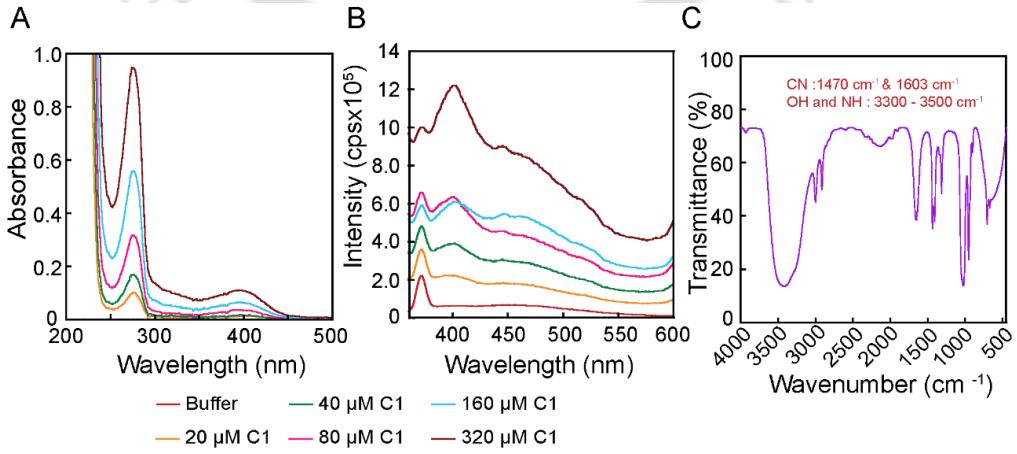

Figure 2.2. (A) UV-visible absorption spectra, (B) Fluorescence emission spectra and (C) FTIR spectra of C1.

containing hydrophobic tail for insertion into the membrane of a target pathogen such as MRSA as envisaged in Figure 2.1. C1 was characterized by ESI-MS and NMR (Appendix, Figure A2.1- A2.2). Absorption spectra of C1 revealed a peak at 290 nm, perhaps due to n-π* transition of the chromophore (Figure 2.2A). Upon excitation at 290 nm, C1 exhibited a fluorescence emission peak at 350 nm (Figure 2.2B). Upon FTIR analysis of C1, the C-N bond stretching frequency at 1470 cm^{-1}, 1603 cm^{-1} and the O-H stretching frequency manifested as a broad peak centered around 2900 cm^{-1} was evident (Figure 2.2C).

2.3.2. Bactericidal Activity of C1

The initial screening experiments indicated that C1 exhibited a wide-spectrum antibacterial activity against both Gram-positive and Gram-negative bacteria (Figure 2.3A). However, it was noted that the target bacteria *Pseudomonas aeruginosa* MTCC

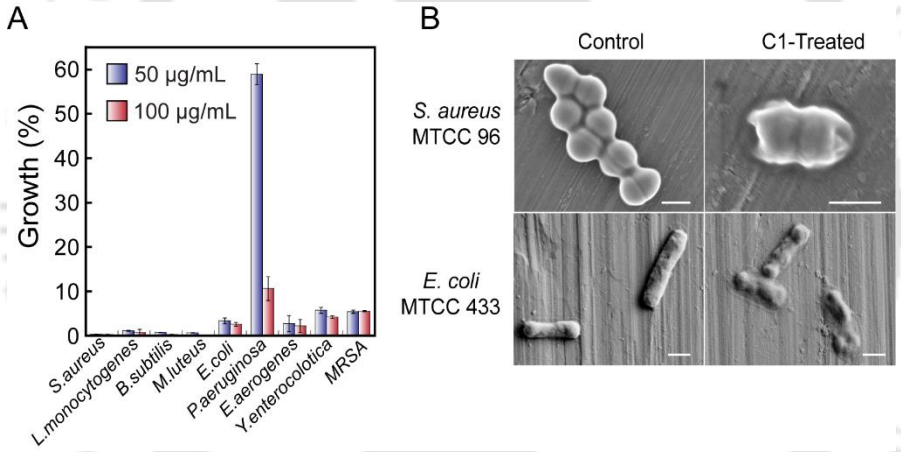

Figure 2.3. (A) Antimicrobial spectrum of C1 against pathogenic bacterial strains. (B) FESEM images of C1-treated target bacteria. Scale bar for the images is 1.0 µm.

Table 2.3. MIC and MKC of C1 against various target bacteria.

Sl. No.	Target Bacteria	MIC	MKC
1.	*S. aureus* MTCC 96	20 µM	40 µM
2.	*L. monocytogenes* Scott A	40 µM	80 µM
3.	*P. aeruginosa* MTCC 2488	80 µM	160 µM
4.	*E. coli* MTCC 433	40 µM	80 µM
5.	*S. aureus* MRSA 100	40 µM	80 µM
6.	*S. aureus* MSSA 104	20 µM	40 µM

2488 was relatively less sensitive to the bactericidal effect of C1 (Figure 2.3A), which can perhaps be accounted by the low permeability of its cell wall (Lambert *et. al.*, 2002). The MIC and MKC of C1 against the clinical MRSA strain *S. aureus* MRSA 100 was 40 µM and 80 µM, respectively (Table 2.3). In the context of the antibacterial activity of C1, it can be assumed that the salicaldehyde head group may form hydrogen bonds with phosphoryl and carboxyl groups present in the membrane phospholipids of bacteria (French *et al.*, 2013) and promote anchoring of C1 onto cell surface, as reported for other bactericidal agents (Cho *et al*., 2007; Suarez *et al*., 2014). The subsequent insertion of C1 into the bacterial membrane can be induced by the hydrophobic tail, eventually leading to cell death. The notable cellular damage in *S. aureus* and *E. coli* cells treated with 40 µM and 80 µM C1, respectively, as observed in FESEM analysis further validated the bactericidal activity of C1 (Figure 2.3B).

2.3.3. Membrane-directed Bactericidal Activity of C1

In order to ascertain the membrane-targeting activity of C1, fluorescence-based assays were pursued. In the first assay, *S. aureus* MTCC 96, *E. coli* MTCC 433 and *S. aureus* MRSA 100 cells were labelled with cFDA-SE. This dye is non-fluorescent and membrane permeable, which is known to accrue in viable cells. Essentially, the ester bond present in the dye is cleaved by intracellular esterases of viable cells to generate a fluorescent molecule, which leads to cell-associated fluorescence (Hoefel *et al*., 2003). Further, the amine reactive fluorophore, conjugates with intracellular proteins and thereby prevents inadvertent leakage of the dye from cells. Hence, the membrane-directed activity of any molecule can be assessed by quantifying the leakage of the dye following membrane damage of labelled target cells (Singh *et al*., 2012). In the present investigation, cFDA-SE labelled target bacteria were treated with varying concentrations of C1 and the leakage of the dye was explicitly observed for every target bacterium for 3 h and 6 h indicating membrane damage. This phenomenon was observed to be more prominent with increase in the concentration of C1 (Figure 2.4A - 2.4C). Based on the quantum of leakage, it was also evident that the membrane-directed bactericidal activity of C1 was superior against *S. aureus* MTCC 96 (Figure 2.4A) as compared to the clinical MRSA strain *S. aureus* MRSA 100 (Figure 2.4C). The superior potency of C1 against *S. aureus* MTCC 96 is also supported by a lower MIC and MKC (Table 2.3). The extent of membrane damage in C1-treated target cells was also ascertained by a PI uptake assay. PI is a cell-impermeant dye, which is internalized only when the cells have a

compromised membrane. Upon intake, PI intercalates with cellular nucleic acids, resulting in strong red fluorescence emission (Virto *et al*., 2005). A dose-dependent increase in PI uptake in the target cells, as observed in fluorescence spectrophotometric studies, corroborated the cFDA-SE leakage-based membrane damage (Figure 2.4D-2.4E).

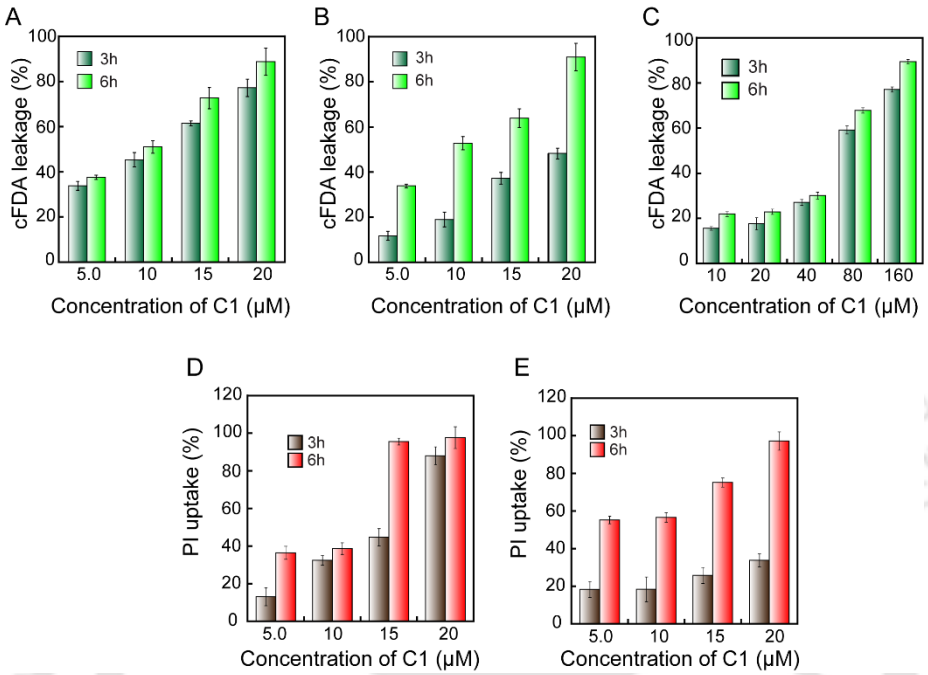

Figure 2.4. cFDA leakage assay on (A) *S. aureus* MTCC 96, (B) *E. coli* MTCC 433 and (C) *S. aureus* MRSA 100. PI uptake assay on (D) *S. aureus* MTCC 96 and (E) *E. coli* MTCC 433.

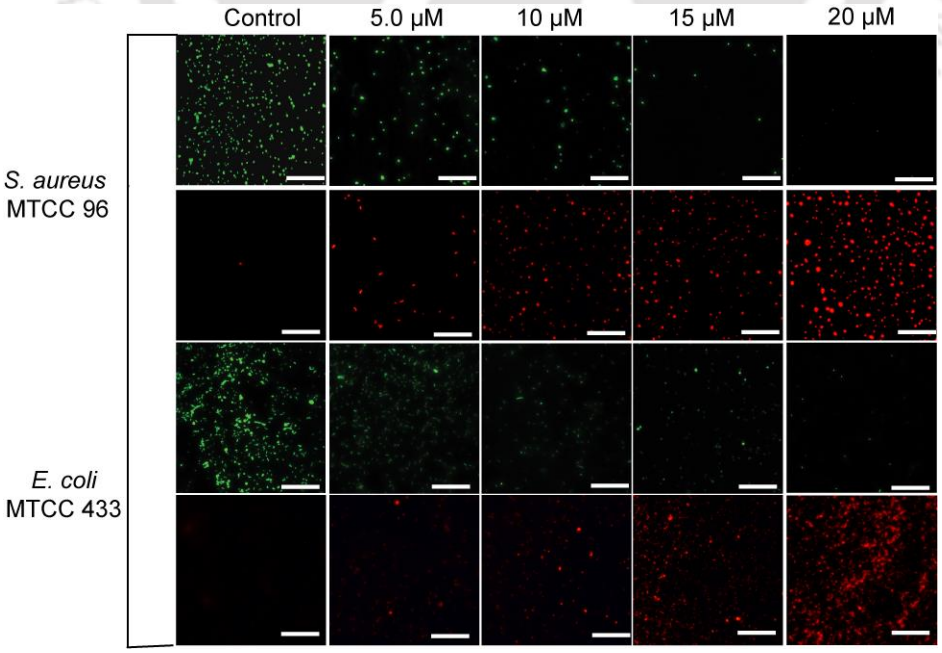

Figure 2.5. Fluorescence microscopy-based live/dead assay. Scale bar for the images is 100 μm.

Fluorescence microscopy based live/dead assay also captured the dose-dependent membrane-targeting activity of C1, wherein it was evident that the density of cFDA-SE labelled cells reduced systematically, with a concomitant increase in the population of PI stained cells (Figure 2.5). A large number of studies have revealed that the loss in cell viability following treatment with a bactericidal agent that is membrane acting can be accounted by membrane depolarization (Song *et al*., 2011; Adhikari *et al*., 2012). In order to ascertain the membrane depolarization in target cells treated with C1, a fluorescence-based assay was conducted with the membrane potential sensitive probe $DiSC_3(5)$. Interestingly, the fluorescence of $DiSC_3(5)$ was increased upon treatment of *S. aureus* MTCC 96 and *E. coli* MTCC 433 cells with C1 (Figure 2.6A-2.6B), suggesting that C1 could disrupt the transmembrane potential (Ψ) in target cells. These results are in accordance with earlier studies, which revealed membrane depolarization in target bacteria treated with bactericidal synthetic amphiphiles (Vudumula *et al*., 2012; Goswami *et al*., 2013). The extent of membrane depolarization was dependent on the concentration of C1 (Figure 2.6A-2.6B) where C1 could render significant membrane depolarization even at levels lower than its MIC (Table 2.3). Further, a notable increase in NPN fluorescence was observed upon treatment of *E. coli* MTCC 433 with C1 followed by a plateau (Figure 2.6C), indicating that C1 could render outer membrane permeabilization in the treated cells, akin to other reported molecules (Rawlinson *et al*., 2010, Helander and Mattila-Sandholm 2000, Singh *et al*., 2012). The extent of outer membrane permeabilization was dose-dependent (Figure 2.6C) and was manifested even when the concentration of C1 was lower than its MIC.

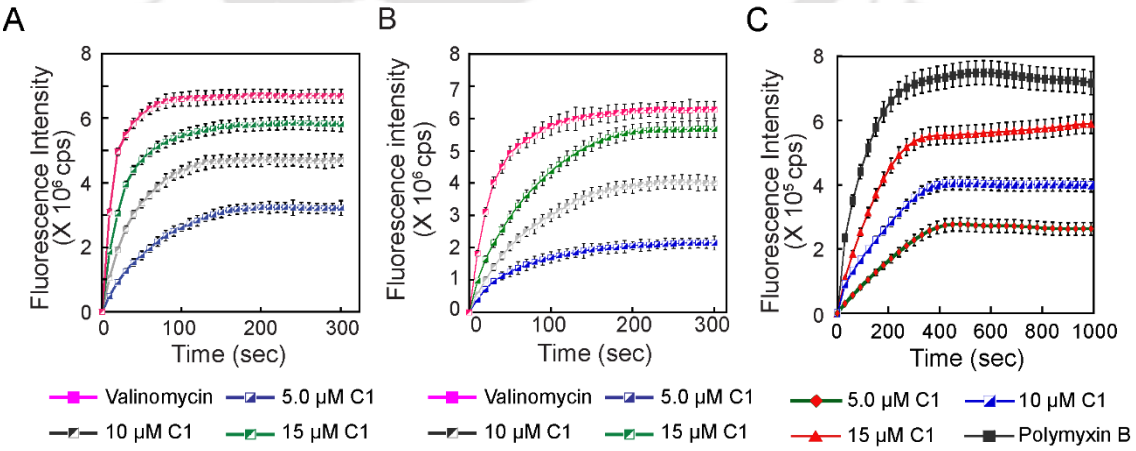

Figure 2.6. $DiSC_3(5)$ assay for ascertaining membrane depolarization in (A) *S. aureus* MTCC 96 and (B) *E. coli* MTCC 433. (C) NPN uptake assay to ascertain membrane permeabilization in *E. coli* MTCC 433 cells.

2.3.4. Bactericidal Activity of C1 in Simulated Fluids

Gastrointestinal pathogenic bacteria can cope with the highly acidic human gastric fluid and subsequently colonize the intestine (Tamplin, 2005; Foster, 1999; Foster, 2004; Cotter *et al*., 2000; Bavaro, 2009; Richard and Foster, 2004). Elimination of gastric fluid-resistant pathogenic bacteria is further compounded by the fact that some antibiotics are liable to become inactive in the acidic milieu (Lamp *et al*., 1992; Mercier *et al*., 2002; Merrell and Camilli, 2002). Given the bactericidal efficacy of C1, it was pertinent to ascertain its bactericidal efficacy in physiologically relevant fluids such as SGF, SIF and SBF in order to strengthen its therapeutic prospect. In this regard, *S. aureus* MTCC 96 and *E. coli* MTCC 433 cells were incubated in separate sets in SBF (pH 7.4) and treated with varying concentrations of C1. Similarly, *L. monocytogenes* Scott A was incubated in separate sets in SIF (pH 8.0) and SGF (pH 2.0) and treated with variable concentrations of C1. In these experiments, essentially there was a decrease in the number of viable cells of the pathogens in all the fluids upon treatment with C1 (Figure 2.7), but when the target bacterial cells were incubated in SBF, SIF and SGF alone, there was hardly any reduction in the cell viability (Figure 2.7). This indicated that pH of the fluids per se could not

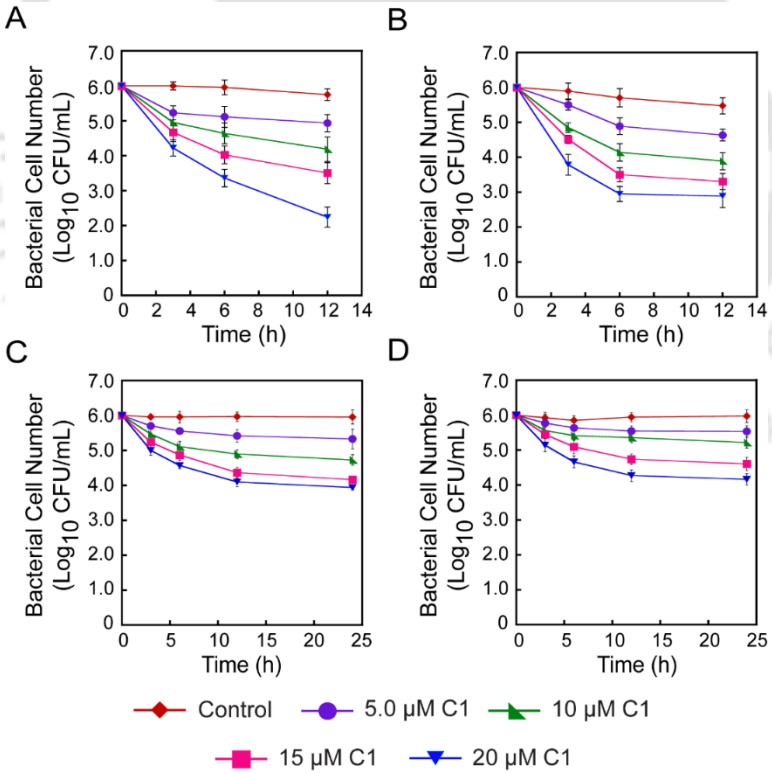

Figure 2.7. Time-kill curves of C1 against (A) *S. aureus* MTCC 96 in simulated body fluid, (B) E. *coli* MTCC 433 in simulated body fluid, (C) *L. monocytogenes* Scott A in simulated intestinal fluid and (D) *L. monocytogenes* Scott A in simulated gastric fluid.

account for the observed decrease in the reduced viability of C1-treated bacteria. Manifestation of the bactericidal activity of C1 in various physiologically relevant fluids is encouraging and in future, experiments based on *in vivo* models can perhaps substantiate these findings.

2. 3. 5. Bactericidal Activity of Antibiotics in Combination with C1

The outer membrane of Gram-negative bacteria or the cell wall in Gram-positive bacteria, may constitute a protective barrier which may contribute to the inherent drug resistance exhibited by pathogenic bacteria (Bolla *et al*., 2011; Nikaido, 2003; Delcour, 2009; Weidenmaier and Peschel, 2008; Kohler *et al*., 2009). In this regard, it has been demonstrated earlier that synthetic antibacterial agents that can breach the bacterial membrane or cell wall can promote antibiotic uptake and thereby enhance elimination of the target bacteria (Saha *et al*., 2008; Goswami *et al*., 2013; Uday *et al*., 2014; Goswami *et al*., 2015). The membrane disrupting activity of C1 (Figure 2.4-2.5) suggested that the amphiphile may hold potential as an adjuvant and increase the efficacy of therapeutic antibiotics against target bacterial cells, which exhibited resistance against the action of such antibiotics. In order to explore this possibility, polymyxin B and erythromycin were chosen as model therapeutic antibiotics in the combinatorial treatment regimen.

Polymyxin B is a cationic basic peptide, whose nature is analogous to a surfactant (Velcov *et al.*, 2013; Vaara, 2010). Polymyxin B binds to a negatively charged site in the lipopolysaccharide layer through its positively charged amino groups in the cyclic peptide portion and subsequently alters bacterial outer membrane permeability (Khondker *et al.*, 2019; Cardoso *et al*., 2007). The permeabilization of the outer membrane results in leakage of cellular molecules, inhibition of cellular respiration and excess water uptake, which ultimately results in cell death. However, literature suggests that polymyxin B is an antibiotic primarily used for resistant Gram-negative infections but has little to no effect on Gram-positive pathogens, since the cell wall of Gram-positive bacteria is too thick to permit access to the underlying membrane (Poirel *et al.*, 2017; Zavascki *et al.*, 2007). Given that combinatorial administration of adjuvants can lead to increase in potency of the antibiotic-mediated therapy (Worthington and Melander, 2013) our endeavor was to study whether the combination of polymyxin B and C1 leads to synergism and alleviation of conventionally resistant Gram-positive bacteria. Also, polymyxin group of antibiotics are known to be relatively neurotoxic and nephrotoxic (Falagas and Kasiakou, 2006). In this regard, administering them in

combinatorial manner is likely to decrease the dose of the antibiotic required for effective therapy and also curb the associated toxicity.

The adjuvant potential of sub-MIC levels of C1 in enhancing the efficacy of sub-MIC levels of polymyxin B was ascertained against *S. aureus* MTCC 96 and *S. aureus* MRSA 100. A prominent inhibition of the growth of target bacteria was observed in combinatorial treatment as against the cells treated with either the antibiotic or amphiphile singularly (Figure 2.8A-2.8B). For instance, upon treatment with increasing concentrations of C1 alone, the growth observed for *S. aureus* MTCC 96 was consistent upto 10 µM C1 whereas ~76% growth was recorded for *S. aureus* MRSA 100 at 20 µM C1 (Figure 2.8A-2.8B). On the other hand, treatment with 160 µM polymyxin B alone resulted in ~ 80% growth for *S. aureus* MTCC 96 and ~43% growth in case of *S. aureus* MRSA 100 (Figure 2.8A-2.8B). Interestingly, in the combination experiments, a higher growth inhibition of the target bacteria could be readily observed. For instance, treatment with a combination of 10 µM C1 and 160 µM polymyxin B resulted in around 10% growth in *S. aureus* MTCC 96, while in case of S. *aureus* MRSA 100, a combination of 10 µM C1 with 40 µM polymyxin B or 20 µM C1 with 10 µM polymyxin B resulted in only 8% growth (Figure 2.8A-2.8B). In case of *S. aureus* MTCC 96, an additive effect was observed, while in case of *S. aureus* MRSA 100, both additive as well as synergistic effects were observed (Table 2.4).

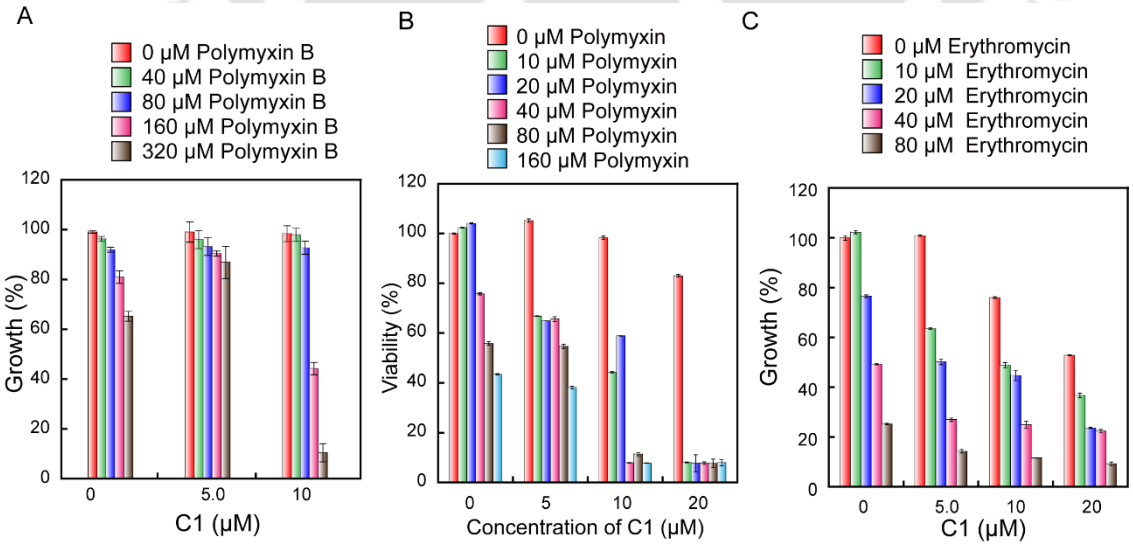

Figure 2.8. Antibacterial activity of C1 in combination with polymyxin B against (A) *S. aureus* MTCC 96, (B) *S. aureus* MRSA 100 and (C) erythromycin against *E. coli* MTCC 433.

Table 2.4. FIC index and nature of interaction of C1 in combination with polymyxin B.

Sl. No.	Target Bacteria	MIC of Antibiotic and C1	Combination Treatment	FIC Index	Effect*
1.	*S. aureus* MTCC 96	Polymyxin B = 320 µM C1 = 20 µM	10 µM C1 + 160 µM Polymyxin B	1.000	Addition
2.	*S. aureus* MRSA 100	Polymyxin B = 320 µM C1 = 40 µM	10 µM C1 + 40 µM Polymyxin B	0.375	Synergy
			20 µM C1 + 10 µM Polymyxin B	0.531	Addition

* The interaction was interpreted as synergy (FIC ≤ 0.5) or addition (FIC > 0.5 to 1.0) following a standard method (Giacometti *et al*., 2000).

Erythromycin is a macrolide that binds to the 50s subunit of the bacterial ribosome complex and impedes the translocation step of protein synthesis by inhibiting the peptidyl transferase reaction. The outer membrane barrier in Gram-negative bacteria can hinder the uptake of erythromycin (Saha *et al*., 2008; Rawlinson *et al*., 2010; Choi and Lee, 2012; Ulvatne *et al.*, 2001). Earlier studies indicate the potency of erythromycin in combination with other antibiotics (Miller *et al.*, 2013) but studies discussing the combination of erythromycin with membrane-directed amphiphiles is sparse. Given the strong membrane-targeting activity of C1 against *E. coli* MTCC 433 (Figure 2.5-2.6), it was encouraging to evaluate the adjuvant potential of C1 against this pathogen. Upon treatment with 20 µM erythromycin, the growth observed for *E. coli* MTCC 433 was 76%, which decreased to 23% on combination with 20 µM C1 and an additive interaction emerged (Figure 2.8C, Table 2.5). Further, when treated with 40 µM erythromycin, the growth was 49% for *E. coli* MTCC 433, which was reduced to 27% and 25% on combination with 5.0 µM C1 and 10 µM C1, respectively (Figure 2.8C), while the effects observed for these combinations were addition and synergy, respectively (Table 2.5).

Table 2.5. FIC index and nature of interaction of C1 in combination with erythromycin.

Sl. No.	Target Bacteria	MIC of Antibiotic and C1	Combination Treatment	FIC Index	Effect*
1.	*E. coli* MTCC 433	Erythromycin = 80 µM C1 = 40 µM	5 µM C1 + 40 µM Erythromycin	0.492	Synergy
			10 µM C1 + 40 µM Erythromycin	0.617	Addition
			20 µM C1 + 20 µM Erythromycin	0.683	Addition

* The interaction was interpreted as synergy (FIC ≤ 0.5) or addition (FIC > 0.5 to 1.0) following a standard method (Giacometti *et al*., 2000).

2.3.6. Antibiofilm Activity of C1

Given the healthcare burden imposed by bacterial biofilms, and the paucity of antibiofilm agents, there is a critical demand for novel antibiofilm therapeutics. Amongst the clinically relevant pathogenic bacterial strains, methicillin-resistant *Staphylococcus aureus* (MRSA) and *Pseudomonas aeruginosa* are of particular concern as they are known to form resilient biofilms. Encouraged by the potent bactericidal and membrane-directed activity of C1 the subsequent endeavor was to ascertain its antibiofilm potential. Solution-based assays revealed that C1 influenced the viability, biomass as well as the matrix formation by the biofilms. On treatment with C1, a dose-dependent biofilm inhibition as well as eradication was observed for both *S. aureus* MTCC 96 and *S. aureus* MRSA 100 (Figure 2.9A-2.9B, Appendix Figure A2.3A-2.3C) and the doses of C1 required for 50% biofilm inhibition ($MBIC_{50}$) were 40 µM and 120 µM for *S. aureus* MTCC 96 and *S. aureus* MRSA 100, respectively (Table 2.6). The concentrations of C1 required to eliminate 50% biofilm ($MBEC_{50}$) was higher than the inhibitory concentrations, and was found to be 160 µM for both *S. aureus* MTCC 96 and *S. aureus* MRSA 100.C1 also exhibited antibiofilm activity against *P. aeruginosa* MTCC 2488 (Appendix, Figure A2.3B and A2.3D).

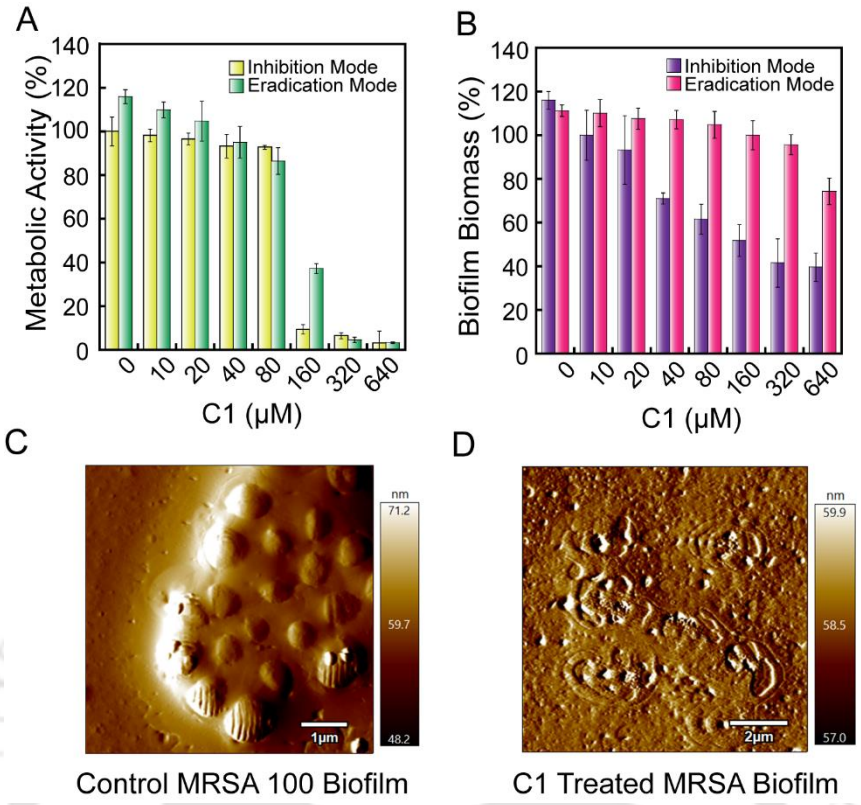

Figure 2.9. Determination of MRSA biofilm metabolic activity by (A) MTT assay and (B) CV assay to ascertain inhibition and eradication of *S. aureus* MRSA 100 biofilm by C1. (C-D) AFM analysis to study eradication of *S. aureus* MRSA 100 biofilm by C1.

Table 2.6. $MBIC_{50}$ and $MBEC_{50}$ of C1 against various target bacteria.

Sl. No.	Target Bacteria	$MBIC_{50}$	$MBEC_{50}$
1.	*S. aureus* MTCC 96	40 μM	160 μM
2.	*S. aureus* MRSA 100	120 μM	160 μM
3.	*P. aeruginosa* MTCC 2488	320 μM	1280 μM

However, the concentrations required for manifestation of the effect were manifold higher than the Gram-positive counterparts (Table 2.6, Appendix Figure A2.4A and A2.4C). Eradication of MRSA and *S. aureus* MTCC 96 biofilm by C1 was also evident in AFM analysis (Figure 2.9C-2.9D, Appendix Figure A2.4). Fluorescence microscopy-based studies further substantiated the antibiofilm activity of C1, wherein a dose-dependent decrease in the biofilm viability (cFDA stained biofilm) as well as the biofilm matrix (congo red stained biofilm) was clearly observed for all the three pathogenic bacteria (Figure 2.10, Appendix Figure A2.5).

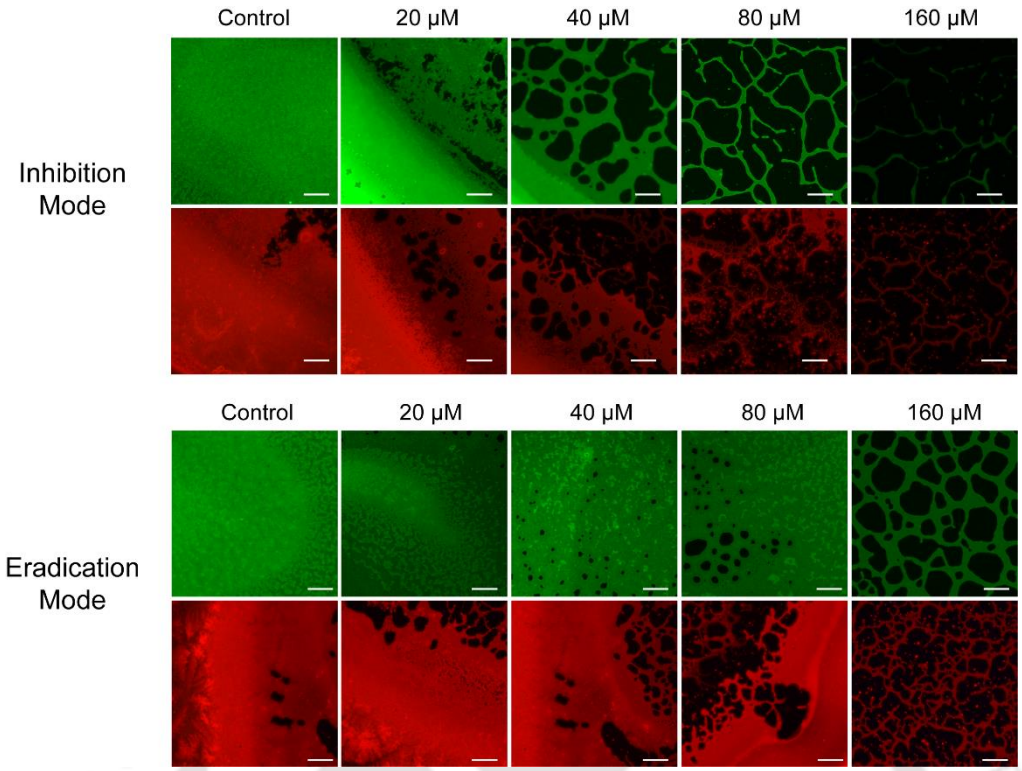

Figure 2.10. cFDA-SE and congo red-based fluorescence microscope analysis to ascertain inhibition and eradication potential of C1 against *S. aureus* MRSA 100 biofilm.

2.3.7. Cytotoxic Effect of C1

At concentrations up to 80 µM, which was equivalent to 2 x MIC against *S. aureus* MRSA 100, C1 was non-toxic to non-cancerous HEK 293 cells, which exhibited ~84% viability (Figure 2.11A). However, for the cancerous cell lines, a toxic effect manifested at much lower doses of C1, especially in case of HT-29 cells (Figure 2.11B). A higher susceptibility of carcinoma cell lines in an *in vitro* based MTT assay has been reported earlier and the phenomenon may be attributed to an enhanced permeation and retention effect (EPR) (Nichols and Han, 2014; Maeda, 2012).

In the context of potential therapeutic application, the target cell selectivity of an antibacterial is vital. The selectivity basically stems from differences in membrane bilayer composition observed between bacterial and mammalian cells. Bacterial membranes are known to harbor a higher content of negatively charged phospholipids in comparison to that present in the membranes of mammalian cells, wherein zwitterionic lipids and cholesterol are largely present (Tang *et al*., 2006, Zasloff, 2002). The ratio of IC_{50} to MIC, which is known as the therapeutic index (TI) reflects the potential of a bactericidal molecule to hinder bacterial growth, without imparting detrimental effects

on the host cells (for instance human cells). In the present study, it was observed that the selectivity of C1 was higher in the case of Gram-positive *S. aureus* MTCC 96 and *S. aureus* MSSA 104, with TI values of 6.0. In case of L. *monocytogenes* Scott, A, *S. aureus* MRSA 100 and *E. coli* MTCC 433, the corresponding TI values were 3.0 (Table 2.7).

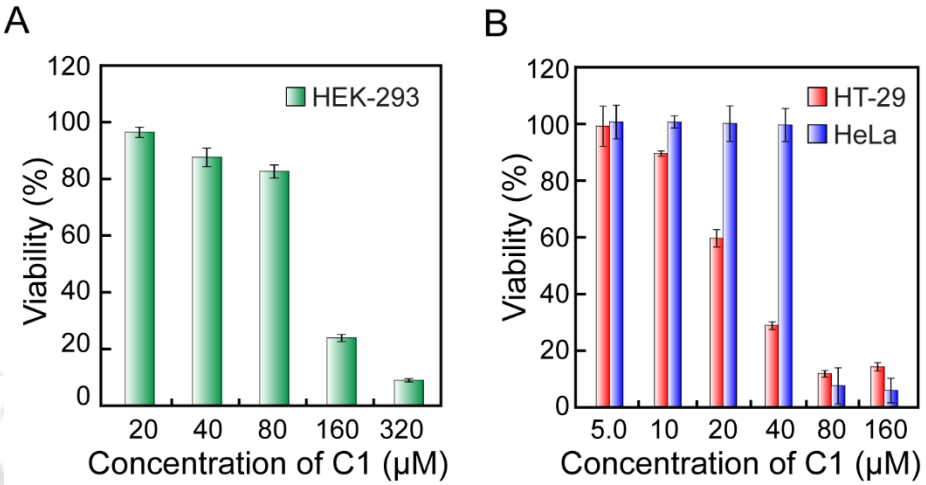

Figure 2.11. MTT assay to determine cytotoxic effect of C1 on (A) HEK 293 cells and (B) HT-29 and HeLa Cells. Each data point represents mean ± standard deviation from six samples.

Table 2.7. Therapeutic index of C1.

Sl. No.	Target Bacteria	MIC (μM)	Therapeutic Index (IC_{50} / MIC)*		
			HEK 293	HT-29	HeLa
1.	*S. aureus* MTCC 96	20	6.00	1.40	3.25
2.	*L. monocytogenes* Scott A	40	3.00	0.70	1.63
3.	*P. aeruginosa* MTCC 2488	80	1.50	0.35	0.82
4.	*E. coli* MTCC 433	40	3.00	0.70	1.63
5.	*S. aureus* MRSA 100	40	3.00	0.70	1.63
6.	*S. aureus* MSSA 104	20	6.00	1.40	3.25

*IC_{50} against HEK 293 cells = 120 μM; HT-29 cells = 28 μM and HeLa cells = 65 μM

2.4. Significant Findings

The salient findings of the present study can be enlisted as follows:

1. The amphiphile C1 exhibited broad-spectrum bactericidal activity and was more active on Gram-positive pathogenic bacteria in comparison to Gram-negative counterparts.
2. Fluorescence-based assays suggested that C1 exhibited membrane-targeting activity and rendered membrane depolarization in pathogenic bacteria.
3. C1 displayed bactericidal activity even in the complex milieu of physiological fluids such as SGF, SIF and SBF, which suggested that the amphiphile holds therapeutic potential in mitigation of *in vivo* bacterial infection.
4. Interestingly, the amphiphile could bring about a significant reduction in the MIC of model therapeutic antibiotics such as polymyxin B and erythromycin against target bacteria and a favorable interaction ensued between C1 and the antibiotics.
5. MTT assay in conjunction with fluorescence microscopy indicated that C1 could inhibit as well as eradicate *S. aureus* biofilm.
6. C1 was non-toxic to HEK 293 cells even at a concentration of 80 μM, which was equivalent to 2 × MIC against a tested MRSA strain.

Based on the leads obtained in the study, it was evident that the amphiphile C1 displayed potent antibacterial and antibiofilm activity against a clinical MRSA strain. On the other hand, it is likely that C1 can self-assemble to form a micelle, based on the prospect of intermolecular hydrogen bond formation and π-stacking of the head group. Conceivably, the micellar form of C1 can encapsulate antibiotics and facilitate generation of a composite bactericidal agent, wherein the membrane-disrupting activity of the amphiphile and the antibacterial effect of the antibiotic can be exploited in tandem for enhanced annihilation of MRSA. On the basis of this premise, the next chapter highlights the development of antibiotic-loaded C1 micelles as a promising anti-MRSA therapeutic material with enhanced capabilities.

Chapter 3

Investigations on the Self Assembly of C1 and Antibiofilm Potential of Antibiotic-loaded C1 Micelle

This chapter essentially demonstrates how the self-assembling attribute of the salicaldehyde-based amphiphile (C1) was leveraged to develop antibiotic-loaded micelles, wherein the activity of the two warheads could be harnessed in tandem for effective annihilation of MRSA cells and prevention of MRSA biofilm formation on surgical silk sutures.

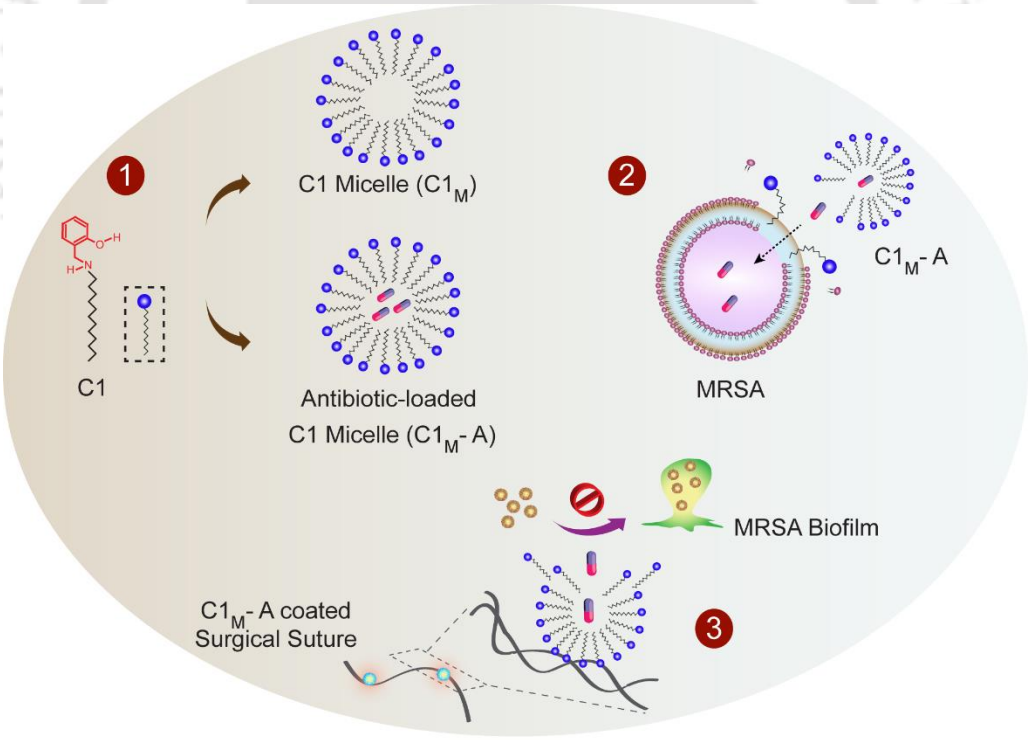

1. Generation of Antibiotic-loaded C1 Micelle ($C1_M$-A)
2. Combination Effect of Antibiotic-loaded C1 Micelle on MRSA
3. MRSA Biofilm Inhibition on Surgical Suture

ABSTRACT

This investigation describes the use of C1 in developing a nanomicellar carrier for antibiotics, wherein the activity of the two warheads are harnessed in tandem for effective elimination of MRSA. A concentration-dependent phase transition of C1 evident in the Π–A isotherms in an LB trough analysis indicated that C1 can aggregate and form a monolayer. The critical micelle concentration (CMC) for C1 in water was 18.5 µM whereas in a varying pH system, the CMC ranged from 23 µM - 34 µM. AFM analysis revealed spherical aggregates of C1 with an average size of 122 nm at concentrations above its CMC. Stable micelles based on C1 ($C1_M$) was generated by titration followed by a dialysis step. While FESEM analysis revealed the oblong shape of $C1_M$, FETEM indicated that the size of $C1_M$ was in the nanoscale range. The antibacterial activity of $C1_M$ was significantly lower than equivalent levels of C1. $C1_M$ was non-toxic to HEK 293 cells upto 80 µM, akin to C1, while at higher concentration (160 µM), $C1_M$ was notably less toxic than equivalent levels of C1. Rifampicin-loaded ($C1_M$-R) and vancomycin-loaded ($C1_M$-V) C1 micelles were generated, wherein the average particle size of $C1_M$-R was 292 nm and was lesser than $C1_M$-V as observed in FESEM, while FETEM analysis confirmed the nanoscale size of the antibiotic-loaded C1 micelles. Interestingly, the anti-MRSA activity of $C1_M$-R and $C1_M$-V were nearly 12-fold and 8-fold higher, relative to the corresponding antibiotics used in equal concentration. At concentrations above their MIC against MRSA, $C1_M$-R and $C1_M$-V were non-toxic to HEK 293 cells. Interestingly, MRSA biofilm formation was hindered in surgical silk suture coated with the antibiotic-loaded C1 micelle.

3.1. Introduction

Methicillin-resistant *Staphylococcus aureus* (MRSA) is implicated in a large number of community as well hospital-acquired infections and as a consequence there is a heightened need to develop effective therapeutic regimes in order to mitigate the crisis (Chambers and Deleo, 2010; Deresinski, 2005; Stryjewski and Corey, 2014; McCarthy *et al*., 2015; Hayden *et al*., 2005; Rehm and Tice, 2010). MRSA strains are known to be highly resistant to prevalent therapeutic antibiotics such as vancomycin and daptomycin and this predicament has aggravated the healthcare burden (Rehm and Tice, 2010; Deresinski, 2009; Hayden *et al*., 2005; Marty *et al.*, 2006). Conceivably, there is an enormous prospect to adopt a judicious medicinal and materials chemistry approach and develop antibacterials that can counter the inherent resistance in MRSA cells and thereby enhance the potency of therapeutic antibiotics (Thangamani *et al.*, 2016; Worthington *et al.*, 2013; LaPlante *et al.*, 2009). Notably, the possibility of a synergistic interaction between an antibacterial and antibiotic in combination is appealing as an anti-MRSA regimen as this premise has been validated in a large number of studies (Thangamani *et al.*, 2016; Worthington *et al.*, 2013; Fischbach *et al.*, 2009; Egim *et al.*, 2011; LaPlante *et al.*, 2009; Houlihan *et al.*, 1997; Tsuji *et al.*, 2005). However, it is to be noted that an important goal of adopting a combination therapy approach is also to achieve elimination of the target pathogen with a reduced dose of the antibiotic, which in turn, is likely to diminish antibiotic-associated host cell toxicity.

In case of a combination therapy directed against MRSA, the ability to break the resistance in target cells holds the key to restoring susceptibility of the pathogen to antibiotics. In this regard, literature reports highlight the potential of small synthetic molecules in combination therapy for alleviation of staphylococcal infection (Hu *et al*., 2015; Harris *et al*., 2012; Hess *et al*., 2014). Amongst the various categories of synthetic antibacterials, membrane-acting amphiphiles hold considerable promise as potent adjuvants that can increase the efficacy of antibiotics in combination therapy (Thiyagarajan *et al.*, 2017). However, from a therapeutic perspective, it is paramount that the amphiphilic adjuvant is biocompatible and non-toxic (Palermo and Kuroda, 2011; Song *et al.*, 2011; Oda *et al*., 2011; Fischer *et al*., 2003; Goswami *et al*., 2013). Hence, there is a need to adopt judicious design principles to develop amphiphilic antibacterials, which are less likely to render host-directed toxicity. Further, both the amphiphile and the antibiotic should be available in effective concentrations at the target site in order to induce a synergistic effect.

Synthetic amphiphiles can readily self-assemble and form micelles based on their inherent hydrophobicity and thus hold promise as micellar vehicles for effective delivery of antibiotics. The application of micelles in the domain of drug delivery and nanomedicine is well documented (Yao *et al.*, 2017; Petkau-Milroy and Brunsveld, 2013; Bartolami *et al.*, 2016; Sorrenti *et al.*, 2013). Literature reports also describe the antibacterial activity of micelles that originate from self-assembling oligomeric and polymeric amphiphiles (Liu *et al.*, 2014; Qiao *et al.*, 2012; Fukushima *et al.*, 2012). In order to ensure that such amphiphiles are non-toxic and used in antibacterial therapy, it is critical that the functional groups present in such amphiphiles are biocompatible. The prospect of a low molecular weight membrane-acting synthetic amphiphile in generating a micellar construct for antibiotic delivery is particularly interesting given the intrinsic resistance of MRSA cells towards antibiotics. Conceivably, the membrane-directed activity of the amphiphile is likely to breach the resistance and catalyze the delivery and increased cellular uptake of the antibiotic payload in tandem, which may yield a beneficial therapeutic outcome. To achieve this goal, the challenge is to develop a design principle for the amphiphile, which favors self-assembly in solution and encapsulation of antibiotic, renders sustained release of the antibiotic and ensures sufficient bioavailability of the dual warheads to achieve effective elimination of MRSA. Based on this premise, in this chapter the self-assembly behavior of the amphiphile C1 is characterized and the potential of the amphiphile as a micellar carrier of therapeutic antibiotics for elimination of a clinical MRSA strain is demonstrated.

3.2. Materials and Methods

3.2.1. Reagents and Growth Media

The reagents and the growth media used in this investigation were procured from various commercial sources as mentioned in section 2.2.1. of Chapter 2.

3.2.2. Bacterial Strain

S. aureus MRSA 100 strain was used in this investigation as a target bacteria. The growth conditions of the strain were as mentioned in section 2.2.4. of Chapter 2 unless stated otherwise.

3.2.3. Aggregation Studies of C1

DLS and LB trough analysis was pursued to study the aggregation propensity of C1. For DLS-based studies, increasing concentration of C1 (10 µM, 20 µM and 40 µM) was taken in a cuvette and was subjected to particle size estimation using water as the solvent. For DLS analysis, three independent experiments, each having multiple replicates were conducted. Surface pressure–mean molecular area (Π–A) isotherm for C1 was determined by LB trough analysis in a KSV 2000 Langmuir-Blodgett System (KSV Instruments, Finland). The width of the trough was 50 cm and the highest working area was 7750 cm^2. Ethanol and water were used to clean the surface of the trough. Subsequently, filter-sterilized MilliQ water (aqueous sub-phase) was added to the trough having two opposing and movable barriers. The trough temperature was sustained at 25°C using a temperature-controlled circulator. To prepare a stock solution, 0.5 mg/mL of C1 was added to chloroform in ice cold conditions. Subsequently, C1 in a range of varying concentration was layered on the aqueous sub-phase at multiple sites with a Hamilton microsyringe. The samples were equilibrated for 15 min during which period the solvent evaporated. Subsequently, the samples were compressed using the barriers at a rate of 1mN min^{-1}. A maximum compression speed of 3.0 mm/ min was maintained for 2100-2300 s. The surface pressure was recorded by a Wilhelmy plate suspended from a microbalance (KSV Instruments). A cartoon representing the anticipated change in the phase of an amphiphile on increasing surface pressure is indicated in Scheme 3.1.

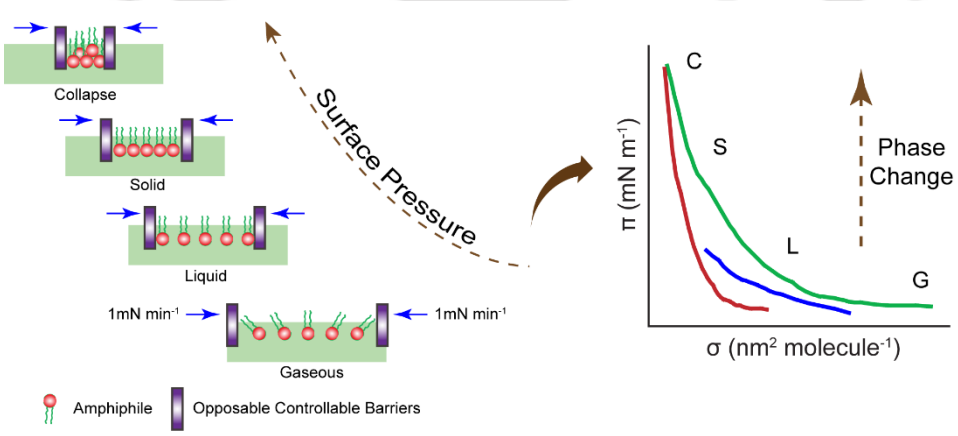

Scheme 3.1. Schematic representation of the change in the phase of an amphiphile on increasing surface pressure. C: collapse; S: solid; L: liquid; G: gaseous.

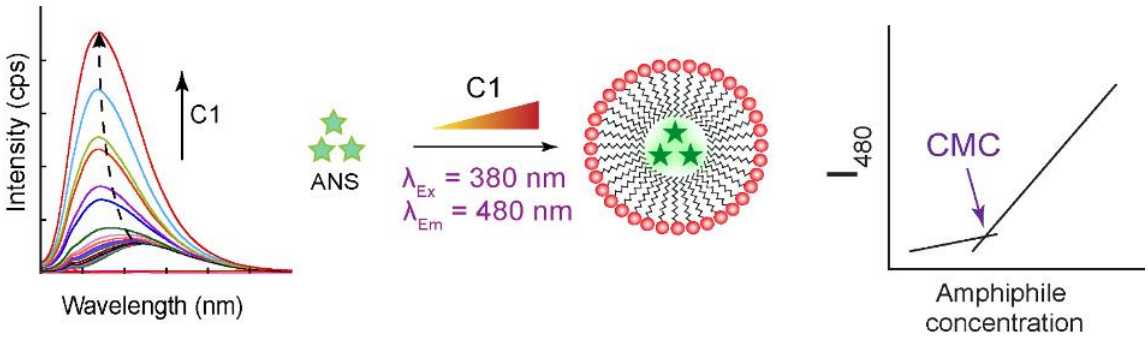

Scheme 3.2. Schematic representation of the principle of the estimation of CMC of C1 using ANS.

3.2.4. Critical Micelle Concentration (CMC) of C1

A 3.0 µM solution of ANS was prepared in water from a 3.0 mM stock solution prepared in DMF. This solution was taken in a 1.0 mL cuvette and its fluorescence emission spectra was measured in a spectrofluorimeter (FluoroMax-4, HORIBA) at an excitation wavelength of 380 nm and an emission range from 400 nm to 700 nm. To this solution, C1 was titrated at increasing concentrations (5.0 µM - 55 µM). For each concentration of C1 used in the titration, the fluorescence emission spectra were again recorded. The inflection point in a plot correlating the emission maxima at 480 nm and the concentration of C1 was noted as the CMC value for C1 in aqueous system. A schematic indicating the principle of determining the CMC of C1 using ANS is shown in Scheme 3.2.

3.2.5. Atomic Force Microscope (AFM) Analysis of C1

For AFM analysis, firstly, the surface of glass cover slips (18 mm x 18 mm) was sterilized with ethanol and a 10 µL aliquot of C1 (40 µM prepared in water) was drop casted onto the cover slip and allowed to dry overnight. AFM images of the sample was then captured with an Agilent 5500 AFM (Agilent Technologies, Chandler, AZ, USA). Nanobiosensors^{TM} cantilevers made of silicon nitride were used having a resonant frequency between 150 to 250 kHz. Images were acquired in intermittent contact mode as depicted in Scheme 3.3. Analysis of the images was accomplished using the WSxM v4.0 Beta 9.1 image viewer software (Horcas *et al.*, 2007).

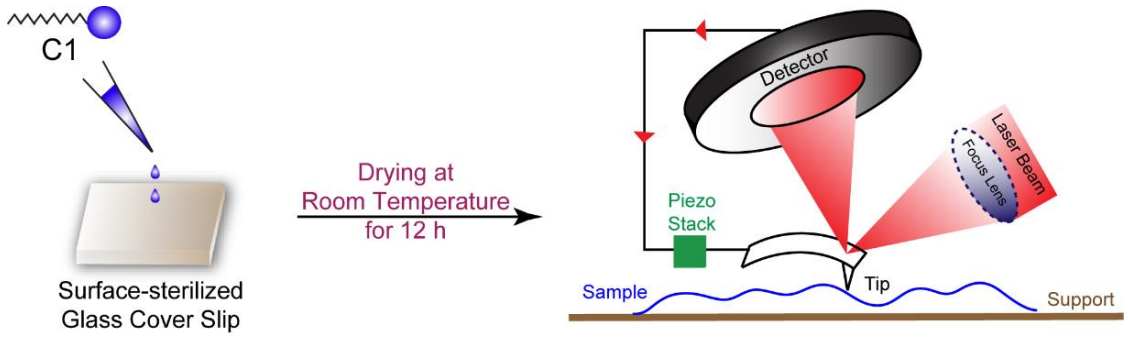

Scheme 3.3. Schematic representation of the protocol used to analyze the morphology of C1 using AFM.

3.2.6. Interaction of C1 with Bacteria

S. aureus MRSA 100 cells were grown overnight in BHI media at 37°C and 180 rpm. The cells were harvested, washed with sterile PBS and then 100 µL of the same was resuspended in 900 µL of PBS to obtain around 10^6 cells. The cell suspension was then incubated with increasing concentrations of C1 (10 µM, 20 µM and 40 µM) in separate sets for 30 minutes at room temperature. Following incubation, the cells were separated by centrifugation at 8000 rpm for 3 min. The supernatant, consisting of free C1 in solution was then subjected to particle size estimation by DLS (Zeta Sizer, Malvern, UK). In a separate set, varying concentrations of C1 alone (10 µM, 20 µM and 40 µM) were also spun down and the supernatant was subjected to particle size estimation by DLS as control. The DLS experiments were performed in three independent sets and every set consisted of multiple replicates. A schematic representing the experimental protocol for determining the interaction of C1 with bacteria is shown in Scheme 3.4.

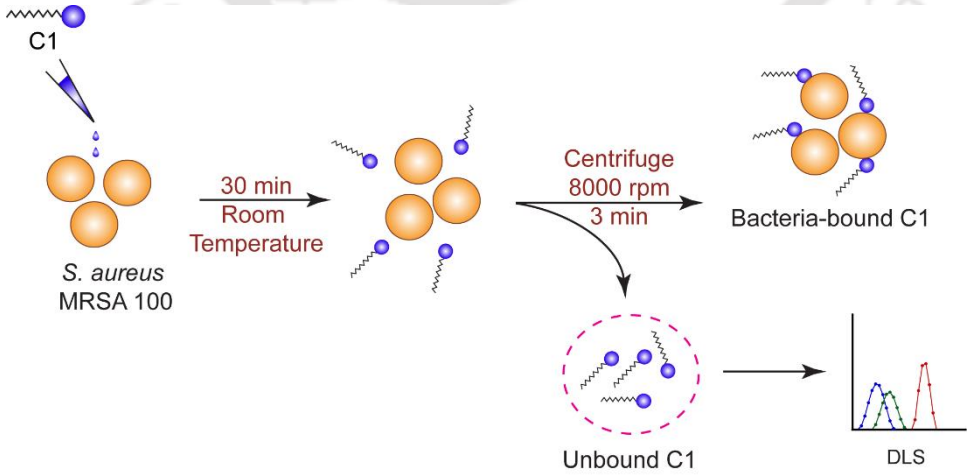

Scheme 3.4. Schematic representation of the protocol used to study interaction of C1 with bacterial cells using DLS.

3.2.7. C1 Micelle ($C1_M$) and Antibiotic-loaded C1 Micelle

In 5.0 mL of DMSO, 50 mg of C1 was added and stirred for 2 h at room temperature (RT). To this solution an equal volume of autoclaved and filter-sterilized MilliQ water was added drop-wise at a rate of 1.0 mL/min and the solution was stirred for another 3 h at RT. Subsequently, this solution was dialyzed in a 2000 Da cut-off bag for 24 h against MilliQ water at 4°C overnight. The dialysate was lyophilized to obtain the micellar form of C1 ($C1_M$). To prepare a stock solution, the freeze-dried sample of $C1_M$ was resuspended in 1.0 mL sterile MilliQ water. A schematic showing the protocol for preparation of $C1_M$ is shown in Scheme 3.5.

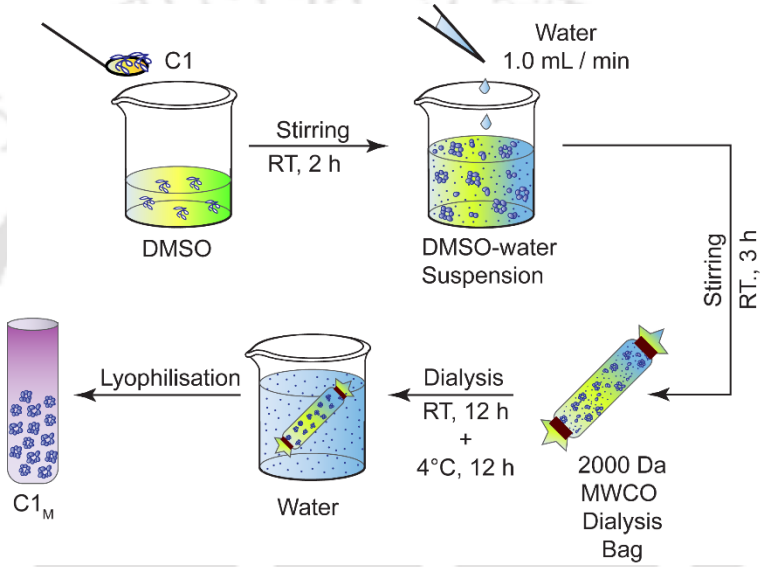

Scheme 3.5. Schematic representation of the protocol used for the preparation of $C1_M$.

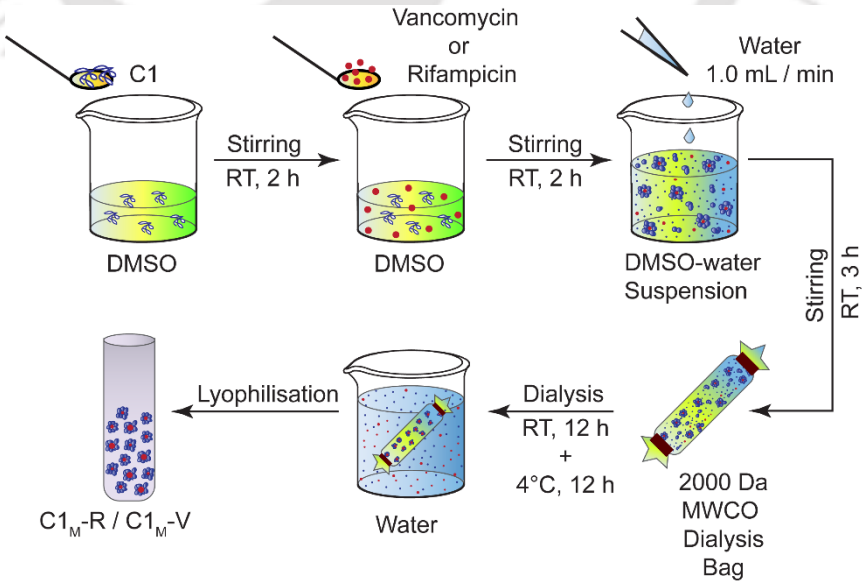

Scheme 3.6. Schematic representation of the protocol used for the preparation of $C1_M$-R and $C1_M$-V.

The antibiotic-loaded C1 micelles were prepared as follows: Initially in 5.0 mL of DMSO, 50 mg of C1 was added and stirred for 2 h at RT. Subsequently, in separate sets either 50 mg of rifampicin or 25 mg of vancomycin was added to the solution of C1. The mixture was allowed to homogenize. To this solution an equal volume of autoclaved and filter-sterilized MilliQ water was added. The addition of water was drop-wise at a rate of 1.0 mL/min and the solution was subjected to stirring for another 3 h at RT. Subsequently, this solution was subjected to dialysis and lyophilization as described earlier for the preparation of $C1_M$. A schematic showing the protocol for preparation of rifampicin-loaded $C1_M$ ($C1_M$-R) and vancomycin-loaded $C1_M$ ($C1_M$-V) is shown in Scheme 3.6. In order to assess the loading of rifampicin and vancomycin in $C1_M$, the absorbance spectra of rifampicin and vancomycin taken at various concentration was measured at 340 nm and 280 nm, respectively and a calibration plot was generated. Freeze-dried $C1_M$-R and $C1_M$-V was reconstituted separately by suspending in 1.0 mL sterile MilliQ water. An aliquot of $C1_M$-R and $C1_M$-V (in sterile MilliQ water) was initially diluted in DMSO (1:1000 v/v) and followed by further dilution in sterile MilliQ water (1:1000 v/v). The absorbance of this solution was measured at 340 nm and 280 nm separately and antibiotic loading in the micelle was estimated using the previously generated calibration plot as shown in Scheme 3.7. The absorbance of $C1_M$-R and $C1_M$-V was also recorded at 290 nm to ascertain the amount of C1 present in the antibiotic-loaded micelle.

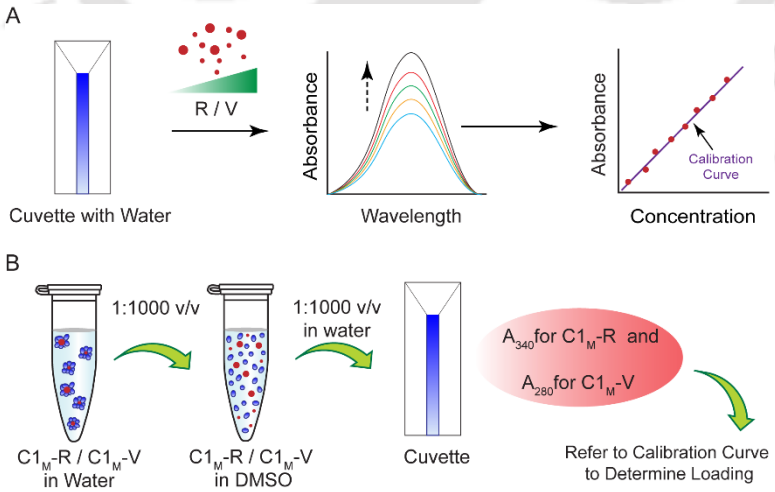

Scheme 3.7. Schematic representation of the protocol used for ascertaining loading of antibiotics onto the micelle. R: Rifampicin V: Vancomycin

The following relationship was used to estimate the encapsulation efficiency (EE%) and the loading content (LC%):

$$Loading\ Content\ (LC\%) = \frac{\textbf{Mass of Drug in Micelle}}{\textbf{Total Mass of Loaded Micelle}} \times 100$$

$$Encapsulation\ Efficiency\ (EE\%) = \frac{\textbf{Mass of Drug in Micelle}}{\textbf{Initial Amount of Feeding of Drug}} \times 100$$

3.2.8. Characterization of $C1_M$, $C1_M$-R and $C1_M$-V

Solution-based characterization of $C1_M$, $C1_M$-R and $C1_M$-V was accomplished by UV-visible spectroscopy, fluorescence spectroscopy and DLS analysis as indicated in Scheme 3.8. The absorbance spectra of $C1_M$, $C1_M$-R and $C1_M$-V was measured in scanning mode from 200 nm to 600 nm from three independent experimental samples. In a separate experiment, particle size estimation of $C1_M$, $C1_M$-R and $C1_M$-V was accomplished by DLS (Zeta Sizer, Malvern, UK). In these experiments, the concentration of $C1_M$ was 79 µM and the concentration of rifampicin and vancomycin in the loaded micelle were 2.9 µM and 0.2 µM, respectively. Three independent sets of samples were used for DLS measurements, each having multiple replicates. In another experiment, a 10 µL aliquot of $C1_M$, $C1_M$-R and $C1_M$-V were analyzed in a field emission scanning electron microscope (Zeiss Sigma, USA) at 2.0 Kv.

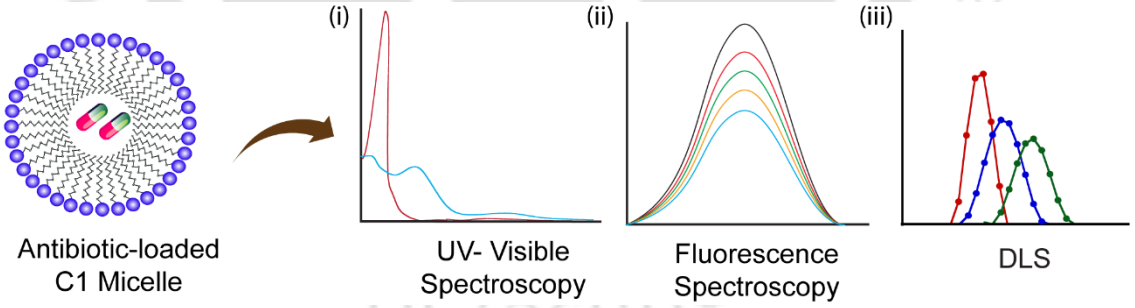

Scheme 3.8. Schematic representation of the methods used to characterize the antibiotic-loaded micelle.

3.2.9. Bactericidal Activity, Antibiofilm Potential and Cytotoxicity of $C1_M$

A time-kill curve analysis was performed to test the bactericidal activity of $C1_M$ against *S. aureus* MRSA 100. Target cells of Gram-positive *S. aureus* MRSA 100 (approximately 10^6 CFU/mL each suspended in sterile PBS) were treated with varying concentration (20 µM - 80 µM each) of $C1_M$ at 37ºC and 180 rpm. Samples were

withdrawn at regular intervals of 3 h, 6 h, 12 h and 24 h and subjected to serial dilution and plating to the ascertain the viable cell number (Log_{10} CFU/mL). The viable cell counts for the untreated target bacterial cells suspended in PBS was also determined at the specific intervals as depicted in scheme 3.9. In a separate experiment, *S. aureus* MRSA 100 cells were treated with C1 and $C1_M$ in separate sets and then the cells were analyzed in a field emission scanning electron microscope (Zeiss Sigma, USA) at 2.0 Kv. Following this, the antibiofilm activity of varying concentrations of $C1_M$ (5.0 µM - 640 µM) in inhibition as well as eradication mode was also ascertained against *S. aureus* MRSA 100 cells using MTT and crystal violet assay using the protocols as mentioned in the previous chapter. Fluorescence microscopy-based analysis of antibiofilm activity of $C1_M$ was also ascertained by cFDA-SE and congo red staining against MRSA biofilm. The cytotoxic effect of $C1_M$ (20 µM - 320 µM) was ascertained on HEK 293 cells by a standard MTT assay (Goswami *et al.*, 2013). For both the bactericidal activity and cytotoxicity, C1 alone at equivalent concentration was also used for comparison.

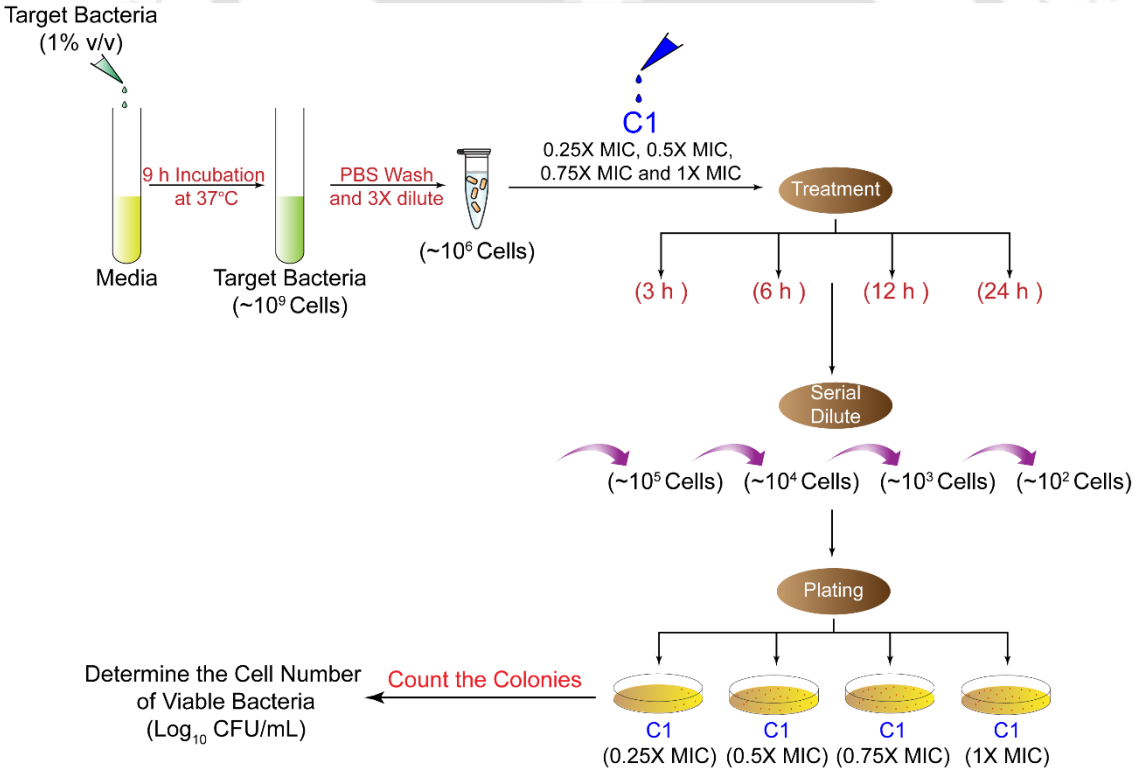

Scheme 3.9. Schematic representation of the protocol used for the generation of a time kill curve.

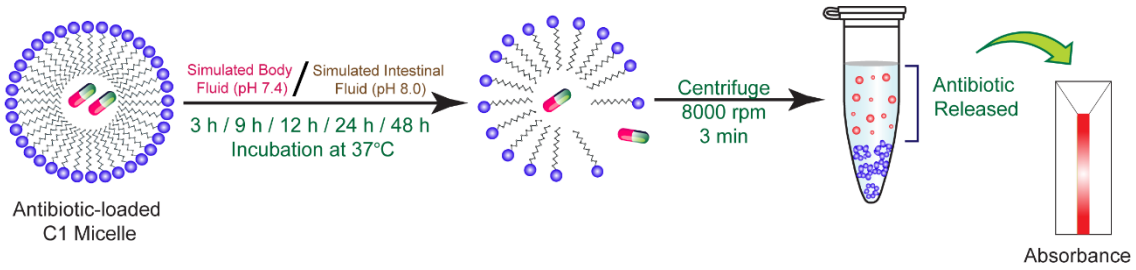

Scheme 3.10. Schematic representation of the methods used to study the release of the antibiotic-loaded onto C1 micelle in SBF and SIF.

3.2.10. In Vitro Release Kinetics

Rifampicin-and vancomycin-loaded $C1_M$ (a final concentration of 14 µM rifampicin and 2.26 µM vancomycin) was resuspended in separate sets in 1.0 mL each of SBF (pH 7.4) and SIF (pH 8.0). Following incubation of the samples in an orbital shaker at 180 rpm and 37°C, samples were withdrawn intermittently (0 h, 3 h, 9 h, 12 h, 24 h and 48 h) and centrifuged at 8,000 rpm for 3 min. The supernatant from the samples were transferred into a fresh microcentrifuge tube and the absorbance spectra of the solutions were recorded from 250 nm to 750 nm (Scheme 3.10). The release of the antibiotics at specific time periods was quantified using a previously generated calibration plot for rifampicin and vancomycin and expressed as % cumulative release. Three independent experimental sets were taken, wherein every set consisted of three replicates.

3.2.11. Anti-MRSA Activity, Uptake Studies of $C1_M$, $C1_M$-R and $C1_M$-V and Cytotoxicity of Antibiotic-loaded C1 Micelle

A cFDA-SE leakage assay was performed on *S. aureus* MRSA 100 strain to ascertain the membrane-directed activity of $C1_M$, $C1_M$ -R, $C1_M$ -V and the antibiotics alone. To separate sets of cFDA-SE labelled *S. aureus* MRSA 100 cells, $C1_M$-R (104 µM $C1_M$ loaded with 3.73 µM rifampicin) and $C1_M$-V (104 µM $C1_M$ loaded with 2.26 µM vancomycin) was added and incubated at 37°C and 180 rpm for 3 h and 6 h. The leakage of cFDA from cells following incubation was estimated by fluorescence measurements as mentioned previously. In order to ascertain antibiotic uptake, *S. aureus* MRSA 100 cell were grown overnight and centrifuged at 8000 rpm for 3 min. The cells were washed with sterile PBS, diluted and resuspended in the same to achieve 10^6 CFU/ mL. In separate sets, the cells were treated with (i) $C1_M$-R or $C1_M$-V, (ii) $C1_M$ combined with rifampicin ($C1_M$ + R) or vancomycin ($C1_M$ + V) and (iii) rifampicin (R) or vancomycin (V). The concentration of C1 in the micelles was 100 µM while the concentration of free

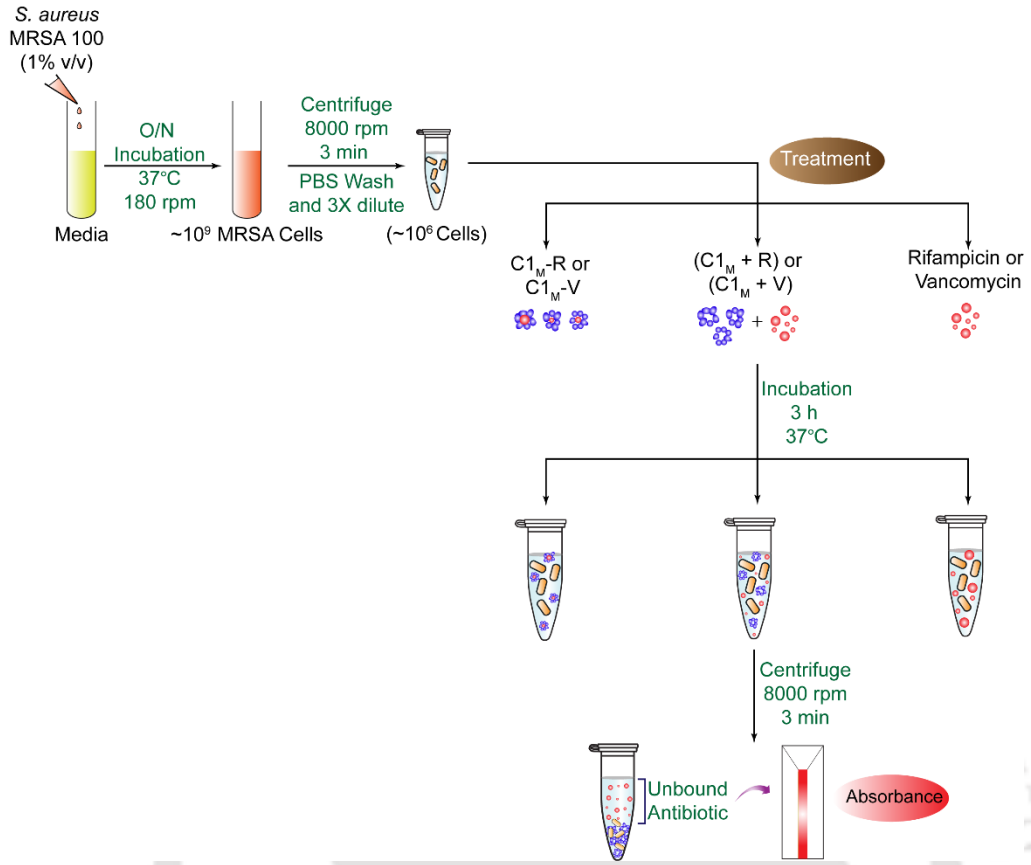

Scheme 3.11. Schematic representation of the methods used to study the uptake of the antibiotic loaded onto C1 micelle into MRSA cells.

rifampicin and vancomycin was 3.59 µM and 2.17 µM, respectively, which was equal to the amount loaded in the micelle. Following treatment for 3 h at 37°C and 180 rpm, the samples were centrifuged at 8000 rpm for 3 min. Antibiotic present in the supernatant (cell-free antibiotic) was estimated by quantifying the absorbance and using a previously generated calibration plot with 1.2 µM – 24.3 µM rifampicin and 0.7 µM – 55.2 µM vancomycin. A schematic representation of the protocol used to estimate antibiotic uptake in cells treated with $C1_M$, $C1_M$ -R and $C1_M$ -V is indicated in Scheme 3.11. In order to ascertain the relative cell free antibiotic, the cell-free or unbound antibiotic present in the samples was normalized on a scale of 1.0 against the unbound antibiotic present in samples treated with only R or V as follows:

$$Relative\ Cell\ Free\ Antibiotic = \frac{Amount\ of\ Unbound\ Antibiotic\ for\ Cells\ Treated\ with\ C1_M - R\ or\ C1_M - V\ or\ (C1_M + R)\ or\ (C1_M + V)}{Amount\ of\ Unbound\ Antibiotic\ for\ Cells\ Treated\ with\ only\ Antibiotic}$$

The cytotoxic effect of $C1_M$-R and $C1_M$-V was ascertained on cultured HEK 293 cells by a standard MTT assay using a standard protocol as mentioned previously (Goswami *et al.*, 2013). The concentrations of C1 present in $C1_M$-R and $C1_M$-V were 32 µM, 65 µM and 130 µM. The corresponding concentrations of rifampicin in $C1_M$-R were 1.21 µM, 2.43 µM and 4.86 µM, while the corresponding concentrations of vancomycin in $C1_M$-V were 0.69 µM, 1.38 µM and 2.76 µM.

3.2.12. Bactericidal Efficacy of Rifampicin and Vancomycin in Combination with C1

In a sterile microtitre plate, 100 µL of BHI media was incorporated with either rifampicin (1.22 µM and 2.43 µM) or vancomycin (0.35 µM and 0.69 µM) in combination with varying concentrations of C1 (5.0 µM, 10 µM and 20 µM). To each well, 10 µL aliquot of *S. aureus* MRSA 100 cell suspension (10^6 CFU suspended in BHI media) was inoculated. The cells were incubated at 37^{o}C and 180 rpm for 12 h. Bacterial cell growth was estimated by measuring absorbance at 600 nm in a microtitre plate reader (Infinite M200, TECAN, Switzerland) and expressed as percentage growth inhibition compared to untreated cells (cells grown in the absence of antibiotics and C1). In separate sets, the effect of varying concentrations of the antibiotic or C1 alone on the growth of target bacteria was also ascertained. For every sample, three independent experiments were performed, each having three replicas.

3.2.13. Coating of Surgical Sutures

Non-absorbable surgical suture of braided silk black (NW 5028) (Ethicon, Johnson & Johnson, India) was used in this study. For coating, $C1_M$, $C1_M$-R and $C1_M$-V (39.5 mg each) were dissolved in separate sets in 1.0 ml 99.8% ethanol (0.79 g), so as to achieve a mass content of 5% (w/w) (Obermeier *et al.*, 2014). The suture pieces (1.5 cm) were dipped aseptically in separate 1.0 ml solution of $C1_M$ or $C1_M$-R or $C1_M$-V. To ensure consistent coating, the sutures were incubated in a shaker for 12 h at 37°C and 180 rpm followed by drying (~ 12 h) in a laminar air flow. Likewise, silk surgical sutures were also coated with only C1 as control. ATR-FTIR analysis was performed to verify suture coating and the amount of species coated per unit length of the suture was ascertained. A cartoon indicating the procedure used to coat silk surgical sutures with $C1_M$, $C1_M$ -R and $C1_M$ -V is depicted in Scheme 3.12.

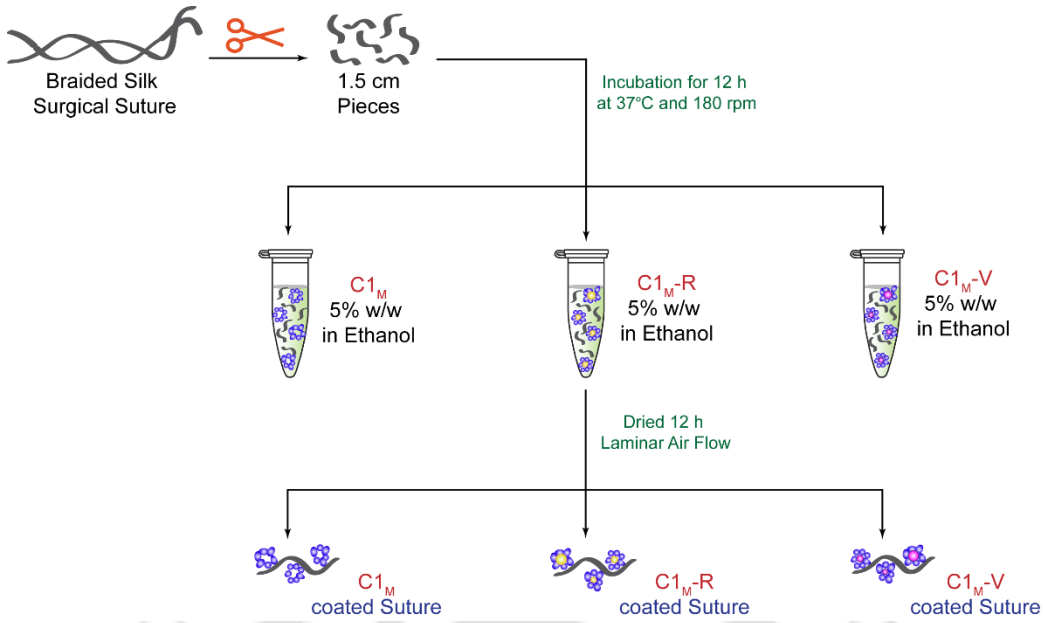

Scheme 3.12. Schematic representation of the methods used to coat silk surgical sutures with $C1_M$, $C1_M$ -R and $C1_M$ -V.

3.2.14. Antibacterial Efficacy and Antibiofilm Potential of Coated Surgical Sutures

An agar plate diffusion test was conducted to determine the antibacterial activity of $C1_M$, $C1_M$-R and $C1_M$-V coated as well as non-coated sutures. Approximately 10^6 cells of *S. aureus* MRSA 100 strain were seeded in BHI soft agar (0.8% agar) and overlaid on a bottom layer of BHI agar (1.5% agar). The sutures were then gently placed on the BHI soft agar surface. Following incubation at 37°C for 24 h, the zone of inhibition around the suture was recorded and its image was captured. In separate sets, $C1_M$, $C1_M$-R and $C1_M$-V coated sutures (1.5 cm, n = 3) were taken in 1.0 ml of sterile PBS (pH 7.4) in microcentrifuge tubes and placed in a shaker incubator at 180 rpm and 37°C for 48 h to facilitate release of the coating. A cFDA-SE leakage assay was conducted against *S. aureus* MRSA 100 cells as described earlier in chapter 2 in order to ascertain the bactericidal activity of the released material. In order to study the antibiofilm activity, coated and non-coated sutures were added to 1.0 ml of BHI broth with 0.25% glucose taken in separate wells of a 6 well plate. An inoculum of the target bacteria (~10^6 CFU /mL *S. aureus* MRSA 100) was added and the setup was kept for incubation at static conditions and a temperature of 37°C for 24 h. Subsequently, the sutures were carefully removed, dried in a laminar hood for 12 h and subjected to FESEM analysis.

3.2.15. Cytotoxic Effect of Coated Sutures

Initially, $C1_M$, $C1_M$-R and $C1_M$-V coated and non-coated sutures (1.5 cm each) were incubated in 1.5 ml microcentrifuge tubes containing 1.0 ml DMEM. The eluates from the sutures were collected following incubation for 24 h at 37°C and 180 rpm. HEK 293 cells were seeded onto 96-well tissue culture plates having DMEM media (5 x 10^3 cells per mL in each well) and following 24 h of growth, the DMEM media in the wells was replaced by the suture eluates and incubated for 24 h. Subsequently, media from each well was aspirated and cell viability was determined by MTT assay in four sets for each tested sample. The absorbance obtained for cells incubated with eluates from non-coated sutures (control) represented 100% cell viability. The absorbance recorded in case of cells exposed to eluates from coated sutures was compared to determine % cell viability.

3.3. Results and Discussion

3.3.1. Aggregation Behavior of C1

Aggregation of C1 was studied using DLS wherein a concentration-dependent increase in the hydrodynamic radii was observed. (Figure 3.1A). LB trough analysis ascertained the ability of C1 to form a monolayer. In the Π–A isotherms, a phase transition from gaseous to solid was manifested and the inflection point for C1 in the range of 50 µM C1-5.0 µM C1 was observed to be 25-45 $Å^2$ (Figure 3.1B). As the concentration of C1 increased, the area per molecule was reduced (Table 3.1), suggesting modification with regard to lateral orientation of the head group of the amphiphile in the air-water interface.

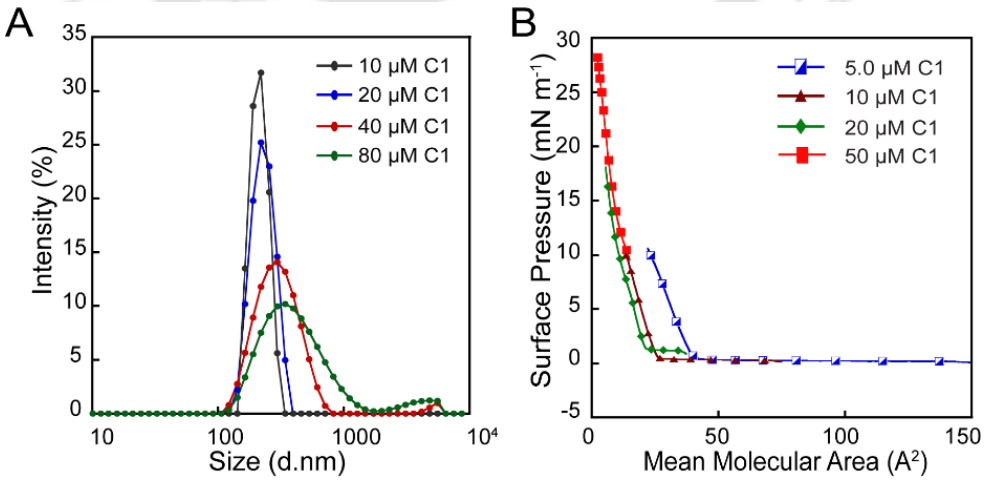

Figure 3.1. (A) Estimation of concentration-dependent size distribution of C1 by DLS and (B) LB trough analysis of C1.

Table 3.1. Estimation of area per molecule for varying concentrations of C1.

C1 (μM)	Number of Molecules ($\times 10^{18}$)	Molecular Area ($Å^2$)	Area per Molecule ($Å^2$) $\times 10^{-18}$
5.0	3.01	40.37	13.40
10	6.02	26.04	4.32
20	12.05	21.49	1.78
50	30.12	18.89	0.62

3.3.2. Micelle formation of C1 and its Anti-MRSA Activity

Owing to its amphipathicity, C1 was observed to have the ability to self-assemble in solution. The titration with C1 led to spectral changes of ANS (Figure 3.2A) and the CMC of C1 in water was 18.5 μM (Figure 3.2B). On exposure to various pH system, it was observed that the CMC of C1 changed nominally at physiological pH (pH 7.4), whereas at pH 2.0 and pH 8.0, the CMC was comparatively high (Figure 3.2B, inset). The head group of C1 is likely to undergo protonation and deprotonation at acidic and basic pH, respectively, which may result in the higher CMC of the amphiphile. Spherical aggregates of C1 having an average size of 122 nm and a height profile of nearly 9.0 nm

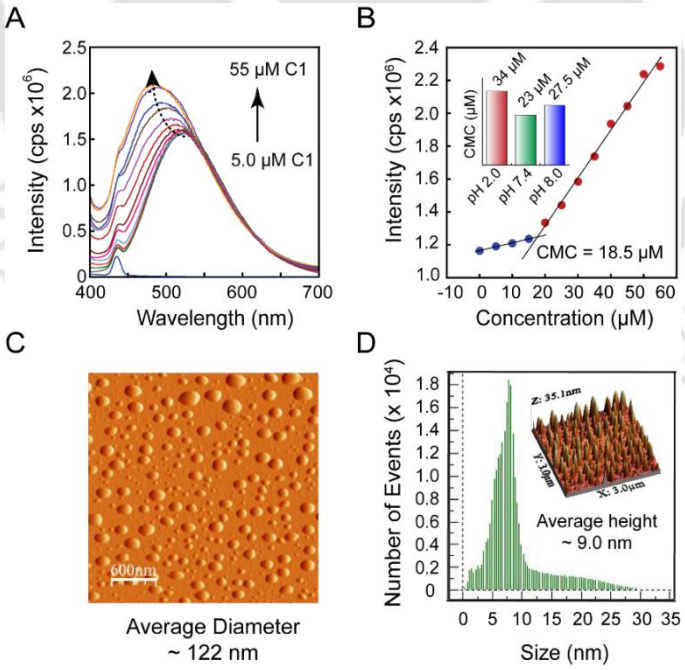

Figure 3.2. (A) Fluorescence emission spectra of ANS upon titration with C1 with a blue shift in the emission maxima indicated by the dotted arrow. (B) The inflection point indicating CMC of C1 in water. Inset indicates CMC of C1 in various pH system. (C-D) 2D topography AFM image and height profile of 40 μM C1. Inset showing 3D topography of C1.

were evident in AFM analysis of the amphiphile at a concentration above its CMC (40 µM) (Figure 3.2C-3.2D). C1 displayed a hydrophilic-lipophilic balance (HLB) of 8.38 when ascertained by Griffin's method (Griffin, 1949; Griffin, 1954). This indicated that the amphiphile's nature was akin to wetting and spreading agent an o/w (oil in water) emulsifier. Micelles generated from C1 can thus be explored for loading antibiotics as payload and thereby derive a composite antibacterial, wherein there could be a possibility of synergy between the warheads (C1 and antibiotic). Notably, this composite system is likely to display favorable pharmacokinetics and also curb the host cell toxicity of antibiotics, as observed in the case of liposome or nano-delivery systems (Drulis-Kawa and Dorotkiewicz-Jach, 2010; Sande *et al*., 2012). In case of the antibiotic-loaded C1 micelle, the antibacterial activity of the amphiphile and the antibiotic can perhaps be leveraged in tandem for enhanced elimination of MRSA, in contrast to liposomes, which essentially are meant for drug delivery. Conceivably, the antibiotic-loaded C1 micellar system may also yield a notable bactericidal effect, given the significant membrane-directed activity and the antibiofilm potential of C1 against *S. aureus* MRSA 100 at concentrations higher than its CMC (Figure 2.9, Table 2.6).

3.3.3. Interaction of C1 with Bacteria

In the DLS experiments, it was observed that the average particle size of cell-free C1 (unbound) was higher than total C1 used initially for interaction with MRSA (Figure and micelle formation in solution by C1 is a dynamic process. Hence, it can be surmised that at concentrations above its CMC, the C1-derived micelle can disassemble and subsequent anchoring of the non-micellar smaller size species of C1 onto MRSA cells as evidenced in the DLS experiments can perhaps lead to prominent bactericidal activity of C1.

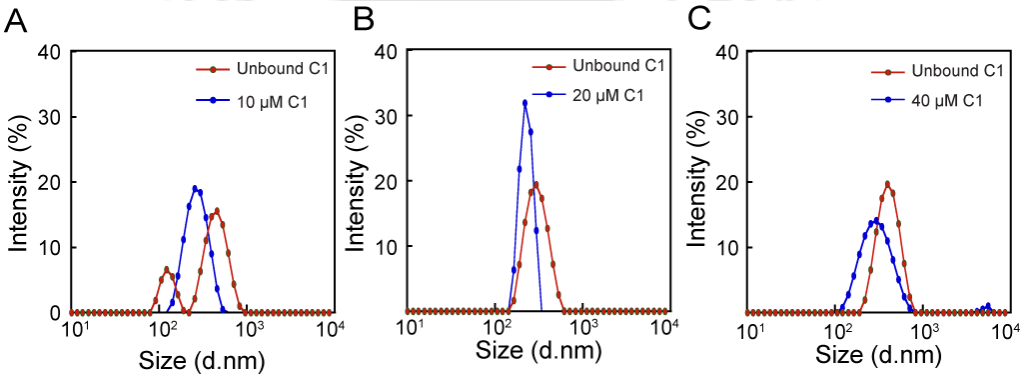

Figure 3.3. (A-C) Particle size distribution of varying concentrations of C1 and unbound C1 following interaction with *S. aureus* MRSA 100 in PBS. C1 was interacted with *S. aureus* MRSA 100 cells in PBS for 30 minutes.

3.3.4. C1 Micelle and Antibiotic-loaded C1 Micelle

Micelles based on C1 ($C1_M$) as well as rifampicin and vancomycin-loaded $C1_M$ ($C1_M$-R and $C1_M$-V, respectively) were generated by titration followed by a dialysis step. Rifampicin and vancomycin were selected as model therapeutic antibiotics given their potential against MRSA (Perlroth *et al.*, 2008; Muller *et al.*, 2013; Rodvold and Mcconeghy, 2014). UV-vis spectra of $C1_M$ resembled the absorption spectra of C1, while the salient absorption peaks of the antibiotic as well as C1 was evident in $C1_M$-R and $C1_M$-V (Figure 3.4.A). DLS analysis indicated that $C1_M$-V was larger in size than both $C1_M$-R and $C1_M$ (Figure 3.4.B). The larger size of vancomycin in comparison to rifampicin may account for this observation. Following 30 min incubation, it was observed that the decrease in hydrodynamic radii of $C1_M$ was only 7% while it was 23% and 18% for $C1_M$-R and $C1_M$-V, respectively. This indicated that $C1_M$ was a stable micelle, owing perhaps to a slower kinetics of disassembly. $C1_M$ and $C1_M$-R were observed to be oblong-shaped in FESEM analysis, with an average particle size of 292 nm and 194 nm, respectively

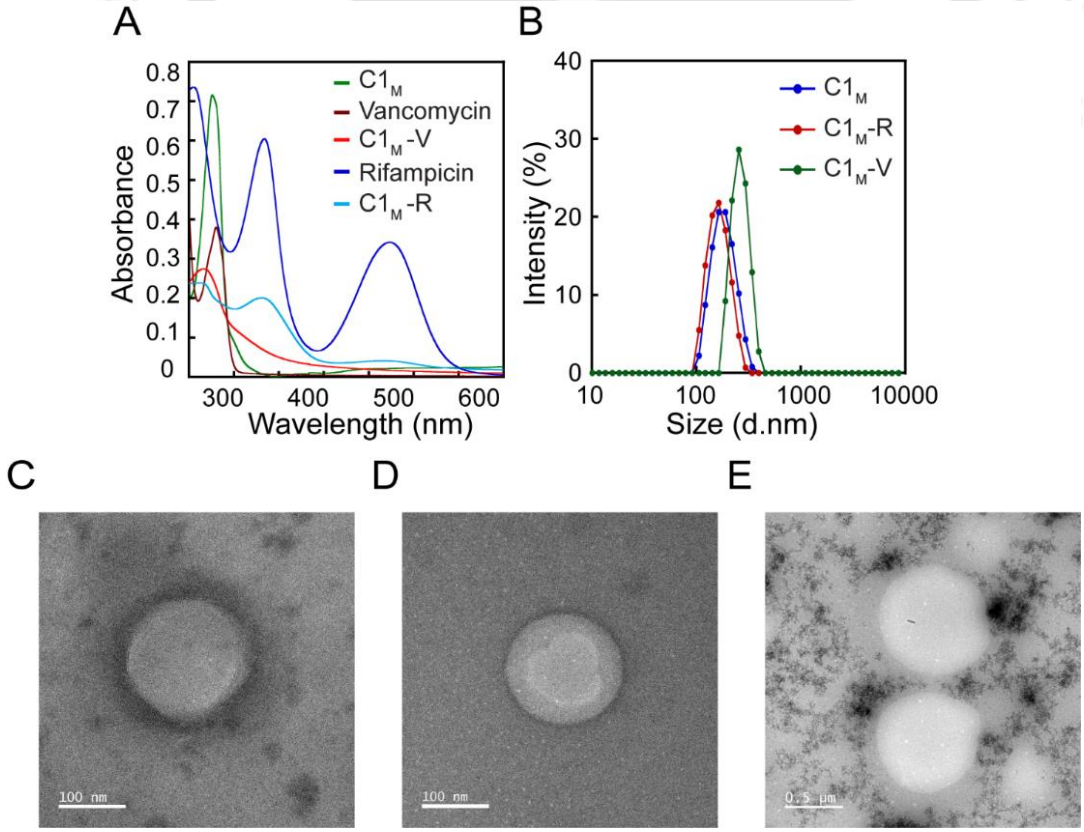

Figure 3.4. (A) UV-visible absorption spectra of $C1_M$-R and $C1_M$-V. (B) Estimation of the particle size of $C1_M$, $C1_M$-R and $C1_M$-V by DLS. FETEM image of (C) $C1_M$, (D) $C1_M$-R and (E) $C1_M$-V.

(Appendix, Figure A3.1A-A3.1D). In comparison, $C1_M$-V was spherical and had a larger average particle size of around 883 nm (Appendix, Figure A3.1E-A3.1F). Further, $C1_M$, $C1_M$-R and $C1_M$-V were observed to be in nanoscale dimensions when subjected to FETEM analysis (Figure 3.4.C-3.4E).

3.3.5. Antibacterial and Antibiofilm Activity of C1 Micelle and its Cytotoxic Potential

The antibacterial activity of $C1_M$ was considerably lower as compared to C1 at equivalent concentrations (Figure 3.5A-B). The availability of the C1 depends on the disassembly of the stable $C1_M$. Since the disassembly of the stable $C1_M$ may be a slower thermodynamic process, the availability of free C1 is perhaps limited, resulting in lower bactericidal activity. FESEM-based imaging also indicated that the extent of cellular damage in $C1_M$-treated cells was much less in comparison to C1-treated cells (Figure 3.5D-E). On treatment with $C1_M$, a dose-dependent biofilm inhibition as well as eradication was observed for *S. aureus* MRSA 100 in both MTT-based as well as crystal violet-based assays (Figure 3.6A-3.6B). However, the doses of $C1_M$ required for 50% biofilm inhibition ($MBIC_{50}$) as well as the concentrations of $C1_M$ required to eliminate

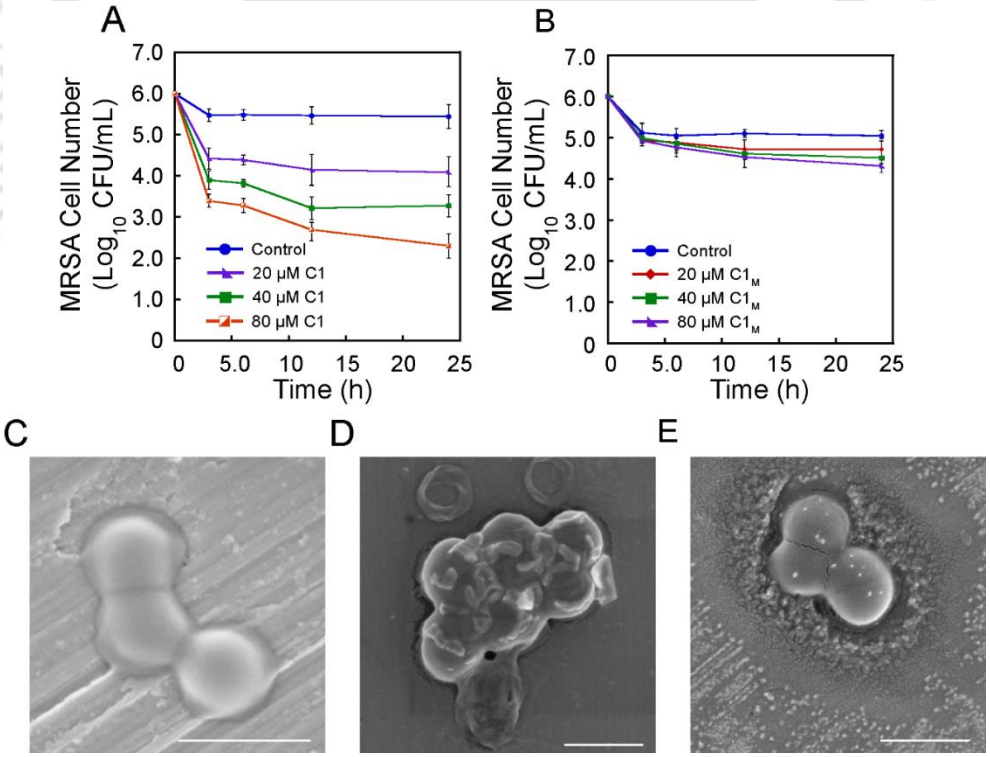

Figure 3.5 Time-kill curves of (A) C1 and (B) $C1_M$ against *S. aureus* MRSA 100 in PBS. FESEM image of (C) Control MRSA cells, (D) C1-treated and (E) $C1_M$-treated *S. aureus* MRSA 100 cells. Scale bar for the images is 1.0 µm.

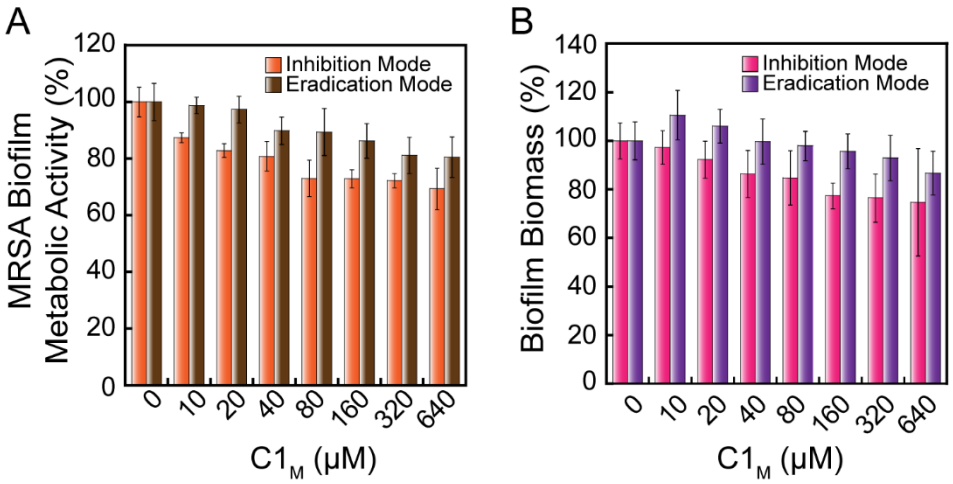

Figure 3.6. Determination of MRSA biofilm metabolic activity by (A) MTT assay and (B) crystal violet assay to ascertain inhibition and eradication of *S. aureus* MRSA 100 biofilm by $C1_M$.

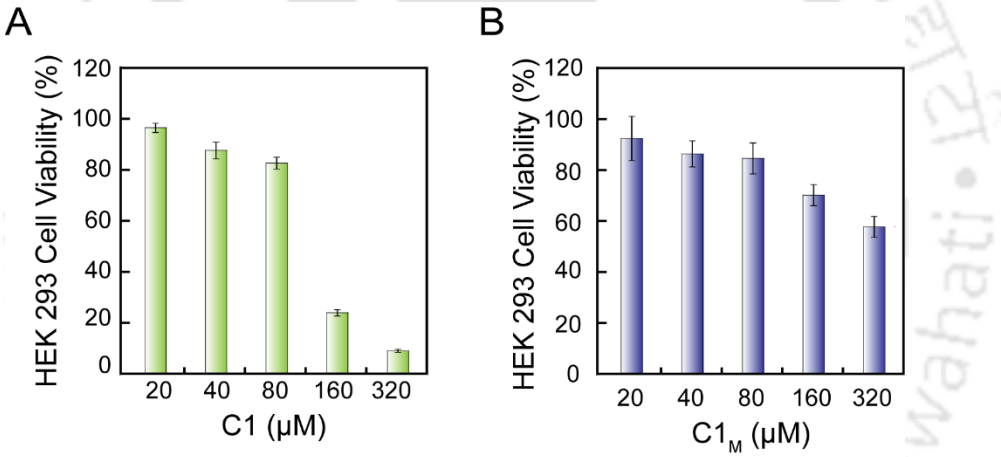

Figure 3.7. MTT assay to ascertain cytotoxicity of (A) C1 and (B) $C1_M$ on HEK 293 cells. Each data point represents mean ± standard deviation from six samples.

50% biofilm ($MBEC_{50}$) were found to be beyond 640 μM, (Figure 3.6A-3.6B) and were manifold higher than the inhibitory and eradication concentrations of C1 (Chapter 2, Table 2.6 and Figure 2.9). The nominal antibiofilm activity of $C1_M$ was also corroborated by fluorescence microscopy-based studies, wherein the annihilation of MRSA biofilm was quite low even at high concentrations of $C1_M$ (Appendix, Figure A3.2). Interestingly, $C1_M$ was non-toxic to HEK 293 cells (~84% viability), akin to C1 at concentrations upto 80 μM, (Figure 3.7A-3.7B). At higher concentration (160 μM), $C1_M$ was less detrimental to HEK 293 cells (~70% cell viability) than C1 at equivalent concentration (~24% viability) (Figure 3.7A-3.7B), highlighting the merit of $C1_M$. At

high concentrations, the micelle formation by C1is a dynamic process largely driven by the equilibrium between the free form of C1 and C1 entrapped into the micelle. On the other hand, $C1_M$ is a relatively stable species. Based on this essential difference between C1 and $C1_M$, the disassembly of a micelle formed by C1 in solution is likely to be facile in comparison to the disassembly observed for the stable $C1_M$. As a consequence, the local concentration of the free form of the amphiphile would be higher in case of C1 as compared to $C1_M$. This phenomenon may account for the manifestation of a higher cytotoxic effect on HEK 293 cells by C1 than $C1_M$ at equivalent concentration.

3.3.6. Drug Loading and Release Studies

On the basis of a calibration plot (Appendix, Figure A3.3), it was noted that the LE and LC of rifampicin was 51.05% and 95.39%, respectively, whereas for vancomycin, the corresponding LE and LC were 23.56% and 68.91%, respectively. It is important to mention that loading of rifampicin and vancomycin into C1 micelle was achieved by physical entrapment and a dialysis step was also included to remove free C1 or untrapped antibiotic. The smaller molecular size and higher hydrophobicity of rifampicin as compared to vancomycin perhaps accounts for its higher loading. Both $C1_M$-R and $C1_M$-V exhibited a sustained release profile of the payload in SIF and SBF, although the kinetics of drug release was slightly faster for vancomycin (Figure 3.8). The favorable release profile of the antibiotics in the tested fluids was encouraging and it suggested that the antibiotic-loaded $C1_M$ may hold therapeutic potential in physiologically relevant niche.

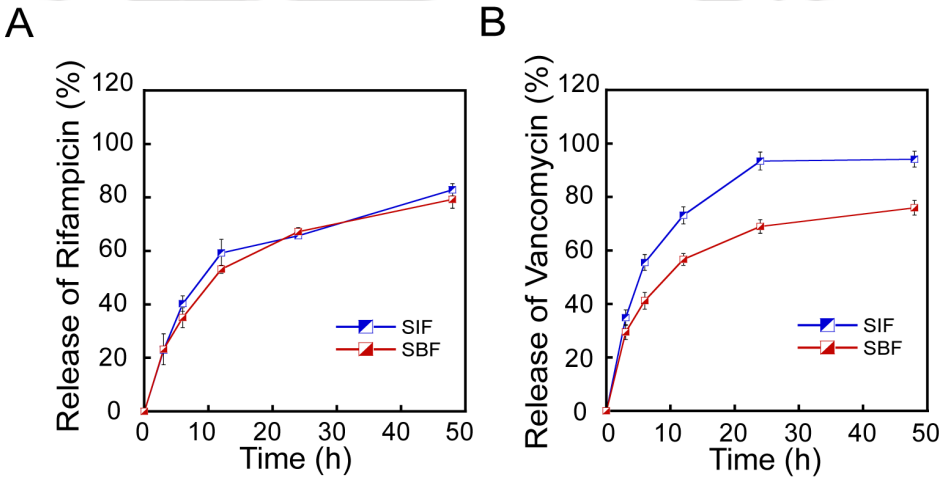

Figure 3.8. *In vitro* release kinetics of (A) rifampicin and (B) vancomycin from loaded $C1_M$ incubated in simulated body fluid (SBF) (pH 7.4) and simulated intestinal fluid (SIF) (pH 8.0).

3.3.7. Enhanced Anti-MRSA Activity of $C1_M$-R and $C1_M$-V and Cytotoxicity of $C1_M$-R and $C1_M$-V

At equivalent concentrations, $C1_M$-R and $C1_M$-V exhibited superior anti-MRSA activity relative to the free antibiotics as determined by a cFDA-SE leakage assay (Figure 3.9A). For instance, the relative anti-MRSA activity of $C1_M$-R was nearly 12-fold higher after 3 h and 18-fold higher after 6 h, respectively, as against rifampicin at equal concentration (Figure 3.9A). This reiterated that the developed micellar system could perhaps harness the activity of C1 and the antibiotic in tandem. Likewise, $C1_M$-V exhibited nearly 8-fold higher potency after 3 h and 5-fold higher potency after 6 h, respectively, as against the antibiotic alone used at equal concentration (Figure 3.9A).

It can be surmised that both $C1_M$-R and $C1_M$-V can disassemble to release C1 and also support sustained release of the payload antibiotic. The released C1 can induce membrane damage in MRSA, which may pave the way for a higher antibiotic uptake and superior accessibility of the target by the antibiotic, eventually culminating into enhanced killing of MRSA. Additional experiments revealed that the cell-free antibiotic was considerably lower in case of MRSA treated with $C1_M$-R or $C1_M$-V in comparison to treatment with either antibiotics alone or $C1_M$ in combination with the antibiotics at equivalent concentration (Figure 3.9B). This again strongly suggested superior uptake of antibiotic in case of treatment with $C1_M$-R or $C1_M$-V. Interestingly, $C1_M$-R and $C1_M$-V were non-toxic to HEK 293 cells at a C1 concentration of 130 µM and the corresponding

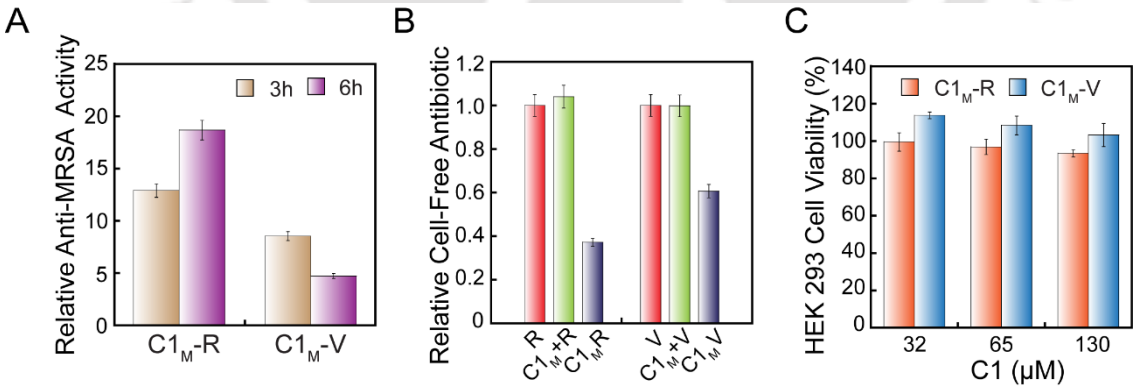

Figure 3.9. (A) Relative anti-MRSA activity of $C1_M$-R and $C1_M$-V (Loaded antibiotic/free antibiotic). (B) Relative levels of cell-free antibiotic following interaction of MRSA cells with rifampicin (R), $C1_M$ + R, $C1_M$-R, vancomycin (V), $C1_M$ + V, $C1_M$-V for 3 h. The concentrations of R, V and $C1_M$ are at equivalent levels in the corresponding samples. (C) Cytotoxicity of $C1_M$-V (0.69 µM, 1.38 µM and 2.76 µM vancomycin for the respective C1 concentrations) and $C1_M$-R (1.21 µM, 2.43 µM and 4.86 µM rifampicin for the respective C1 concentrations) on HEK 293 cells as determined by MTT assay.

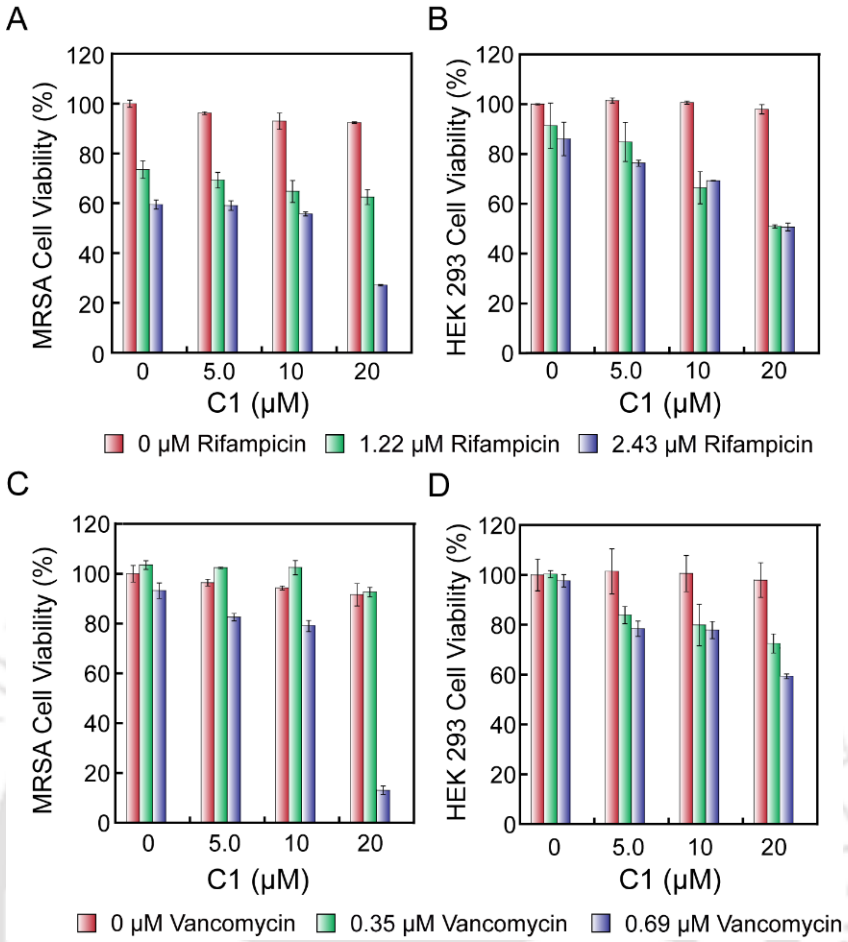

Figure 3.10. (A) Antibacterial activity of C1 in combination with rifampicin against *S. aureus* MRSA 100. (B) MTT assay to ascertain the effect of C1 in combination with rifampicin on HEK 293 cells. (C) Antibacterial activity of C1 in combination with vancomycin against *S. aureus* MRSA 100. (D) MTT assay to ascertain the effect of C1 in combination with vancomycin on HEK 293 cells.

concentration of rifampicin and vancomycin being 4.86 μM and 2.76 μM, respectively (Figure 3.9C). With regard to the combinatorial treatment, 20 μM C1 in combination with either 2.43 μM rifampicin or 0.69 μM vancomycin could annihilate MRSA (Figure 3.10A and 3.10B). Notably, in this case, the toxicity exerted on HEK 293 cell was also considerable (viability less than 60%) (Figure 3.10B and 3.10 D). However, in case of the developed $C1_M$-R and $C1_M$-V systems, which exhibited high anti-MRSA activity and lower toxicity (Figure 3.10) it is to be noted that the concentration of both C1 and the antibiotics were well above their MICs against the MRSA strain, which highlighted the favorable therapeutic index of the developed $C1_M$-R and $C1_M$-V systems.

3.3.8. $C1_M$, $C1_M$-R and $C1_M$-V Coated Surgical Suture

Conceivably, the antibiotic-loaded micellar systems $C1_M$-R and $C1_M$-V hold promise as an antibacterial coating, based on the published literature on antimicrobial coated sutures (Li *et al.*, 2012; Obermeier *et al.*, 2015; Chen *et al.*, 2015) and the ominous concern with regard to infections associated with surgical sutures caused by adhering bacteria (Katz *et al.*, 1981; Owens and Stoessel, 2008). $C1_M$, $C1_M$-R and $C1_M$-V coated silk surgical sutures were generated by a dip-coating process and the magnitude of coating was determined (Table 3.2). FESEM analysis revealed that in case of the suture coated with the micellar species, the strands were enveloped perhaps due to coating of the suture in contrast to the well separated and more conspicuous strands observed in non-coated suture (Figure 3.11A). Further, ATR-FTIR revealed the presence of the characteristic stretching frequency of C1 in the $C1_M$ coated suture (Figure 3.11B), indicating C1 micelle coating in this sample.

Table 3.2. Amount of $C1_M$, $C1_M$-R and $C1_M$-V coated on surgical silk suture.

Sl. No.	Sample	Amount of species coated per unit length of suture (mg/cm)
1.	$C1_M$ coated suture	0.177
2.	$C1_M$-R coated suture	0.210
3.	$C1_M$-V coated suture	0.187

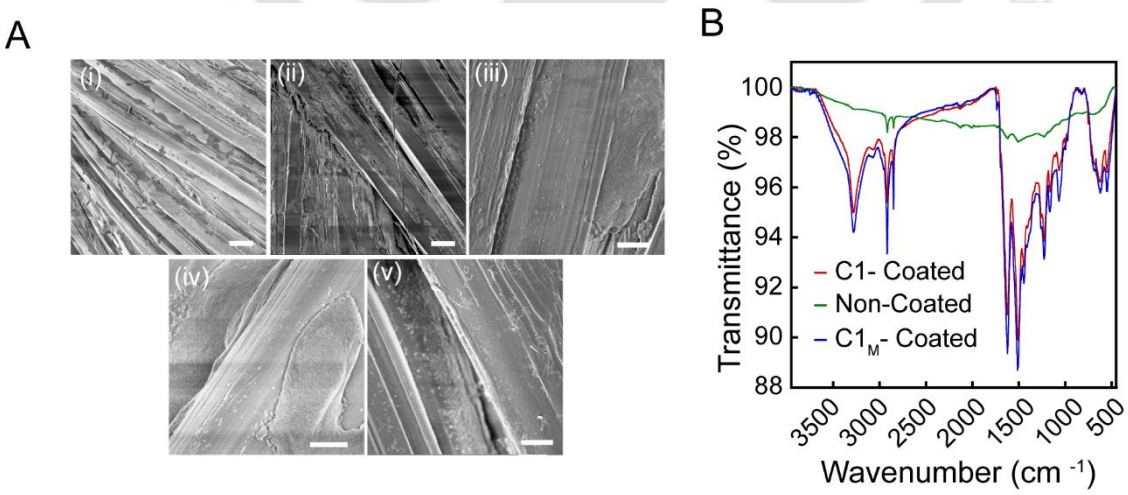

Figure 3.11. (A) FESEM images of (i)Non-coated silk suture and silk sutures coated with (ii) C1, (iii) $C1_M$, (iv) $C1_M$-R and (v) $C1_M$-V. Scale bar for the images is 2.0 µm. and (B) FTIR analysis of $C1_M$-coated silk surgical suture.

3.3.9. Mitigation of MRSA Biofilm on $C1_M$, $C1_M$-R and $C1_M$-V Coated Surgical Suture

A distinct zone of inhibition was noted for $C1_M$-R against *S. aureus* MRSA 100 in an agar diffusion assay, which was absent in case of the non-coated and $C1_M$ coated suture (Figure 3.12A). The inhibition zone was much less in case of $C1_M$-V, likely owing to reduced coating and slower diffusion of the large-sized vancomycin in agar as compared to rifampicin. The eluates from $C1_M$-R coated suture incubated in PBS (pH 7.4) could render higher levels of membrane damage in MRSA in comparison to the eluates obtained from $C1_M$-V coated suture (Figure 3.12B), which again is perhaps due to lesser magnitude of coating of the suture with $C1_M$-V. Further, the membrane damage manifested by the eluates obtained from $C1_M$-R and $C1_M$-V were higher than that observed in case of $C1_M$ (Figure 3.12B). It may be mentioned here that the eluate from C1-coated suture could induce copious membrane perturbation in MRSA cells, but was toxic to HEK 293 cells (Figure 3.12C). Interestingly, the eluates from $C1_M$-R and $C1_M$-V coated sutures were not detrimental to the viability of HEK 293 cells (~85%)

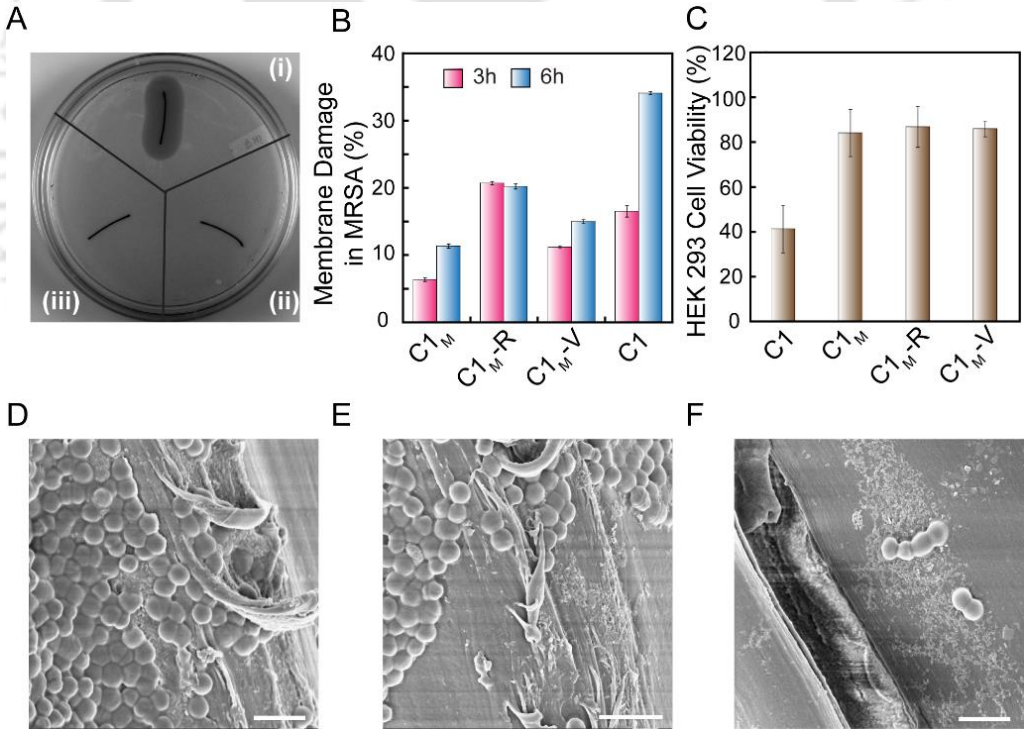

Figure 3.12. (A) Agar diffusion assay against *S. aureus* MRSA 100 with (i) $C1_M$-R coated, (ii) $C1_M$ coated, (iii) Non-coated suture surgical silk sutures. (B) Membrane-directed activity of the eluates from $C1_M$, $C1_M$-R, $C1_M$-V and C1 coated sutures against *S. aureus* MRSA 100. (C) Effect of C1, $C1_M$, $C1_M$-R and $C1_M$-V coated sutures on the viability of HEK 293 cells determined by MTT assay. FESEM images of *S. aureus* MRSA 100 biofilm grown on (D) non-coated, (E) $C1_M$ coated and (F) $C1_M$-R coated suture. Scale bar for the images is 2.0 µm.

(Figure 3.12C). This indicated that the sutures coated with $C1_M$-R and $C1_M$-V were biocompatible and may hold promise in preventing establishment of MRSA infection in sutures. FESEM analysis also clearly revealed that $C1_M$-R coating could thwart MRSA biofilm formation on the surgical suture as against non-coated and $C1_M$-coated sutures (Figure 3.12D-3.12E).

3.4. Significant Findings

The salient findings of the present study are as follows:

1. The salicaldehyde-based amphiphile C1 could readily self-assemble in solution, resulting in the formation a micelle ($C1_M$).

2. A sustained release of rifampicin and vancomycin in physiologically relevant fluids was observed in case of the micellar constructs $C1_M$-R and $C1_M$-V. Both $C1_M$-R and $C1_M$-V were non-toxic to HEK 293 cells even at concentrations much higher than their MICs against an MRSA strain.

3. A significantly higher level of killing of clinical MRSA could be achieved by $C1_M$-R and $C1_M$-V in comparison to free antibiotics alone, suggesting that following disassembly, C1 could induce membrane damage and thereby facilitate higher uptake of the released payloads rifampicin and vancomycin. This synergy between the two warheads perhaps leads to superior elimination of MRSA.

4. The micellar constructs hindered MRSA biofilm formation on surgical sutures, which represents a grave problem in the clinics.

The present study illustrates how the self-assembly of the membrane-targeting amphiphile C1 can be explored to develop a micellar system for delivery of therapeutic antibiotics. Further the biocompatible nature of the micellar construct and its ability to hinder MRSA biofilm formation on surgical sutures augers well. Recognizing the fact that the self-assembly attribute of the salicaldehyde-based amphiphile C1 can be exploited to develop an efficient bactericidal platform, it was pertinent to explore the possibility of generating a structural variant of the salicaldehyde amphiphile and evaluate its efficacy. Based on this premise, the next chapter provides a detailed investigation on the aggregation behavior and the bactericidal activity of a napthaldehyde-based amphiphile.

Chapter 4

Evaluation of the Antibacterial Activity of Napthaldehyde-based Synthetic Amphiphile (C2)

This chapter illustrates the antibacterial potential of a napthaldehyde-based amphiphile (C2). The self-assembling attribute, membrane-targeting activity, adjuvant potential and the antibiofilm activity of the amphiphile is reported in this chapter.

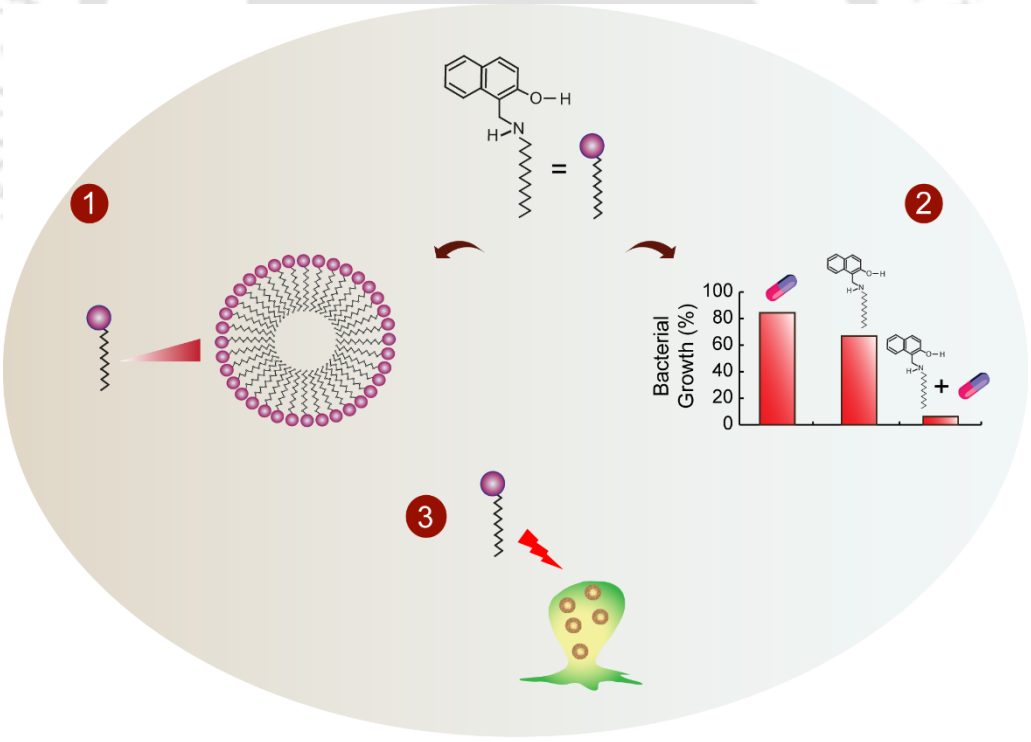

1 Facile Self Assembly of C2 2 Adjuvant Activity of C2

3 Antibiofilm Potential of C2

ABSTRACT

In this chapter the antibacterial potential of a napthaldehyde-based synthetic amphiphile referred to as compound 2 (C2) has been reported. The amphiphile C2 was synthesized by forming Schiff-base followed by reduction using sodium borohydride and its characterization was accomplished by ESI-MS, NMR and FTIR. UV-visible absorption spectra of C2 indicated absorption bands at 290 nm, 340 nm and 430 nm, while two fluorescence emission peaks were observed at 360 nm and 435 nm upon excitation of the amphiphile at 290 nm. LB trough analysis indicated the propensity of C2 to form a monolayer. The self-aggregation behavior of C2 was studied by ANS-based fluorescence spectroscopy, which indicated that the critical micelle concentration (CMC) for C2 was 7.0 µM in water. AFM analysis revealed that at concentrations above CMC, C2 formed spherical aggregates of around 400 nm. In an initial screening experiment against various target pathogens, it was observed that C2 exhibited broad- spectrum bactericidal activity. The MIC of C2 against the clinical MRSA strain *S. aureus* MRSA 100 was 320 µM. The bactericidal activity of C2 was corroborated by FESEM analysis, which provided evidence for cellular damage and distortion of typical morphology in C2-treated cells of *E. coli* MTCC 433. A cFDA-SE leakage assay as well as a PI uptake assay indicated a dose-dependent membrane-directed activity of C2. Further, fluorescence microscopy-based live/dead assay with cFDA-SE and PI also indicated loss of cell viability and membrane damage in C2-treated target cells. A significant inhibition of the growth of target pathogen was observed when the cells were subjected to a combined treatment of C2 and the model antibiotics polymyxin B and erythromycin indicating the adjuvant potential of C2. A synergistic effect was evident at 160 µM C2 in combination with 20 µM erythromycin. Estimation of the metabolic activity of biofilm cells by an MTT based assay suggested a dose-dependent inhibition of *S. aureus* MTCC 96 biofilm by C2. Fluorescence microscopy using cFDA-SE and congo red staining also indicated inhibition of biofilm formation by *S. aureus* MTCC 96 in presence of high concentrations of C2. An MTT based cytotoxicity assay indicated that at concentrations equivalent to its MIC against *S. aureus* MTCC 96 (160 µM), C2 was non-toxic to cultured HEK 293 cells.

4.1. Introduction

Antibiotic-resistant pathogenic bacteria continue to be an ominous healthcare burden owing to their inherent resistance against prevalent antibiotics. Thus, there is an urgent need to counter the resistance mechanism in these pathogens and potentiate the efficacy of antibiotics. Antimicrobial agents that display a membrane-targeting activity hold significant therapeutic promise as the possibility of the development of resistance against such molecules warrants extensive refurbishment of membrane components, which is physiologically challenging for the target bacteria (Steinbuch and Fridman, 2016). Amongst the synthetic molecules, membrane-targeting amphiphiles have been shown to hold considerable potential against antibiotic-resistant pathogenic bacteria (Findlay *et al*., 2010; Gokel and Negin, 2012; Thiyagarajan *et al*., 2014; Mingeot-Leclercq *et al.*, 2016; Salta, *et al*., 2017; Mitra *et al.*, 2019). A large number of reports highlight the structure-activity correlation of synthetic amphiphiles. In particular, the structure of the head group and their relative position seem to bear an impact on the antibacterial activity of synthetic amphiphiles (Mitra *et al*., 2009; LaDow *et al*., 2011; Goswami *et al*., 2013). The head group of a bactericidal synthetic amphiphile is critical in initiating strong interactions with the target bacterial cells. In the context of therapeutic applications, it is necessary to select a biocompatible head group in order to prevent any host cell toxicity. In the previous studies reported in Chapter 2 and Chapter 3, it was illustrated that the synthetic amphiphile C1 having a salicaldehyde head group exhibited promising antibacterial activity against pathogenic bacteria including MRSA. Given the pivotal role of the head group in the activity of a bactericidal synthetic amphiphile, the essential motivation in this investigation was to replace the salicaldehyde head group of the amphiphile C1 with a napthaldehyde group and thereby generate a new amphiphile C2. Conceivably, such an alteration of the head group is likely to change the hydrophilic-lipophilic balance (HLB) of the molecule. It thus becomes imperative then to ascertain the emerging structure-function relationship in C2 in terms of its self-assembly attribute, bactericidal activity, membrane-directed activity and cytotoxic potential. Based on this tenet, the present investigation reports the self-assembly attribute of the amphiphile C2 in solution. The bactericidal activity against target pathogens including MRSA, membrane-directed activity, adjuvant potential and the *in vitro* cytotoxic effect of C2 is also described in this study.

4.2. Materials and Methods

4.2.1. Growth Media and Chemicals

Nutrient broth (NB), Brain-Heart Infusion (BHI) broth and crystal violet (CV) dye were obtained from HiMedia, Mumbai, India. Dimethyl sulfoxide (DMSO), chloroform, methanol and ethanol were procured from Merck, India. 5(6)-carboxyfluorescein diacetate succinimidyl ester (cFDA-SE), propidium iodide (PI), congo red (CR), erythromycin, polymyxin B, 1-N-phenyl naphthylamine (NPN), 3,3'-dipropylthiadicarbocyanine iodide ($DiSC_3(5)$), 3-(4,5-dimethyl-2-thiazolyl)-2,5-diphenyl-2H-tetrazolium bromide (MTT), Dulbecco's Modified Eagle Medium (DMEM) and trypsin–EDTA were procured from Sigma-Aldrich (USA). Foetal bovine serum (FBS) was procured from Gibco™, Thermo Scientific.

4.2.2. Synthesis of Napthaldehyde Amphiphile (C2)

2-hydroxy-napthaldehyde (2.69 mM) was taken in a round bottom flask to which a slight excess amount of dodecyl amine (2.90 mM) was added with ethanol as solvent. The mixture was stirred for 6 h followed by the solvent evaporation in a rotavapor and the obtained precipitate (Schiff base) was reconstituted in ethanol followed by reduction using sodium borohydride, which was added pinch by pinch until the effervescence stopped and the solution became colourless. The solution was then kept for stirring for 12 h and the solvent was again evaporated. The mixture was separated using a separating funnel and the crude product was purified by column chromatography to obtain 60% yield. A schematic representation of the synthesis of C2 is indicated in Scheme 4.1.

4.2.3. Characterization of C2

The molecule C2, as synthesized was subjected to ESI-MS and NMR analysis. FTIR spectra of C2 was recorded in KBr pellets at 4.0 cm^{-1} resolution in an infrared

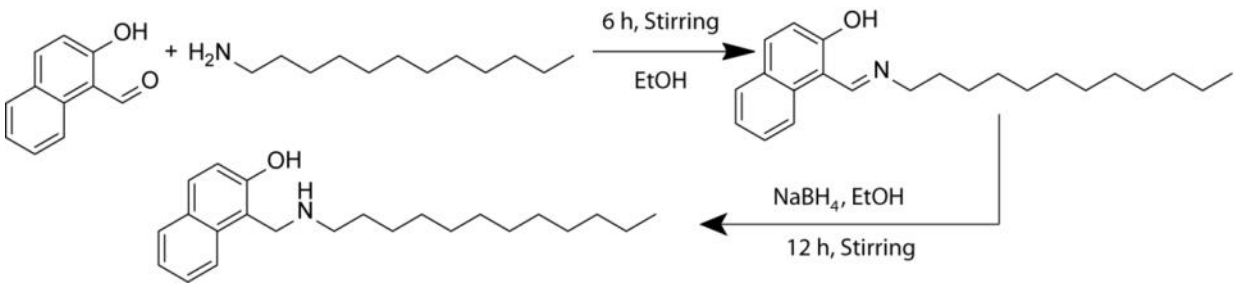

Scheme 4.1. Schematic representation of the synthesis route of C2.

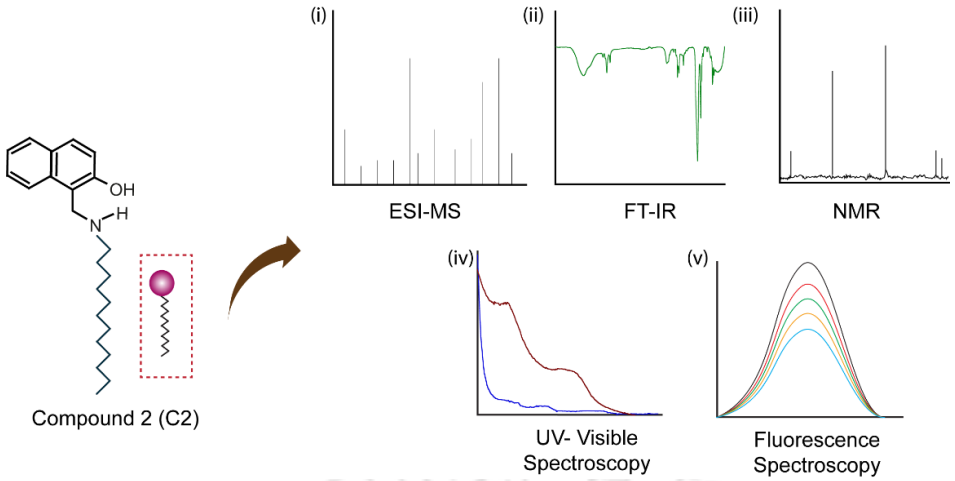

Scheme 4.2. Cartoon illustrating the techniques used to characterize C2.

spectrometer (Spectrum One, Perkin-Elmer). Scans were performed for every sample in the range of 4000 cm^{-1} to 400 cm^{-1}. A background spectrum for pure KBr was also measured. Further, a stock solution of C2 (20 mM) was prepared in DMSO and diluted in water in separate sets to prepare the amphiphile solution in the range of 20 µM - 320 µM. The absorbance of the solutions was recorded in a spectrophotometer (Lambda 25, Perkin-Elmer) in scanning mode from 200 nm to 500 nm. In a separate experiment, the fluorescence emission spectra of varying concentrations of C2 (20 µM-320 µM) in a range from 300 nm to 550 nm was measured in a spectrofluorometer (FluoroMax-4, HORIBA) upon excitation of C2 at 290 nm. Fluorescence measurements were recorded from three independent experimental samples for every amphiphile concentration. A schematic indicating the techniques used to characterize C2 is indicated in Scheme 4.2.

4.2.4. Aggregation Studies with C2

The propensity of C2 (50 µM) to form aggregates was visualized by atomic force microscopy (AFM). The monolayer formation of C2 was ascertained by measuring surface pressure–mean molecular area (Π–A) isotherm using a KSV 2000 Langmuir-Blodgett System (KSV Instruments, Finland) as mentioned previously for C1 in section 3.2.3 of Chapter 3. Critical micellar concentration (CMC) of C2 was ascertained by ANS-based fluorescence measurements as described previously for C1 in section 3.2.4 of Chapter 3. The concentration-dependent aggregation of C2 was also studied by dynamic light scattering (DLS) (Zeta Sizer, Malvern, UK) in three independent sets wherein every set consisted of five replicates. A cartoon representing the techniques used to study the aggregation of C2 is indicated in Scheme 4.3.

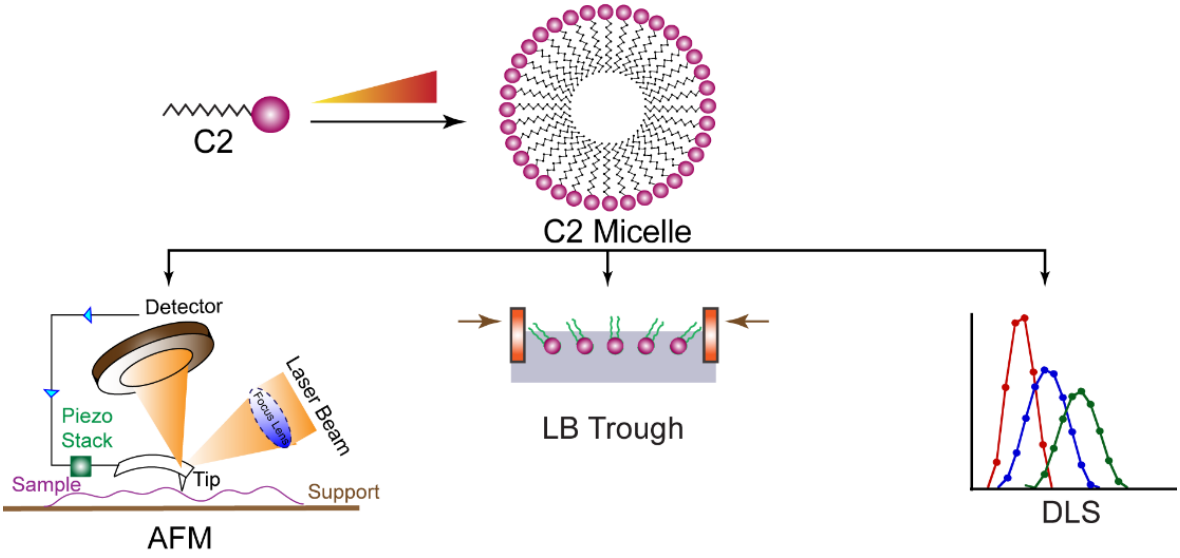

Scheme 4.3. Cartoon illustrating the techniques used to study aggregation behavior of C2.

4.2.5. Bacterial Strains and Growth Conditions

The target bacterial strains consisted of Gram-positive *Staphylococcus aureus* MTCC 96 (*S. aureus*), methicillin-resistant *Staphylococcus aureus* (MRSA) MRSA 100, methicillin-susceptible *Staphylococcus aureus* (MSSA) MSSA 104 and *Listeria monocytogenes* Scott A (*L. monocytogenes*). The Gram-negative strains consisted of *Escherichia coli* MTCC 433 (*E. coli*) and *Pseudomonas aeruginosa* MTCC 2488 (*P. aeruginosa*). The target bacterial strains were grown under conditions described previously in section 2.2.4 of Chapter 2.

4.2.6. Antibacterial Activity Spectra of C2

To evaluate the antibacterial spectra of C2, target bacterial cultures were inoculated at 1% (v/v) in requisite growth medium in a microtiter well plate and propagated overnight at 37°C and 180 rpm in presence of 50 µg/ml and 100 µg/ml of C2 as described previously for C1 in section 2.2.5 of Chapter 2. The growth of the strains was then verified by measuring absorbance at 600 nm in a microtiter plate reader (Infinite M200, TECAN, Switzerland). The minimum inhibitory concentration (MIC) of C2 was further ascertained against *S. aureus* MTCC 96, *L. monocytogenes* Scott A, *P. aeruginosa* MTCC 2488, *E. coli* MTCC 433, *S. aureus* MRSA 100, and *S. aureus* MSSA 104 by a standard microtitre dilution method as described previously for C1 in section 2.2.6 of Chapter 2.

4.2.7. Field Emission Scanning Electron Microscope (FESEM) Analysis to Study the Antibacterial Activity of C2

Overnight grown cells of *E. coli* MTCC 433 was collected by centrifugation, washed twice with sterile PBS and resuspended in the same. The cells were then treated with 640 µM of C2 for 12 h at 37°C. Untreated cells were also incubated in sterile PBS under the same conditions as control samples. Following incubation, untreated as well as treated cells were collected by centrifugation, washed with sterile PBS and sterile MilliQ water and finally suspended in sterile MilliQ water. A 10 µL aliquot of each sample was spotted on separate aluminium foil covered glass stub and air dried in the laminar hood. The samples were then mounted on a carbon tape covered metal stub and gold (Au) coating was done twice. Finally, the samples were analyzed in a field emission scanning electron microscope (Zeiss Sigma, USA) at 2.0-3.0 Kv and the images were recorded. A cartoon depicting the FESEM-based protocol used to ascertain the antibacterial potential of C2 is shown in Scheme 4.4.

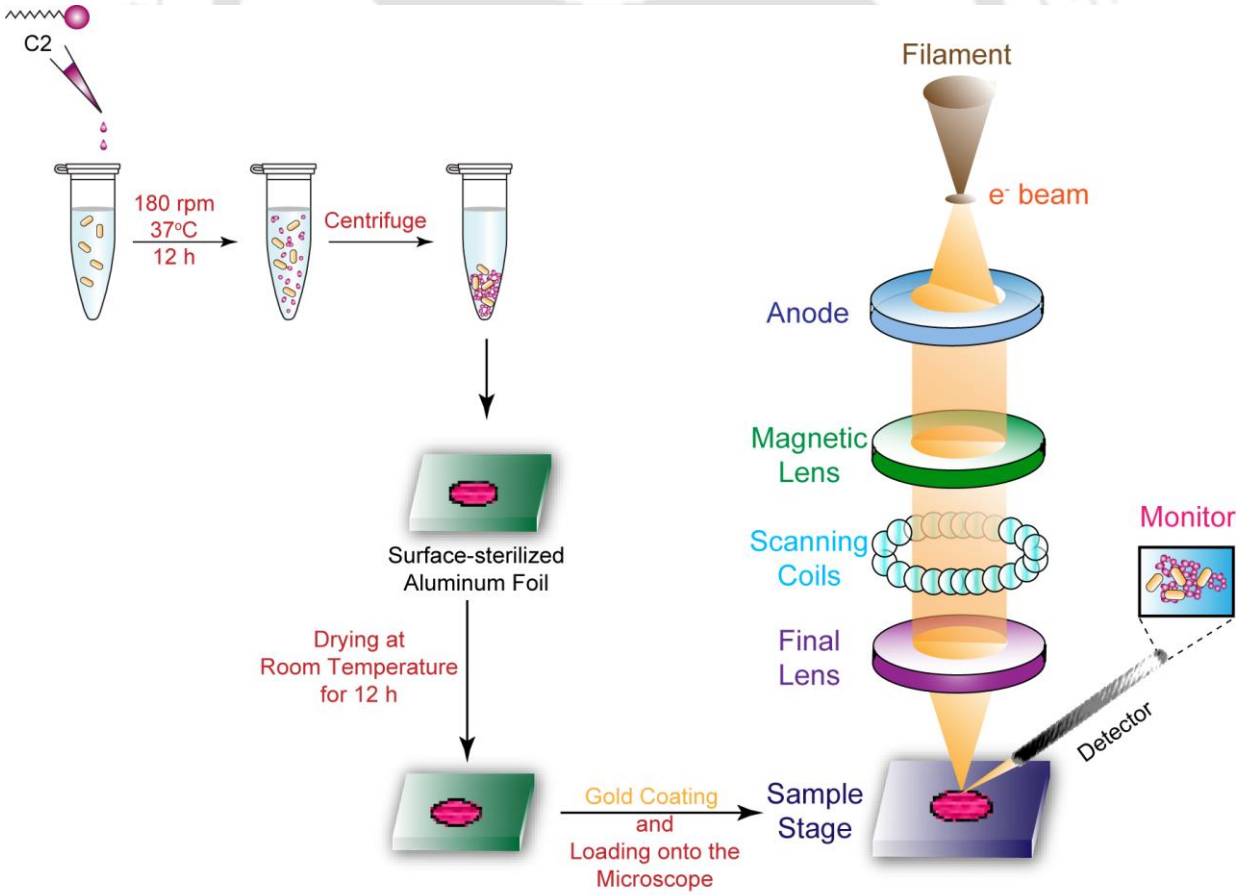

Scheme 4.4. Cartoon illustrating the FESEM-based protocol used to visualize the antibacterial potential of C2.

4.2.8. Membrane-Directed Bactericidal Activity of C2

The membrane-directed bactericidal activity of various concentrations of C2 (50 µM, 100 µM, 150 µM and 200 µM) was ascertained against *S. aureus* MTCC 96, *E. coli* MTCC 433 and *S. aureus* MRSA 100 by a cFDA-SE leakage assay and propidium iodide (PI) uptake assay at intermittent periods of incubation (3 h and 6 h) following a standard protocol as described previously for C1 in section 2.2.8 of Chapter 2. Fluorescence measurements were recorded from three independent experimental samples using a spectrophotometer (FluoroMax-4, HORIBA). For fluorescence microscope based live dead assay, cells of *S. aureus* MTCC 96 and *E. coli* MTCC 433 were labelled with cFDA-SE followed by treatment with C2 (50 µM, 100 µM, 150 µM and 200 µM) at 37ºC and 180 rpm for 6 h. In a separate set, cells treated with C2 (50 µM, 100 µM, 150 µM and 200 µM) at 37ºC and 180 rpm for 6 h were labelled with PI, spotted on a clean glass slide, air dried and observed under fluorescence microscope (Eclipse Ti-U, Nikon, USA) with a filter that allowed blue light excitation at 445-495 nm for cFDA-SE and green light excitation at 495-570 nm in case of PI stained cells and the images of the cells were recorded as shown in a cartoon representation in Scheme 4.5.

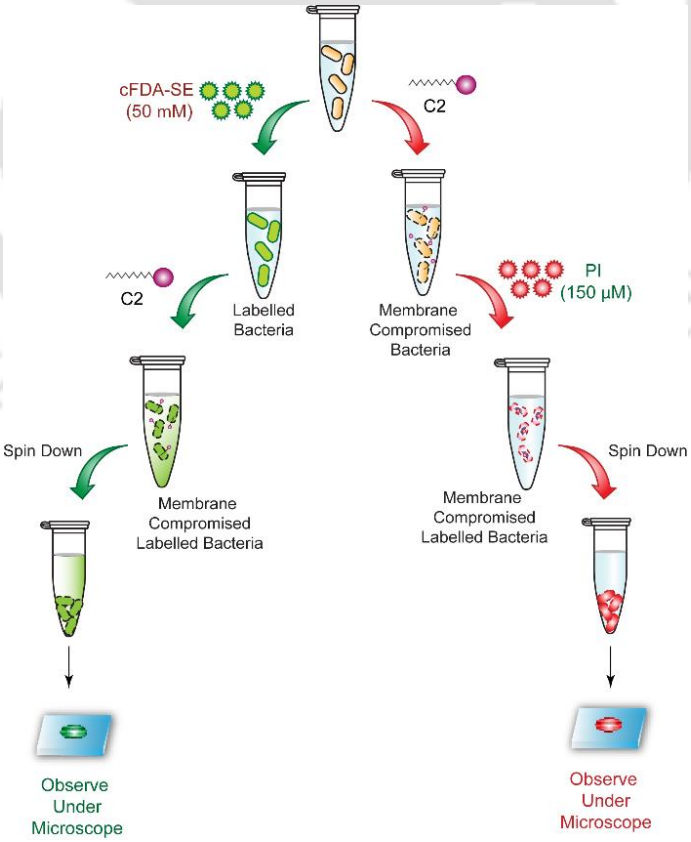

Scheme 4.5. Schematic illustrating the protocol used for fluorescence microscopy-based screening of the antibacterial activity of C2.

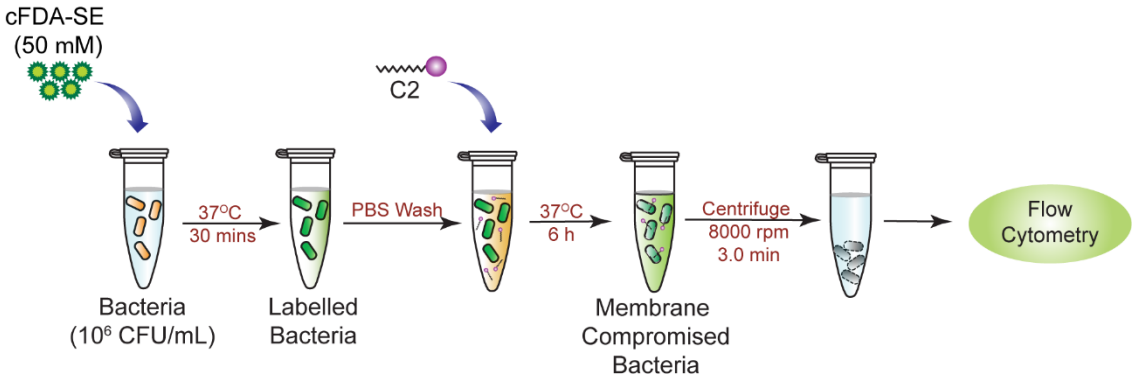

Scheme 4.6. Schematic illustrating the protocol used for flow cytometry based screening of the antibacterial activity of C2.

4.2.9. Flow Cytometry-based Studies

The membrane-directed bactericidal activity of varying concentrations of C2 (100 µM and 200 µM) was ascertained against *S. aureus* MTCC 96 and *E. coli* MTCC 433 by a cFDA-SE dye retention-based flow cytometry assay after 6 h incubation. Cells were harvested from overnight grown cultures by centrifugation at 8000 rpm for 5 min, washed with sterile phosphate buffer and labelled with cFDA-SE (final concentration of 50 µM) at 37°C for 30 min. The labelling reaction was terminated by pelleting the cells followed by washing with phosphate buffer to remove excess dye and resuspended in 1.0 mL of sterile PBS. 100 µM and 200 µM of C2 was then added in separate sets to the cFDA-SE labelled cells and incubated at 37°C and 180 rpm for 6 h in dark. As a control, only labelled bacteria devoid of C2 treatment was also incubated under the same conditions. After incubation, the cells were harvested by centrifugation and reminiscent carboxyfluorescein retained in the cells was measured using an FITC channel in a BD FACS Caliber flow cytometer. A schematic representation of the flow cytometry study to ascertain the antibacterial activity of C2 is shown in Scheme 4.6.

4.2.10. Bactericidal Activity of Erythromycin and Polymyxin B in Combination with C2

The adjuvant potential of C2 in combination with erythromycin and polymyxin B was ascertained against *E. coli* MTCC 433 and *S. aureus* MTCC 96, respectively. Initially a bacterial cell suspension (10^6 CFU/mL) of the respective target bacteria were inoculated in separate sets into sterile growth media and incubated overnight. On the following day, 10^6 CFU of *E. coli* MTCC 433 cells were inoculated into a sterile 96 well plate containing 100 µL of NB media incorporated with varying concentrations of erythromycin (40 µM - 320 µM) in combination with varying concentrations of C2 (80 µM

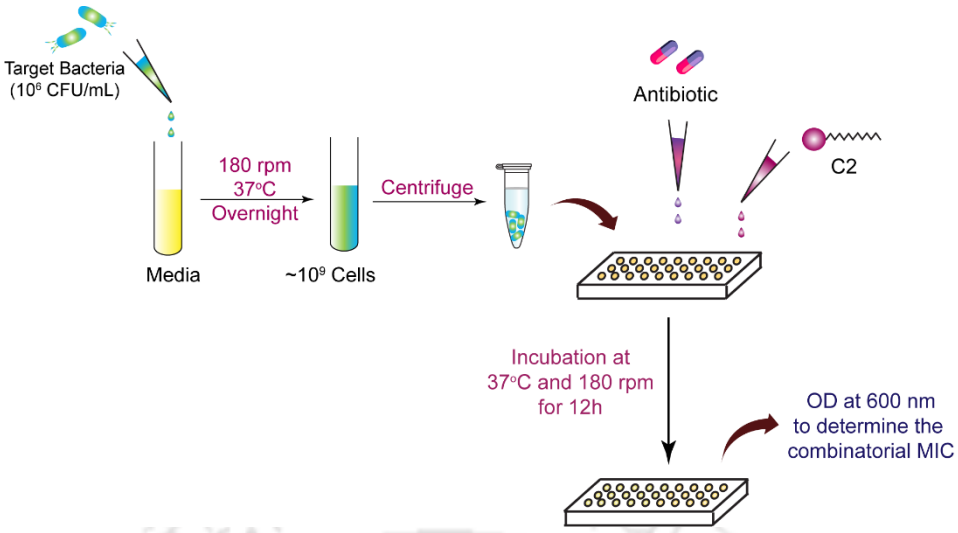

Scheme 4.7. Schematic illustrating the protocol used to determine the antibacterial activity of antibiotics in combination with C2.

- 320 µM). Similarly, in a separate set, BHI media containing varying concentrations of polymyxin B (10 µM - 320 µM) was combined with varying concentrations of C2 (40 µM - 640 µM) and inoculated with 10^6 CFU of *S. aureus* MTCC 96 cells. The cells along with the combinatorial treatments were incubated overnight at 37°C and 180 rpm. The cell growth was estimated by measuring absorbance at 600 nm in a multimode plate reader (Infinite M200, TECAN, Switzerland) and expressed as percentage growth inhibition compared to untreated cells (cells grown in the absence of antibiotics and C2). The effect of varying concentrations of the antibiotics or C2 alone on the growth of target bacteria was also ascertained. For every sample, three independent experiments were performed, each having three replicas. Data analysis and calculation of standard deviation was performed with Microsoft Excel 2016 (Microsoft Corporation, USA). The interaction of C2 and the antibiotics was quantified and expressed as the fractional inhibitory concentration (FIC) index as mentioned previously in Chapter 2 section 2.2.10. A schematic representation of the protocol used to study the combination effect of C2 with the antibiotics is depicted in Scheme 4.7.

4.2.11. Effect of C2 on Biofilm Formation

For inhibition studies, *S. aureus* MTCC 96 and *S. aureus* MRSA 100 biofilm was grown in BHI media supplemented with 0.25% glucose in sterile 96 well microtiter plate in presence of varying concentrations of C2 (5.0 µM - 640 µM for *S. aureus* MTCC 96 biofilm and 40 µM - 640 µM for *S. aureus* MRSA 100 biofilm) and incubated for 24 h

in a static and humid chamber at 37°C. Following incubation for 24 h, media from the wells was aspirated to remove non-adherent bacterial cells and subsequently, the metabolic activity of biofilm cells was estimated by performing an MTT assay and the biofilm biomass was estimated by crystal violet assay as described previously in section 2.2.11.1 of Chapter 2. The minimum biofilm inhibition concentration ($MBIC_{50}$) for C2 was also determined.

In another experiment, for studying eradication of *S. aureus* MTCC 96 and *S. aureus* MRSA 100 biofilms, a 24 h pre-grown biofilm of both the strains was treated with varying concentrations of C2 (5.0 µM - 640 µM for *S. aureus* MTCC 96 biofilm and 40 µM - 640 µM for *S. aureus* MRSA 100 biofilm) and incubated for 24 h in a static and humid chamber at 37°C. Untreated biofilm was also incubated under the same conditions as control. Subsequently, the metabolic activity of biofilm cells and the biofilm biomass was estimated by performing an MTT assay and crystal violet assay, respectively, as described previously in section 2.2.11.1 of Chapter 2. The minimum biofilm eradication concentration ($MBEC_{50}$) for C2 was determined as the concentration, which resulted in 50% reduction in biofilm metabolic activity as compared to untreated control sample. All the experiments were performed in three independent sets and every set consisted of three replicates. Data analysis and calculation of standard deviation was performed with Microsoft Excel 2010 (Microsoft Corporation, USA).

For fluorescence microscopy studies, *S. aureus* MTCC 96 and *P. aeruginosa* biofilm was grown in presence of varying concentrations of C2 (160 µM, 320 µM and 640 µM) and incubated for 24 h in a static and humid chamber at 37°C. Following incubation for 24 h, media from the wells was removed, the wells were washed with sterile PBS and stained separately with cFDA-SE and congo red by following a standard procedure as described in section 2.2.11.2 of Chapter 2. The stained samples were then observed under a fluorescence microscope as depicted in Scheme 4.8.

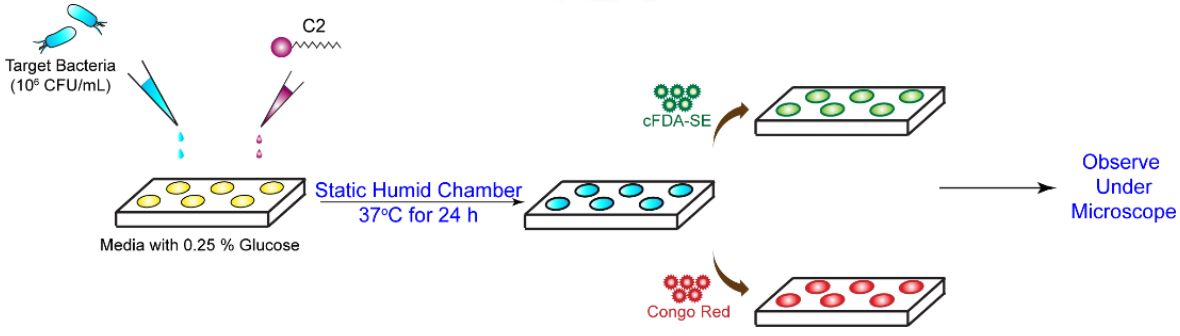

Scheme 4.8. Schematic illustrating the fluorescence microscopy protocol used to evaluate the antibiofilm potential of C2.

4.2.12. In Vitro Cytotoxic Effect of C2

The cytotoxic effect of C2 on HEK 293, HeLa and HT-29 cells were ascertained by a standard MTT assay as described in section 2.2.12 of Chapter 2. The amphiphile concentrations used for these assays was in the range of 20 µM - 620 µM. The MTT assay was performed in six sets for each tested concentration.

4.3. Results and Discussion

4.3.1. Design Rational and Characterization of Napthaldehyde-based Amphiphile (C2)

Membrane-targeting synthetic amphiphiles are promising therapeutic agents against antibiotic-resistant pathogenic bacteria (Findlay *et al*., 2010; Gokel and Negin 2012; Thiyagarajan *et al*., 2014; Mingeot-Leclercq *et al*., 2016; Salta, *et al*., 2017; Mitra *et al*., 2019). A large number of reports highlight the structure-activity correlation of synthetic amphiphiles. For instance, multiplicity of cationic head groups, head group structure and relative positioning of the head groups on the aromatic core have also been implicated in the antibacterial activity of synthetic amphiphiles (Mitra *et al*., 2009; LaDow *et al*., 2011; Goswami *et al*., 2013). The head group of a bactericidal synthetic amphiphile holds the

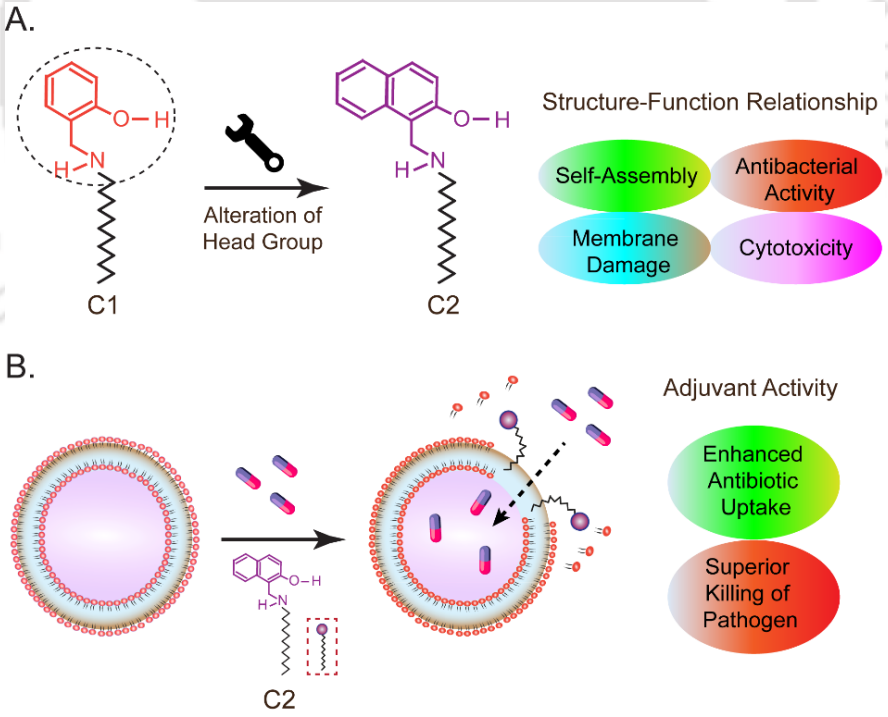

Figure 4.1. Cartoon indicating the design principle of the synthetic amphiphile C2. (A) The salicaldehyde head group of C1 is replaced by a napthaldehyde head group in C2, which may result in a new structure-function relationship. (B) The membrane-directed activity of C2 can facilitate an adjuvant activity resulting in higher antibiotic uptake and enhanced killing of the target pathogenic bacteria.

key to set-off strong interactions with bacterial cells. Herein, it is critical that the head group is biocompatible in order to minimize unwarranted host cell toxicity. In the previous studies described in Chapter 2 and Chapter 3, it was evident that the synthetic amphiphile C1 having a salicaldehyde head group displayed potent antibacterial activity against pathogenic bacteria including MRSA. It is widely acknowledged that the head group is a critical determinant in the activity of a bactericidal synthetic amphiphile. Hence in the present investigation, the motivation was to replace the salicaldehyde head group of the amphiphile C1 with a napthaldehyde group and generate a new amphiphile C2. It was conceived that alteration of the head group would likely change the hydrophilic-lipophilic balance (HLB) of the molecule and may lead to a new structure-function relationship in C2 in terms of its self-assembly attribute, bactericidal activity, membrane-directed activity and cytotoxic potential (Figure 4.1A). Further, it was envisaged that the new amphiphile C2 may be explored as an adjuvant, wherein the membrane-targeting activity of C2 can be leveraged to breach the inherent resistance of pathogenic bacteria, resulting in superior antibiotic uptake and enhanced killing of the target pathogen (Figure 4.1B). C2 was characterized by ESI-MS, NMR and FTIR (Appendix, Figure A4.1-A4.4). The logP value of C2 was 8.07, which indicated that C2 is more hydrophobic than C1 and the HLB value of C2 was 10.07 as compared to 8.38 for C1, which suggested that C2 can form an 'oil in water emulsion' more easily than C1.UV-visible absorption spectra of C2 indicated multiple absorption bands, namely at 290 nm, 340 nm and 430 nm (Figure 4.2A). Upon excitation of C2 at 290 nm, fluorescence emission peaks were observed at 360 nm and 435 nm (Figure 4.2B).

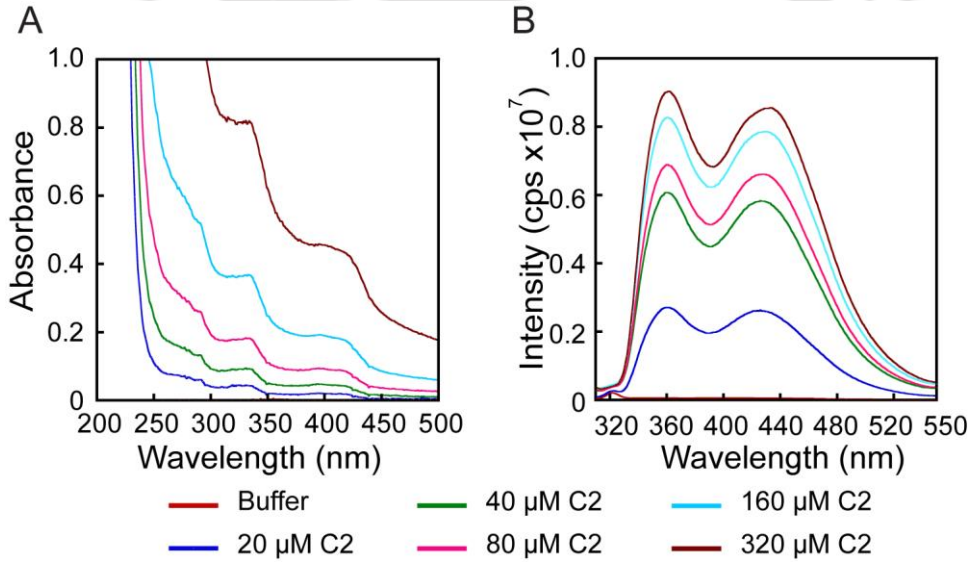

Figure 4.2. (A) UV-visible spectra of C2. (B) Fluorescence emission spectra of C2.

4.3.2. Aggregation Behavior of C2

LB trough and atomic force microscope (AFM) analysis indicated the propensity of C2 to form a monolayer as well as self-aggregate. The Π–A isotherms for varying concentrations of C2 indicated a phase transition and a decrease in the area per molecule (Figure 4.3A, Table 4.1), which was analogous to that observed for C1. Spherical aggregates of C2 (50 µM) with an average size of ~402 nm and a height profile of around 9.0 nm were evident in AFM analysis (Figure 4.3B-C), indicating the inherent propensity of C2 to self-assemble, likely driven by the hydrophobic tail, intermolecular hydrogen bonding and π-stacking interactions of the head group. The strong self-aggregation behavior of C2 was also captured in its low CMC (7.0 µM in water) (Figure 4.4A-B), which was less than that of C1 (18.5 µM in water) as reported in Chapter 3 Figure 3.2B. The higher hydrophobicity of C2 perhaps accounted for its lower CMC as compared to C1. DLS analysis indicated a concentration-dependent increase in the hydrodynamic radius of C2 in solution (Figure 4.4C).

Table 4.1. LB trough analysis of C2.

Sl. No.	C2 (µM)	Number of Molecules ($\times 10^{18}$)	Molecular Area ($Å^2$)	Area per Molecule ($Å^2$) $\times 10^{-18}$
1.	5.0	3.012	62.330	20.690
2.	10	6.023	54.353	9.020
3.	50	30.115	55.160	1.830

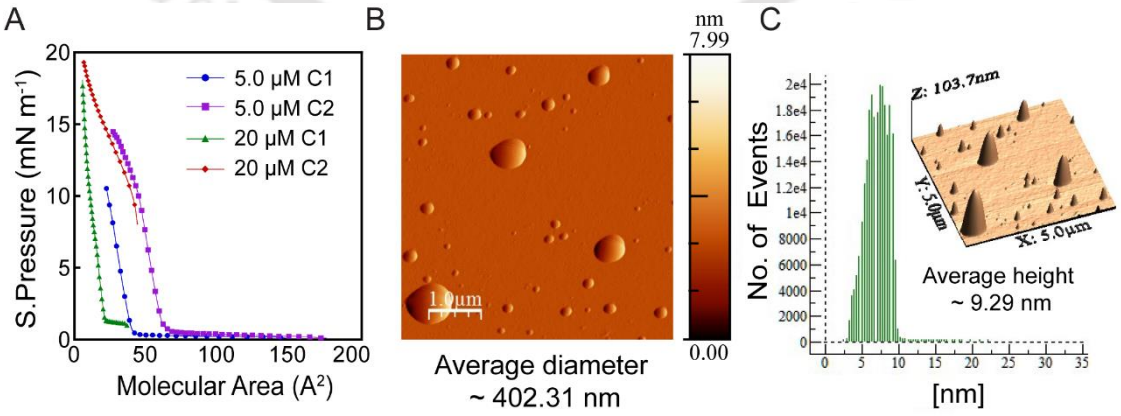

Figure 4.3. (A) Π–A isotherms for C2. (B) 2D topography AFM image of C2 (50 µM). (C) AFM image of C2 (50 µM) depicting the height profile. Inset indicates 3D topography AFM image of C2.

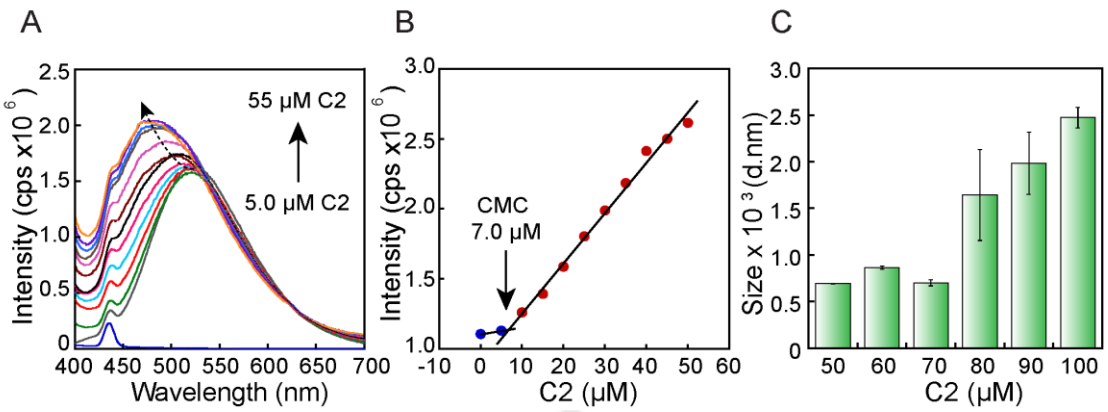

Figure 4.4. (A) Fluorescence emission spectra of ANS. The dotted arrow indicates a blue shift in the emission maxima with increasing concentrations of C2. (B) Changes in the fluorescence intensity of ANS (3.0 μM) following interaction and with varying concentrations of C2. (C) DLS based size distribution of varying concentration of C2.

4.3.3. Antibacterial Activity of C2

C2 exhibited a broad-spectrum bactericidal activity, (Figure 4.5A, Table 4.2) albeit of a lesser magnitude than C1 (Chapter 2, Figure 2.3A, Table 2.3). For instance, the MIC of C2 against the clinical strain *S. aureus* MRSA 100 was 320 μM (Table 4.2) as against 40 μM for C1 (Table 2.3). It may be mentioned here that the MIC of C2 against the Gram-negative target bacteria such as *E. coli* MTCC 433 and *P. aeruginosa* MTCC 2488 was distinctly higher as compared to the Gram-positive target strains (Table 4.2). The presence of an outer membrane permeability barrier in Gram-negative bacteria (Bolla *et al.*, 2011; Nikaido, 2010) may account for the relatively higher MICs. The bactericidal activity of C2 was also corroborated by FESEM analysis (Figure 4.5B).

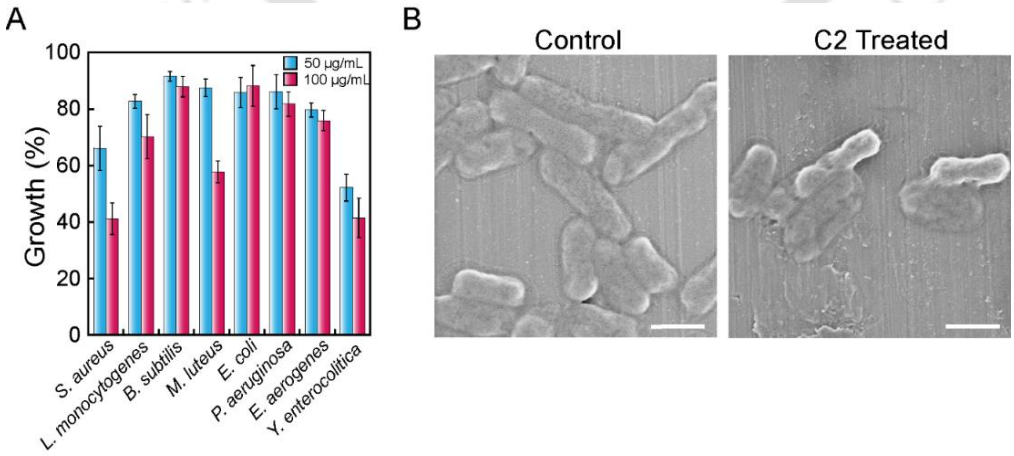

Figure 4.5. (A) Screening of the bactericidal activity of C2 against various pathogenic bacteria. (B) FESEM analysis for determining the antibacterial activity of C2 against *E. coli* MTCC 433. Scale bar for the images is 1.0 μm.

Table 4.2. MIC of C2 against various target bacteria.

Sl. No.	Target Bacteria	MIC of C2 (μM)
1.	*S. aureus* MTCC 96	160
2.	*L. monocytogenes* Scott A	320
3.	*P. aeruginosa* MTCC 2488	640
4.	*E. coli* MTCC 433	640
5.	*S. aureus* MRSA 100*	320
6.	*S. aureus* MSSA 104*	320

* Strains provided by Prof. Benu Dhawan (AIIMS, New Delhi, India) and Prof. Kasturi Mukhopadhyay (JNU, New Delhi, India)

Analogous to the salicaldehyde head group present in C1, the napthaldehyde head group of C2 may be involved in hydrogen bond interaction with phosphoryl and carboxyl groups known to be present in the bacterial membrane (French *et al.*, 2013) and thereby support anchoring of C2 onto cell surface, akin to other reported bactericidal agents (Cho *et al.*, 2007; Suarez *et al.*, 2014). The hydrophobic tail of C2 subsequently triggers membrane insertion in target bacteria, leading to cell death. The lower CMC of C2 as compared to C1 suggested a higher propensity of C2 to self-assemble and form a micelle. However, the bactericidal activity of C2 is likely governed by the available non-micellar or free form of the amphiphile, which is anticipated to be lower than C1, given the lower CMC value of C2. This may account for the lower antibacterial potency of C2 as compared to C1.

4.3.4. Membrane-directed Activity of C2

The membrane-targeting activity of C2 on target cells of *S. aureus* MTCC 96 and *E. coli* MTCC 433 was observed at high concentrations and this phenomenon was also dose-dependent (Figure 4.6.). The cFDA-SE leakage assay indicated that the membrane-targeting activity of C2 was superior against *S. aureus* MTCC 96 as compared to *E. coli* MTCC 433 (Figure 4.6.A and 4.6.C). The higher levels of membrane damage observed in case of *S. aureus* MTCC 96 cells is also consistent with a lower MIC of C2 against this target pathogen in comparison to *E. coli* MTCC 433

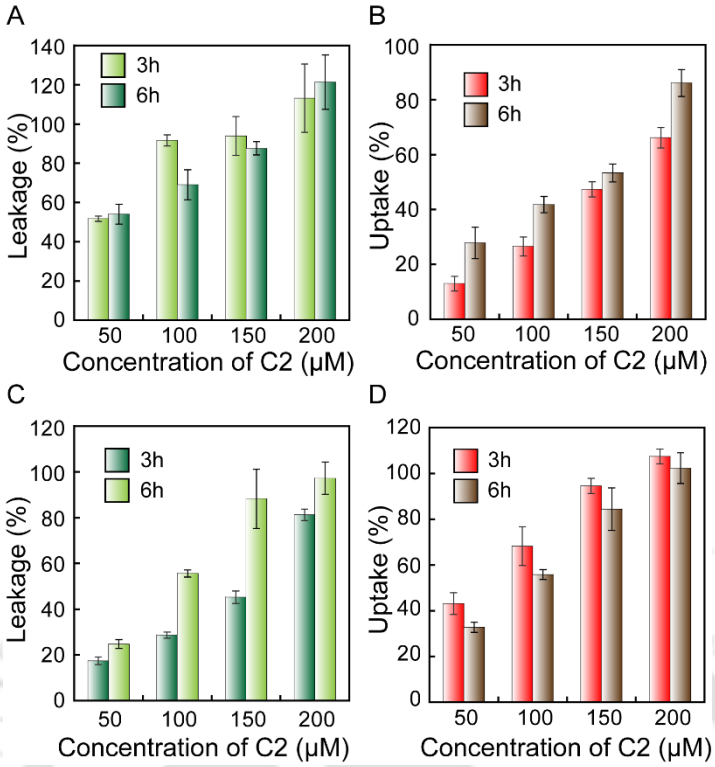

Figure 4.6. Assessment of membrane-directed activity of C2 against (A-B) *S. aureus* MTCC 96, (C-D) *E. coli* MTCC 433. A and D represents cFDA-SE leakage assay while B and E represents PI uptake assay.

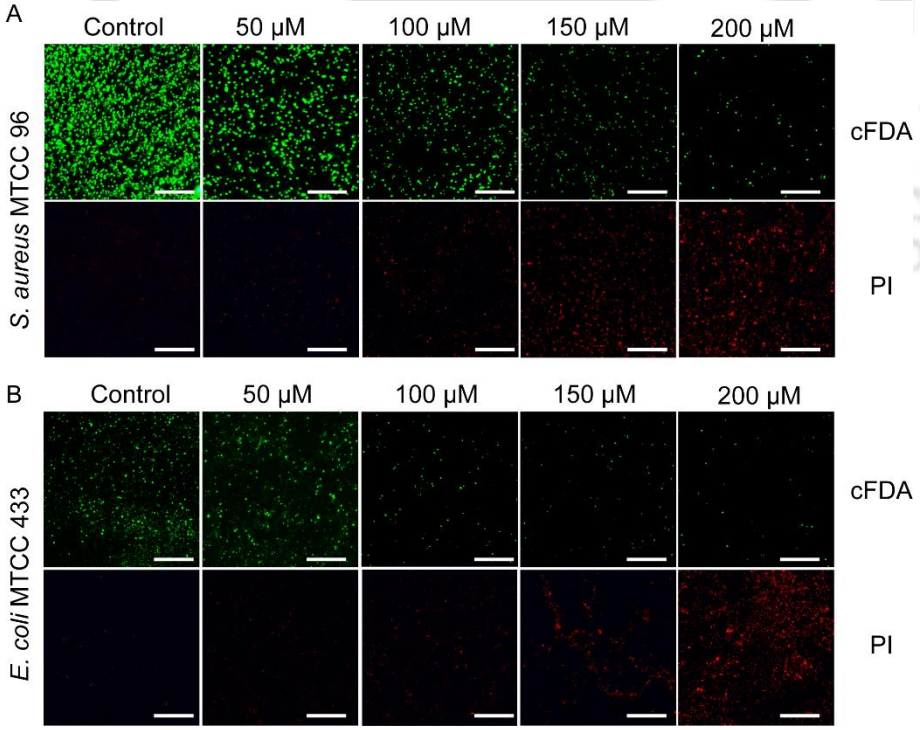

Figure 4.7. Fluorescence microscope-based live/dead assay with C2-treated (A) *S. aureus* MTCC 96 and (B) *E. coli* MTCC 433, respectively, using cFDA and PI. Scale bar for the images is 100 μm.

(Table 4.2). The quantum of membrane disruption in C2-treated target cells was also validated by a PI uptake assay (Figure 4.6.B and 4.26D), wherein the essential trend was analogous to that observed in the cFDA leakage assay. The dose-dependent membrane-targeting activity of C2 was also evident in fluorescence microscopy based live/dead assay (Figure 4.7.A and 4.7.B).

4.3.5. Flow Cytometry-based Studies

The bactericidal potential of C2 was also validated by studying the amount of cFDA dye retention in labelled cells of *S. aureus* MTCC 96 and *E. coli* MTCC 433 on treatment with various doses of C2 (100 µM and 200 µM) using a flow cytometry-based assay. In case of untreated samples (control), the fluorescence histogram indicated the presence of a large population of viable cells exhibiting strong cFDA-SE fluorescence (Figure 4.8A-B). Upon treatment with 100 µM and 200 µM of C2, there was a distinct shift in the position of the peak as compared to control (Figure 4.8A-B). This decrease in fluorescence of the labelled cells may be attributed to the membrane damage caused by C2 leading to a decrease in the amount of the cFDA retained by the cells, which is captured as a shift in the position of the fluorescence emission peak for C2-treated cells.

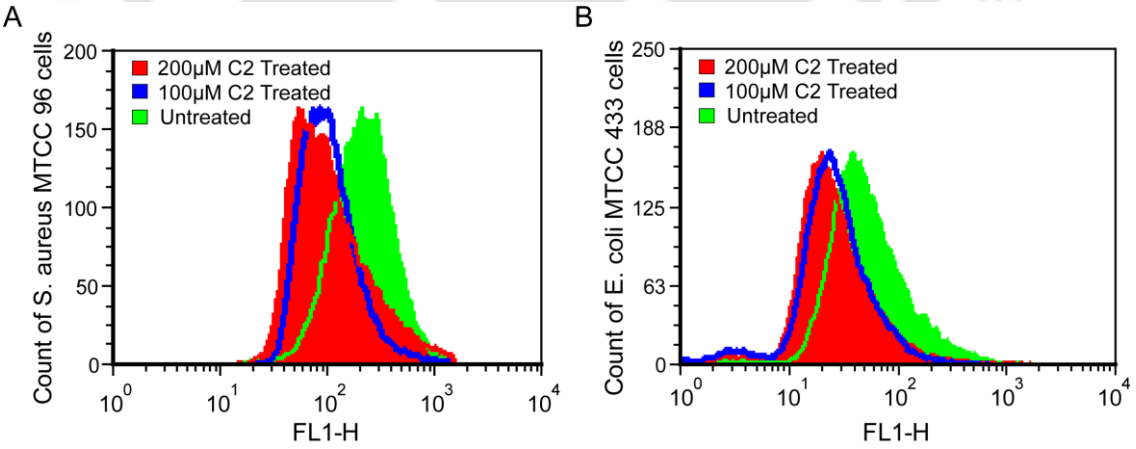

Figure 4.8. Flow cytometry-based assay to ascertain the effect of C2 treatment on (A) *S. aureus* MTCC 96 and (B) *E. coli* MTCC 433 cells labelled with cFDA-SE.

4.3.6. Adjuvant Potential of C2

The adjuvant potential of C2 in combination with polymyxin B against *S. aureus* MTCC 96 and erythromycin against *E. coli* MTCC 433 was ascertained. Upon combinatorial treatment an increase in the growth inhibition of the target pathogens,

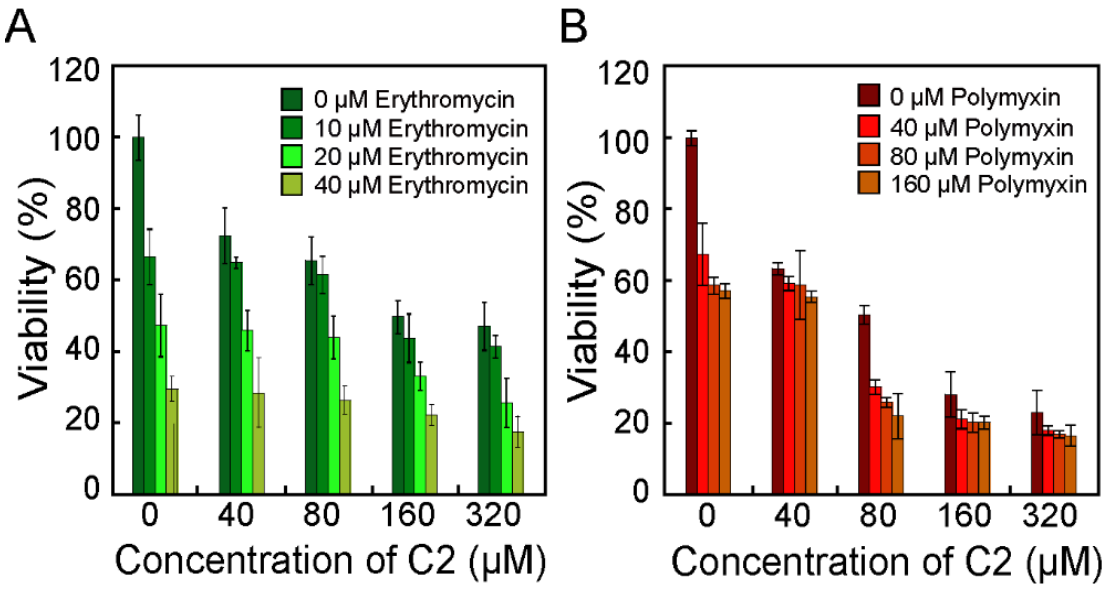

Figure 4.9. Antibacterial activity of C2 in combination with (A) erythromycin against *E. coli* MTCC 433 and (B) polymyxin B against *S. aureus* MTCC 96.

was observed in comparison to the cells treated with either the antibiotic or amphiphile singularly (Figure 4.9). On treatment with 40 µM erythromycin, the growth observed for *E. coli* MTCC 433 was 29%, which decreased to 17% on combination with 320 µM C2 and an additive interaction was evident (Figure 4.9A, Table 4.3).

The target pathogen *E. coli* MTCC 433 is likely to harbor an outer membrane permeability barrier, which is characteristic of a Gram-negative bacterium (Bolla *et al.*, 2011; Nikaido, 2010). The outer membrane barrier in Gram-negative bacteria can hinder the uptake of erythromycin (Saha *et al.*, 2008; Rawlinson *et al.*, 2010; Choi and Lee, 2012; Ulvatne *et al.*, 2001). The presence of a resilient membrane barrier may account for the relatively lower levels of killing of *E. coli* MTCC 433 cells by erythromycin alone (Figure 4.9B).

Given the membrane-targeting activity of C2 (Figure 4.6 C-D), against *E. coli* MTCC 433, it can be presumed that the amphiphile perhaps is able to breach the membrane and pave the way for superior antibiotic uptake in the combinatorial regimen, leading to higher levels of pathogen elimination by erythromycin (Figure 4.8B). On the other hand, when treated with 160 µM polymyxin B, the growth for *S. aureus* MTCC 96 was 57%, which was reduced to 22% on combination with 80 µM C2 and an additive effect was observed for this combination (Figure 4.9B, Table 4.3).

Table 4.3. FIC Index and nature of interaction of C2 against various target bacteria in combination studies.

Sl. No.	Target Bacteria	MIC	Combination	FIC Index	Effect
1.	*S. aureus* MTCC 96	Polymyxin B = 320 uM C2 = 160 uM	80 µM C2 + 40 µM Polymyxin B	0.625	Addition
			80 µM C2 + 80 µM Polymyxin B	0.750	Addition
			80 µM C2 + 160 µM Polymyxin B	1.000	Addition
2	*E. coli* MTCC 433	Erythromycin = 80 uM C2 = 640 uM	40 µM C2 + 40 µM Erythromycin	0.563	Addition
			80 µM C2 + 40 µM Erythromycin	0.625	Addition
			160 µM C2 + 20 µM Erythromycin	0.500	Synergy
			320 µM C2 + 20 µM Erythromycin	0.750	Addition
			160 µM C2 + 40 µM Erythromycin	0.750	Addition
			320 µM C2 + 40 µM Erythromycin	1.000	Addition

* The interaction was interpreted as synergy (FIC ≤ 0.5) or addition (FIC > 0.5 to 1.0) following a standard method (Giacometti *et al*., 2000).

4.3.7. Antibiofilm Activity of C2

There is an alarming rise in the frequency of grave infections caused by staphylococcal biofilm and this predicament is further exacerbated by the inherent resistance of the biofilm towards prevalent therapeutic antibiotics (Suresh *et al.*, 2019; Mohammed *et al*., 2018). Given the growing concern with regard to staphylococcal biofilm infections and based on the bactericidal activity of C2 against *S. aureus* (Figure 4.6 - 4.7), the

subsequent endeavor in this investigation was to ascertain the prospect of C2 as an antibiofilm agent against *S. aureus* MTCC 96 as well as the clinical *S. aureus* MRSA 100 strain. MTT-based assays suggested a dose-dependent inhibition as well as eradication potential of C2 against both the *S. aureus* biofilms (Figure 4.10.A-B, Appendix, Figure A4.5A-B). The concentration of C2 required to inhibit 50% biofilm ($MBIC_{50}$) was 150 µM and 274 µM for *S. aureus* MTCC 96 and *S. aureus* MRSA 100 respectively, whereas, the concentration of C2 required to eliminate 50% biofilm ($MBEC_{50}$) was 350 µM and 480 µM for *S. aureus* MTCC 96 and *S. aureus* MRSA 100, respectively. Fluorescence microscopy revealed that C2 was able to inhibit *S. aureus* biofilm as well as *P. aeruginosa* biofilm formation in a dose-dependent manner (Figure 4.10 C, Appendix, Figure A4.5C). However, the dose of C2 required for inhibition of *P. aeruginosa* biofilm formation was manifold higher than that required in case of *S. aureus* biofilm (Figure 4.10C, Appendix, Figure A4.5C).

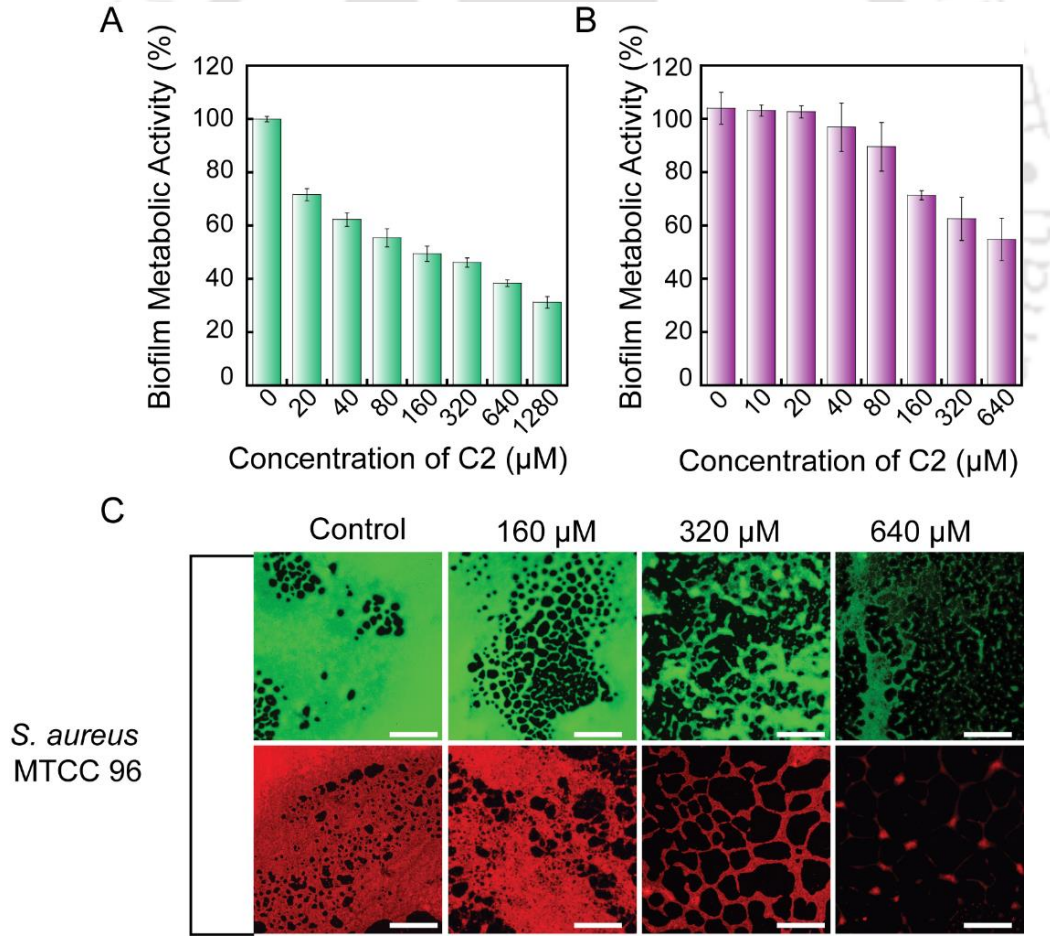

Figure 4.10. MTT assay to ascertain (A) inhibition and (B) eradication of *S. aureus* MTCC 96 biofilm by C2. (C) Fluorescence microscopic analysis to study inhibition of *S. aureus* MTCC 96 biofilm growth in presence of C2.

4.3.6. Cytotoxic Effect of C2

The cytotoxic potential of C2 was tested against HEK 293, HT-29 and HeLa cells. It was observed that upto 160 µM, C2 was non-toxic to HEK 293 cells (~90 % cell viability) (Figure 4.11A). However, for the cancerous cell lines, a toxic effect manifested at much lower doses of C2. In case of HeLa cells, C2 was observed to be non-toxic upto a concentration of 80 µM (Figure 4.11B), whereas in case of HT-29 cells, C2 was toxic at doses as low as 40 µM (Figure 4.11C). The higher susceptibility of carcinoma cell lines to C2 may be attributed to an enhanced permeation and retention effect (EPR) (Nichols and Han, 2014; Maeda, 2012).

In the context of potential therapeutic application of C2, it was pertinent to determine its therapeutic index (TI), which essentially reflects its target cell selectivity. In the present study, considering HEK 293 cells as the host cells, it was observed that the TI values (IC_{50}/MIC) for C2 was 2.625 and 1.312 for *S. aureus* MTCC 96 and *S. aureus* MRSA 100, respectively (Appendix, Table A4.1).

Based on earlier results, it was evident that the therapeutic potential of C2 as an antibacterial was inferior as compared to C1, which exhibited a corresponding TI value of 6.0 and 3.0 against *S. aureus* MTCC 96 and *S. aureus* MRSA 100, respectively (Chapter 2, Table 2.7). A lower TI value for C2 in comparison to C1 was also noted for other bacterial pathogens as well (Appendix, Table A4.1, Chapter 2, Table 2.7).

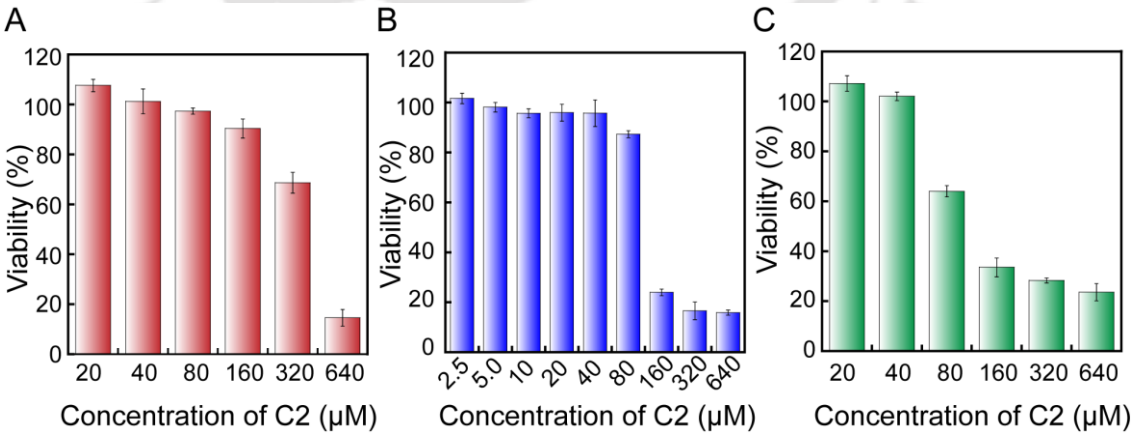

Figure 4.11. MTT assay to determine cytotoxic effect of C2 on (A) HEK 293 cells, (B) HeLa cells and (C) HT-29 cells. Each data point represents mean ± standard deviation from six samples.

2.4. Significant Findings

The essential findings of the present study were as follows:

1. The napthaldehyde-based amphiphile C2 could self-assemble in solution, with a CMC of 7.0 µM in water. The CMC of C2 was lower than that of C1 (18.5 µM in water), which suggested that C2 had a higher propensity to self-assemble as compared to C1, likely due to its inherently higher hydrophobicity.

2. The amphiphile C2 displayed broad-spectrum bactericidal activity and was more active on Gram-positive pathogenic bacteria in comparison to Gram-negative counterparts. However, the magnitude of the bactericidal activity of C2 was less than C1.

3. Fluorescence-based assays indicated that C2 displayed membrane-targeting activity on target pathogens, albeit of a lesser magnitude than C1.

4. The amphiphile C2 could potentiate the efficacy of antibiotics such as polymyxin B and erythromycin against target bacteria and a favorable interaction was observed between C2 and the antibiotics.

5. MTT assay and fluorescence microscopic analysis revealed that C2 could inhibit *S. aureus* biofilm. However, the effective concentrations of C2 required for manifestation of an antibiofilm effect was higher than that of C1.

6. C2 was non-toxic to HEK 293 cells at a concentration of 160 µM, which was equivalent to the MIC against *S. aureus* MTCC 96 strain.

Based on the results obtained in the study, it was evident that the amphiphile C2 could readily self-assemble given its high hydrophobicity and the possibility of intermolecular hydrogen bond formation and π-stacking of the head group. However, it was important to note that alteration of the salicaldehyde head group of the amphiphile C1 with a napthaldehyde group in C2 resulted in a change in the hydrophilic-lipophilic balance of the molecule and a new structure-function relationship emerged wherein the overall bactericidal potential of C2 was reduced as compared to C1. Based on the design principle, it can be conceived that the head groups of the amphiphiles C1 and C2 are likely to render supramolecular interactions and form hydrogen bonds with phosphoryl groups of bacterial lipoteichoic acid (LTA), which may enhance their localization on target cells. Further, the head groups of C1 and C2 can also render metal coordination

and thereby hinder metal acquisition in the target pathogen, which augers well as an antibacterial therapeutic strategy. In line with this notion, the subsequent chapter investigates the supramolecular interaction of C1 and C2 with LTA and their metal complexation and probes the overall effect of the interactions on the bactericidal activity of the amphiphiles.

Chapter 5

Impact of Supramolecular Interaction vis-a-vis Metal Coordination on the Bactericidal Activity of C1 and C2

This chapter investigates the effect of supramolecular interaction of the amphiphiles with bacterial lipoteichoic acid (LTA) and metal complexation in the context of their bactericidal activity. The fundamental understanding emerging from this work provides a framework to generate pluri-active synthetic amphiphiles as potential therapeutics against antibiotic-resistant pathogenic bacteria.

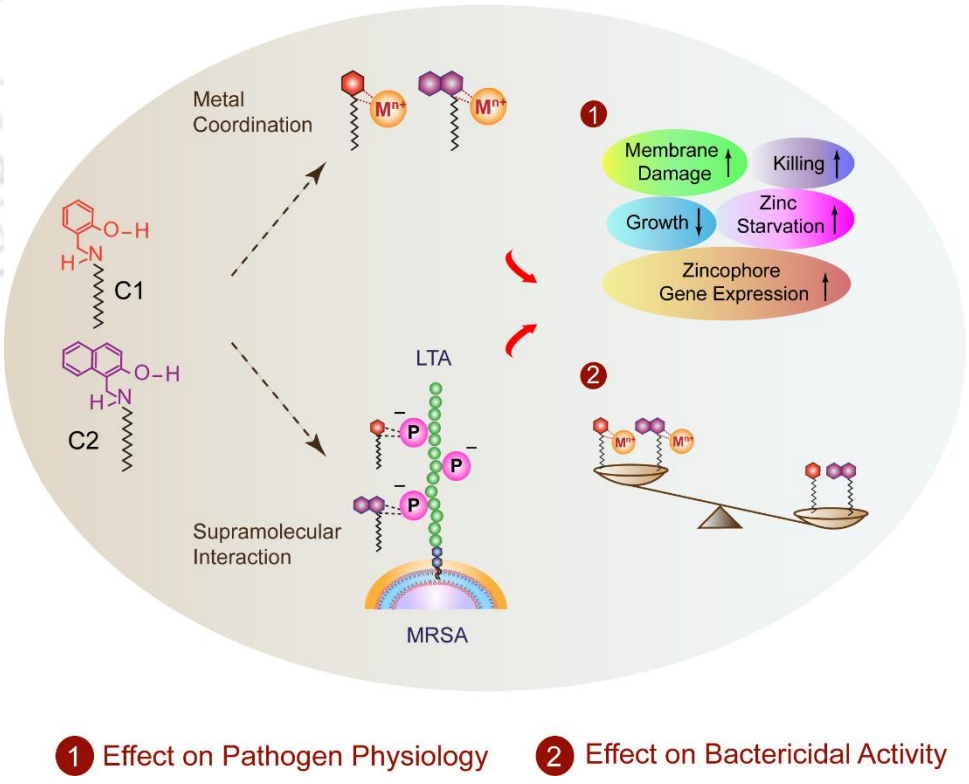

ABSTRACT

The present investigation essentially describes the implications of supramolecular interaction and metal coordination on the bactericidal potential of the synthetic amphiphiles C1 and C2 against drug-resistant pathogenic bacteria. Formation of amphiphile-metal complex was evidenced through ESI-MS, FTIR, FETEM-EDX and ITC analysis. Growth of the drug-resistant *S. aureus* MRSA 100 strain was remarkably impaired, with a 72% and 76% decrease in growth rate in presence of 5.0 µM C1 or 20 µM C2, respectively, as compared to free cells or cells grown in presence of equivalent levels of amphiphile-metal complexes, suggesting that the amphiphiles could perhaps sequester metal and induce metal starvation in MRSA. C1 and C2 rendered superior membrane damage in MRSA cells and were comparatively less toxic to human embryonic kidney (HEK 293) cells as opposed to their corresponding metal complexes. ITC analysis revealed that the binding of C1 and C2 to staphylococcal lipoteichoic acid (LTA) was stronger than the corresponding zinc complexes of the amphiphiles, which likely accounted for the higher bactericidal potency of the amphiphiles. Gene expression studies indicated that C1 imposed a concentration-dependent metal starvation response in MRSA as there was an upregulation of *cntL* gene and downregulation of *cntA* gene, which are involved in synthesis of the zincophore staphylopine (stp) and transport of stp-Zn complex, respectively. The study provides a fundamental understanding on how the chemistry-driven multimodal interaction of the amphiphile translates into growth inhibition and metal starvation in MRSA cells and contributes to future development of such pluri-active bactericidal amphiphiles for the mitigation of the healthcare burden imposed by MRSA.

5.1. Introduction

The emergence of drug-resistance in pathogenic bacteria has surpassed the current pace of discovery of novel antibiotics and has triggered the need for development of potent therapeutics in order to mitigate an alarming healthcare crisis (Brown and Wright, 2016; de Kraker *et al*., 2016; Petchiappan and Chatterji, 2017). Synthetic chemistry conceived through rational target selection and drug design has provided a viable conduit to develop a library of robust antibacterial molecules and leverage the lead molecules for therapeutic applications (Wright *et al*., 2014). In this regard, targeting metal acquisition with synthetic molecules may offer opportunities for therapeutic intervention against a pathogenic bacterium such as staphylococci as metals are critical to its virulence and infection process (Corbin *et al*., 2008; Remy *et al*., 2013; Hood and Skaar, 2012; Kehl-Fie, *et al*., 2011). For instance, Schiff bases and their complexes with Cu and Fe have been previously studied for their antibacterial activity against *Staphylococcus aureus* (Negm and Zaki 2008). Furthermore, metal-complexes have been found to be more potent antibacterial than the Schiff bases themselves (Negm and Zaki 2008). Various studies have shown a relationship between the metal ions and bacteria upon using metal complexes as antibacterial agents (Scozzafava *et al*., 2001; Scozzafana *et al.*, 2000). Studies have also shown that biologically active compounds become more bacteriostatic upon chelation with metal ions (Chohan *et al.*, 2002).

Metal coordination is a feasible handle for controlling the self-assembly of amphiphilic molecules. Complexation may lead to a change in the ionic charge or molecular geometry of an amphiphile, manifested as a prominent change in the aggregate morphology (Owen *et al*., 2007). Even naturally occurring surfactants have been known to exhibit metal-dependent phase changes, from planar lamellae to a reversed hexagonal phase for cardiolipin (Vasilenko *et al.*, 1982; Vail *et al.*, 1979; Rand and Sengupta, 1971). On the other hand, marinobactins can forms micelles above their CMC, but the size decreases on coordination with Fe (III), whereas, the micelles rearrange to form large vesicles in the presence of excess Fe (III) Owen *et al*., 2007. Owen *et al*., 2005. Martinez *et al*., 2003). Transition of synthetic single-tailed amphiphiles into vesicles upon coordination of transition-metals such as Ag(I), Co (II), and Fe (III) have also been reported (Luo *et al.*, 2002a or b, Apostol *et al.*, 2005).

In the present study, the amphiphiles C1 and C2 were rationally designed to bind metals and perturb metal acquisition and induce a metal starvation response in the target pathogen. However, based on the reports, which suggest modulation of the self-assembly

behavior and antibacterial activity of surfactants on interaction with metals, the subsequent endeavor was to determine how metal complexation can impact the aggregation behavior and bactericidal activity of the amphiphiles C1 and C2. In pathogenic bacteria, metal transporters are frequently employed to acquire metals needed for critical physiological processes. Hence, metal chelating molecules can starve the bacteria of the metal by competing with these transporters. In *Staphylococcus aureus*, such a transporter is staphylopine, which plays a vital role in zinc acquisition (Grim *et al.*, 2017; Capdevila *et al*., 2016). It would thus be interesting to study the effect of amphiphiles having metal complexing property on these transporters at the molecular level. Further, the design of the head groups of C1 and C2 also offer a window of opportunity to initiate supramolecular interactions with lipoteichoic acid (LTA) in Gram-positive pathogens, which is known to be a virulence factor (Weidenmaier and Peschel, 2008). A strong interaction between the amphiphiles and LTA is likely to enhance the local concentration of the molecule in the vicinity of the pathogen, prolonging the contact time with the target membrane and enhancing the killing efficiency.Given the propensity of the amphiphiles C1 and C2 to display multimodal chemistry, it is critical to juxtapose the impact of metal complexation on their bactericidal activity vis-a-vis supramolecular interaction with bacterial lipoteichoic acid. To this end, the present study assesses the potential of C1 and C2 to sequester physiologically relevant metals such as zinc, iron, etc., and trigger growth inhibition and a metal starvation response in MRSA cells.

5.2. Materials and Methods

5.2.1. Reagents and Growth Media

Brain-Heart Infusion (BHI) Broth was obtained from HiMedia, Mumbai, India. Dimethyl sulfoxide (DMSO), ethanol and methanol were procured from Merck, India. 2-hydroxy-napthaldehyde, dodecyl amine, sodium borohydride, 5(6)-carboxy fluorescein diacetate succinimidyl ester (cFDA-SE), 3-(4,5-dimethyl-2-thiazolyl)-2,5-diphenyl-2H-tetrazolium bromide (MTT), 8-anilino-1-naphthalenesulfonate (ANS), zinc perchlorate ($Cl_2O_8Zn.6H_2O$), $FeSO_4.6H_2O$, $MnCl_2$, $CaCl_2$, $MgCl_2$, Dulbecco's Modified Eagle Medium (DMEM), trypsin–EDTA and lipoteichoic acid (LTA) and primers were procured from Sigma-Aldrich (USA). Gibco™ Fetal Bovine Serum, TRIzol™ Max™ Bacterial RNA Isolation Kit and SYBR 1- STEP QRT-PCR KIT Invitrogen™ were procured from Thermo Fisher Scientific.

5.2.2. Bacterial Strain

S. aureus MRSA 100 strain was used in this investigation as a target bacterium. The growth conditions of the strain were as mentioned in section 2.2.5. of Chapter 2 unless stated otherwise. The MRSA strain was kindly provided by Prof. Benu Dhawan, All India Institute of Medical Sciences (AIIMS), New Delhi and Prof. Kasturi Mukhopadhyay, Jawaharlal Nehru University (JNU), New Delhi.

5.2.3. Preparation and Characterization of C1- and C2-Metal Complexes

For formation of a 10:50 mM stock solution of each of the metal complexes, 2.91 mg of C1 and 3.42 mg of C2 was weighed separately. 18.62 mg of $Cl_2O_8Zn.6H_2O$ (MW =372.38), 12.99 mg $FeSO_4.6H_2O$ (MW = 259.98), 6.292 mg of $MnCl_2$ (MW = 125.84), 5.5493 mg of $CaCl_2$ (MW = 110.99) and 10.16 mg of $MgCl_2$ (MW = 203.29) were also weighed and then mixed with the previously weighed C1 and C2 in separate tubes and dissolved in 1.0 mL of DMSO. The tubes were then incubated at 37°C and 180 rpm overnight to accomplish metal complexation (Scheme 5.1). The metal complexation of C1 and C2 was validated by ESI-MS and the complexation ratios were also ascertained. FESEM-EDX (Zeiss Sigma, USA) and FETEM-EDX (INCA, JEOL JEM 2100F, Japan) analysis of the C1 and C2 metal complexes were also pursued to ascertain metal complexation. The UV-visible spectra of the metal complexes were compared to that of C1 and C2 in water as a solvent system and the absorbance was recorded using a spectrophotometer (Lambda 25, Perkin-Elmer) in scanning mode from 250 nm to 700 nm

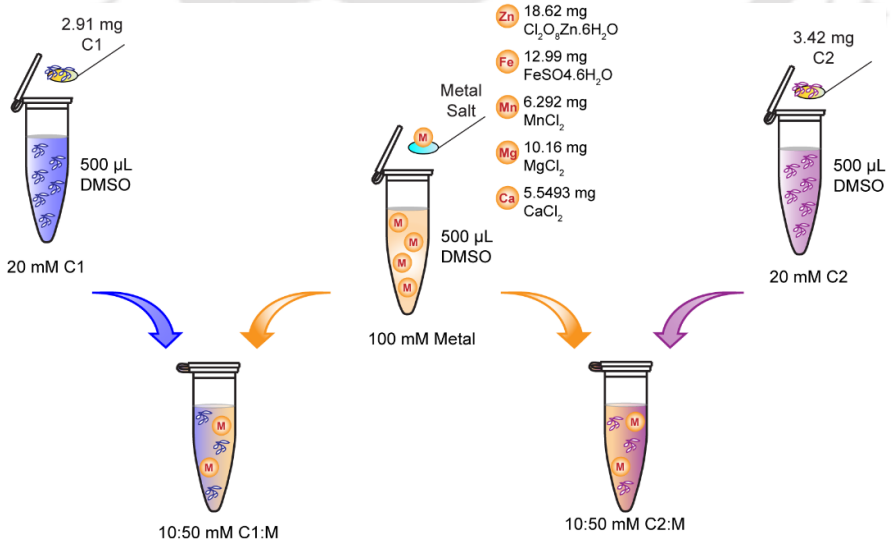

Scheme 5.1. Schematic representation of the protocol used to prepare C1 and C2 metal complexes.

The FTIR spectra of C1 and C2 metal complexes was recorded using an infrared spectrometer (Spectrum One, Perkin-Elmer) in the range of 4000 cm^{-1} to 450 cm^{-1}. The binding of C1 and C2 (50 µM each) to the corresponding metal salts alone (250 µM each) was determined by Isothermal Calorimetry (ITC) technique (Wiseman *et al*., 1989). ITC measurements were made at 25°C using a VP-ITC device (MicroCal, Northampton, USA). To prevent the formation of air bubbles, the buffers were degassed under vacuum prior to experiment. For all the samples, the integrated heat effects, after correction for heats of dilution were analyzed by non-linear regression (Microcal Origin, version 5.0).

5.2.4. Determination of Critical Micelle Concentration (CMC) of C1- and C2-Metal Complexes

To a 3.0 µM ANS solution (in water) in a cuvette, increasing concentrations of each 1:5 metal complex of C1 and C2 (5: 25 µM – 100: 500 µM) was titrated in separate sets. The fluorescence emission spectra of the solutions were measured from 400 to 700 nm at an excitation wavelength of 380 nm. The spectra were measured from three independent experimental samples and plotted as a function of the concentration of each species to ascertain the CMC value from the point of inflection as mentioned previously in section 3.2.4 of Chapter 3. In order to visualize the aggregation after metal complexation, FETEM analysis (JEOL JEM 2100F, Japan) of the C1 and C2 metal complexes were also pursued.

5.2.5. Interaction of Metals with C1- and C2-based Micelles

A 3.0 µM ANS solution in water was taken in a cuvette and emission spectra of the solution was measured from 400 to 700 nm at an excitation wavelength of 380 nm. In separate sets, C1 and C2 were added at a concentration (80 µM), which was manifold above their CMCs and the fluorescence emission spectra of the solution was again measured to observe the increase in ANS fluorescence to a maximum due to aggregation of C1 or C2. Subsequently, each of the metal salt solutions were titrated in increasing concentrations onto this solution in separate sets and the fluorescence emission spectra of the solution was measured again. Fluorescence measurements were recorded from three independent experimental samples for every amphiphile and metal combination (Scheme 5.2).

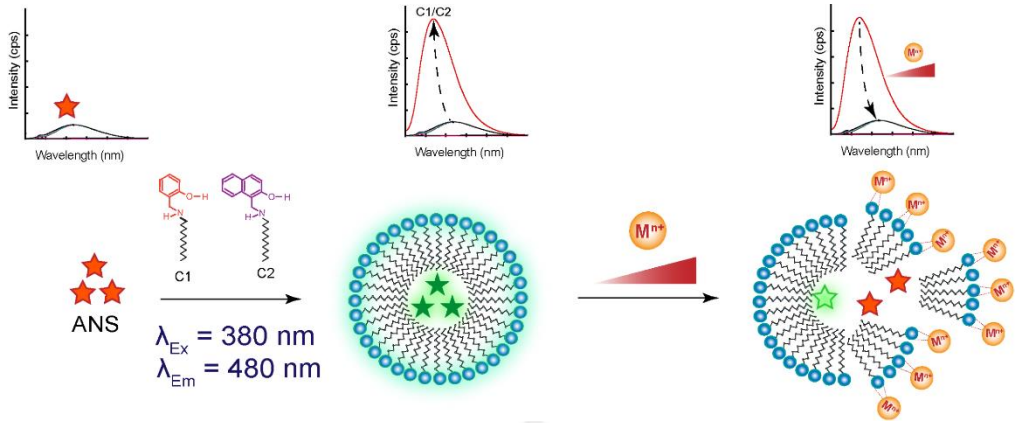

Scheme 5.2. Schematic representation of the protocol used to study interaction of metals with C1- and C2-based micelles.

5.2.6. Effect of Amphiphile and Amphiphile-Metal Complex on Bacterial Growth

In separate sets, target cells of *S. aureus* MRSA 100 (approximately 10^6 CFU/mL) were inoculated in BHI medium containing varying concentrations of either C1 or C2 (5.0 µM - 80 µM each) or the 1:5 metal complexes of each amphiphile (5:25 µM – 80:400 µM) and incubated at 37°C and 180 rpm. Samples were withdrawn at regular intervals of 0 h, 1 h, 2 h, 3 h, 4 h, 5 h, 6 h, 7 h, 8 h and 9 h and the absorbance of the cultures were recorded at 600 nm in a multimode plate reader. The growth of untreated MRSA cells suspended in BHI alone was also determined at the specified intervals. The absorbance values obtained for all the samples were used to construct the growth curves as depicted in (Scheme 5.3) and the specific growth rate (µ) of the cells in all the experimental samples was calculated from the slope of the curve by following a standard method (Zwietering *et al.*, 1990).

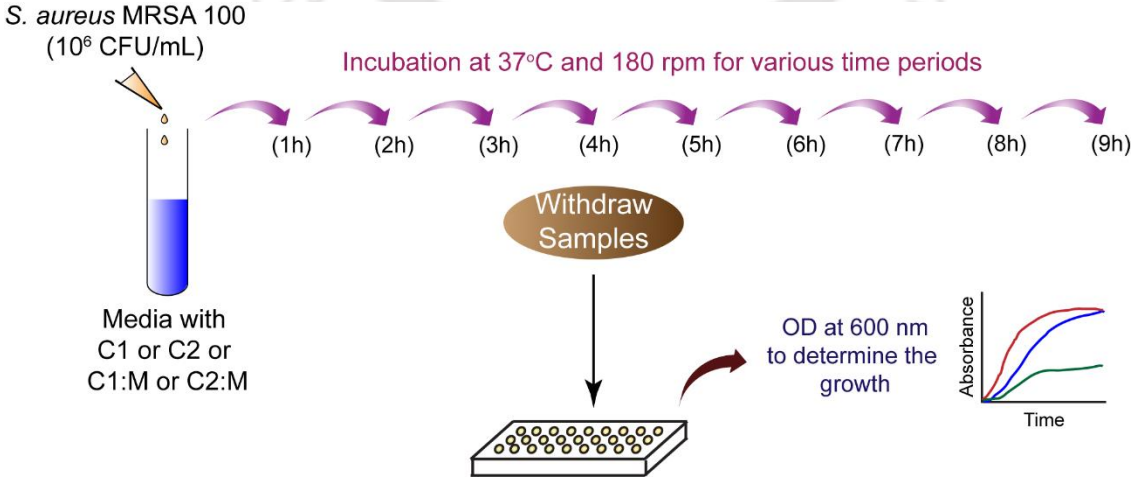

Scheme 5.3. Schematic representation of the protocol used to study the effect of C1, C2 and their metal complexes on the growth of *S. aureus* MRSA 100.

5.2.7. Membrane-directed Activity of C1- and C2-Metal Complexes

The membrane directed activity of C1- and C2-metal complexes (5.0: 25 µM and 20:100 µM) were evaluated against *S. aureus* MRSA 100 by following a cFDA-SE leakage assay as described earlier in section 2.2.8 of Chapter 2. The extent of the dye leakage was then compared with that obtained for treatment with C1 or C2 alone at equivalent concentrations.

5.2.8. Zinc Supplementation Studies with C1 and C2

Target bacterial cultures were inoculated at 1% (v/v) in requisite growth medium in a microtiter well plate and propagated overnight at 37°C and 180 rpm overnight. Biofilm of *S. aureus* MTCC 96 and *S. aureus* MRSA 100 was grown in sterile 96-well microtiter plate in BHI medium supplemented with glucose (0.25%) and varying concentrations of C1 and C2 (10 µM to 320 µM and 40 µM to 640 µM, respectively) for *S. aureus* MRSA 100 and (5.0 µM to 320 µM and 20 µM to 1280 µM, respectively) for *S. aureus* MTCC 96. After 24 h of biofilm growth, the spent media was aspirated and fresh media containing 50 µM and 100 µM of zinc perchlorate was added to the wells in separate sets, and biofilm growth was allowed to proceed for a further 24 h. Subsequently, the biofilm metabolic activity was accessed by an MTT based assay (Scheme 5.4) as mentioned before in Chapter 2 Section 2.2.11.1. In a control experiment, biofilm of *S. aureus* MTCC 96 and *S. aureus* MRSA 100 was grown in a sterile 96-well microtiter plate in BHI medium supplemented with glucose (0.25%) without the amphiphiles. After 24 h of biofilm growth, 50 µM and 100 µM zinc perchlorate was added to the wells, and

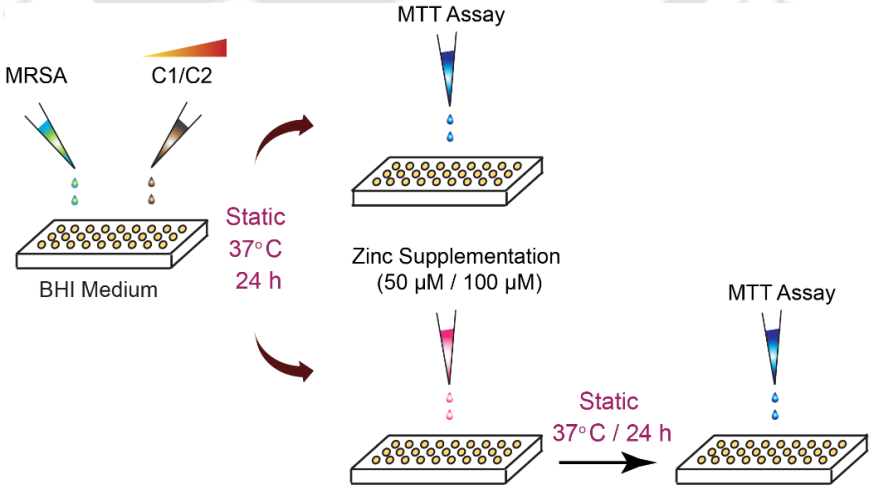

Scheme 5.4. Schematic representation of the protocol used to study the effect of zinc on the regeneration of C1, C2 treated *S. aureus* MRSA 100 biofilm.

biofilm growth was allowed to proceed for a further 24 h. Biofilm metabolic activity was then ascertained by MTT as mentioned before. All experiments were performed in triplicate.

5.2.9. Cytotoxicity of C1- and C2-Metal Complexes

The cytotoxic effect of C1 and its metal complexes (10 µM to 160 µM) and C2 and its metal complexes (20 µM to 640 µM) respectively, was ascertained on model human embryonic kidney cells (HEK 293) by a standard MTT assay (Goswami *et al*., 2013). The MTT assay was performed in six sets for each tested concentration. The therapeutic indices of C1, C2 and the metal complexes against HEK 293 cells with reference to the pathogenic bacteria was also determined.

5.2.10. Gene Expression Studies

Target cells of *S. aureus* MRSA 100 (approximately 10^6 CFU/mL) were grown in separate sets in (i) BHI media (ii) BHI media incorporated with C1 (5.0 µM - 40 µM), (iii) BHI media incorporated with 100 µM zinc and (iv) BHI media incorporated with 100 µM zinc and C1 (5.0 µM - 40 µM). The cells were grown in the specified media at 37^{o}C and 180 rpm. Following incubation for 24 h, the cells were harvested, and RNA was isolated from the cells using TRIzol™ Max™ Bacterial RNA Isolation Kit and the RNA yield was quantified using IMPLEN NanoPhotometer® NP80. Gene specific primers were designed for 16s rRNA, *cntA* and *cntL* genes using Primer3 (v. 0.4.0). The sequence of the primers is indicated in Table 5.1. A quantitative real time PCR was conducted with 200 ng of RNA from each sample using SYBR 1- STEP qRT-PCR Kit on a 36-Well Rotor, QIAGEN Rotor-Gene Q ® qRT-PCR machine. Reverse transcription was accomplished by incubating the reaction mixture at 50^{o}C for 3 min.

Table 5.1. Primers used for gene expression studies.

Sl. No.	Target Gene	Oligo Sequence (5' to 3')	Amplicon size
1.	16S rRNA	Forward: GAAAGCCACGGCTAACTACG Reverse: CATTTCACCGCTACACATGG	202 bp
2.	*cntA*	Forward: GCGTCTGAACGCTCTTTACC Reverse: CATCAATGGCGAAACATCAG	231 bp
3.	*cntL*	Forward: TGGATATGCACCTGAACCAA Reverse: CAATTTAATGCTTGGCGTGA	237 bp

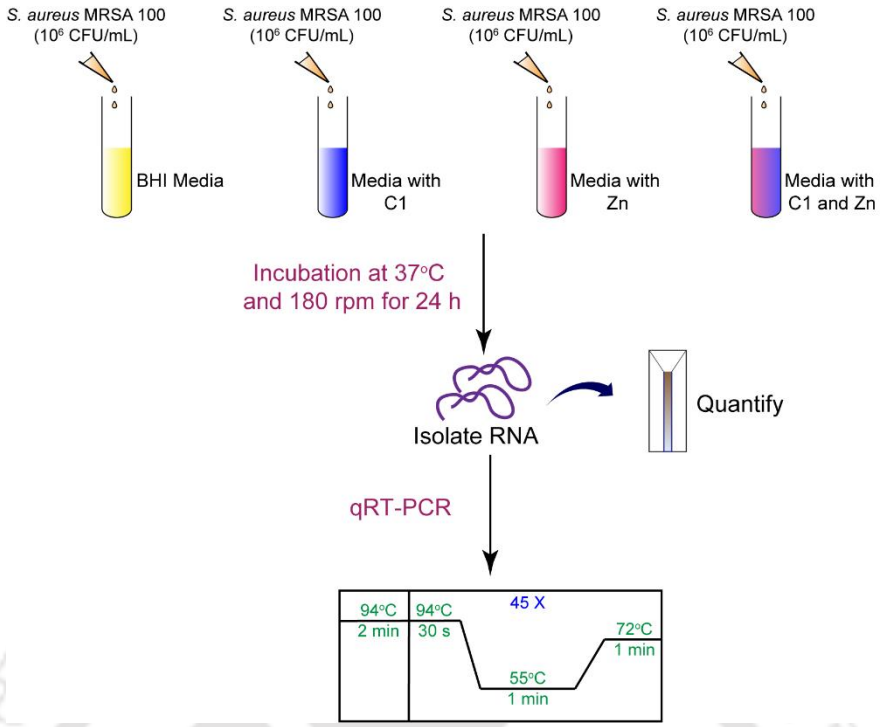

Scheme 5.5. Schematic representation of the protocol used to study gene expression of *S. aureus* MRSA 100 grown in presence of C1 alone and C1 with zinc supplementation.

Subsequently, the PCR conditions were as follows: (1) initial hold temperature of 94°C for 2 min, (2) cycling conditions included a denaturation step at 94°C for 30 sec, annealing at 55°C for 1.0 min, extension at 72°C for 1.0 min for a total of 45 cycles (Scheme 5.5.). Analysis of RT-PCR data was done using the LinRegPCR (2014.x) software and the cycle threshold (C_T) values were calculated after baseline correction. The fold change in gene expression values was ascertained by the $\Delta\Delta C_T$ method (Livak and Schmittgen, 2001).

5.2.11. Binding of C1, C2 and Metal Complexes with Lipoteichoic Acid (LTA) and Bacterial Cells

The binding of C1, C2 and their respective metal complexes onto lipoteichoic acid (LTA) was determined by Isothermal Calorimetry (ITC) technique. ITC measurements were made at 25°C using a VP-ITC device (MicroCal, Northampton, USA). To prevent the formation of air bubbles, the buffers were degassed under vacuum prior to experiment. In the binding studies, a 5.0 µM solution of LTA prepared in Tris-buffered saline (TBS) was loaded onto the cell and titrated in separate sets against C1 or C2 (50 µM each) or C1- or C2-metal complexes (50:250 µM each). For all the samples, the integrated heat

effects, after correction for heats of dilution were analyzed by non-linear regression (MicroCal Origin, version 5.0). The binding of metal complexes (100:500 µM) to the target cells of *S. aureus* MRSA 100 was visualized by FETEM mapping studies (INCA, JEOL JEM 2100F, Japan).

5.3. Results and Discussion

5.3.1. Design Rationale of Synthetic Amphiphiles

It is evident from the structure of C1 and C2 that apart from having an inherent hydrophobicity and a high propensity to self-assemble, the head groups of the amphiphiles can also render supramolecular interactions and form hydrogen bonds with phosphoryl groups of lipoteichoic acid (LTA), which constitutes a major bacterial cell wall glycopolymer and is also present in MRSA (Schneewind and Missiakas, 2014; Weidenmaier and Peschel, 2008). Targeting the accessible LTA of MRSA with C1 or C2 can be an efficient strategy to anchor and enhance the local concentration of the amphiphile, which may in turn trigger membrane damage in the target cells as conceived

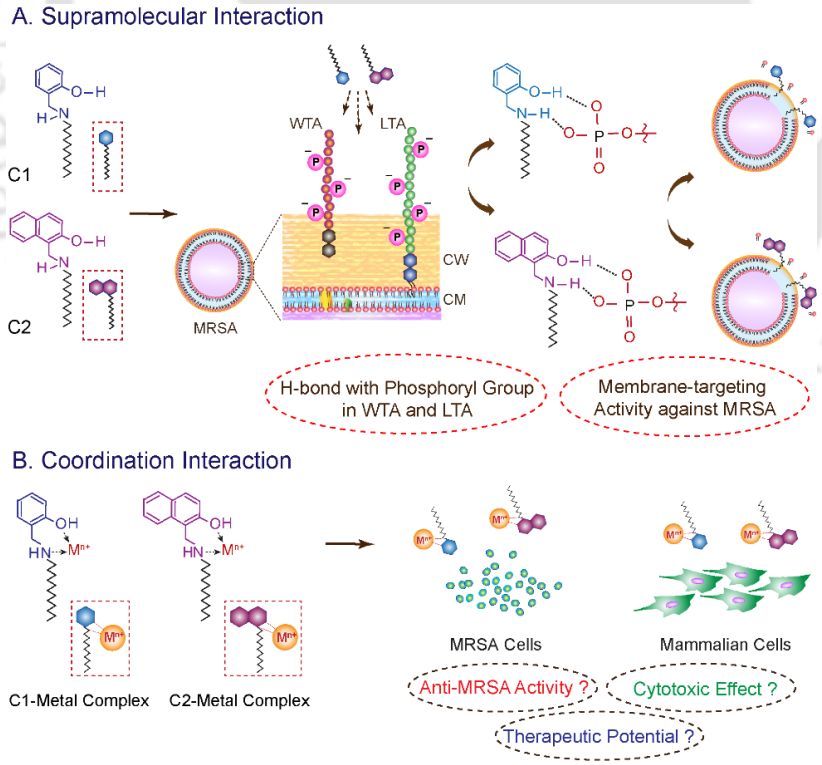

Figure 5.1. Cartoon illustrating the plausible role of (A) supramolecular interaction and (B) coordination interaction of salicaldehyde (C1) and napthaldehyde (C2)-based amphiphiles in the context of their cell envelope interaction, membrane targeting bactericidal activity, cytotoxic effect and therapeutic potential.

in Figure 5.1A. Further, the head groups of C1 and C2 can also bind metals (Figure 5.1B) and potentially interfere with metal acquisition in the target pathogen, which augers well given the integral role of metals in the physiology and infection caused by drug-resistant pathogenic bacteria (Corbin *et al.*, 2008; Hood and Skaar, 2012; Klein and Lewinson, 2011). Further, such metal complexing amphiphiles are likely to influence expression of genes involved in metallophore synthesis such as staphylopine (stp), which is implicated in metal starvation (Grim *et al.*, 2017; Capdevila *et al.*, 2016). However, it is also pertinent to determine the anti-MRSA activity, the cytotoxic effect and the therapeutic potential of the amphiphile-metal complex (Figure 5.1B).

5.3.2. Metal Complexation by Amphiphiles

C1 and C2 were tethered with metal coordinating head groups for possible disruption of metal acquisition by pathogenic bacteria. Facile complexation of physiologically relevant metals such as zinc and iron by the amphiphiles was evidenced by ESI-MS, EDX, UV-visible spectroscopy and FTIR analysis (Figure 5.2A-5.2D, Appendix Figure A5.1-A5.3). ITC indicated that zinc binds to C1 and C2 with an affinity of 3.38×10^4 M^{-1} and 1.02×10^5 M^{-1}, respectively (Figure 5.3A-5.3B). Presumably the deprotonation ability of the phenolic OH and the stability of the conjugate base of C2 is higher, which may facilitate stronger binding with the metal ion as compared to C1.

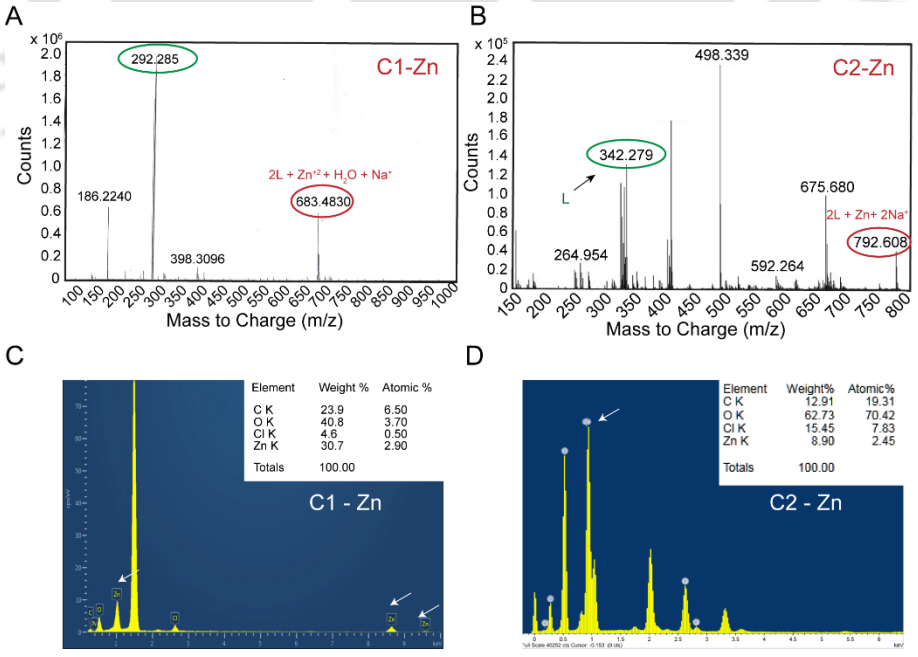

Figure 5.2. ESI-MS of (A) C1-Zn (II) and (B) C2-Zn (II) complex. EDX analysis for zinc complexation by (C) C1 and (D) C2.

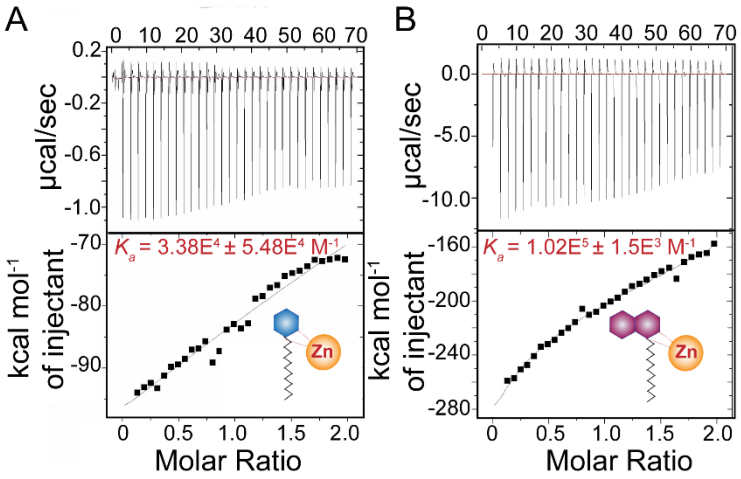

Figure 5.3. ITC analysis to study the interaction of (A) C1 and (B) C2 with zinc.

5.3.3. Aggregation Behavior of the Amphiphile Metal Complexes

Metal complexation by amphiphiles also influenced their self-assembly as evidenced by the increase in the CMC values (Figure 5.4A, Appendix Figure A5.4). The intermolecular hydrogen bonding and π-stacking interactions of the head group is perhaps reduced following metal complexation, which may result in a higher CMC. FETEM analysis indicated that the amphiphile-metal complexes were mostly spherical in shape and had an average size of around 100-300 nm (Figure 5.4B, Appendix Figure A5.5). Upon interaction of varying concentrations of C1 (10 µM – 80 µM) with increasing concentration of Zn, a decrease in the fluorescence intensity of ANS was observed (Appendix, Figure A5.6A), which indicated disaggregation of C1 in solution. However, it was noted that at low C1 concentrations (10 µM and 20 µM), the reduction in the fluorescence intensity of ANS was less, suggesting that addition of low concentrations of Zn was sufficient to induce disaggregation of the amphiphile. However, at higher concentrations of C1 (40 µM and 80 µM), which were way above the CMC, a rapid drop of fluorescence intensity of ANS could be observed upon interaction with 100 µM Zn, followed by a rather slow and prolonged decline at higher concentrations of Zn. This suggested that at higher C1 concentrations, micelle formation in solution was perhaps a favored process, which entailed a higher concentration of Zn in order to trigger the disassembly of the micelles. Hence in order to ascertain the effect of other metals on C1 micelle disassembly, the subsequent endeavor was to study this interaction with Ca, Fe and Mn. A notable decrease in the fluorescence intensity of ANS entrapped in dynamic micelles of C1 (80 µM) was observed upon titration with increasing concentrations of the metal salts, wherein Fe could render maximum disassembly of the micelles (Figure

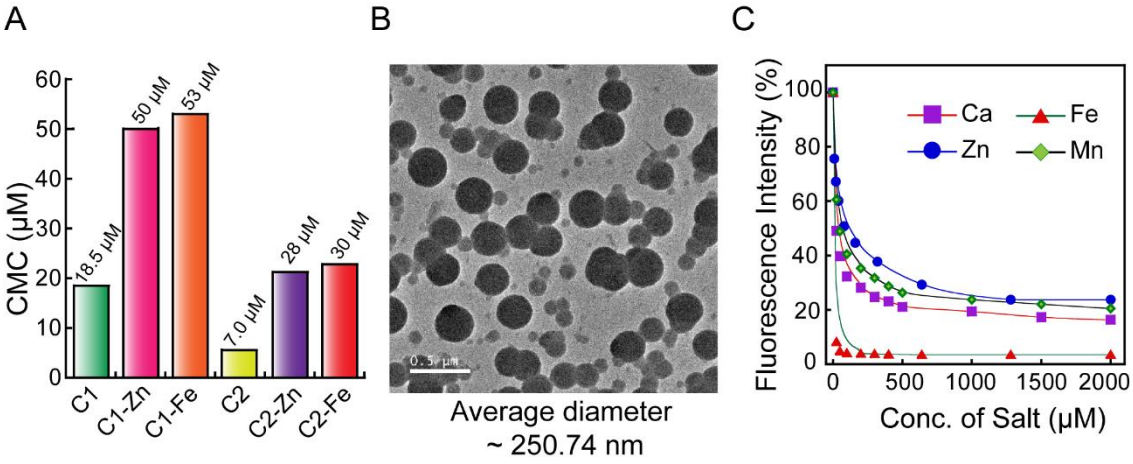

Figure 5.4. (A) CMCs of amphiphiles and their metal complexes. (B) FETEM image of C2-Zn complex. (C) Changes in the fluorescence intensity of ANS (3.0 μM) entrapped in C1 micelle (80 μM) in presence of varying concentrations of metal salts.

5.4C). In order to validate the effect of the metals on the disassembly of micelles generated from amphiphiles having a lower CMC, a similar experiment was conducted wherein it was observed that on titrating various concentrations of the metals onto 80 μM C2, a decrease in fluorescence intensity of ANS, similar to C1 was observed (Figure A5.6B). However, even at metal concentration as high as 2000 μM, the maximum decrease in the fluorescence intensity of ANS was rendered by Fe, being only 20% (Figure A5.6B). This indicated that disaggregation of micelles originating from amphiphiles with lower CMC requires extremely high concentrations of metal.

5.3.4. Comparative Bactericidal Activity and Cytotoxicity of Amphiphiles and their Metal Complexes

The subsequent endeavor was to ascertain the comparative bactericidal activity of the amphiphiles and their metal complexes against a drug-resistant pathogen. Given the fact that metals such as zinc and iron are cardinal to cell growth and infection process of a drug-resistant pathogen (Corbin *et al.*, 2008; Hood and Skaar, 2012; Klein and Lewinson, 2011) and C1 and C2 were designed to sequester metals, it was pertinent to decipher the effect of metal complexation by the amphiphiles on the growth of the target pathogen. In presence of 5.0 μM C1 or 20 μM C2, which was below their respective MICs against *S. aureus* MRSA 100 (Table 2.3) in Chapter 2 and Table 4.2 in Chapter 4), growth of the pathogen was significantly curbed with an extended lag phase as compared to untreated cells or cells grown in presence of amphiphile-metal complex for a period

of 9 h (Figure 5.5A-B, Appendix Figure A5.7). The dramatic growth inhibition effect observed at such low amphiphile concentrations is likely a combined effect of the membrane-directed activity and the ability of the amphiphiles to sequester metals and perhaps induce metal starvation in MRSA. This also highlights the therapeutic benefit of designing antibacterials having multimodal activity as a potent effect on the pathogen was observed even at very low amphiphile concentrations. The relevance of metal sequestration in the observed growth inhibition rendered by the amphiphiles was validated by the extent of growth suppression. The decrease in the growth rate of MRSA cells was around 72% and 76% in presence of 5.0 µM C1 or 20 µM C2, respectively, and

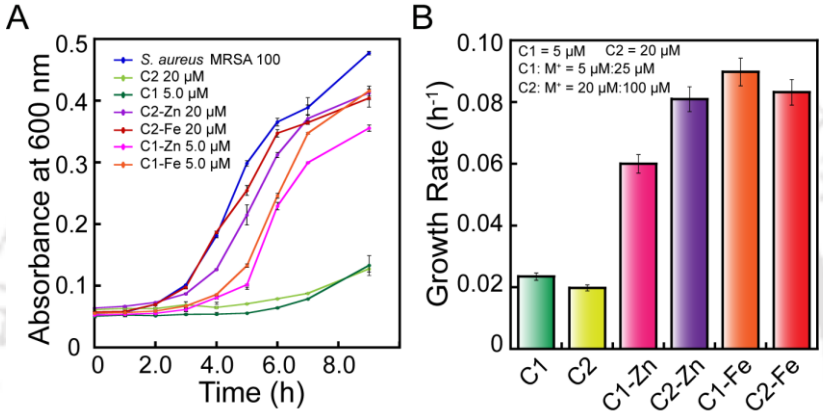

Figure 5.5. Effect of amphiphile and their metal complex on (A) the growth and (B) growth rate of *S. aureus* MRSA 100.

Table 5.2. Effect of amphiphiles and their metal complexes on the growth rate of *S. aureus* MRSA 100.

Sl. No.	Species	Growth Rate (h^{-1})	% Decrease in Growth Rate
1.	C1 (5.0 µM)	0.0235	71.759
2.	C2 (20 µM)	0.0198	76.202
3.	C1-Zn (5:25 µM)	0.0600	27.885
4.	C2-Zn (20:100 µM)	0.0810	2.644
5.	C1-Fe (5:25 µM)	0.0898	19.964
6.	C2-Fe (20:100 µM)	0.0832	25.846
7.	C1-Mn (5:25 µM)	0.0778	30.659
8.	C2-Mn (20:100 µM)	0.0930	17.112
9.	C1-Mg (5:25 µM)	0.0683	11.870
10.	C2-Mg (20:100 µM)	0.0771	0.516

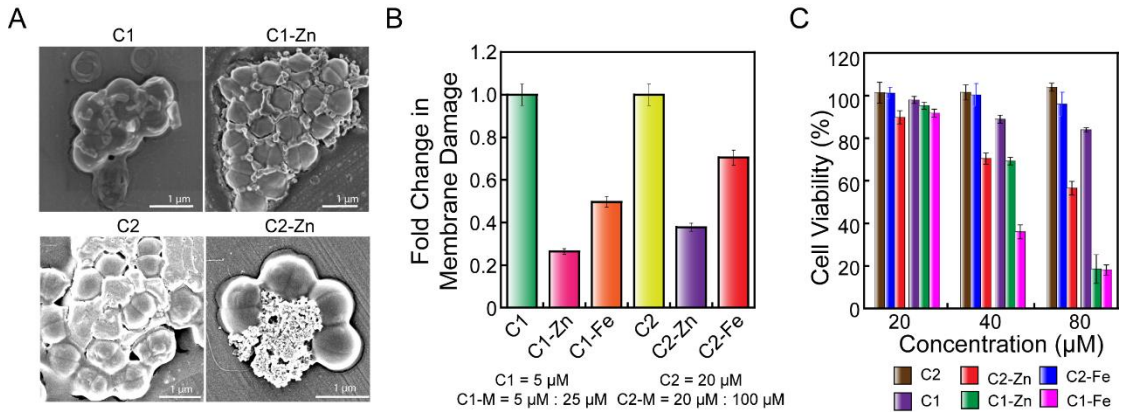

Figure 5.6. (A) FESEM image of *S. aureus* MRSA 100 cells treated with C1, C2 and their zinc complexes. (B) Fold change in membrane damage of *S. aureus* MRSA 100 cells by amphiphiles and their metal complex. (C) MTT assay to ascertain cytotoxic effect of amphiphiles and their metal complex on HEK 293 cells.

the growth was completely obliterated at higher concentration, while the effect exerted on the growth rate by the corresponding metal complexes of C1 and C2 was comparatively less at equivalent concentration (Table 5.2). However, at higher concentrations of amphiphile-metal complex, the growth inhibition phenomenon was comparable to that observed for equivalent concentrations of the amphiphiles alone (Appendix, Figure A5.7). FESEM analysis also indicated that the morphological perturbation of MRSA cells treated with amphiphile-metal complex was less conspicuous as compared to treatment with the amphiphile alone (Figure 5.6A, Appendix, Figure A5.8). A superior membrane damage rendered by C1 and C2 on MRSA cells as opposed to their corresponding metal complexes (Figure 5.6B, Appendix,

Table 5.3. Therapeutic index of C1and C2-metal complexes.

Sl. No.	Species	Therapeutic Index* (IC_{50} / MIC)	Sl. No.	Species	Therapeutic Index** (IC_{50} / MIC)
1.	C1	3.00	6.	C2	1.31
2.	C1-Fe	0.25	7.	C2-Fe	0.25
3.	C1-Zn	0.13	8.	C2-Zn	0.25
4.	C1-Mg	1.00	9.	C2-Mg	1.00
5.	C1-Mn	0.50	10.	C2-Mn	0.50

Figure A5.9) can perhaps be attributed to the higher conformational flexibility of the amphiphiles facilitating insertion and disruption of the membrane of MRSA cells, akin to other reported studies (Zhang *et al*., 2017; Palermo *et al*., 2012). It is also possible that the counter anion in amphiphile- metal complex, which is not present in the amphiphile alone may hinder its interaction with the negatively charged phospholipid present in bacterial membrane (Epand and Epand, 2009; Mingeot-Leclercq *et al.*, 2016) and account for the lack of a notable membrane-directed bactericidal activity. It was also observed that the amphiphile-metal complexes were more toxic to HEK 293 cells as compared to the amphiphiles, especially at higher concentrations (40 µM - 160 µM for C1 and 160 µM - 640 µM for C2) (Figure 5.6C, Appendix, Figure A5.10). The counter anion present in the metal complexes may interact with the positive charge known to be present in the zwitterionic phospholipids in mammalian cells (Zasloff, 2002) and assist in anchoring them close to the membrane, leading to their superior insertion and enhanced toxicity. The therapeutic index (IC_{50}/MIC) of the amphiphiles towards MRSA was superior than the metal complexes (Table 5.3).

5.3.5. Antibiofilm Activity of C1 and C2 upon Zn Supplementation

Metal-ion chelators are known to be potent biofilm inhibitors (Kapoor *et al.,* 2017). The role of Zn chelation in inhibition of biofilm formation, by C1 and C2 was verified by Zn supplementation experiments. To this end, initially, the amphiphiles were observed to have a dose-dependent inhibitory effect on *S. aureus* MRSA 100 and *S. aureus* MTCC96 biofilm formation. On addition of 50 µM and 100 µM of Zn in separate sets, a revival

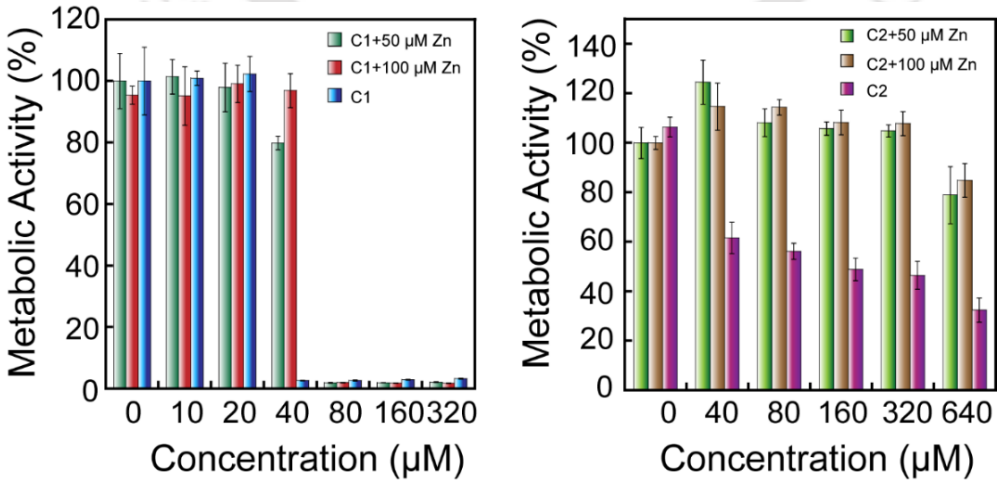

Figure 5.7. Effect of Zn Supplementation on the metabolic activity of (A) C1 and (B) C2 treated biofilm of *S. aureus* MRSA 100.

of the biofilm metabolic activity could be seen for both C1- and C2-treated wells of *S. aureus* MRSA 100 and *S. aureus* MTCC 96 biofilm suggesting that Zn starvation may be an additional phenomenon along with membrane damage induced by the amphiphiles for manifestation of biofilm inhibitory effects (Figure 5.7, Appendix Figure A5.11). However, the biofilm revival effect, in presence of excess Zn was found to be more profound in C2 treated biofilm as compared to C1 treated ones for both the target bacterial strains. (Figure 5.7, Appendix Figure A5.11). This may be attributed to the fact that at high C1 concentrations, copious and irreversible membrane damage might have been already inflicted to a large number of bacterial cells, consequently the cells were killed and the biofilm revival was poor. It is also to be noted that whereas C1 and C2 alone at 40 µM could significantly prevent biofilm formation, on addition of both 50 µM and 100 µM of Zn, the growth of both the *S. aureus* biofilms was observed to be completely regenerated (Figure 5.7, Appendix Figure A5.11). Hence, zinc supplementation experiments validated the pivotal role of zinc in *S. aureus* biofilm formation and highlighted effectively that the amphiphiles could cause zinc deprivation and inhibit staphylococcal biofilm.

5.3.6. Impact of Amphiphile on the Expression of Metallophore Gene in MRSA

Bacterial pathogens are known to produce metallophores to resist metal starvation such as the zincophore staphylopine (stp) produced by *S. aureus* (Grim *et al.*, 2017; Ghssein *et al.*, 2016). Using Zn as a model metal, it was envisaged that C1-imposed Zn starvation may influence the expression levels of the genes *cntL* and *cntA* involved in stp synthesis and Zn transport, respectively (Grim *et al.*, 2017; Capdevila *et al*., 2016). In BHI medium, wherein the Zn concentration is 4.8 µM (Geoghegan *et al*., 2010) there was an 8.8-, 9.3- and nearly 36-fold increase in the expression of *cntL* gene (Figure 5.8), in presence of 5.0 µM, 20 µM and 40 µM C1, respectively. Upregulation of *cntL* in MRSA is presumably to resist C1-imposed Zn starvation by enhancing the levels of stp. In zinc-replete BHI medium (100 µM Zn), on treatment with 5.0 µM C1, excess Zn could perhaps overcome C1-mediated Zn starvation resulting in downregulation of *cntL* (0.6-fold). With increasing C1 concentrations (20 µM and 40 µM), levels of *cntL* expression increased to 2-fold and 13-fold, respectively, due to C1-imposed zinc sequestration although the levels were lower than the corresponding *cntL* expression levels in BHI medium alone (Figure 5.8A). While *cntL* expression increased gradually with C1 concentration, *cntA* gene expression levels were observed to decrease and were

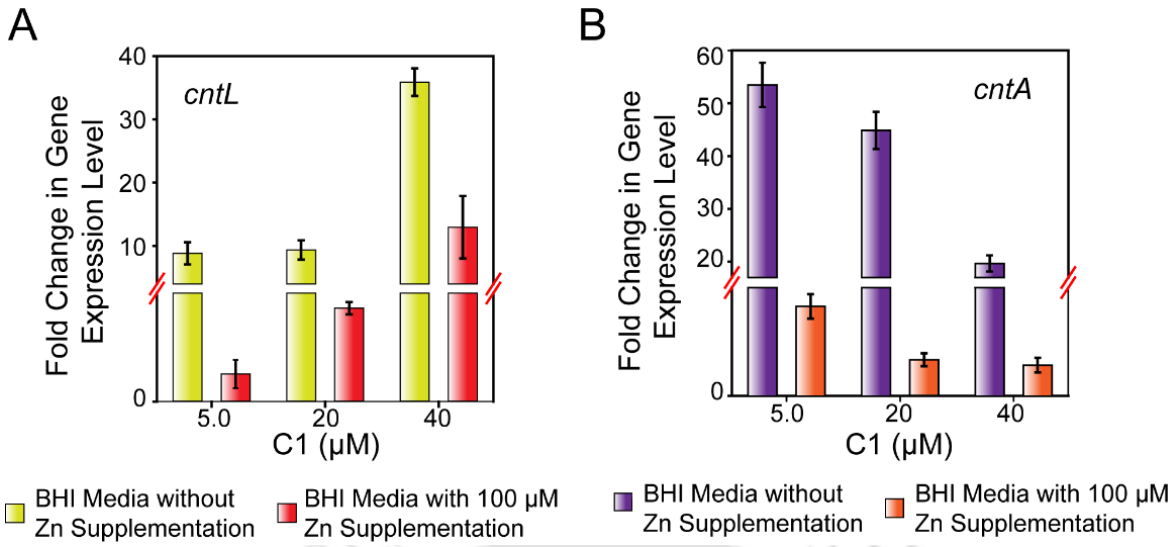

Figure 5.8. Quantitative real-time PCR analysis to determine the fold change in the expression levels of (A) *cntL* and (B) *cntA* genes in *S. aureus* MRSA 100 cells treated with varying concentrations of C1 in BHI medium.

found to be 53.5-, 44.8- and 19.6-fold, in presence of 5.0 µM, 20 µM and 40 µM C1, respectively, in media alone (Figure 5.8B). At the lowest concentration of C1, Zn starvation effect is low as the amount of Zn available to form stp-Zn complex for transport into the cell is adequate. Hence the expression of *cntA* gene involved in the transport of stp-Zn complex is high. However, on increasing the concentration of C1, Zn starvation increases, the quantum of stp-Zn complex formation decreases, leading to a decrease in the expression of its transporter *cntA* (Figure 5.8B). In zinc-replete BHI medium (100 µM Zn), on treatment with 5.0 µM C1, downregulation of *cntL* expression lead to low levels of stp and stp-Zn complex formation even though excess Zn was present. This resulted in a lower level of *cntA* expression (2.5-fold) as compared to the expression in media alone (53.5-fold) (Figure 5.8B). On increasing the concentration of C1, although *cntL* gene expression levels increased, the levels of stp was perhaps not able to counter Zn sequestration brought about by high levels of C1. Collectively, the observed growth suppression (Figure 5.5A-B, Appendix, Figure A5.7) in tandem with gene expression studies (Figure 5.8) substantiates that Zn starvation is indeed implicated in the antibacterial activity of the amphiphile C1.

5.3.7. Binding of C1- and C2-Metal Complexes with Lipoteichoic Acid (LTA) and Bacterial Cells

In order to acquire a mechanistic insight, ITC studies were carried out to decipher the binding affinity of C1 or C2 and their respective metal complexes towards the staphylococcal cell wall ligand LTA. ITC analysis indicated favorable binding of C1 and C2 to staphylococcal LTA, with an association constant (K_a) of 4.29 x 10^5 M^{-1} and 1.32 x 10^6 M^{-1}, respectively (Figure 5.9A-5.9B, Table 5.4). Facile binding of C1 and C2 to staphylococcal LTA may promote strong anchoring and subsequent membrane insertion of the amphiphile as evident in their potent membrane-directed activity (Figure 5.6B, Appendix Figure A5.9). Apart from hydrogen bond formation between the amphiphile head groups and the phosphoryl group of LTA, hydrophobic interaction is also likely to participate in amphiphile-LTA binding. Hence, based on its greater hydrophobicity as compared to C1, it is anticipated that C2 will bind LTA more strongly. However, stronger binding of C2 to LTA as against C1 does not necessarily translate into higher bactericidal activity. It may be mentioned that the binding affinity of Zn for LTA was less than both C1 and C2 (Appendix, Figure A5.12, Table 5.4). The K_a values for binding of preformed zinc complexes of C1 and C2 with LTA were 1.93 x 10^5 M^{-1} and 3.01 x 10^5 M^{-1}, respectively (Figure 5.9B, Table 5.4, Appendix Figure A5.11C) which indicated that the amphiphile-zinc complexes could also bind to bacterial LTA, albeit with inferior affinity as compared to the amphiphiles (Table 5.4). Since the head group of the amphiphiles are involved in coordination, it can be construed that following metal complexation, the probability of hydrogen bond formation between the head group of the amphiphiles and

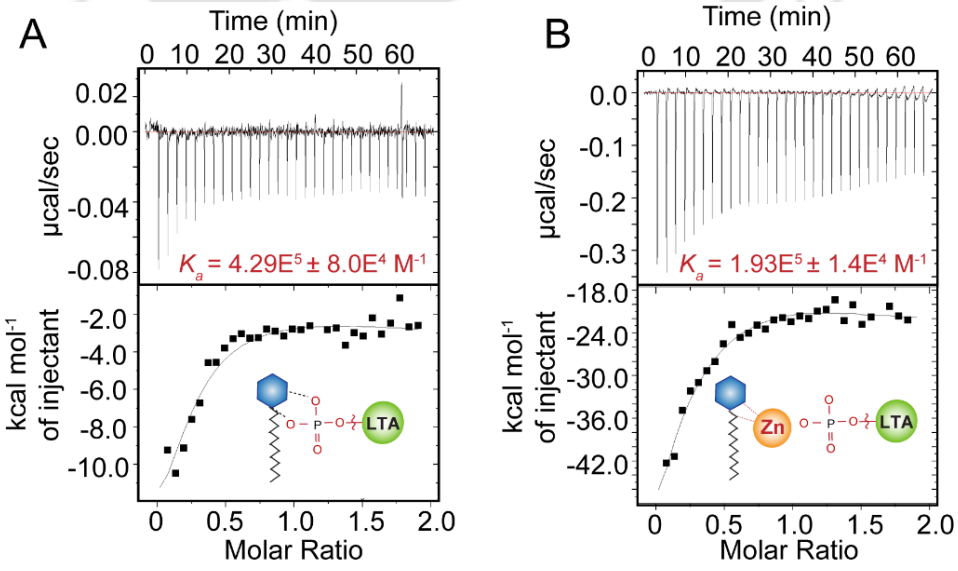

Figure 5.9. (A) ITC analysis of (A) C1 and (B) C1-Zn complex with staphylococcal LTA.

Table 5.4. Determination of association constant (K_a) from ITC-based binding studies.

Sl. No.	Interacting Species	K_a
1.	LTA 5.0 µM - C1 50 µM	$4.29 \times 10^5\ M^{-1} \pm 8.0\ E^4\ M^{-1}$
2.	LTA 5.0 µM - C1: Zn 50:250 µM	$1.93 \times 10^5\ M^{-1} \pm 1.4\ E^4\ M^{-1}$
3.	C1 5.0 µM - Zn 50 µM	$3.38 \times 10^4\ M^{-1} \pm 5.6\ E^4\ M^{-1}$
4.	LTA 5.0 µM - C2 50 µM	$1.32 \times 10^6\ M^{-1} \pm 5.3\ E^4\ M^{-1}$
5.	LTA 5.0 µM – C2: Zn 50:250 µM	$3.01 \times 10^5\ M^{-1} \pm 6.5\ E^4\ M^{-1}$
6.	C2 5.0 µM - Zn 50 µM	$1.02 \times 10^5\ M^{-1} \pm 1.5\ E^3\ M^{-1}$

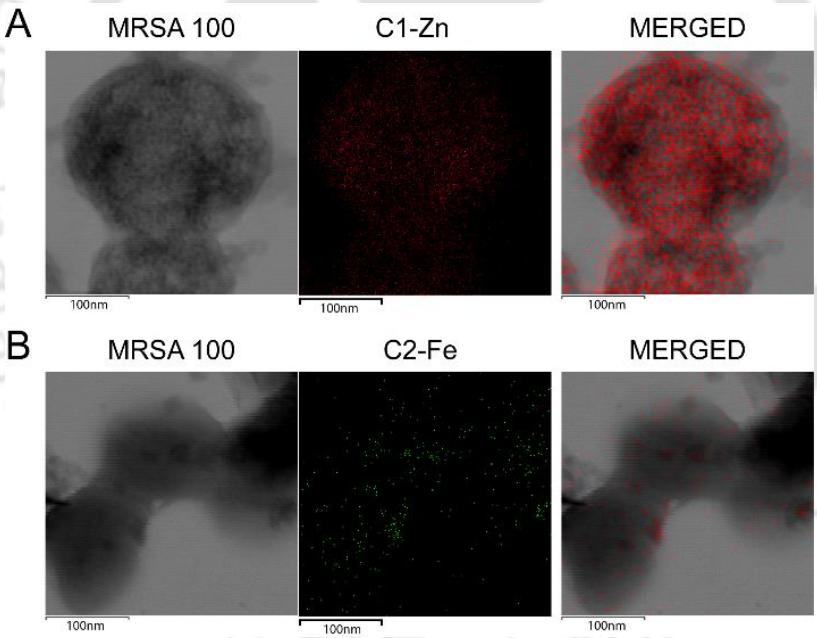

Figure 5.10. FETEM-based mapping analysis indicating the presence of cell associated (A) C1-Zn complex and (B) C2-Fe complex.

LTA is reduced, which may in turn reduce the strength of binding between amphiphile-metal complex and LTA in contrast to amphiphile-LTA binding. However, even moderate binding of amphiphile zinc complex to bacterial LTA may assist in their tethering onto the cell surface. FETEM-based mapping analysis indeed substantiated the evidence for binding of the amphiphile-metal complexes onto the cell surface of MRSA (Figure 5.10, Appendix, Figure A5.13).

5.4. Significant Findings

The key findings of the present study are as follows:

1. The amphiphiles C1 and C2 highlighted in the current study are prototype antibacterials, whose chemistry not only enabled binding to bacterial cell wall ligand LTA through supramolecular interaction, but also facilitated membrane disruption at very low concentrations as well as trigger a metal starvation response in the target pathogen MRSA.

2. Although membrane-targeting synthetic antibacterials are known, the added ability of the amphiphiles C1 and C2 to bind metals augers well. The amphiphiles could significantly hinder the growth of MRSA at very low concentrations, unlike the amphiphile-metal complex, highlighting the relevance of metal starvation by amphiphiles in the growth inhibition of the pathogen.

3. Gene expression studies corroborated that the amphiphile C1 could trigger a zinc starvation response in MRSA.

Synthetic chemistry constitutes a vital platform for drug discovery against antibiotic-resistant pathogenic bacteria. In this context, the amphiphiles C1 and C2, which display a multifaceted mode of action are promising scaffolds since their design rationale not only expands the activity profile of the amphiphiles unlike conventional antibiotics, but also targets a profound pathogen physiology through metal starvation. Given that metals such as zinc is known to have a critical footprint in the growth and biofilm formation by MRSA, the subsequent chapter illustrates the potential of the amphiphile C1 in hindering MRSA biofilm formation in models, which can mimic clinical problems such as device- and extracellular matrix-associated biofilm infection and ascertains the *in vivo* toxicity and the potential of the amphiphile C1 as a topical wound healing agent in a mice model.

Chapter 6

Assessment of Antibiofilm Efficacy, *In Vivo* Toxicity and Wound Site Application Potential of Synthetic Amphiphiles

This chapter illustrates the potential of the synthetic amphiphiles in inhibition of MRSA biofilm grown in models that mimic the in vivo extracellular matrix (ECM) environment and in an orthopedic implant. The study also reports the acute toxicity and wound healing application potential of C1 in a BALB/c mice model.

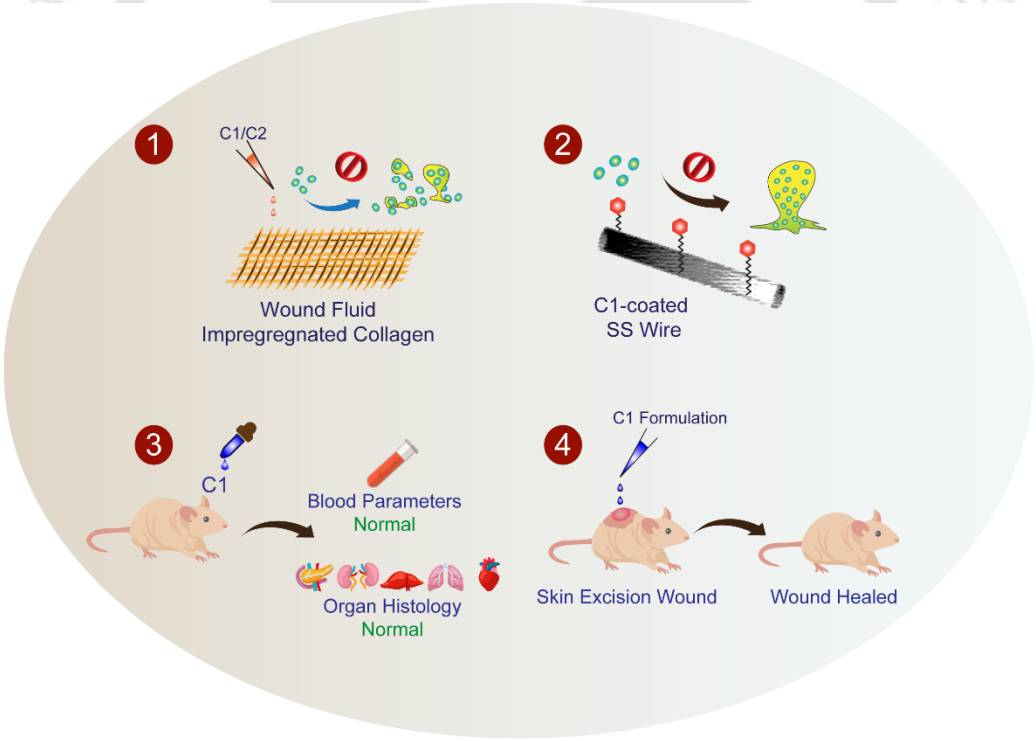

1 MRSA Biofilm Inhibition on Collagen Matrix 2 MRSA Biofilm Inhibition on Orthopaedic SS Wire

3 Acute Toxicity Studies on BALB/c Mice 4 Skin Excision Wound Healing by C1

ABSTRACT

This study determines the efficacy of the synthetic amphiphiles in inhibiting MRSA biofilm in models mimicking the *in vivo* milieu and reports the *in vivo* acute toxicity and the potential of C1 in wound healing application. C1 and C2 rendered a dose-dependent inhibition of *S. aureus* MRSA 100 biofilm formation on collagen-coated wells, wherein the $MBIC_{50}$ of C1 and C2 were 60 µM and 640 µM, respectively. Collagen-impregnated C1 and C2 could also hinder MRSA biofilm formation and decrease the number of non-adherent cells. Following treatment with C1 and C2, FESEM studies revealed considerable cellular damage in MRSA cells embedded in a 3D collagen matrix saturated with simulated wound fluid, indicating that the amphiphiles hold potential as antibacterials to mitigate wound site infections by MRSA. Interestingly, C1-coated orthopedic S. S. wire could prevent MRSA biofilm adhesion in a dose-dependent manner and could also decrease the metabolic activity of the residual biofilm in the vicinity. Further, the eluates from the C1-coated wires were non-toxic to cultured HEK 293 cells, highlighting the therapeutic potential of C1 as an implant-associated antibacterial coating. Quantitative real-time PCR analysis indicated that the expression of the adhesin *fnbA* was essentially low in MRSA biofilm and was observed to be downregulated in non-adherent MRSA cells on treatment with C1, indicating that C1 could hinder both cell-cell adhesion and transition of MRSA planktonic cells to biofilm. Further, the δ-toxin (*hld)* gene expression in the biofilm cells increased with the dose of C1 (10 µM to 20 µM), which perhaps accounted for inhibition of biofilm adhesion and high biofilm to planktonic cell transition. With regard to acute toxicity, a sighting study conducted on BALB/c mice with oral administration of 300 mg and 1000 mg of C1, per kg body weight of the animal indicated that C1 was essentially non-toxic. A main study conducted over a period of 8 days on multiple female BALB/c mice with oral administration of 1000 mg/kg of C1, revealed a consistent body weight, stable hematological parameters and normal histopathological features of vital organs in the animals. Interestingly, topical application of C1 (50 mg/kg and 100 mg/kg) on a skin excision wound model in female BALB/c mice over a period of 14 days rendered almost total wound closure, a higher reduction in wound area, superior fibrous tissue proliferation and tissue reorganization, and higher collagen content in the skin as compared to the vehicle, disease and positive control group, thereby indicating that C1 holds considerable potential as a topical skin wound healing agent.

6.1. Introduction

Staphylococcus aureus is a human pathogen that is implicated in a gamut of clinical infections such as bacteremia and infective endocarditis, osteoarticular, skin and soft tissue, pulmonary and device-related infections (Archer, 1998; Calfee, 2012; Hidron *et al.*, 2008; Chambers and DeLeo, 2008; Tong *et al.*, 2015). In particular, the rise of methicillin-resistant *Staphylococcus aureus* (MRSA) has reached an epidemic proportion and the overall healthcare burden of infections, especially caused by MRSA is increasing globally in both healthcare and community settings (Tong *et al.*, 2015; Lee *et al.*, 2018). Antimicrobial therapy against infections caused by invasive MRSA are often ineffective since MRSA is known to readily form biofilms in both tissues as well as medical implant (Arciola *et al.*, 2018; Stoodley *et al.*, 2011; Oliveira *et al*., 2018; Shah *et al*., 2013; Darouiche, 2004; Ribeiro *et al.*, 2012). The biofilm cells are enveloped by a matrix, which can not only protect the cells from the host immune response but can also act as a penetration barrier to antibiotics (Hall and Mah, 2017; Fuente-Nunez *et al*., 2013; Otto, 2008). Thus, the presence of this recalcitrant adaptation renders rapid progression of the infection process, especially in medical implants and orthopedic devices and increases the rate of treatment failure.

Many forms of staphylococcal infection are associated with the formation of a bacterial biofilm on either native tissue (e.g., cartilage, bone) or implanted biomaterials (e.g., catheters, orthopedic devices). Conceivably, colonization of implantable medical devices by MRSA biofilm can be averted by either modifying the surface of the device so as to reduce attachment of cells, or by tethering bactericidal agents in the device, which can hinder initiation of biofilm formation. Although there are reports that highlight these strategies but the benefits have been rather limited (Rodrigues *et al*., 2011; Hetrick and Schoenfisch, 2006; Aricola *et al.*, 2012). One of the crux of the problem is that during the infection process, the cells can adhere onto human matrix proteins that are known to deposit on the device's surface. For instance, collagen adhesion plays a potential role in the pathogenesis induced by *S. aureus* (Kouidhi et al., 2010) and hence tissues such as bone, cartilage and skin, which are rich in collagen are liable to *S. aureus* infections. A bridging matrix protein molecule such as collagen can thus rapidly enhance the initial attachment of MRSA cells, a process which is critical to subsequent biofilm formation and exacerbate the therapeutic challenge. Hence, there is a need to discover lead compounds that can deter MRSA biofilm formation on collagen and thereby curb device-related infections. In this context, antibiotics have been entrapped in collagen, albumin,

and gelatin sealed grafts to enhance their antibacterial activity (Zilberman and Elsner, 2008).

A large proportion of hospital-acquired infections are caused by microbial adhesion and biofilm formation on medical devices, consequently leading to tissue destruction, systemic spread of the pathogen and malfunctioning of the device, which can result grave illness and fatality (Hall-Stoodley *et al.*, 2004; Bryers, 2008; Darouiche, 2001). The implant colonization may involve deposition of host macromolecules like collagen and fibronectin onto the material of the implant and the subsequent infection is recalcitrant to bactericidal agents as the pathogen is enveloped in a slime enclosed protective barrier (Costerton *et al.*, 1999; Habash and Reid, 1999). In order to prevent the infection from spreading, surgical removal of the device may be the only option. As an alternative, physiochemical modification of the biomaterial surface, device coatings, antibiotic-loaded cements used in orthopedic applications infusing antibacterials in polymeric prosthetics and the deployment of electric fields to modulate antibiotic therapy have been proposed (Darouiche, 2001; Hall-Stoodley *et al.*, 2004; Veenstra *et al.*, 1999; Zilberman and Elsner, 2008; Hetrick and Schoenfisch, 2006). It is critical that an implant coating should be able to facilitate high release of the antibacterial during the initial period of post-implantation in order to prevent adhesion of pathogenic bacteria at the surgical site. Subsequently, a slow release of the antibacterial is desirable so that bacterial infection can be prevented until proliferation of a fibrous capsule and tissue reintegration is accomplished (Anderson, 2001; Zilberman and Elsner 2008).

In the context of antibacterial drug discovery, it is imperative to establish the *in vivo* efficacy of the candidate molecule. Herein, animal models can be employed to fill the void between *in vitro* drug discovery and clinical trials (Marra, 2014). Animal models not only help in assessing the effects within the complex system of the whole animal, they also help to probe the effects of external environmental factors mimicking a realistic system, such as progression of infection, tissue distribution and availability of effective concentration of a drug for pathogen elimination, which is not possible in the *in vitro* studies, thereby helping to extrapolate these results for human application. Amongst the animal models, rodents are preferred, especially mice owing to their small size, requirement of a lesser dose of the drug, which permits a lower scale of synthesis for initial screening and an overall lower cost of maintenance (Marra, 2014).

S. aureus is known to asymptomatically colonize human skin. In the course of an injury, breakage of the skin may lead to wound infection, which can manifest as abscesses, carbuncles, and also disseminate into the blood stream (Archer 1998; Watkins *et al.*, 2012; Tong *et al.*, 2015; Marra and Yinduo 2014). Infection of a skin wound can delay the wound healing process. Conceivably, bactericidal molecule that can thwart pathogen invasion of the wound area is likely to promote wound healing. Relevant disease models for topical treatment of skin infections have been reported in the literature, wherein the potential of antibiotics and other synthetic compounds have been tested for their wound healing properties (Kugelberg *et al.*, 2005; Simonetti *et al.*, 2017; Murthy *et al.*, 2013).

Based on the aforementioned premise and given the promising activity of C1 against MRSA biofilm, in this chapter the translational potential of the amphiphile C1 is determined. The study reports the potential of C1 in inhibiting MRSA biofilm grown on collagen, simulated wound fluid-infused collagen as well as on an orthopedic stainless-steel wire so as to mimic clinical problems such as extracellular matrix- and device-associated biofilm infection. Further, the investigation also determined the *in vivo* toxicity and the potential of C1 as a topical wound healing agent in a mice model.

6.2. Materials and Methods

6.2.1. Growth Media and Chemicals

Brain-Heart Infusion (BHI) broth, peptone, sodium chloride, crystal violet (CV) dye, hematoxylin and eosin stains were obtained from HiMedia, Mumbai, India. Dimethyl sulfoxide (DMSO), chloroform, acetic acid, isopropanol, sodium acetate, citric acid, sodium hydroxide pellets, methanol and ethanol were procured from Merck, India., Skim milk was obtained from Nestle. Congo red (CR), 3-(4,5-dimethyl-2-thiazolyl)-2,5-diphenyl-2H-tetrazolium bromide (MTT), collagen from human placenta (Type IV), hydroxyproline, p-DMAB, chloramine T, Dulbecco's Modified Eagle Medium (DMEM) and trypsin–EDTA were procured from Sigma-Aldrich (USA). Orthopaedic S. S. wire was procured from Kaushik Orthopaedic Corp., India. Gibco™ Fetal Bovine Serum, TRIzol™ Max™ Bacterial RNA Isolation Kit and SYBR 1- STEP qRT-PCR KIT Invitrogen™ were procured from Thermo Fisher Scientific. Trichrome staining kit (Connective Tissue Stain) was procured from Abcam, USA.

6.2.2. Bacterial Strain and Growth Conditions

S. aureus MRSA 100 was used as the target strain in this investigation. The strain was grown under conditions as described previously in section 2.2.4. of Chapter 2 unless stated otherwise.

6.2.3. Collagen Coating in Microtitre Plate Wells

A 1.0 mg/mL stock solution of collagen (Type IV) was made in filter-sterilized PBS (pH 5.5) and stored in -20^{o}C prior to the experiments. F16 Maxisorp Loose NUNC-Immuno Module Strips of 16 well (2 x 8) were filled with 200 µL of collagen solution (50 µg/mL) and incubated overnight at 4^{o}C under static conditions for uniform coating. After the incubation period, the remaining collagen solution was aspirated and the wells were washed gently with sterile PBS to remove any unbound collagen. Blocking of the wells were done by adding 200 µL of 0.1% w/v skim milk made in sterile water and incubated for 30 min at 4^{o}C under static conditions. This was followed by aspiration and a PBS wash to remove any unbound species. The plates were then kept for drying for 24 h in sterile conditions to obtain the collagen-coated wells. A schematic of the protocol used for the preparation of collagen coating in microtitre plate wells is shown in Scheme 6.1.

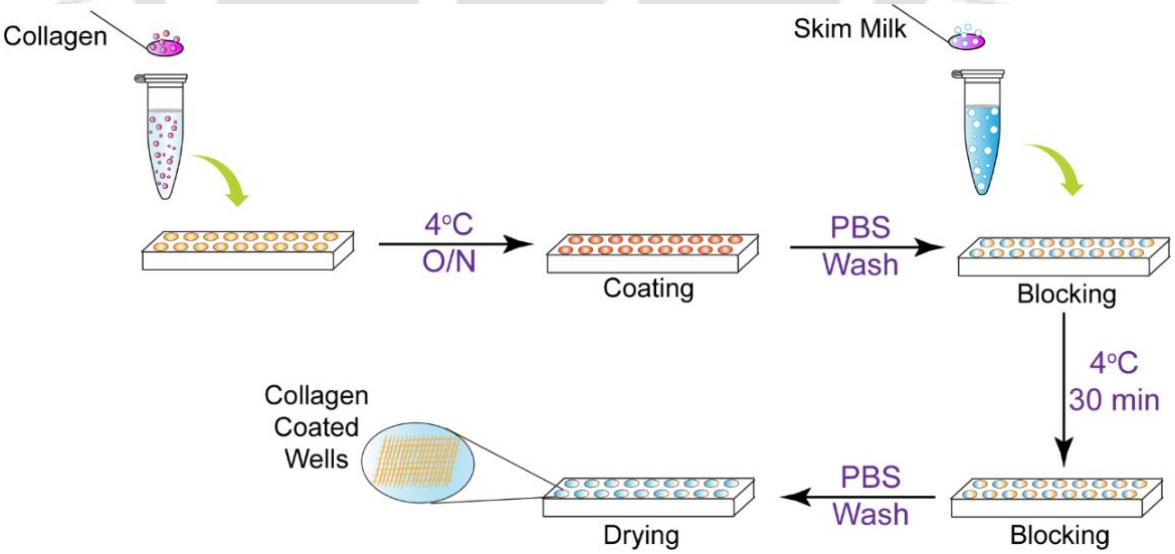

Scheme 6.1. Schematic of the protocol used for the preparation of collagen coating in microtitre plate wells.

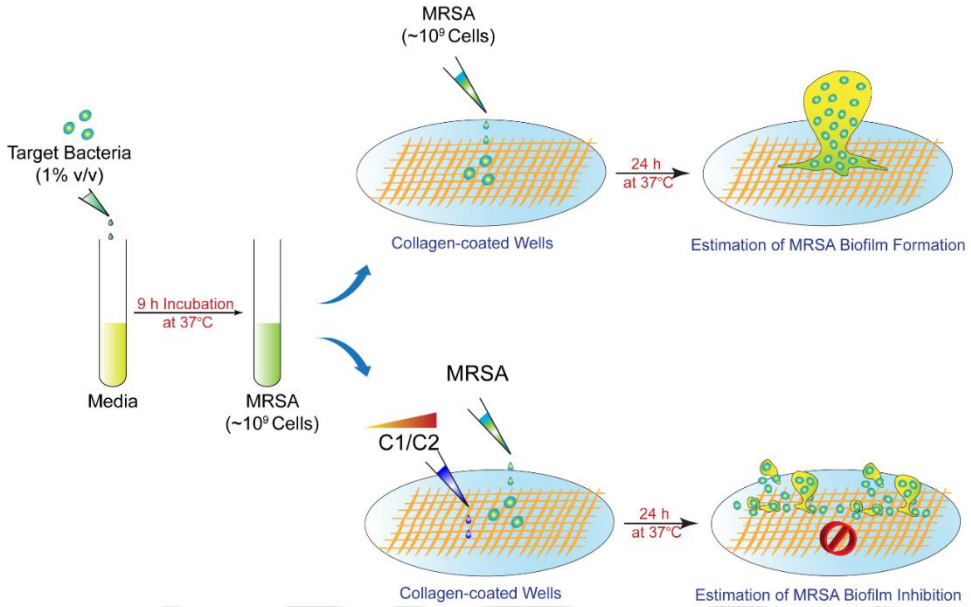

Scheme 6.2. Schematic showing the protocol for estimating MRSA biofilm inhibition on collagen coated wells.

6.2.4. Antibiofilm Activity of C1 and C2 in Collagen Coated Wells

The target bacteria *S. aureus* MRSA 100 was inoculated at 1% level in BHI medium and propagated overnight at 37°C and 180 rpm. In the wells of a microtitre plate previously coated with collagen, the bacteria was inoculated (approximately 10^6 CFU/mL) in separate sets in BHI media containing 0.25 % w/v glucose and varying concentrations of C1 (5.0 µM, 10 µM, 20 µM, 40 µM, 80 µM, 160 µM, 320 µM) or C2 (10 µM, 20 µM, 40 µM, 80 µM, 160 µM, 320 µM and 640 µM) and incubated overnight at 37°C in a static humid chamber. On the following day, the spent media containing the non-adherent bacterial cells were transferred into a fresh 96 well plate and the absorbance was measured at 600 nm to ascertain the effect of the amphiphiles. The adherent biofilm cells were analyzed by MTT assay to study the metabolic activity and as well as crystal violet assay to ascertain the biofilm biomass adhering onto collagen using a standard protocol as mentioned previously in chapter 2 section 2.2.11.1. Control samples having only collagen coating without biofilm were also subjected to MTT and crystal violet assay to normalize the measurements.

6.2.5. MRSA Biofilm Inhibition in Amphiphile-Impregnated Collagen

From a 1.0 mg/mL stock solution of collagen (Type IV), a sub-stock (50 µg/mL) was made. Varying volumes of C1 and C2 from a 50 mM stock in DMSO were added to the

collagen sub-stock solution to obtain the effective concentrations of 5.0 µM, 10 µM, 20 µM, 40 µM, 80 µM, 160 µM, 320 µM and 640 µM in separate sets. 200 µL of these collagen-amphiphile mixtures were then added in multiple sets to different wells of F16 Maxisorp Loose NUNC-Immuno Module Strips and incubated overnight at 4°C under static conditions for uniform coating. The following day, the spent solution containing the unbound collagen-amphiphile mixture was aspirated and the wells were washed gently with sterile PBS to remove any unbound species. Blocking of the wells was done by adding 200 µL of 0.1% w/v skim milk made in sterile water and incubating for 30 min at 4°C under static conditions followed by aspiration, PBS wash and drying for 24 h in sterile conditions as shown in Scheme 6.3. On the coated wells, *S. aureus* MRSA 100 cells (approximately 10^6 CFU/mL) were inoculated in BHI media having 0.25 % w/v glucose and incubated at 37°C in a static humid chamber. After an overnight incubation, the absorbance of the non-adherent bacterial cells was measured as mentioned previously and the metabolic activity of the biofilm adhering onto the C1 and C2-impregnated collagen was analyzed by MTT assay and the biofilm biomass was estimated by crystal violet assay using a standard protocol as mentioned previously in

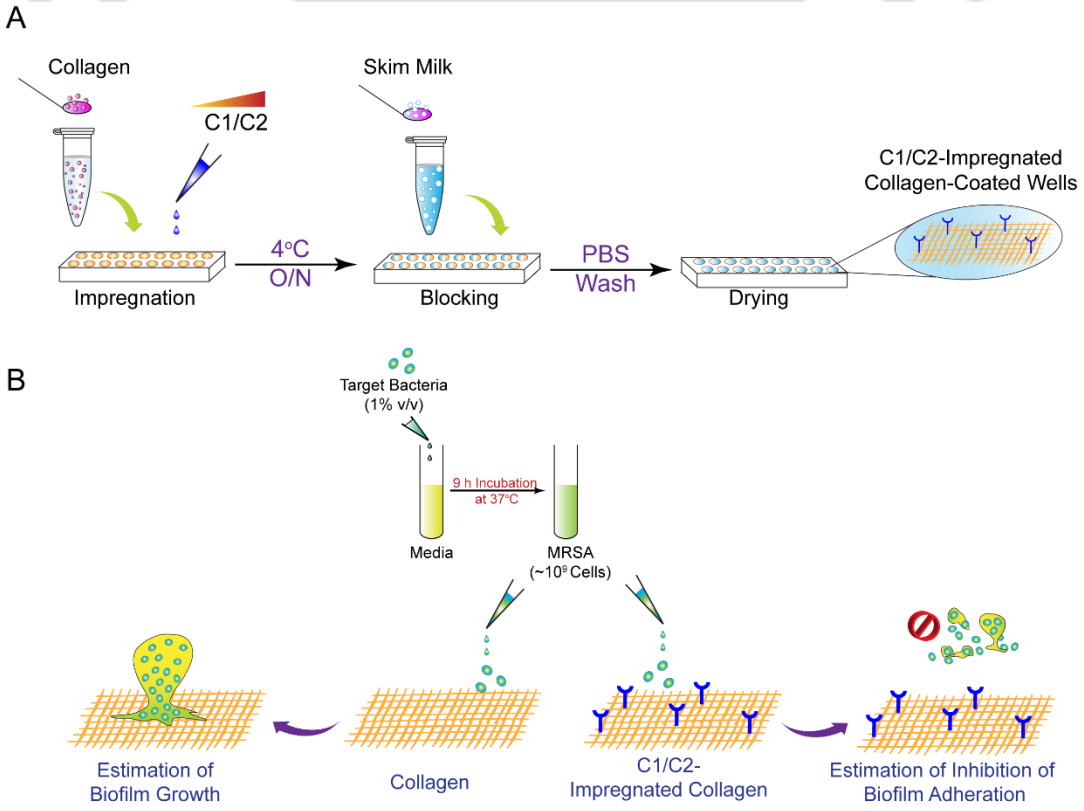

Scheme 6.3. Schematic showing the protocol for ascertained biofilm growth inhibition in amphiphile-impregnated collagen.

chapter 2 section 2.2.11. Control samples having only C1 and C2-impregnated collagen without biofilm were also subjected to MTT and crystal violet assay to normalize the measurements.

6.2.6. Effect of Amphiphiles on Biofilm Grown in Simulated Wound Fluid (SWF)-Infused 3D Collagen Matrix

Initially, a peptone water solution was constituted by preparing 0.1% peptone w/v in 0.5% saline pH 7.4. The simulated wound fluid was then prepared by mixing fetal bovine serum (FBS) and peptone water in 50% v/v proportion as indicated in Scheme 6.4A. Subsequently, to make the 3D collagen matrices (10 mL), the following reagents were mixed sequentially in the order mentioned below:

1. 1.0 mL of 0.1 % v/v acetic acid was taken in a tube.
2. 2.0 mL collagen from 10 mg/mL stock solution of collagen Type IV made in sterile PBS was added to the acetic acid solution.
3. The mixture was incubated in ice and 6.0 mL of cold SWF was added.
4. Finally, 1.0 mL of 0.1 M NaOH was added to the above solution.

Following sequential addition, the solution was mixed thoroughly in ice cold conditions and 200 µL of this collagen solution was added to 96 well plates and incubated at 37^{o}C for 1 h for complete polymerization and 3D matrix formation. This was followed by overnight incubation at 4^{o}C (Price *et al*., 2016). A schematic for the preparation of SWF-infused 3D collagen matrix is indicated in Scheme 6.4B. In a parallel experiment, the target bacteria *S. aureus* MRSA 100 was inoculated at 1% level in SWF: BHI medium (1:1) and propagated overnight at 37^{o}C and 180 rpm. The following day, the collagen 3D matrix containing wells were washed with sterile PBS and dried in a laminar hood. A 100 µL aliquot of the overnight grown MRSA culture, diluted to 10^6 cells in SWF: BHI medium (1:1) was added to each well of the 96 well plate in combination with varying concentrations of C1 and C2 (10 µM, 20 µM, 40 µM, 80 µM, 160 µM and 320 µM) in separate sets and incubated at 37^{o}C under static conditions for 24 h. As a control, 100 µL of SWF: BHI media (1:1) without bacteria was added to separate wells and incubated under same conditions. After 24 h incubation, the spent SWF media containing the non-adherent biofilm cells was transferred to a new plate and the absorbance at 600 nm was measured, while the adherent biofilm growth on the 3D collagen matrix was visualized by FESEM analysis as represented in Scheme 6.4C.

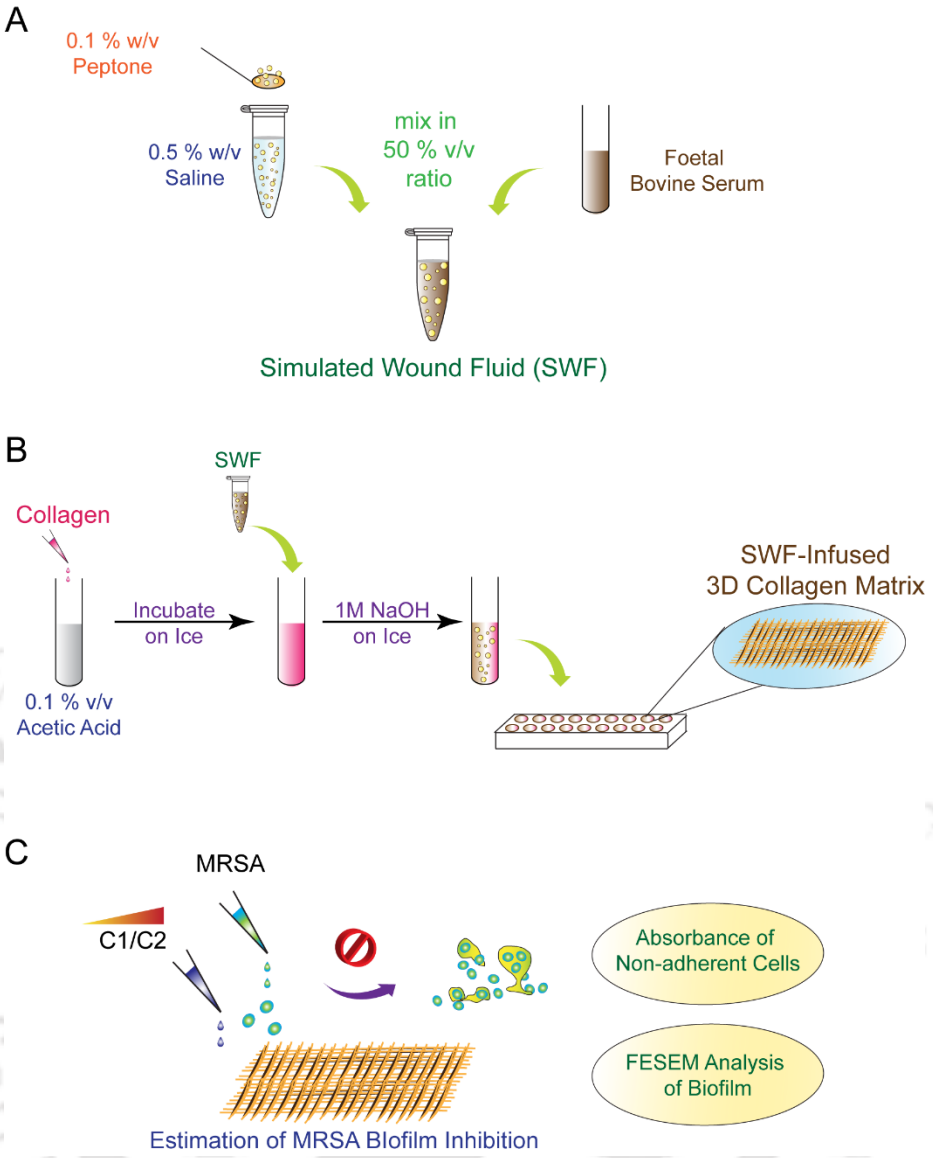

Scheme 6.4. Schematic representation of the protocol for (A) preparation of simulated wound fluid, (B) preparation of SWF-infused 3D collagen matrix and (C) estimation of biofilm growth inhibition by C1 and C2 in SWF-infused 3D collagen matrix.

6.2.7. Coating of Orthopaedic S.S. Wire by C1

Orthopedic stainless-steel wire (S. S. wire) was cut into 1.5 cm pieces. For coating, a 5.0 % w/w solution of C1 was made in absolute ethanol (39.5 mg C1 in 1.0 mL ethanol) and serially diluted to achieve varying coating concentrations (2.5% w/w, 1.25% w/w, 0.625% w/w and 0.3125% w/w) of C1 in ethanol. The absorbance of these stock solutions was measured to ascertain the initial coating concentration and a calibration plot was generated. The 1.5 cm S. S. wires were surface-sterilized and subsequently dipped in the coating solutions and incubated overnight at 37^{o}C and 180 rpm to achieve uniform coating. Following incubation, the wire pieces were removed and dried in sterile

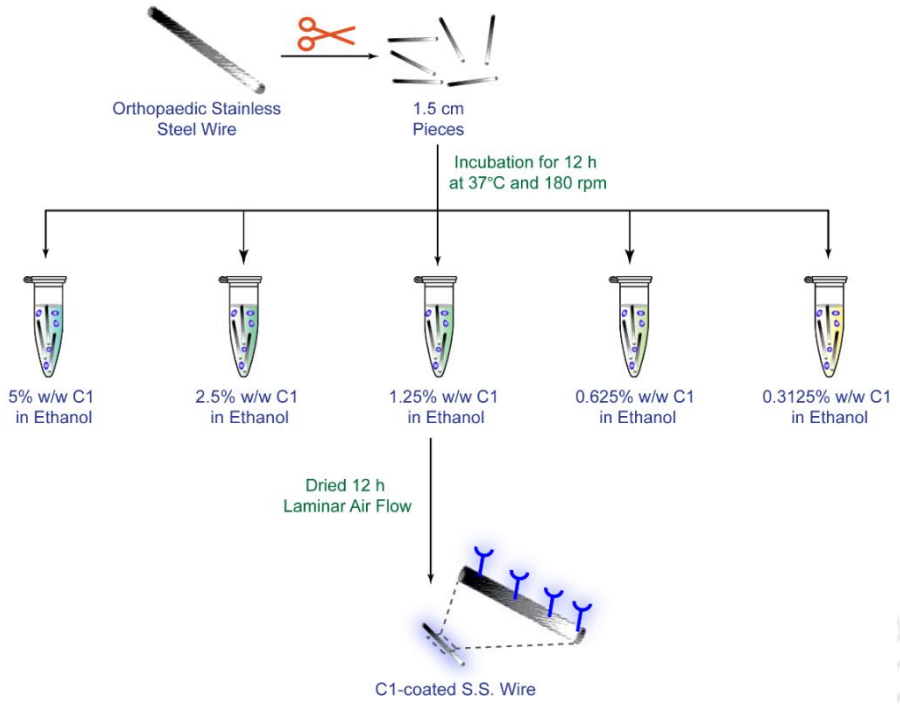

Scheme 6.5. Schematic showing the protocol used to generate C1-coated orthopedic S. S. wire.

conditions in a laminar hood to obtained C1-coated S. S. wire as shown in Scheme 6.5. The absorbance of all the coating solutions after removal of the wires was measured again and the residual C1 remaining in the ethanol solution was determined using the previously generated calibration plot. The difference in the amount of initial coating concentration of C1 and the residual concentration of C1 was used to determine the amount of the amphiphile coated onto the wires. The C1 coated-S. S. wire was also subjected to FESEM analysis. The coating efficiency was calculated as follows:

$$Coating\ Efficiency = \frac{Bound\ C1\ onto\ S.S.Wire}{Total\ C1\ in\ Solution\ Used\ for\ Coating}\ x\ 100$$

6.2.8. Antibiofilm Activity and Cytotoxic Studies of C1-coated Orthopedic S. S. Wire

S. aureus MRSA 100 was inoculated at 1% level in BHI medium and propagated overnight at 37°C and 180 rpm. The following day, 12 well plates were inoculated with approximately 10^6 CFU/mL target bacteria in BHI media having 0.25% glucose and the 1.5 cm pieces of C1-coated Orthopedic S.S. wires having varying coating percentages (5.0 % w/w, 2.5% w/w, 1.25% w/w, 0.625% w/w and 0.3125% w/w) were introduced into the wells in multiplicates of separate sets. The plate was then incubated at 37°C

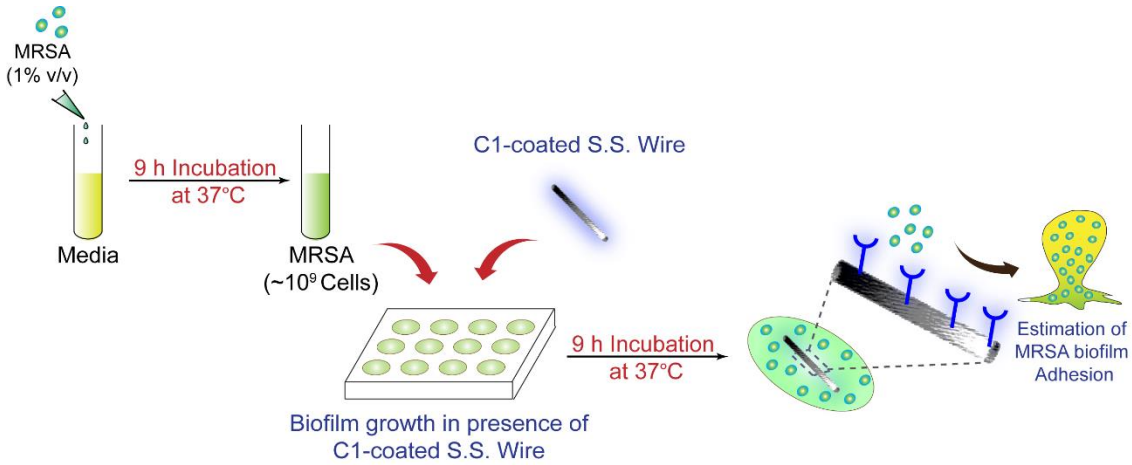

Scheme 6.6. Cartoon illustrating the protocol used to study inhibition of biofilm formation on C1-coated S.S. wire.

under static condition for 24 h to allow biofilm growth, following which the spent media was gently aspirated and the wires containing the grown biofilm were removed and kept for drying under sterile laminar air flow and then visualized under FESEM. Following removal of the wire, the viability of the residual biofilm present in the well was ascertained by a standard MTT assay as mentioned previously in section 2.2.11.1 of Chapter 2 (Scheme 6.6). For ascertaining the cytotoxic potential, the 1.5 cm pieces of C1-coated S.S. wires having varying coating percentages were incubated overnight in separate tubes containing DMEM media at 37°C and 180 rpm for elution of C1 from the wire into the media. These eluates were now added to HEK 293 cells grown to 80% confluency and a standard MTT based assay was performed to ascertain the cell viability in presence of the eluates.

6.2.9. Gene Expression Studies

Target cells of *S. aureus* MRSA 100 (approximately 10^6 CFU/mL) were grown in BHI media incorporated with 0.25% glucose and C1 (10 µM and 20 µM) in separate sets at 37°C and 180 rpm. Following incubation for 48 h, the unbound planktonic cells as well as the bound biofilm cells were harvested, and RNA was isolated from both using TRIzol™ Max™ Bacterial RNA Isolation Kit and the RNA yield was quantified using IMPLEN NanoPhotometer® NP80. Gene specific primers were designed for *16s rRNA*, *fnbA*, and *hld* genes using Primer3 (v. 0.4.0). The sequence of the primers is indicated in Table 6.1.

Table 6.1. Primers used for gene expression studies.

Sl. No.	Target Gene	Oligo Sequence (5' to 3')	Amplicon size
1.	16S rRNA	Forward: GAAAGCCACGGCTAACTACG Reverse: CATTTCACCGCTACACATGG	202 bp
2.	*fnbA*	Forward: ACCAGTACCACCTGCCAAAG Reverse: ACCAATGAAGCAATCAGAAAACACT	369 bp
3.	*hld*	Forward: AAGAATTTTTATCTTAATTAAGGAAGGAGTG Reverse: TTAGTGAATTTGTTCACTGTGTCGA	110 bp

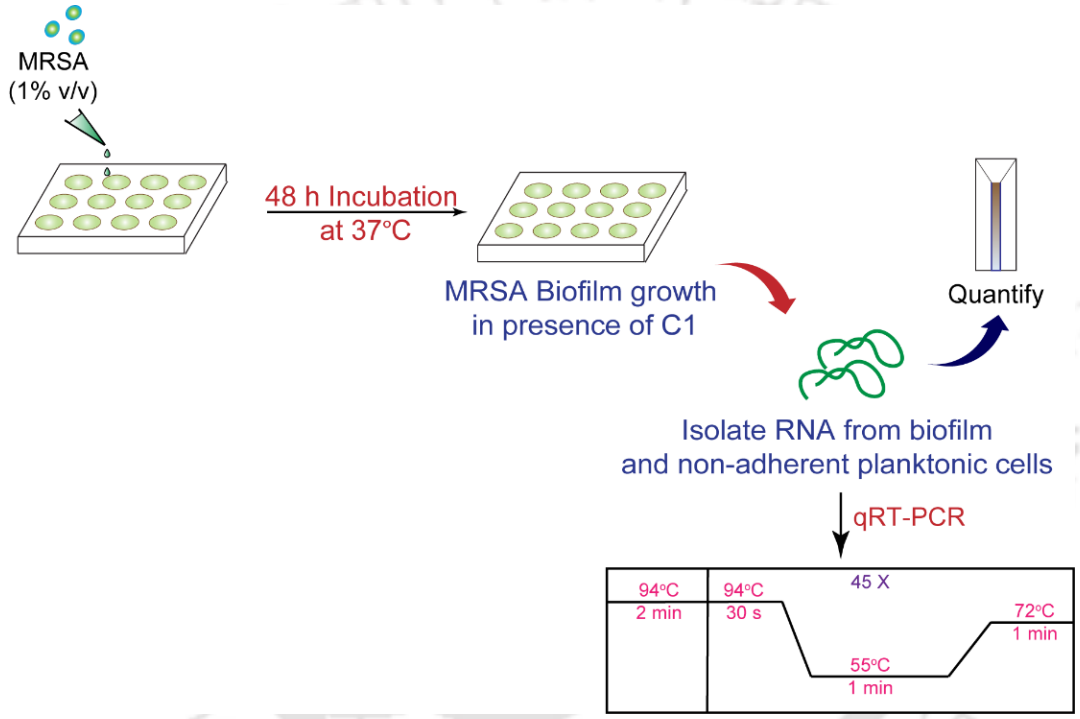

Scheme 6.7. Schematic representation of the protocol used to study gene expression in *S. aureus* MRSA 100 biofilm grown in presence of C1.

A quantitative real time PCR was conducted with 50 ng of RNA from each sample using SYBR 1- STEP qRT-PCR Kit on a 36-Well Rotor, QIAGEN Rotor-Gene Q ® qRT-PCR machine. The PCR conditions were as described in section 5.2.10 of Chapter 5. Analysis of RT-PCR data was done using the LinRegPCR (2014.x) software and the cycle threshold (C_T) values were calculated after baseline correction. The fold change in gene expression values was ascertained by the $\Delta\Delta C_T$ method (Livak and Schmittgen, 2001). A schematic representation of the protocol used for the gene expression study is indicated in Scheme 6.7.

6.2.10. Acute Toxicity Studies of C1 on BALB/c Mice

The acute toxicity studies on BALB/c mice were performed at the National Institute of Pharmaceutical Education and Research (NIPER), Guwahati, India, in accordance with the institutional animal ethics committee and national guidelines (NIPER/PA/19/28). Healthy adult BALB/c mice (5-6 weeks old male and female) weighing around 24-28 g were obtained from National Institute of Nutrition, Hyderabad, India. For the studies, the animals were selected in such a way that the variation in their body weights was maintained below 20%. Each animal was housed in a single cage having a controlled environmental condition (23±2°C temperature, 50±10 % relative humidity, 12 h light and 12 h dark cycle). The animals were fed with standard animal chew and drinking water. To ascertain the *in vivo* toxicity of C1, an initial sighting study and a subsequent main acute toxicity study based on single dosing was performed. A schematic representation of the protocol used in the sighting and main study is shown in Scheme 6.8. The details of these studies are as follows:

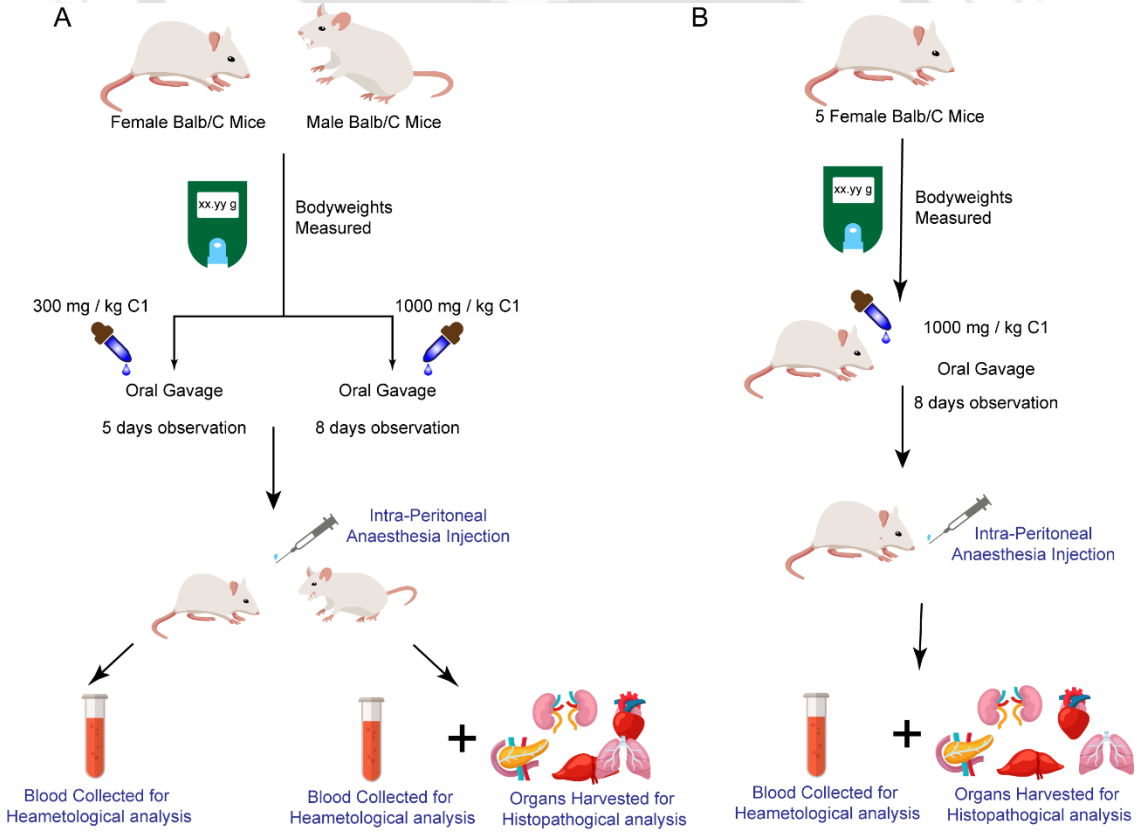

Scheme 6.8. Cartoon illustrating the protocol used for ascertaining the acute toxicity of C1 through (A) sighting study and (B) main study.

6.2.10.1. Sighting Study

For the sighting study, 1 male and 1 female BALB/c mice were initially weighed and found to be 28.35 g and 24.51 g, respectively. According to their bodyweights a dose for amphiphile C1 (300 mg/kg) was formulated wherein a stock solution of C1 was prepared by dissolving 18.75 mg of the amphiphile in 1.0 mL of corn oil and 0.45 mL and 0.40 mL was administered immediately to the male and female animals, respectively, within 30 min using an oral gavage. The mice were kept under observation for 5 Days and the clinical signs of the animals and their bodyweights were monitored on a daily basis. Following this, as per the OECD guidelines, a higher dose of 1000 mg/kg of C1 was formulated by making a stock solution of 57.3 mg/mL C1 in corn oil and 0.48 mL and 0.46 mL was administered to a new male and a new female BALB/c mouse weighing 27.3 g and 26.3 g, respectively. The animals were observed for 7 days and the clinical signs of the animals and their bodyweights were monitored on a daily basis. At the end of treatment period on Day 8, animals were fasted for 4 h, anaesthetized by an intraperitoneal injection containing a mixture of 8:1 v/v ratio of ketamine and xylazine half diluted in PBS and blood was collected by cardiac puncture for both the treated and control animals in vials with anticoagulant (EDTA) for subsequent observation of the hematological parameters using a Blood Analyser (Seimens Advia 2120i, Munich, Germany). Following blood collection, both the animals were euthanized by cervical dislocation and the vital organs like lung, liver, kidney, heart and spleen were immediately excised, trimmed of fat and connective tissue, washed with normal saline and fixed in 10% -buffered formalin solution. Post-fixation, the tissues were dehydrated and embedded in paraffin following a standard procedure (McInnes, 2017). Thin tissues sections of 5 µm thickness were cut on microtome, deparaffinized, rehydrated and stained with hematoxylin and eosin staining solutions by following a standard method (McInnes, 2017). The images of the tissue sections were captured under a microscope (Invitrogen Evos FL Auto 2.0).

6.2.10.2. Main Study

For the main study, 5 female BALB/c mice were taken. All the mice were administered a single oral dose of 1000 mg/kg C1 in corn oil by following the procedure mentioned previously and observed for 7 days to assess the reproducibility of the sighting study and ascertain the maximum tolerated dose (MTD). On the 8th day, body weights were measured followed by blood collection for hematological analysis. After sacrifice, organ

collection was done immediately and fixed in 10 % buffered formalin solution followed by staining with hematoxylin and eosin for histopathological analysis.

6.2.11. Wound Healing Studies of C1 on BALB/c Mice Skin Excision Model

For the skin excision wound healing studies, six groups were made wherein each consisted of 5 female BALB/c mice. All the mice were anaesthetized and shaved on the back and a skin excision wound was inflicted using an 8 mm biopsy punch. The initial body weights were noted, wound diameter was measured followed by photography of the wound area. For making the treatment formulation, C1 was dissolved in petroleum jelly at 60^{o}C to form a homogeneous emulsion. Topical dosing was started from Day 1 itself, immediately after wound excision in all the 6 groups, which consisted of: (1) normal control (shaved animal with no skin punch), (2) vehicle control (skin punched and petroleum jelly applied), (3) disease control (skin punched and with no application), (4) low dose treatment group (skin punched and 50 mg/kg C1 solubilized in petroleum jelly), (5) high dose treatment group (skin punched and 100 mg/kg C1 solubilized in

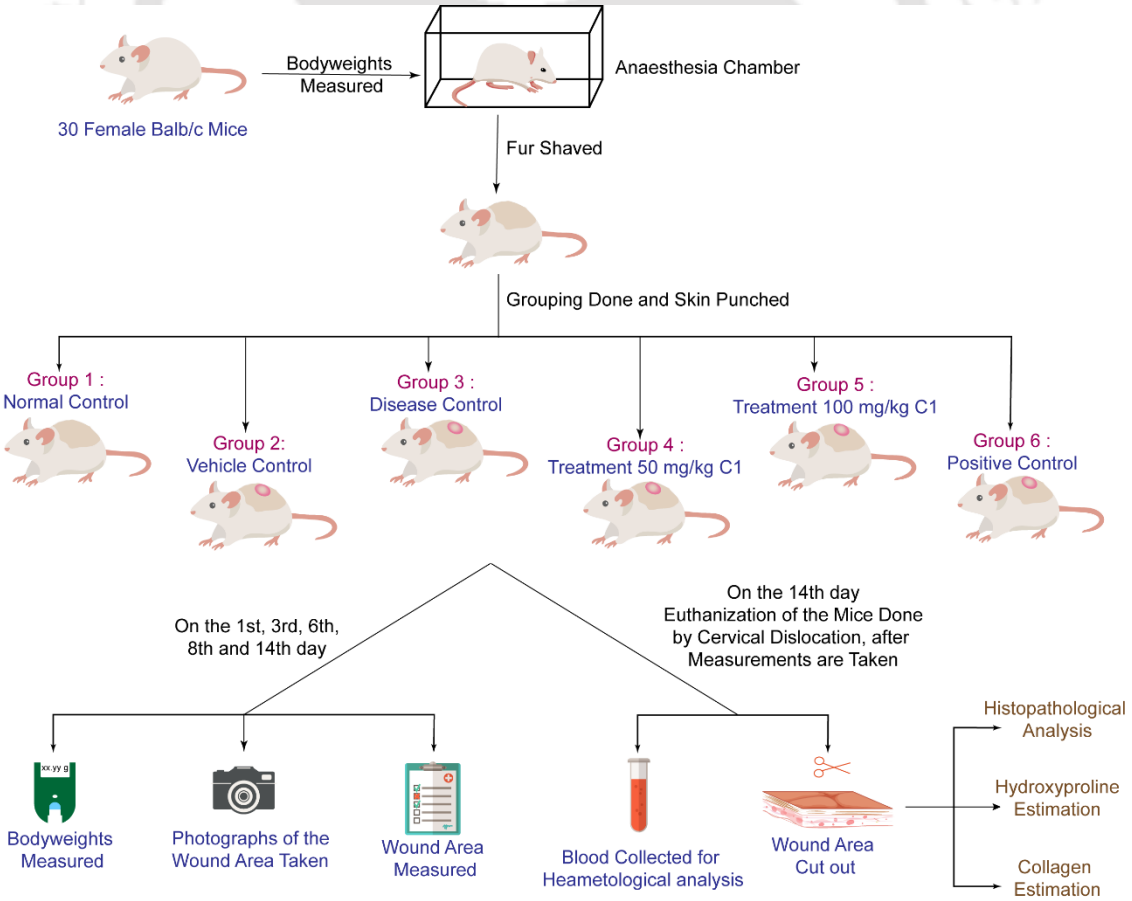

Scheme 6.9. Cartoon illustrating the protocol used for the wound healing study.

petroleum jelly) and (6) positive control (skin punched and 5% w/w Povidone Iodine ointment applied). The treatments were applied to the wound topically every alternate day along with all the controls during the course of the 14-day experiment. Photographs of the wound area was taken and wound diameter along with the body weights were regularly recorded for every 3 - 4 Days. The animals were monitored on the 1st, 3rd, 6th, 8th and 14th day, and the decrease in wound area over the duration of the study was determined. At the experimental end point, on the 14th day, after taking wound area photographs, body weight and wound area diameter measurement, the animals were sacrificed and the blood was collected for analysis of the hematological parameters. The wounded area of the skin was cut out, and split into 4 pieces. The first was kept in ice cold sterile PBS for hydroxyproline estimation and the 2nd and 3rd pieces were stored in phosphate-buffered formalin at room temperature for histopathological analysis and Masson's Trichome staining for collagen content estimation, respectively. The 4th piece was immediately transferred to -80^{o}C as a backup tissue to be used later if required. A cartoon showing the protocol used for the wound healing study is indicated in Scheme 6.9.

6.2.12. Hydroxyproline Estimation in Wound Tissue

On the 14th day, after sacrificing the animals, a piece of skin from the wound area was collected and analyzed for hydroxyproline content. The wound tissue samples were weighed individually, suspended in sterile PBS and homogenized using an Eppendorf tissue lyser (Qiagen, Tissue lyser II) in ice cold conditions (Scheme 6.10A). The lysed samples were stored at -20^{o}C. The details of the hydroxyproline assay is as follows:

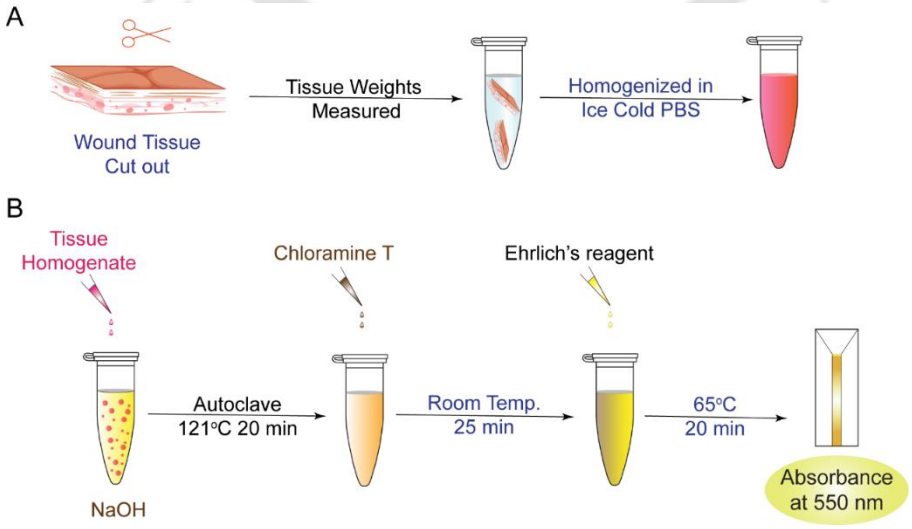

Scheme 6.10. Cartoon illustrating the protocol used for estimation of hydroxyproline.

6.2.12.1. Reagents

The following reagents were prepared for the hydroxyproline assay:

(1) 1.0 mg/mL stock of hydroxyproline made in sterile water

(2) Acetate citrate buffer (pH 6.5): 1.2 g sodium acetate trihydrate, 0.46 g citric acid, 0.12 mL acetic acid and 0.34 g NaOH was weighed in a tube and 8.0 mL of water was added. The pH was adjusted to 6.5 and the volume was made up to 10 mL

(3) Ehrlich's Reagent (1.0 M): 1.5 g p-DMAB was dissolved in a 2:1 mixture of isopropanol and perchloric acid (7.0 mL:3.5 mL).

(4) Chloramine T Reagent (0.056 M): 0.127g of chloramine T was dissolved in 2.0 mL of 50 % v/v isopropanol in water and then the volume was made up to 10 mL using the acetate citrate buffer.

(5) 2.0 N NaOH solution.

6.2.12.2. Standard Curve

For the standard curve, 1.0 mg/mL stock solution of pure hydroxyproline was serially diluted to obtain concentrations of 25 µg/mL - 1.325 µg/mL A 25 µL aliquot from each concentration was mixed with 25 µL of 2.0 N NaOH and 450 µL of chloramine T reagent was added to each vial and kept at room temperature for 25 min. Subsequently, 0.1 mL of Ehrlich's reagent was added and the tubes were incubated at 65^{o}C for 20 min. The absorbance of the solution was then measured at 550 nm and a standard curve of concentration versus absorbance was plotted (Reddy and Enwemeka, 1996). Multiple replicates of each sample were taken for generating the standard curve.

6.2.12.3. Homogenized Samples

For the homogenized samples, 25 µL of each sample was mixed with 25 µL of 2.0 N NaOH and autoclaved at 121^{o}C for 20 min for complete hydrolysis. Following this, chloramine T and Ehrlich's reagent were added to the samples as mentioned for the standard. The absorbance at 550 nm was measured (Scheme 6.10B) and the values were compared with the values in the calibration curve to ascertain the hydroxyproline content of each sample per mg weight of the tissue.

6.2.13. Masson's Trichome Staining for Collagen Content Estimation

The skin tissue sections from wound area of each group of animals was firstly deparaffinized using xylene and then rehydrated using ethanol and water. Bouin's fluid

was preheated to 62ºC in a fume hood and the slides were placed in this fluid for 20 min followed by cooling for 5 min. The slides were then rinsed with distilled water and kept aside. Equal volumes of Wiegert's (A) and Wiegert's (B) solution were mixed to make a working solution of Wiegert's Iron Hematoxylin and the slides were stained in this solution for 3 min followed by a washing step. Subsequently, Biebrich Scarlet / Acid Fuchsin solution was added to the slides and incubated for 8 min, washed and differentiated in Phosphomolybdic/Phosphotungstic acid solution for 8 min. Without rinsing, Aniline Blue solution was applied to the slide and incubated for 5 min, for counter staining of collagen, then rinsed with distilled water followed by application of a 1% v /v solution of acetic acid to the slides for 2 min. The slides were then gently rinsed with water, followed by dehydration with 2 changes of 95% alcohol and 2 changes of absolute alcohol and finally cleared in xylene and mounted in D.P.X. synthetic resin. The images of the stained slides were captured in a microscope (Invitrogen Evos FL Auto 2.0) and the blue stained collagen was visualized.

6.3. Results and Discussion

6.3.1. Antibiofilm Activity of C1 and C2 in Collagen Coated Wells

Collagen adhesion plays a potential role in the pathogenesis induced by *S. aureus* (Kouidhi *et al.*, 2010) and hence collagen rich tissues such as bone, cartilage and skin are prone to *S. aureus* infections (Tong *et al.*, 2015; Patti *et al.*, 1994). The collagen binding protein is a well characterized adhesin, which is expressed in staphylococci during the course of infection and is implicated in tissue colonization and initiation of biofilm formation (Elasri *et al*., 2002; Madani *et al*., 2017). Encouraged by the antibiofilm potential of C1 and C2 as reported earlier in Chapter 2 and Chapter 4, the subsequent endeavor was to study their antibiofilm potential on a collagen-coated surface. On treatment with both C1 and C2, in separate sets, a dose-dependent inhibition of MRSA biofilm formation on collagen-coated wells was evident from the decrease in the metabolic activity as well as the biofilm biomass for *S. aureus* MRSA 100 cells (Figure 6.1A-B and Figure 6.1D-E). MRSA biofilm grown on collagen in presence of 80 µM C1 exhibited only 15% metabolic activity and 25% biomass, highlighting the prospect of C1 as an antibiofilm agent for potential collagen-rich tissue or wound site application. The doses of C1 and C2 required for 50% biofilm inhibition ($MBIC_{50}$) on collagen-coated wells for *S. aureus* MRSA 100 was found to be 60 µM and 640 µM, respectively. The concentrations of C2 required to inhibit the biofilm were higher than the inhibitory

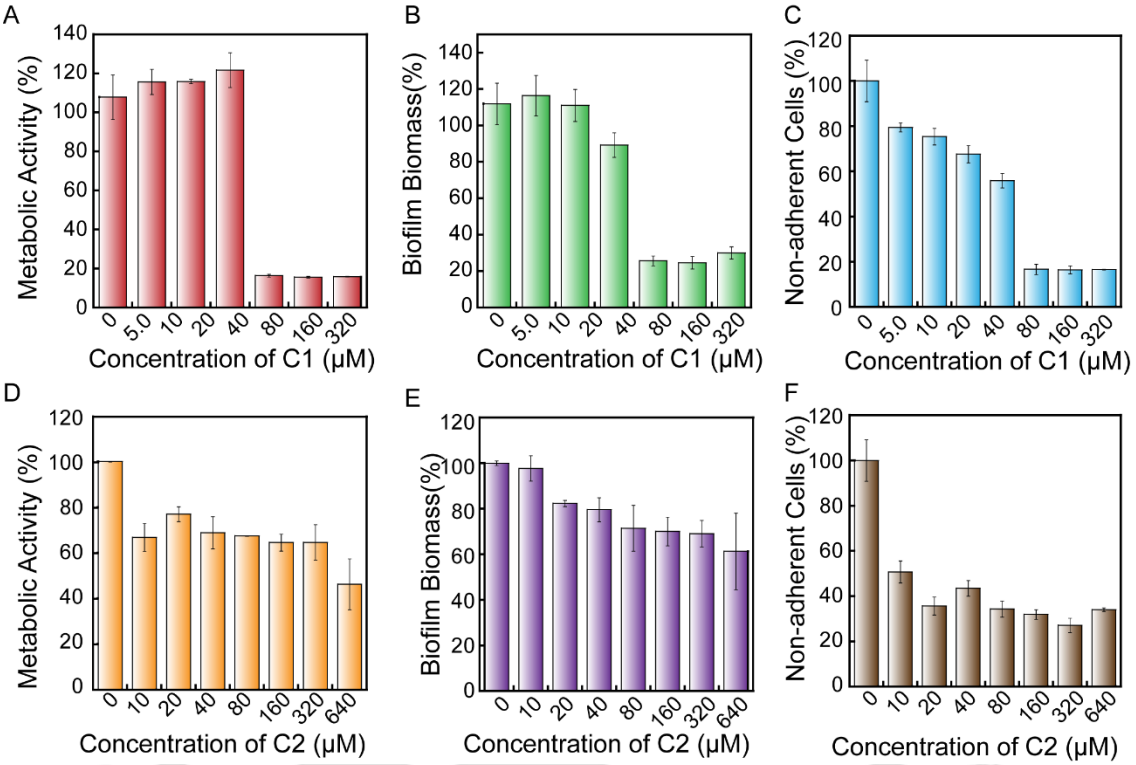

Figure 6.1. Determination of (A and D) metabolic activity by MTT assay, (B and E) biomass by CV assay of *S. aureus* MRSA 100 biofilm grown on collagen. Reduction of non-adherent *S. aureus* MRSA 100 cell number ascertained by optical density on treatment with (C) C1 and (F) C2.

concentrations of C1, perhaps due to its higher propensity to aggregate in the hydrophobic environment provided by collagen, thereby decreasing the available local concentration of the free form of the amphiphile, which is required for its bactericidal activity. Moreover, in case of C1, the non-adherent bacteria experienced a dose-dependent growth inhibitory effect, similar to its biofilm counterpart (Figure 6.1C). In case of C2, the propensity of biofilm formation was higher. Hence, the corresponding number of non-adherent cells were low enough for C2 to exhibit bactericidal activity even at a concentration of 10 μM (Figure 6.1F).

6.3.2. MRSA Biofilm Inhibition in Amphiphile-Impregnated Collagen

Encouraged by the potent antibiofilm activity of the amphiphiles in collagen-coated wells, the subsequent endeavor was to ascertain the antibiofilm potential of C1 and C2 impregnated into collagen and coated onto the wells. This was based on the notion that the propensity of the deposition of a human matrix protein such as collagen on the surface

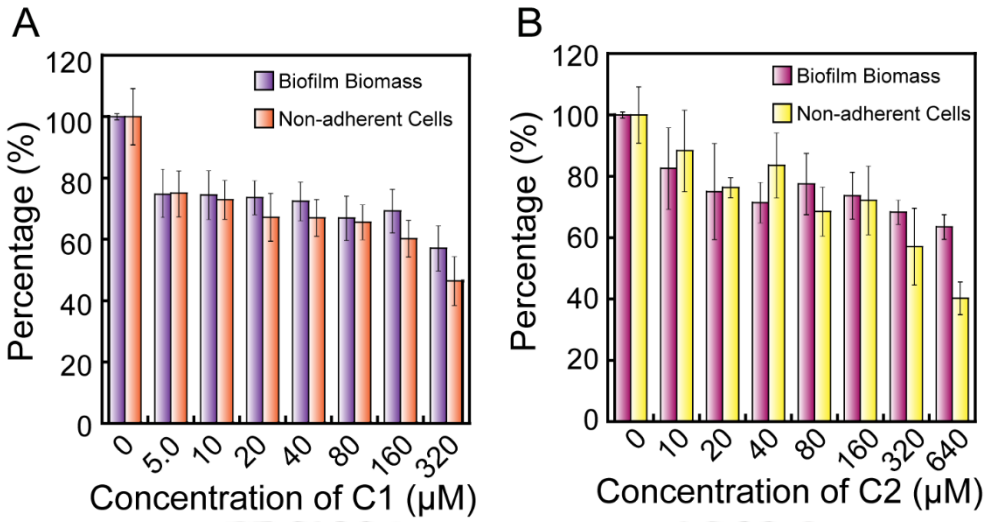

Figure 6.2. Determination of MRSA biofilm biomass and non-adherent cell number of *S. aureus* MRSA 100 biofilm in (A) C1 and (B) C2-impregnated collagen.

of in-dwelling medical devices is high (Patti *et al.,* 1994) and under such circumstances, an antibacterial candidate molecule should be able to act in the collagen matrix encased milieu and hinder biofilm formation on the device. Solution-based crystal violet assays revealed that the impregnated amphiphiles could reduce the *S. aureus* MRSA 100 biofilm biomass in a dose-dependent manner, which indicated that the amphiphiles could leach out of the collagen matrix and inhibit biofilm formation (Figure 6.2A-B). A concentration-based decrease in the number of non-adherent cells was also observed, which indicated that C1 and C2 could diffuse out of the collagen matrix and eliminate the free-floating planktonic cells suspended in the media (Figure 6.2A-B). However, the doses of C1 and C2 required for biofilm inhibition as well as killing of the non-adherent planktonic cells, in this model, were found to be considerably higher than the doses required in non-impregnated form (Figure 6.1), which may be due to the fact that the release of the amphiphiles from the hydrophobic collagen is slow and the effective local concentration is low. Biofilm inhibition was observed to be marginally higher in case of C1-impregnated collagen (Figure 6.2.A-6.2. B).

6.3.3. Antibiofilm Effect of C1 and C2 in Simulated Wound Fluid Infused Collagen Matrix

In the subsequent study, the objective was to develop a model system using collagen as a platform and infusing simulated wound fluid containing serum to form a soft tissue

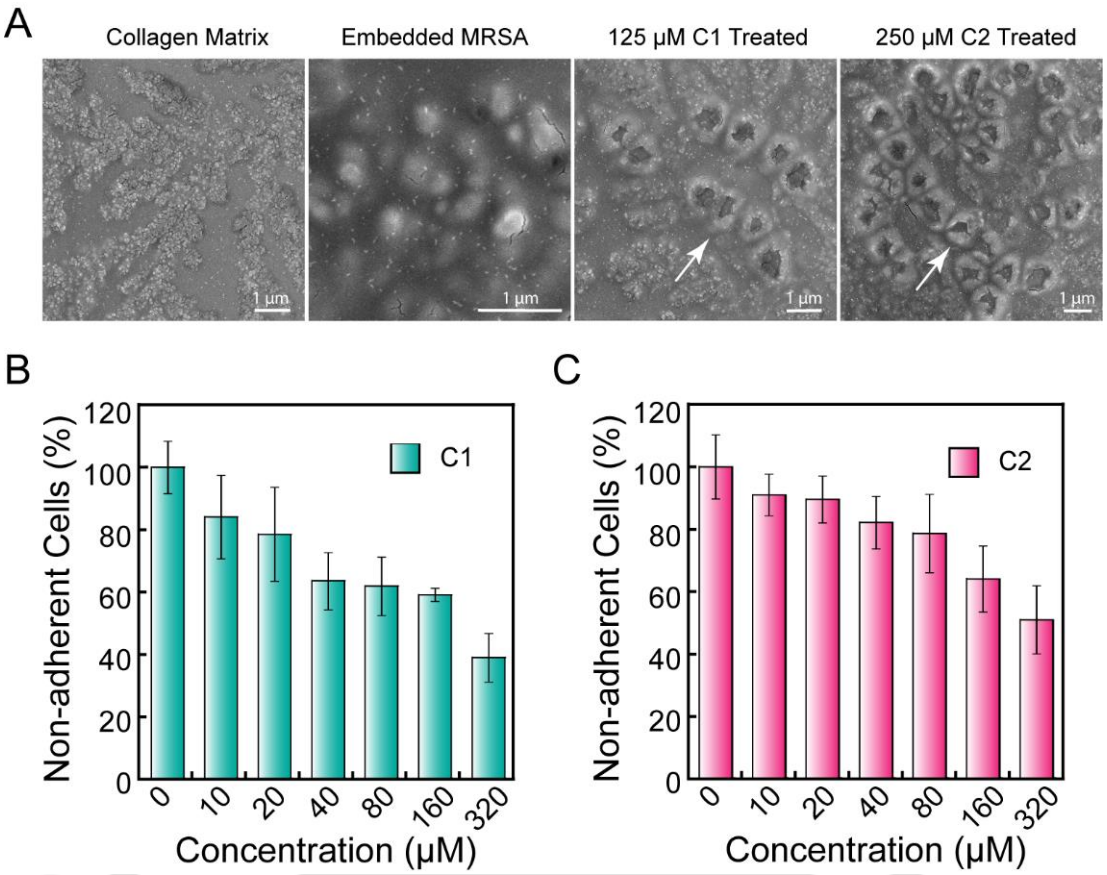

Figure 6.3. (A) FESEM images of *S. aureus* MRSA 100 biofilm grown in SWF-infused 3D collagen matrix. White arrow in case of C1 and C2 treatment depicts cellular damage. Reduction of non-adherent cell number of *S. aureus* MRSA 100 biofilm grown in SWF-infused 3D collagen matrix on treatment with (B) C1 and (C) C2.

wound mimetic environment for studying MRSA biofilm growth (Price *et al.*, 2016). This study was undertaken as *S. aureus* is known to be frequently associated with soft tissue wound infections (Tong *et al*., 2015). The initial screening experiments indicated that at the tested concentrations of C1 and C2, MRSA biofilm formation on a collagen-coated well was inhibited. Hence, the subsequent endeavor was to mimic a more realistic infection model on a 3D collagen matrix saturated with simulated wound fluid. To this end, FESEM studies indicated a prominent membrane damage and loss of the characteristic morphology for collagen matrix embedded MRSA cells upon treatment with C1 (125 µM) and C2 (250 µM), in contrast to the untreated cells, which retained their typical morphology and exhibited cell-cell adhesion (Figure 6.3.A). Further, both C1 and C2 could also bring about a reduction in the number of non-adherent cells in the vicinity of the collagen matrix, wherein the anti-MRSA activity of C1 was observed to be superior than C2 (Figure 6.3.B-6.3.C).

6.3.4. Antibiofilm Activity and Cytotoxicity Studies of C1-coated Orthopedic S.S. Wire

Implant associated infections are of great concern owing to the extensive use of life saving implantable devices in modern healthcare (Arciola *et al*., 2018; Stoodley *et al*., 2011; Oliveira *et al*., 2018; Shah *et al*., 2013). Literature suggests that, majority of the implantable device associated infections are caused by the staphylococcal species, with *S. aureus* being the predominant strain (Oliveira *et al*., 2018; Darouiche, 2004; Ribeiro *et al*., 2012). In order to address this problem, the implant can perhaps be coated with an antibiofilm agent, which can inhibit initial attachment of the cells on the surface of the

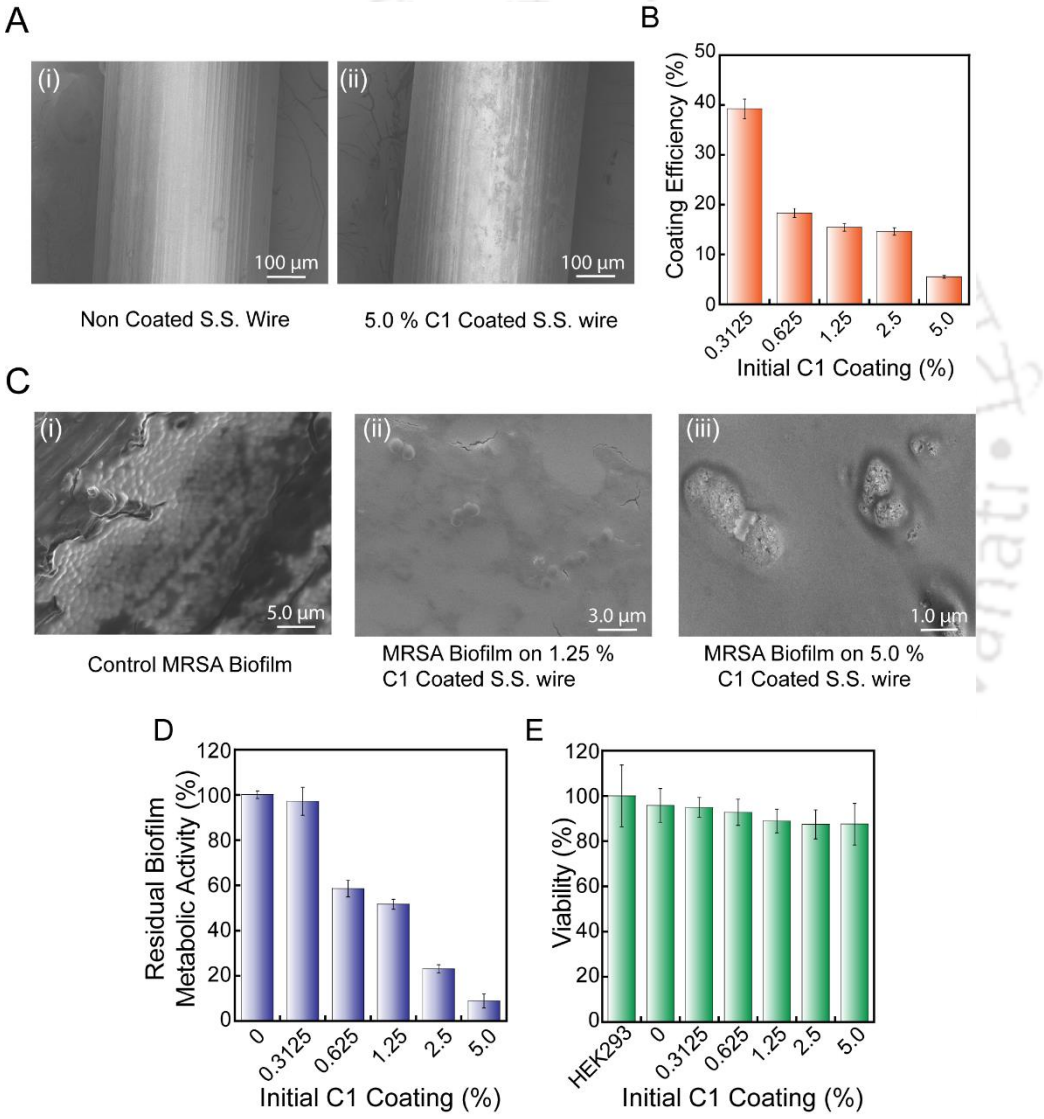

Figure 6.4. (A) FESEM images of the surface of the non-coated and C1-coated S. S. wire (B) The concentration dependent coating efficiency of C1 on the S. S. wire (C) Reduction of adherent biofilm of *S. aureus* MRSA 100 biofilm grown on non-coated and C1 coated S. S. wire (D) Dose-dependent decrease in the metabolic activity of the residual biofilm (E) Toxicity studies of C1-coated S. S. wire on HEK 293 cells.

implant (Hetrick and Schoenfisch, 2006). In a previous study, an antimicrobial peptide (AMP) has been shown to be effective in killing bacterial cells, when grafted on titanium-based prosthetics (Barnes and Cooper 2015). Synthetic amphiphiles, being AMP mimics, can also be a good anti-fouling agent. Hence, in the present study, the amphiphile C1 was tested for its potential as an antimicrobial coating on orthopedic S.S. wires. FESEM analysis indicated that the surface of the C1-coated S. S. wire (5.0 µM C1 coating) appeared encased as compared to the bare and smooth surface of the non-coated wire (Figure 6.4A). The coating efficiency was observed to be best at lower concentration and decreased slowly as the concentration was increased, indicating a saturation effect (Figure 6.4B). The antibiofilm potency of the C1-coated S.S. wires was studied by FESEM and solution-based assay. Interestingly, the coated S. S. wires seem to prevent MRSA biofilm adhesion as compared to the non-coated wire, wherein a thick mat of biofilm cells could be observed (Figure 6.4C). Further, in presence of the coated implant, a dose-dependent decrease in the metabolic activity of the residual biofilm trying to colonize in the vicinity of the wire was observed (Figure 6.4D). This implied that coating of C1 not only reduced implant-associated biofilm formation but also rendered an inhibitory effect on biofilm cells for 24 h by a sustained release of the amphiphile from the coated wire, which also highlights the stability of the coating. In order to test the safety of the coated S. S. wire to be used as an implant, it was pertinent to assess its toxic potential. To this end, the eluates from the C1 coated wires were found to be non-toxic to cultured HEK 293 cells (Figure 6.5E).

6.3.5. Effect of C1 on the Expression of fnbA and hld Genes in MRSA Biofilm

Expression of various microbial surface components which recognize adhesive matrix molecules (MSCRAMMs) that can bind to one or more host extracellular matrix factors such as collagen and fibronectin among others and expression of certain virulence factors such as the δ-toxin play an important role in staphylococcal biofilm formation and dispersion (Seo *et al.*, 2008; Aricola *et al.,* 2012; Archer *et al.,* 2011; McCarthy *et al.*, 2015; Vuong *et al.*, 2004). For antibiofilm therapy, it is important to note that differences in the physiological properties between established biofilms and actively growing planktonic cells can influence the sensitivity or selectivity of drug molecules towards them (Joo and Otto, 2012; Hall and Mah, 2017). In order to interpret what kind of differential gene expression events led to the phenotypic differences in adherent and non-

adherent cells during biofilm formation on treatment with C1, in this study quantitative real-time PCR was performed for one adhesion (*fnbA*) and one dispersion-related gene (*hld*) involved in *S. aureus* biofilm development. *fnbA* encodes for fibronectin binding protein A, which enhances *S. aureus* adhesion to the substratum and promotes biofilm formation (Menzies 2003; Vergara-Irigaray *et al.* 2009; Kulkarni *et al.*, 2012). Quantitative real-time PCR analysis indicated that the expression of *fnbA* gene in MRSA was essentially low in biofilm on treatment with C1 (Figure 6.5A). In case of the non-adherent cells, the expression levels of *fnbA* gene was even lower and downregulated upon treatment with C1 (Figure 6.5A) and this tenet may account for the inability of these cells to adhere and transition from planktonic to biofilm phase. The δ-toxin (*hld*) of *S. aureus* belongs to the phenol-soluble modulin (PSM) peptide family and is a key contributor in the infection with highly virulent community-associated MRSA strains and can strongly influence biofilm structuring, detachment, and the systemic dissemination of biofilm-associated infection (Joo *et al*., 2011; Cheung *et al*., 2014; Wang *et al*., 2007; Peschel and Otto, 2013; Periasamy *et al*., 2012). On treatment with 10 µM C1, the expression levels of *hld* in biofilm cells was comparable to the non-treated biofilm, while a marginal downregulation was observed in case of the non-adherent cells (Figure 6.5B). However, on treatment with higher concentration of C1 (20 µM), the levels of *hld* expression in the biofilm cells increased, which could perhaps be attributed to the inhibition of biofilm adherence and enhancement of biofilm to planktonic transition. (Figure 6.5B). The levels of *hld* expression in non-adherent planktonic cells on treatment with 20 µM C1 was only marginally lower than the cells treated with 10 µM C1.

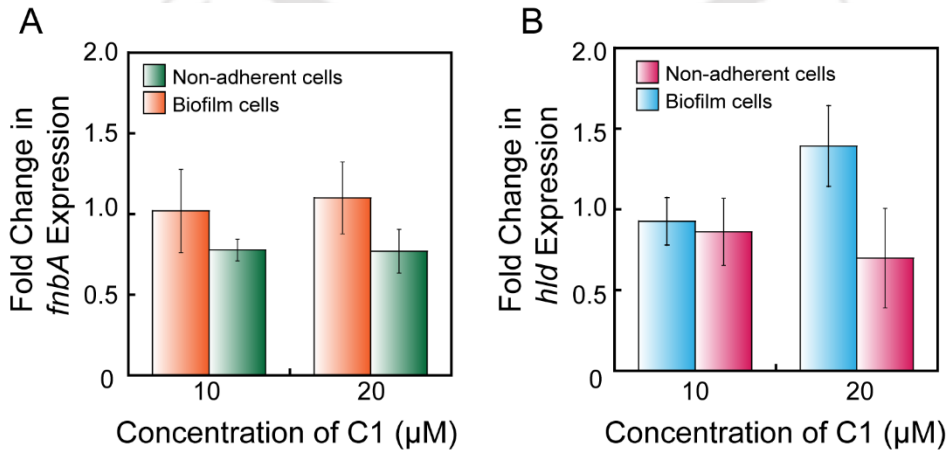

Figure 6.5. qRT-PCR to ascertain expression levels of (A) *fnbA* and (B) *hld* genes in *S. aureus* MRSA 100 biofilm and non-adherent cells in presence of C1.

6.3.6. Acute Toxicity Studies of C1 on BALB/c Mice

The sighting study indicated that, up on administration of C1 in low dose (300 mg/kg) to one male and one female BALB/c mice, no evident visible toxicity was observed upon single administration of the test molecule observed over a period of 5 days. Further, no abnormal clinical signs were observed and the body weights were consistent (Appendix Table A6.1). Hence it could be concluded that single administration of test molecule seems to be safe at 300 mg/kg. Based on the OECD guidelines, the subsequent endeavor was to conduct a similar study in presence of an extremely high dose (1000 mg/kg). In these studies, up to Day 8 no visible toxicity was evident upon single administration of test molecule. A 2-4% reduction in body weights in both male and female mice were observed up to Day 7. However, on Day 8, the body weights of both animals reverted to normal (Appendix Table A6.2). Through all the days of the study, no abnormal clinical signs were observed. Hence, the molecule seems to be safe at 1000 mg/kg. The sighting study indicated that administration of C1 (1000 mg/kg) did not produce any drastic variation in the hematological parameters in treated mice of both genders (Appendix Table A6.3-A6.4), whereas histopathological analysis of the vital organs showed normal morphology and characteristics (Appendix Figure A6.1). These observations were further corroborated in the main study using five female BALB/c mice, where no mortality, no abnormal clinical signs such as change in respiration, change in eye color or skin, general motor activity and alertness were evident on administration of 1000 mg/kg of C1. The administration of C1 was well tolerated without any significant change in the food and water intake in the mice. The body weights of the animals were observed to be consistent as evident from a less than 10% change (Table 6.2.). The hematological analysis indicated that the administration of 1000 mg/kg C1 did not significantly alter majority of tested hematological parameters (Table 6.3). With regard to RBC, it has been advocated that a decrease in its count can imply either reduced production or a higher loss owing to hemolysis or hemorrhage (Everds *et al*., 2015). In the present study, it was observed that the average RBC count of all the five tested animals were within the range, although a slight increase in the hemoglobin content was

Table 6.2. Body weight (in gram) of female BALB/c mice after oral dosing of 1000 mg/kg C1.

Day 1	Day 3	Day 5	Day 7
26.54 ± 2.54	26.62 ± 2.58	26.6 ± 2.54	26.74 ± 2.53

Table 6.3. Hematological screening in 1000 mg/kg C1 treated female BALB/c mice for acute toxicity study.

Sl. No.	Parameter	Estimated Values	Control Values
1.	Platelets (x 10^3 cells/µL)	1264 ± 288.81	1521 ± 36
2.	RBC (x 10^6 cells/µL)	8.97 ± 0.23	9.715 ± 0.77
3.	Haemoglobin (g/dL)	19.57 ± 0.81	21.05 ± 0.95
4.	Hematocrit (%)	42.30 ± 0.80	49.30 ± 2.10
5.	Mean Corpuscular Volume (fL)	47.20 ± 1.25	50.85 ± 1.85
6.	Mean Corpuscular Haemoglobin (pg)	21.83 ± 1.20	21.75 ± 0.75
7.	Neutrophil (%)	20.63 ± 4.92	8.70 ± 0.40
8.	Lymphocytes (%)	68.03 ± 9.97	84.55 ± 0.85
9.	Monocytes (%)	2.03 ± 1.17	1.50 ± 0.30
10.	WBC (x 10^3 cells/µL)	8.45 ± 0.43	6.96 ± 0.26
11.	Eosinophils (%)	5.87 ± 4.80	4.30 ± 0.90
12.	Basophils (%)	0.33 ± 0.49	0.10 ± 0.07
13.	Leucocytes (%)	3.17 ± 1.27	0.85 ± 0.15

observed (Table 6.3). On the other hand, WBCs are critical sentinels of the immune system and infections, chemotherapy, administration of immunosuppressant drugs and stress can lead to a reduction in their numbers (Dempsey *et al*., 2003; Bonilla and Oettgen, 2010; Walker and Warnatz 2006). This study identified that C1 dose dependently elevated the neutrophils, marginally reduced lymphocytes and also increased platelets. However, the total WBC count was observed to remain unchanged on increasing the dose of C1 from 300 mg/kg to 1000 mg/kg (Table 6.3, Appendix Table A6.4). Collectively these results indicate that C1 did not cause any drastic significant changes in any of the hematological parameters implying that 1000 mg/kg C1 is a tolerated dose showing no evident toxicity.

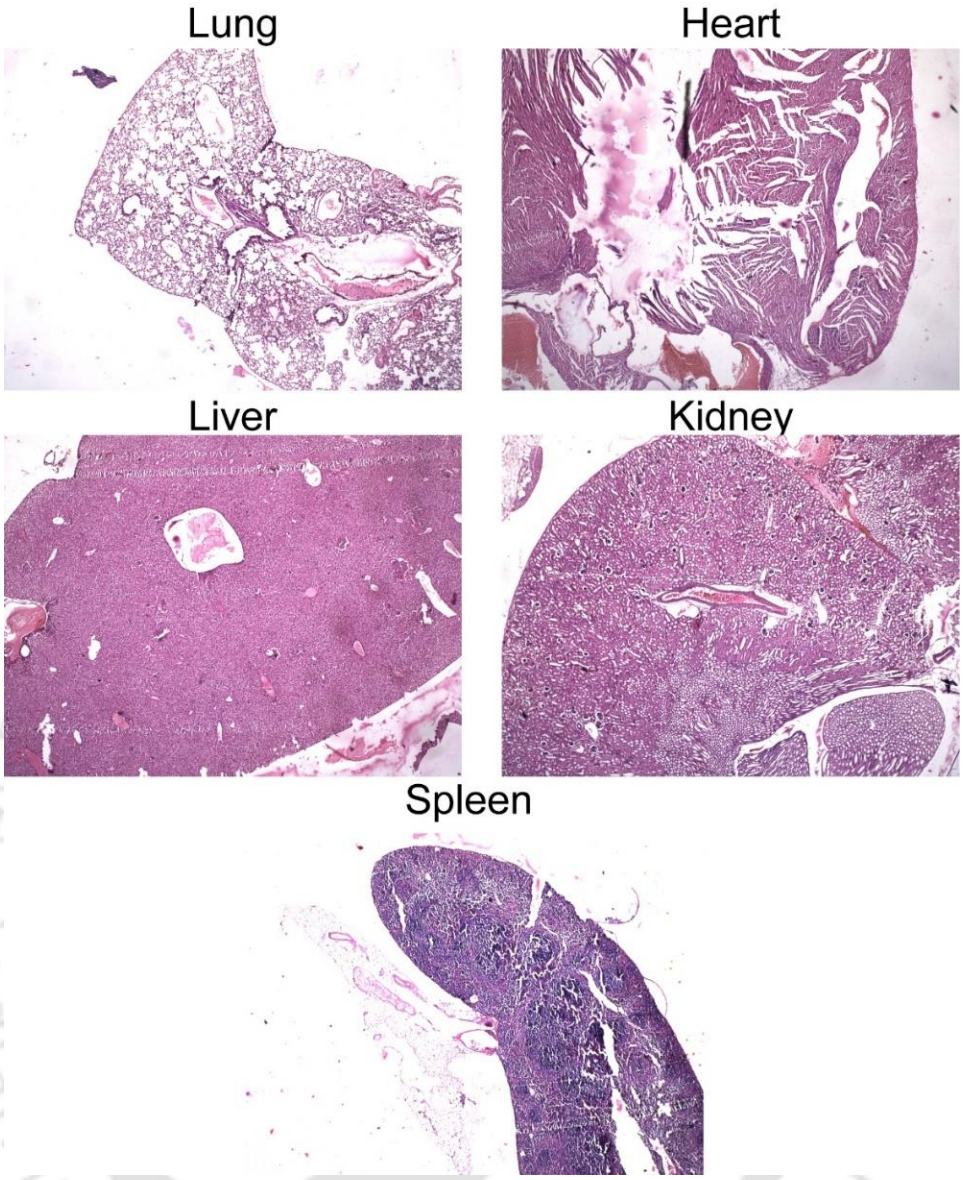

Figure 6.6. Representative sections of hematoxylin and eosin stained organs obtained from female BALB/c mice subjected to treatment with 1000 mg/kg C1 in the main acute toxicity study. (Images were taken at 10x magnification)

Hence single dose up to 1000 mg/kg was considered as maximum tolerated dose (MTD) and 1/10 th of the dose was used subsequently in efficacy study *i.e* wound healing study. Gross morphological examination and histopathological analysis of all the vital organs excised immediately after euthanasia including heart, kidney, liver, lungs and spleen showed no pathological changes or inflammation in any of the animals, which indicated the lack of toxic effects of C1 on any vital organ (Figure 6.6., Appendix Figure A6.2).

6.3.7. Wound Healing Studies of C1 on BALB/c Mice Skin Excision Model

A skin wound is prone to microbial infection, which, in turn can delay the natural wound-healing process. In this context, intervention with an antibacterial agent can hinder bacterial colonization of the wound area and thereby enhance the healing of the wound. Based on this premise, it was conceived that the bactericidal amphiphile C1 can perhaps be explored as an agent, which facilitates wound healing on topical application. Hence, a skin excision model on BALB/c mice was chosen to validate this hypothesis. For this study, the selected doses (50 mg/kg and 100 mg/kg) for topical application were based on the maximum tolerated oral dose of C1 (1000 mg/kg). The dose selection and dosing schedule in animal model wound healing studies was based on the rationale that they can be extrapolated for future clinical trial studies. The following parameters were considered in the assessment of the wound healing potential of C1.

6.3.7.1. Body Weight and Wound Closure

In the present study, the experiments were conducted on female BALB/c mice for 14 days wherein upon two times observation daily, no clinical signs of behavioral abnormality, morbidity and mortality was observed. With regard to body weight, less than 10% change was observed over time for all the six experimental groups (Figure 6.7).

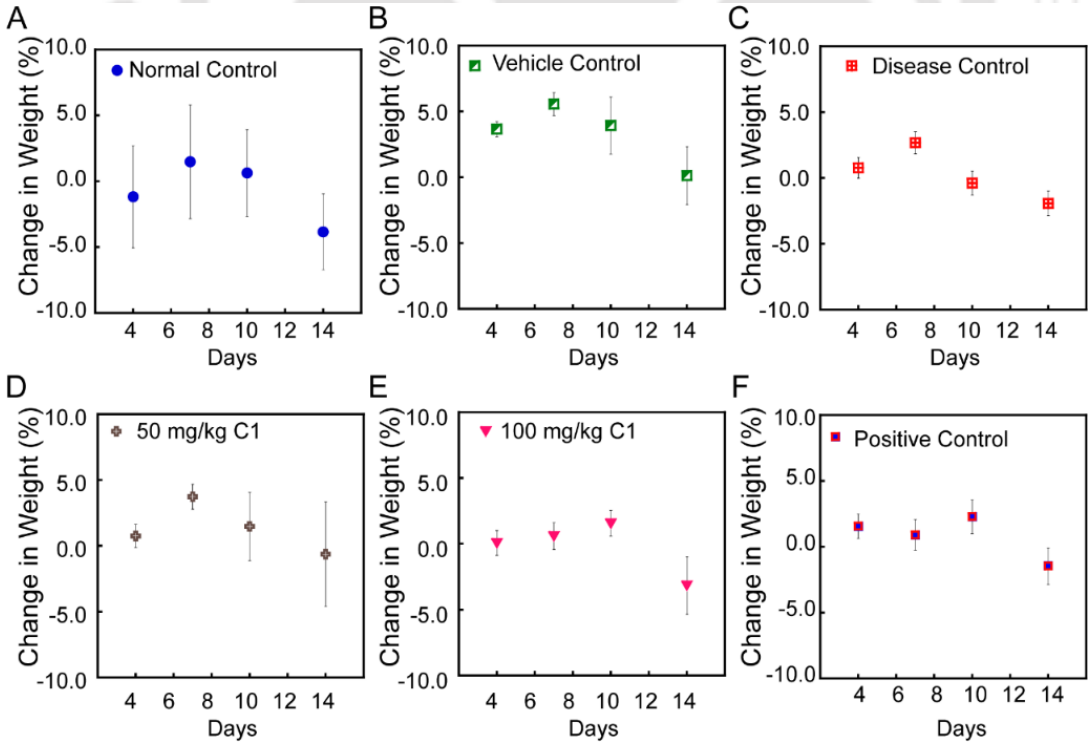

Figure 6.7. Change in the body weights of experimental groups over the duration of the study.

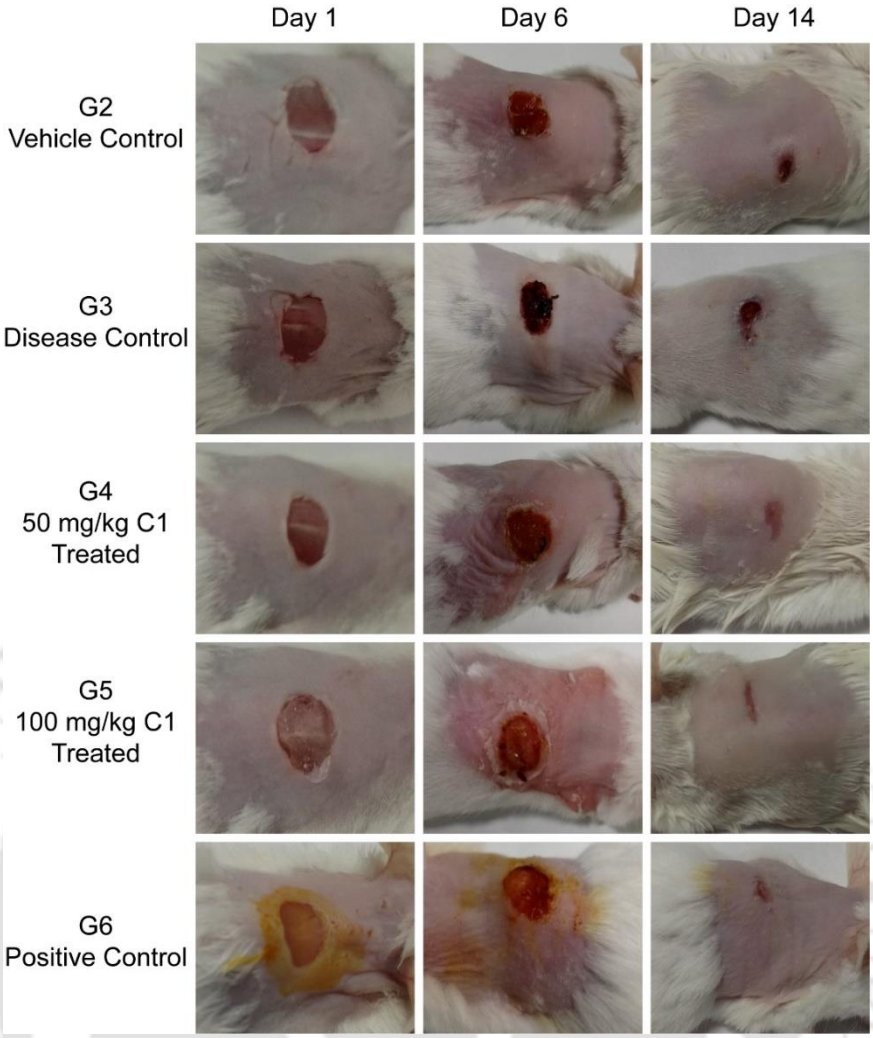

Figure 6.8. Representative image panels for visualization of wound closure over the duration of the study.

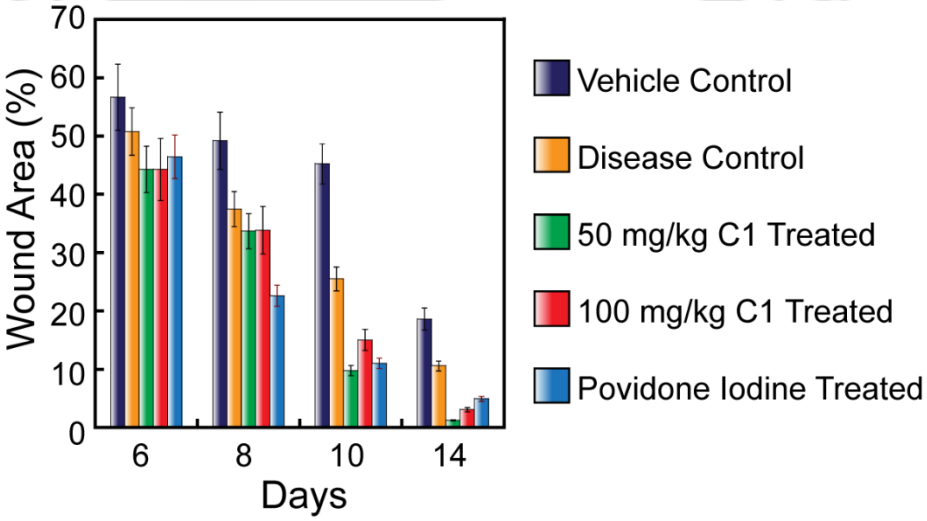

Figure 6.9. Decrease in wound area in the experimental groups over the duration of the study. (n=5 animals)

The gradual closure of the wound post excision was documented as presented in Figure 6.9, Appendix Figure A6.3. The vehicle control and disease control group exhibited minute wound contraction as compared to the animals treated with 50 mg/kg and 100 mg/kg of C1 (Figure 6.9, Appendix Figure A6.3). Following application of C1 topically, the wound closure was gradual between day 1 and day 8 followed by a very rapid closure of the wound, culminating in almost total closure and shedding of the eschar by the 14th day, which was comparable to the standard group (with 50 mg of povidone iodine 5% w/w, Figure 6.9, Appendix Figure A6.3). However, in case of vehicle control (only petroleum jelly) and disease control group, wound closure was of a much lesser extent on day 14 as evident from the presence of a still persisting eschar (Figure 6.8, Appendix Figure A6.3). With regard to wound area, it is observed that there was a gradual decrease over time. Notably, on the 14th day post skin excision, the reduction in the mean wound area was maximum for the groups treated with 50 mg/kg C1 and 100 mg/kg C1, with the final wound area amounting to only 1.3 % and 3.1% of the initial size of the inflicted wound (Figure 6.9). It may be mentioned here that this decrease in the wound area was found to be even more than the positive control group where the average wound area after 14 days was 5%, indicating that the wound-healing property of C1 was comparable to that of povidone iodine, which is also commercially known as betadine, a prevalent topical ointment. In the vehicle control and disease control group, the natural decrease in the wound area was also evident. However, the decrease was significantly lower than C1-treated groups. (Figure 6.9).

6.3.7.2. Hematology and Histopathological Analysis

On topical application, there is a probability of the drug leaching into the vascular system through the exposed wound and imparting toxicological effects on the subject. Hence, to determine whether application of C1 led to any changes in the blood parameters, blood from all the animals was collected by cardiac puncture in vials prior to sacrifice and analysis of hematological parameters was done as depicted in Table 6.4. In this study, on treatment with C1, the RBC counts across all the experimental groups were comparable (Table 6.4) indicating that C1 was safe for topical application as it did not significantly alter the red blood cell count. In this study, a prominent observation was that the neutrophil levels were elevated for the treatment groups (G4 and G5) along with the positive control group (G6) (Table 6.4). The high neutrophil levels seem to suggest that topical application of C1 may promote higher levels of neutrophil infiltration in the

wound area, which in turn, may result in higher levels of pro-inflammatory cytokine secretion and monocyte differentiation into macrophages (Delavary *et al*., 2011; Hubner *et al*., 1996; Werner and Grose, 2003). The role of these macrophages is critical in wound healing as they are known to promote clearance of senescent cells and wound debris as well as induce collagen production, angiogenesis and re-epithelialization (Baum and Arpey, 2005). Hence, the aforementioned observations reaffirm that C1 holds considerable potential as topical wound healing agent. Treatment with C1 also led to

Table 6.4. Hematological screening in female BALB/c mice post wound healing.

Sl.No.	Parameter	G1	G2	G3	G4	G5	G6
1.	Platelets (x 10^3 cells/µL)	1521.00 ±36	1569.00 ±216.42	1100.25 ±469.92	1266.00 ±82.87	1414.00 ±198.24	1391.00 ±327.78
2.	RBC (x 10^6 cells/µL)	9.72 ±0.77	10.18 ±0.47	9.70 6±0.20	9.24 ±0.06	9.31 ±0.27	9.82 ±0.47
3.	Haemoglobin (g/dL)	21.05 ±0.95	21.68 ±0.66	21.27 5±0.22	20.23 ±0.92	20.18 ±0.55	21.20 ±1.77
4.	Hematocrit (%)	49.30 ±2.1	51.33 ±1.42	49.33 ±1.08	43.90 ±1.73	44.10 ±1.71	47.13 ±4.48
5.	Mean Corpuscular Volume (fL)	50.85 ±1.85	50.50 ±1.71	50.55 ±1.43	47.53 ±1.96	47.35 ±1.46	48.00 ±3.31
6.	Mean Corpuscular Haemoglobin (pg)	21.75 ±0.75	21.35 ±0.54	21.83 ±0.61	21.93 ±1.10	21.70 ±0.26	21.57 ±1.02
7.	Neutrophil (%)	8.70 ±0.40	8.40 ±2.03	11.30 ±1.07	34.33 ±21.66	19.25 ±2.71	20.93 ±3.25
8.	Lymphocytes (%)	84.55 ±0.85	84.53 ±5.45	83.85 ±1.56	63.65 ±16.89	76.03 ±3.96	83.95 ±4.59
9.	Monocytes (%)	1.50 ±0.30	1.08 ±0.66	0.88 ±0.56	0.93 ±0.85	0.75 ±0.19	1.00 ±0.35
10.	WBC (x 10^3 cells/µL)	6.96 ±0.26	11.45 ±4.64	9.71 ±1.27	3.99 ±1.24	2.68 ±1.80	6.24 ±0.46
11.	Eosinophils (%)	4.30 ±0.90	4.45 ±3.86	1.40 ±0.42	8.15 ±4.50	7.10 ±3.99	4.27 ±1.99
12.	Basophils (%)	0.10 ±0.07	0.18 ±0.05	0.08 ±0.05	0.10 ±0.10	0.33 ±0.45	0.23 ±0.21
13.	Leucocytes (%)	0.85 ±0.15	1.38 ±0.25	2.53 ±0.96	1.53 ±0.57	1.93 ±0.57	1.77 ±0.31

a marginal reduction in the lymphocyte count as compared to the control groups (Table 6.4). The platelet counts were found to be normal for all the mice. Platelets are essentially involved in the initial phase after wound where they help in clot formation (Delavary *et al*., 2011), irrespective of the treatment, which can be validated by the comparable platelet counts within all the groups.

Histopathological study of wound healing process is normally used for evaluating the efficacy of pharmacological products, which promote and accelerate dermal skin substitutes. The phases of cutaneous wound repairing can be categorized into four phases such as homeostasis, inflammation (early and late), proliferation and remodeling phases (Delavary *et al*., 2011). A number of criteria are considered to determine the level of histopathological change such as the depth and length of healed wound, epithelial stratification, leucocytes and macrophage infiltration, fibroblast proliferation, extent of elastin formation and the most important is collagen fiber as it plays a dominant role in maintaining the structural integrity and enhances wound healing (Delavary *et al*., 2011). In the present study, histopathological analysis of the skin sections from the wound area was carried out by hematoxylin and eosin staining. In the normal control group, normal skin histology was observed, while in the vehicle control animals, cellular infiltration of neutrophils and congested blood vessels were evident (Figure 6.10). However, in the disease control, no tissue reaction or indication of healing was seen as proliferating

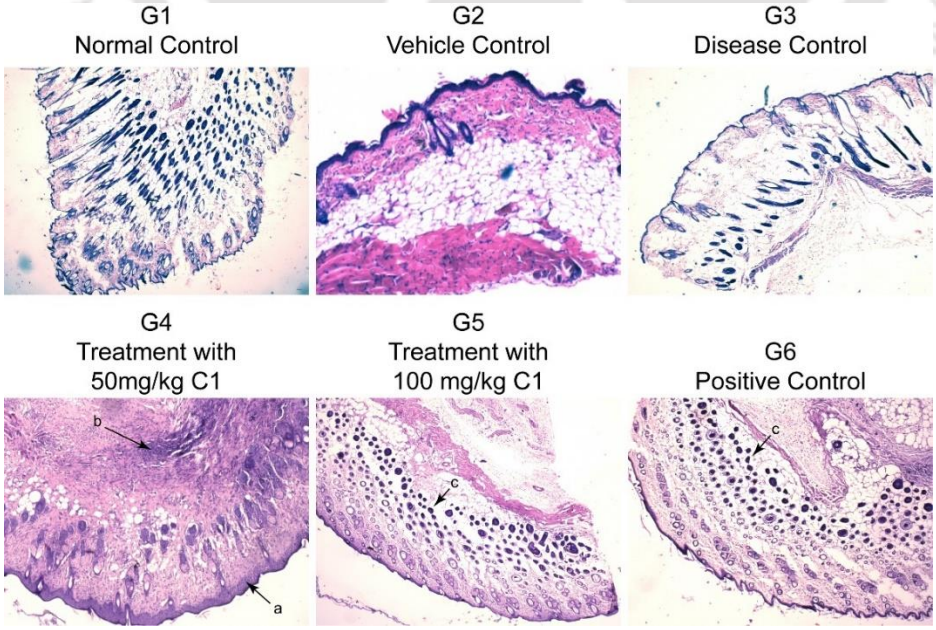

Figure 6.10. Histopathological analysis of skin sections obtained from the wound area of various experimental groups. a: stratum spinosum; b: fibroblast infiltration; c: follicle.

fibroblast, granulation tissue or infiltrating cells could not be detected, and a visible loss of dermal connective tissue was apparent (Figure 6.10). On topical treatment of the mice wounds with 50 mg/kg C1, mild hyperplasia of the stratum spinosum layer of the epidermis, dense fibrous tissue proliferation and tissue reorganization by keratinization and epithelization was observed, which strongly indicates healing (Figure 6.10). On treatment with higher dose of C1 (100 mg/kg) moderate hyperplasia of the stratum spinosum layer of the epidermis, heavy deposition of fibrous connective tissue resulting in dense fibrosis (scarring), follicular hyperplasia and tissue reaction, which are indications of wound healing was seen (Figure 6.10). In the context of wound healing on topical application, the lower dose of C1 was observed to be better than the higher dose. In the positive control, although follicular hyperplasia was seen, tissue reaction or indication of healing, depicted by the number of proliferating fibroblasts, was observed to be lower than the ones treated with C1 (Figure 6.10).

6.3.7.3. Hydroxyproline Estimation of Wound Tissue

Collagen plays a key role in providing mechanical strength to connective tissues of the musculoskeletal system such as bone, cartilage, and tendon (Nair *et al*., 2014). Hence, collagen quantification is germane to studying tissues and probing their disease states. In this context, hydroxyproline content is recognized as a marker for collagen quantification, given its roles in imparting stability and its exclusive presence in collagen (Eleswarapu *et al*., 2011; Rigozzi *et al*., 2013; Edwards and O'Brien, 1980). The hydroxyproline assay, uses a simple colorimetric technique that generates a chromophore from hydroxyproline via reaction with perchloric acid and 2- propanol to dissolve p-dimethylaminobenzaldehyde (DMAB), present in Ehrlich's reagent (Cissell *et al*., 2017). Hydroxyproline assay was done for all the tissue samples collected after sacrifice and the amount of hydroxyproline content per unit tissue weight for each sample was estimated and found to be increased in the groups treated with 50 mg/kg and 100 mg/kg C1 as compared to vehicle and disease control groups (Figure 6.11) which implies more collagen deposition and superior healing due to treatment with C1 compared to vehicle control or disease control animals. Enhanced levels of hydroxyproline was also evident for the positive control group. However, the levels were found to be lower than the C1 treated groups (Figure 6.11).

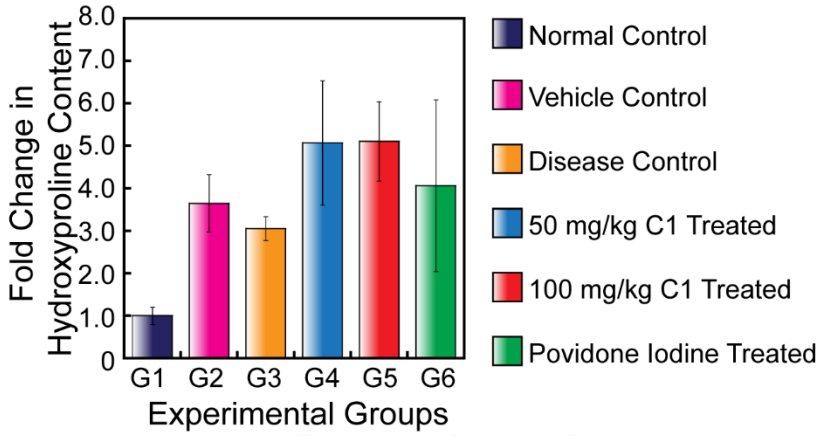

Figure 6.11. Hydroxyproline content estimation in various experimental groups of female BALB/c mice.

6.3.7.4. Mason's Trichrome Staining for Collagen Detection

Conventional hematoxylin and eosin (H&E) staining is not able to differentiate salient histopathological characteristics related to the wound healing process such as collagen deposition and scab formation. Hence, a method which can stain collagen and bring about a differentiation in the morphological and anatomical structures in the skin tissue is desirable as it can provide a clearer insight of the wound healing process. In this regard, in the present study the skin fragments excised from the wound site were subjected to the Mason's Trichrome staining as the method is able to differentiate clearly the muscle fiber

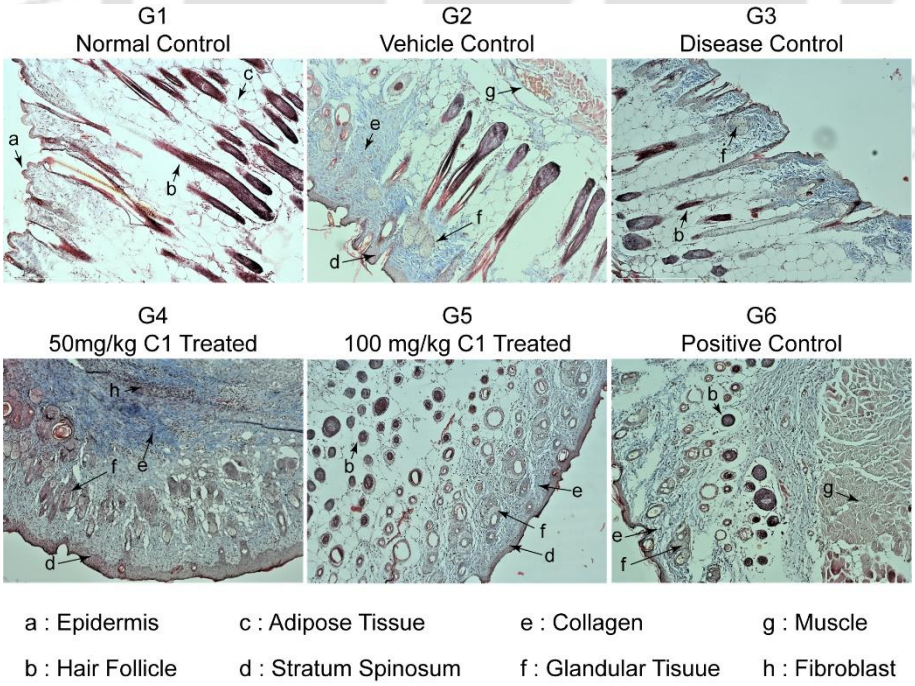

Figure 6.12. Microscopic images of Mason's Trichrome staining of skin sections obtained from the wound area of various experimental groups at magnification of 10x.

(red color), cytoplasm and adipose cell (light red or pink), cell nuclei (dark brown to black) and collagen fiber (blue). In the normal control mice, a thin epidermis and very little collagen content was observed. Hair follicles and fat cells were also visible and were representative of normal healthy murine skin (Figure 6.12). In the vehicle control, proliferation of the stratum spinosum layer of the epidermis was observed and an increased collagen deposition was visible. Few glands were also seen, but, no infiltration of neutrophils or lymphocytes were evident (Figure 6.12). In the disease control group, very little amount of collagen was visible. Hair follicles and glands were also minimal and little or no proliferation of the stratum spinosum layer was seen (Figure 6.12). In the 50 mg/kg and 100 mg/kg C1 treated animals, hyperplasia of the stratum spinosum was observed. In case of treatment with 50 mg/kg C1, the collagen content was visibly high compared to control group, and fibroblast proliferation depicted by the dense fibroblast tissue was noticeable and glandular proliferation was also profound (Figure 6.12). In the 100 mg/kg treatment, follicular hyperplasia along with glandular hyperplasia was also evident, however the collagen content was visibly lesser than the 50 mg/kg C1 treated group. The positive control group also exhibited follicular hyperplasia but glandular proliferation was lesser than the treated ones and collagen content was also not very high (Figure 6.12). These results point to the fact that 50 mg/kg C1 was perhaps a more effective dose than 100 mg/kg C1 for wound healing application. Although, an initial toxicity study performed with single oral dose of 1000 mg/kg C1, did not result in any obvious toxic effect, a repeated administration of a comparatively lower dose of 100 mg/kg topically may have caused mild skin toxicity. Hence, further repeat dose exposure studies are required to confirm the differential efficacy at the 50 and 100 mg/kg doses.

6.4. Significant Findings

The salient findings of the present study can be enlisted as follows:

1. The amphiphiles C1 and C2 could inhibit *S. aureus* MRSA 100 biofilm growth in collagen-coated microtiter well. A similar effect of C1 was also observed for the non-adherent planktonic cells.

2. In case of amphiphile-impregnated collagen, the dose-dependent effect of C1 and C2 on MRSA biofilm growth was also observed albeit less in magnitude as compared to biofilm grown on collagen.
3. C1 could hinder MRSA biofilm formation on a 3D collagen matrix infused with simulated wound fluid, highlighting the prospect of the amphiphile as an antibiofilm agent for potential wound site application.
4. The viability of *S. aureus* MRSA 100 biofilm decreased on an orthopedic stainless-steel wire (SS wire) coated with C1, while the eluates from SS wire coated with C1 were non-toxic to HEK 293 cells.
5. Quantitative real-time PCR analysis indicated that the expression of *fnbA* gene, in biofilm as well as non-adherent planktonic cells of *S. aureus* MRSA 100 decreased upon treatment with C1, corroborating its antibiofilm potential. Conversely, the expression of *hld* gene, which is involved in biofilm dispersion was enhanced as the concentration of C1 was increased in the biofilm cells. However, *hld* expression was considerably low in the non-adherent planktonic cells treated with C1.
6. Acute toxicity studies performed on both male and female BALB/c mice with a dose as high as 1000 mg/kg indicated that C1 was essentially non-toxic.
7. Interestingly, the amphiphile C1 could bring about a significant wound healing and reduction in the wound area in a skin excision wound model experiment conducted on female BALB/c mice.

Based on the leads obtained in the study, it is evident that the amphiphile C1 displayed potent antibiofilm activity against a clinical MRSA strain in a simulated wound environment. On the other hand, the *in vivo* nontoxic nature of C1 suggested that the druggable dose of the amphiphile is manifold higher than its MIC against the MRSA strain. It is envisaged that the wound healing activity of C1 can be leveraged for formulating a topical antibacterial using C1.

SUMMARY AND FUTURE PERSPECTIVE

SUMMARY AND FUTURE PERSPECTIVE

The prevalence of antibiotic-resistant pathogenic bacteria is assuming an ominous proportion and is a grave healthcare concern. Owing to this predicament, there is an urgent need to develop antibacterials that act on profound targets and are less likely to trigger resistance development. In this backdrop, the present investigation, which describes the self-assembly and metal binding attributes of rationally designed salicaldehyde and napthaldehyde-based amphiphiles and reports their antibacterial activity and therapeutic potential augers well in addressing the pressing need of drug discovery to combat life-threatening pathogens. The significant leads of the study and the future prospect is discussed in the following section:

(1) The design rational of the synthetic amphiphiles C1 and C2 enabled facile self-assembly through hydrophobic tail, intermolecular hydrogen bonding and π-stacking interactions of the head group. In terms of exploiting the self-assembly attribute, the present study presents a powerful application wherein the nano-micelle generated from the amphiphile C1 could be leveraged to encapsulate antibiotics and thereby generate a composite antibacterial, which not only breaches the resistance barrier of the pathogen but also paves the way for superior cellular uptake of antibiotic, resulting in enhanced killing of the pathogen. The design principle of the synthetic amphiphile described in the present study may serve as a prototype and inspire the development of analogous dual-warhead synthetic antibacterials in future for mitigating the peril of drug-resistant bacteria.

(2) The potent membrane-directed activity of the amphiphiles are counter-productive to resistance development in pathogens and thus hold prospect in antibacterial therapy as alternatives to antibiotics. Further, the membrane-directed activity of the amphiphiles could be exploited to potentiate the efficacy of therapeutic antibiotics in combination, as evident from the results presented in the present study. In future, these results can be validated and the adjunctive potential of the amphiphiles can be tested in an *in vivo* model.

(3) Besides displaying facile self-assembly, the head groups of the amphiphiles C1 and C2 are also tailored by design to render supramolecular interactions and form hydrogen bonds with phosphoryl groups of lipoteichoic acid (LTA), which encompasses a major bacterial cell wall glycopolymer in pathogens such as MRSA and is also considered to be an adhesin and a virulence factor. In the present study, it was demonstrated through ITC experiments that C1 and C2 could bind strongly to bacterial LTA. Targeting the accessible LTA of pathogenic bacteria with C1 or C2 perhaps promotes cellular anchorage and enhances the local concentration of the amphiphile, which in turn translates into copious membrane damage in the target cells. In future it would be interesting to carry out *in vivo* studies and investigate whether the LTA binding propensity of the amphiphiles can be exploited to prevent pathogen adhesion onto host cells and thereby prevent the infection process.

(4) The head groups of the amphiphiles C1 and C2 were also designed to bind metals and potentially hinder metal acquisition in the target pathogen, which augers well as a therapeutic strategy as metals play a key role in cellular physiology and the infection process of drug-resistant pathogenic bacteria. In the present study, the benefit of the metal binding propensity of the amphiphiles was evident as a remarkable growth inhibition of the pathogen MRSA was observed even at very low amphiphile concentrations. Further, the metal starvation induced in the pathogen by the amphiphile C1 was also validated by gene expression studies, which unraveled that C1 could clearly influence the expression of genes implicated in the synthesis of the zincophore staphylopine (stp) and the transport of stp-Zn complex into the cell. Based on these leads, it may be interesting to extend this study and ascertain whether the metal binding amphiphiles can interfere with the *in vivo* infection process of staphylococci especially in an abscess model.

(5) The prevalence of life-threatening implant-associated infections caused by MRSA biofilm underpins the need for an effective therapeutic intervention. In the present investigation, this significant issue is addressed through multiple experiments. For instance, the antibiotic-loaded C1 micelle could be used to inhibit MRSA biofilm formation on silk surgical suture and hence holds potential to prevent device-associated infections. Further, collagen-impregnated amphiphiles C1 and C2 could hinder MRSA biofilm formation and

the amphiphiles could also render substantial cellular damage in MRSA cells embedded in a 3D collagen matrix saturated with simulated wound fluid, indicating their potential as antibacterials to mitigate wound site infections by MRSA. Interestingly, C1-coated orthopedic S. S. wire could also hinder MRSA biofilm adhesion and thus holds potential as an implant-associated antibacterial coating. The antibiofilm potential of C1 was further validated by gene expression studies, which clearly demonstrated that the amphiphile C1 could hinder expression of the adhesin *fnbA* implicated in biofilm formation and enhance the expression of *hld* involved in biofilm dispersion. In future, it would be interesting to tether the amphiphile through prudent materials chemistry and develop a surface-active coating for implants and test the same for prevention of biofilm infection in an *in vivo* infection model.

(6) In the context of antibacterial drug discovery, it is crucial to establish the *in vivo* efficacy of the candidate molecule. An acute toxicity study conducted on BALB/c mice indicated that the amphiphile C1 was non-toxic upon oral administration of 1000 mg/kg body weight of the animal. Interestingly, topical application of C1 on a skin excision wound model in female BALB/c mice over a period of 14 days rendered nearly complete wound closure, while histopathology and collagen estimation provided strong evidence for wound healing. Infection of a skin wound by staphylococci such as MRSA can delay the wound healing process. Given the strong-anti MRSA potential of C1, it will be worthwhile to ascertain in an animal model whether the amphiphile C1 on topical application can thwart MRSA invasion of a wound area and thereby promote wound healing.

The present investigation essentially provides a broad guideline to the research community working at the interface of synthetic chemistry, molecular microbiology and materials science and motivated to develop synthetic antibacterials that display multimodal activity, are non-toxic and hold therapeutic potential against life-threatening antibiotic-resistant bacteria. A cartoon indicating the salient findings of the present investigation is indicated in **Scheme 1**.

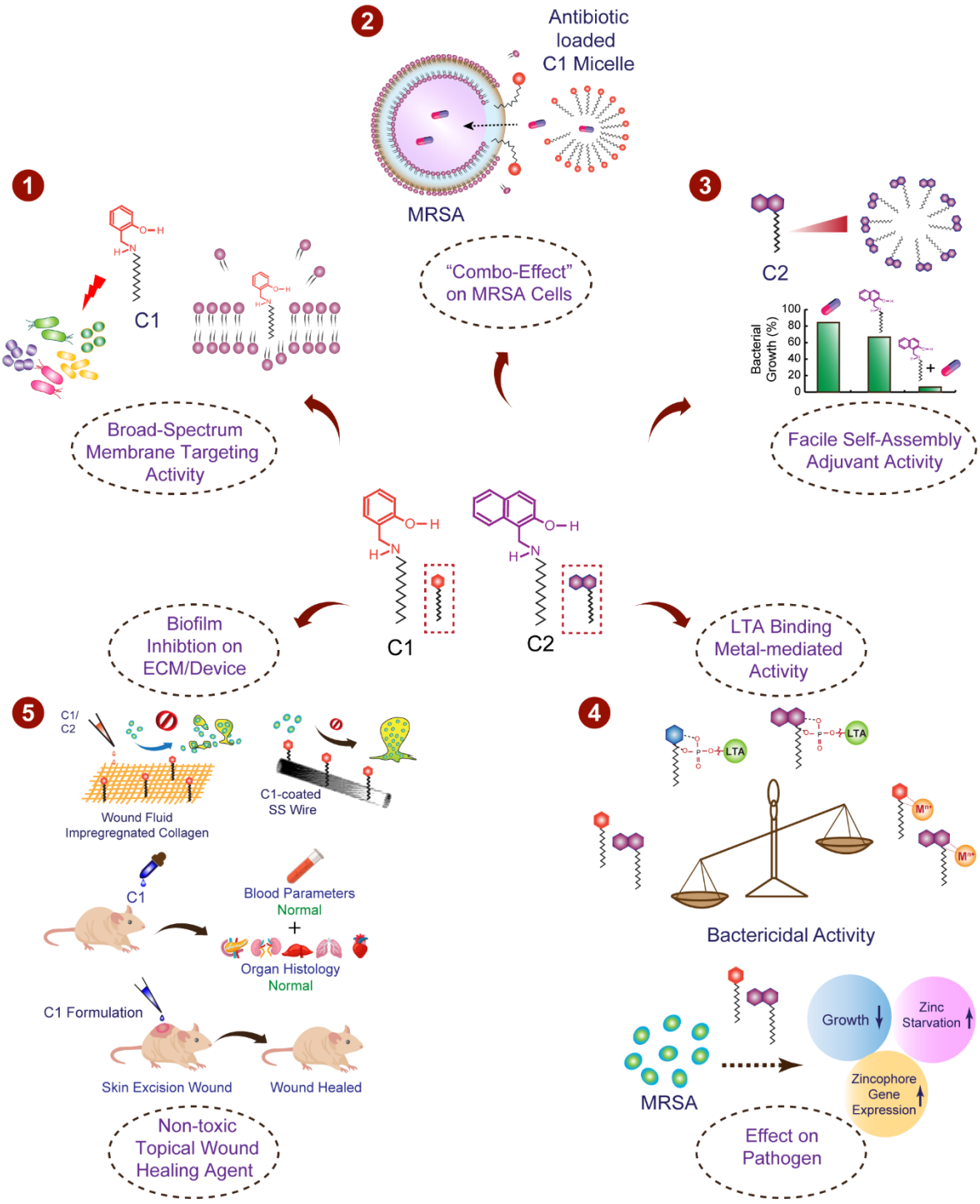

Scheme 1. Graphical representation of the significant findings of the present investigationn.

BIBLIOGRAPHY

1. Adhikari, M. D.; Das, G.; Ramesh, A. Retention of nisin activity at elevated pH in an organic acid complex and gold nanoparticle composite. *Chem. Commun*., **2012**, *48*, 8928-8930.

2. Alekshun, M. N.; Levy, S. B. Molecular mechanisms of antibacterial multidrug resistance. *Cell*, **2007,** *128*, 1037–1050.

3. Allam, A.; Maigre, L.; de Sousa, R. A.; Dumont, E.; Vergalli, J.; Pages, J-M.; Artaud, I. New amphiphilic neamine conjugates bearing a metal binding motif active against MDR *E. aerogenes* Gram-negative bacteria. *Eur. J. Med. Chem*. **2017**, *127*, 748-756.

4. Anderson, J.M. Biological responses to materials. *Annu. Rev. Mater. Res.,* **2001,** *31,* 81–110.

5. Apostol, M.; Baret, P.; Serratrice, G.; Desbrieres, J.; Putaux, J.-L.; Stebe, M.-J.; Expert, D.; Pierre, J.-L. Self-Assembly of an amphiphilic iron (III) chelator: mimicking iron acquisition in marine bacteria, *Angew. Chem.*, **2005**, *117*, 2636-2638.

6. Archer, G. L. *Staphylococcus aureus:* A Well-Armed Pathogen. *Clin. Infect. Dis*., **1998**, *26*, 1179–1181.

7. Archer, G. L. Staphylococcus aureus: a well-armed pathogen. *Clin. Infect. Dis.* **1998**, 26, 1179–1181.

8. Archer, N. K.; Mazaitis, M.; Costerton, W.; Leid, G.; Powers, M. E.; Shirtliff, M. E. *Staphylococcus aureus* biofilms. *Virulence,* **2011**, *2,* 445-459.

9. Arciola, C. R.; Campoccia, D.; Speziale, P.; Montanaro, L.; Costerton, J. W. Biofilm formation in Staphylococcus implant infections. A review of molecular mechanisms and implications for biofilm-resistant materials. *Biomaterials* 2012, *33*, 5967-5982.

10. Arciola, C.R.; Campoccia, D.; Montanaro, L. Implant infections: adhesion, biofilm formation and immune evasion, *Nat. Rev. Microbiol*. **2018,** *16*, 397-409.

11. Arpin, C.; Noury, P.; Boraud, D.; Coulange, L.; Manetti, A.; Andre, C.; M'Zali, F.; Quentin, C. NDM-1-producing *Klebsiella pneumoniae* resistant to colistin in a French community patient without history of foreign travel, *Antimicrob. Agents Chemother.* **2012,** *56*, 3432-3434.

12. Baldassarri, L.; Bertuccini, L.; Ammendolia, M.G.; Arciola, C.R.; Montanaro, L. Effect of iron limitation on slime production by *Staphylococcus aureus*. *Eur. J. Clin. Microbiol. Infect. Dis*. **2001**, *20*, 343-345.

13. Barnes, L.; Cooper, I.R. Biomaterials and Medical Device Associated Infections,1st Edition, Elsevier, **2015,** 1-278.

14. Bartolami E.; Bouillon C.; Dumy P.; Ulrich, S. Bioactive clusters promoting cell penetration and nucleic acid complexation for drug and gene delivery applications: from designed to self-assembled and responsive systems. *Chem. Commun*., **2016**, *52*, 4257-4273.

15. Baum, C.L.; Arpey, C.J. Normal cutaneous wound healing: clinical correlation with cellular and molecular events. *Dermatol. Surg*., **2005**, *31*, 674–686.

16. Bavaro, M. F. *Escherichia coli* O157: What every internist and gastroenterologist should know. *Curr. Gastroenterol. Rep*. **2009**, *11*, 301-306.

17. Bera, S.; Zhanel, G. G.; Schweizer, F. Antibacterial activities of aminoglycoside antibiotics-derived cationic amphiphiles. Polyol-modified neomycin B-, kanamycin A-, amikacin-, and neamine-based amphiphiles with potent broad-spectrum antibacterial activity. *J Med Chem*. **2010**, *53*, 3626-3631.

18. Blair, J. M.; Webber, M. A.; Baylay, A. J.; Ogbolu, D. O.; Piddock, L. J. Molecular mechanisms of antibiotic resistance. *Nat. Rev. Microbiol*. **2015**, *13*, 42-51.

19. Bolla, J. M.; Alibert-Franco, S.; Handzlik, J.; Chevalier, J.; Mahamoud, A.; Boyer, G.; Kiec´-Kononowicz, K; Pages, J. M. Strategies for bypassing the membrane barrier in multidrug resistant Gram-negative bacteria. *FEBS Lett.*, **2011,** *585*, 1682–1690.

20. Bonifer, K.; Fitzgerald, G.; Floyd, J. L.; McKenna, K.; Minahan, N. T.; Walsh, B.; Seifert, K.; Caran, K. L. Colloidal and antibacterial properties of novel triple-headed, double-tailed amphiphiles: Exploring structure–activity relationships and synergistic mixtures. *Bioorg. Med. Chem*. **2015**, *23*, 3566–3573.

21. Bonilla, F.A., Oettgen, H.C. Adaptive immunity. *J. Allergy Clin. Immunol.,* **2010**, *125*, S33-40.

22. Bordi, C.; de Bentzmann, S. Hacking into bacterial biofilms: a new therapeutic challenge. *Ann. Intensive Care*. **2011**, *1*, 19.

23. Brahmachari, S.; Debnath, S.; Dutta, S.; Das, P. K. Pyridinium based amphiphilic hydrogelators as potential antibacterial agents. *Beilstein J. Org. Chem*. **2010**, *6*, 859-868.

24. Brink, A. J.; Coetzee, J.; Clay, C. G.; Sithole, S.; Richards, G. A.; Poirel, L.; Nordmann, P. Emergence of New Delhi Metallo-Beta-Lactamase (NDM-1) and *Klebsiella pneumoniae* Carbapenemase (KPC-2) in South Africa, *J. Clin. Microbiol.* **2012,** *50*, 525-527.

25. Brown, E.D.; Wright, G.D. Antibacterial drug discovery in the resistance era. *Nature* **2016**, *529*, 336-343.

26. Bryers, D. Medical biofilms. *Biotechnol. Bioeng*., **2008**, *100*, 1-18.

27. Burilova, E.A.; Pashirova, T.N.; Lukashenko, S.S.; Sapunova, A.S.; Voloshina, A.D.; Zhiltsova, E.P.; Campos, J.R.; Soutod, E.B.; Zakharova, L.Y. Synthesis, biological evaluation and structure-activity relationships of self-assembled and solubilization properties of amphiphilic quaternary ammonium derivatives of quinuclidine. *J. Mol. Liquids* **2018**, *272*, 722–730.

28. Calfee, D. P. Methicillin-resistant *Staphylococcus aureus* and vancomycin-resistant *Enterococci*, and other Gram-positives in healthcare. *Curr. Opin. Infect. Dis.*, **2012**, *25*, 385–394.

29. Capdevila, D. A.; Wang, J.; Giedroc, D. P. Bacterial strategies to maintain zinc metallostasis at the host-pathogen interface. *J. Biol. Chem*. **2016**, *291*, 20858-20868.

30. Cardoso; Luciana S.; Araujo M. I.; Góes A.M.; Pacífico L.G.; Oliveira R.R.; Oliveira. S.C. Polymyxin B as Inhibitor of LPS contamination of *Schistosoma Mansoni* recombinant proteins in human cytokine analysis. *Microb. Cell Fact.*, **2007**, *6*, 1–6.

31. Centers for Disease Control and Prevention. Antibiotic resistance threats in the United States (2013). Available from: http://www.cdc.gov/drugresistance/ threat-report-2013/pdf/ar-threats-2013-508.pdf

32. Chambers, H. F.; Deleo, F. R.; Waves of resistance: *Staphylococcus aureus* in the Antibiotic Era. *Nat. Rev. Microbiol*, **2010,** *7*, 629–641.

33. Charteris, W. P.; Kelly, P. M.; Morelli, L.; Collins, J. K. Development and application of an *in vitro* methodology to determine the transit tolerance of potentially probiotic *Lactobacillus* and *Bifidobacterium* species in the upper human gastrointestinal tract. *J. Appl. Microbiol.*, **1998**, *84*, 759–768.

34. Chen X.; Hou D.; Wang L.; Zhang Q.; Zou J.; Sun G. Antibacterial surgical silk sutures using a high-performance slow-release carrier coating system. *ACS Appl. Mater. Interfaces*, **2015**, *7*, 22394-22403.

35. Chen, L.; Gao, L.; Fang, W.; Golubovic, L. How the antimicrobial peptides kill bacteria: Computational Physics Insights 1 Introduction. *Commun. Comput. Phys.,* **2012**, *11*, 709–725.

36. Chen, L.; Mirza, R.; Kwon, Y.; DiPietro, L. A.; Koh, T. J. The murine excisional wound model: contraction revisited. *Wound Repair Regen*. **2015**, 23, 874–877.

37. Cheung, G. Y.; Joo, H. S.; Chatterjee, S. S.; Otto, M. Phenol-soluble modulins–critical determinants of staphylococcal virulence. *FEMS Microbiol. Rev.*, **2014**, *38*, 698–719.

38. Cho, S.; Wang, Q.; Swaminathan, C. P.; Hesek, D.; Lee, M; Boons, G. J.; Mobashery, S.; Mariuzza, R.; Structural insights into the bactericidal mechanism of human peptidoglycan recognition proteins. *Proc. Natl. Acad. Sci. U. S. A*., **2007**, *104*, 8761-8766.

39. Chohan, Z.H.; Perrvez, H.; Kausar, S.; Supuran C.T.; Synthesis and characterization of antibacterial Co(II), Cu(II), Ni(II), and Zn(II) complexes of acylhy- drazine derived pyrrolyl compounds. *Synth. React. Inorg. Met. -Org. Chem.* **2002**, *32*, 529–543.

40. Choi, H.; Lee, D. G. Antimicrobial peptide pleurocidin synergizes with antibiotics through hydroxyl radical formation and membrane damage, and exerts antibiofilm activity. *Biochim Biophys Acta*. **2012**, *1820*, 1831-1838.

41. Cissell, D. D.; Link, J. M.; Hu, J. C.; Athanasiou, K. A. A Modified Hydroxyproline Assay Based on Hydrochloric Acid in Ehrlich's Solution Accurately Measures Tissue Collagen Content. *Tissue Eng C*, **2017**, *23*, 243-250.

42. Collin, F.; Karkare, S.; Maxwell, A. Exploiting bacterial DNA gyrase as a drug target: current state and perspectives. *Appl Microbiol Biotechnol*. **2011**, *92*, 479-497.

43. Corbin B.D.; Seeley, E.H.; Raab, A.; Feldmann, J.; Miller, M.R.; Torres, V.J.; Anderson, K.L.; Dattilo, B.M.; Dunman, P.M.; Gerads, R.; Caprioli, R.M.; Nacken, W.; Chazin, W.J.; Skaar, E.P. Metal chelation and inhibition of bacterial growth in tissue abscesses. *Science* **2008**, *319*, 962-965.

44. Costerton, J. W.; Montanaro, L.; Arciola, C. R. Bacterial communications in implant infections: A target for an intelligence war. *Int. J. Artif. Organs* **2007**, *30*, 757-763.

45. Costerton, J. W.; Stewart, P. S.; Greenberg, E. P. Bacterial Bioflms: A Common Cause of Persistent Infections. *Science*, **1999**, *284*, 1318-1322.

46. Cottenye, N.; Anselme, K.; Ploux, L.; Vebert-Nardin, C. Vesicular structures self-assembled from oligonucleotide-polymer hybrids: mechanical prevention of bacterial colonization upon their surface tethering through hybridization. *Adv. Funct. Mater*. **2012**, *22*, 4891–4898.

47. Cotter, P. D.; Gahan, C. G.; Hill, C. Analysis of the role of the *Listeria monocytogenes* F0F1-AtPase operon in the acid tolerance response. *Int. J. Food Microbiol*. **2000**, *60*, 137-146.

48. Cramton, S.E.; Ulrich, M.; Götz, F.; Döring, G. Anaerobic conditions induce expression of polysaccharide intercellular adhesin in *Staphylococcus aureus* and *Staphylococcus epidermidis*. *Infect. Immun*. **2002**, *69*, 4079-4085.

49. Cucarella, C.; Solano, C.; Valle, J.; Amorena, B.; Lasa, I.; Penades, J. R. Bap, a *Staphylococcus aureus* surface protein involved in biofilm formation. *J. Bacteriol*. **2001**, *83*, 2888-2896.

50. Culyba, M. J.; Mo, C. Y.; Kohli, R. M. Targets for combating the evolution of acquired antibiotic resistance. *Biochemistry*, **2015**, *54*, 3573–3582.

51. Dai, T.; Kharkwal, G..; Tanaka, M.; Huang, Y-Y.; de Arce, V. J. B.; Hamblin, M. R. Animal models of external traumatic wound infections. *Virulence* **2011**, *2*, 296-315.

52. Darouiche, R. O. Device-Associated Infections: A Macroproblem that Starts with Microadherence. *Clin. Infect. Dis.*, **2001**,*33*, 1567–1572.

53. Darouiche, R.O. Treatment of infections associated with surgical implants. *N. Engl. J. Med.*, **2004**, *350*, 1422-1429.

54. Davies, D. Understanding biofilm resistance to antibacterial agents. *Nat. Rev. Drug Dis*., **2003**, *2*, 114-122.

55. Davies, J.; Davies, D. Origins and evolution of antibiotic resistance. *Microbiol. Mol. Biol. Rev.*, **2010**, *74*, 417–433.

56. de Almeida, N. R.; Han, Y.; Perez, J.; Kirkpatrick, S.; Wang, Y.; Sheridan, M. C. Design, synthesis, and nanostructure-dependent antibacterial activity of cationic peptide amphiphiles. *ACS Appl. Mater. Interfaces* **2019**, *11*, 2790-2801.

57. de Kraker, M. E. A.; Stewardson, A.; Harbarth, S. Will 10 million people die a year due to antimicrobial resistance by 2050? *PLoS Med*. **2016**, *13*, e1002184.

58. Delavary, B. M.; van der Veer, W.M.; van Egmond, M.; Niessen, F. B.; Beelen, R. H. J. Macrophages in skin injury and repair. *Immunobiol*., **2011**, *216*, 753-762.

59. Delcour, A. H. Outer membrane permeability and antibiotic resistance. *Biochim.Biophys. Acta*., **2009**, *1794*, 808-816.

60. Dempsey, P.W.; Vaidya, S.A.; Cheng, G. The art of war: Innate and adaptive immune responses. *Cell. Mol. Life Sci.,* **2003**, *60*, 2604–2621.

61. Deresinski S. Vancomycin heteroresistance and methicillin-resistant *Staphylococcus aureus. J. Infect. Dis*., **2009**, *199*, 605.

62. Deresinski, S., Methicillin-Resistant *Staphylococcus aureus*: An evolutionary, epidemiologic, and therapeutic odyssey. *Clin. Infect. Dis*., **2005**, *40*, 562-573.

63. Diemond-Hernandez, B.; Solorzano-Santos, F.; Leanos-Miranda, B.; Peregrino-Bejarano, L.; Miranda-Novales, G. Production of icaADBC-encoded polysaccharide intercellular adhesin and therapeutic failure in pediatric patients with Staphylococcal device-related infections. *BMC Infect*. *Dis*. **2010**, *10*, 68.

64. Drulis-Kawa and A. Dorotkiewicz-Jach, Liposomes as delivery systems for antibiotics. *Int. J. Pharm*., **2010**, *387*, 187–198.

65. Edwards, C. A.; O'Brien, W. D. Modified assay for determination of hydroxyproline in a tissue hydrolyzate. *Clin. Chim. Acta*, **1980**, *104*, 161–167.

66. Ejim L.; Farha M. A.; Falconer S. B.; Wildenhain J.; Coombes B. K.; Tyers M.; Brown E. D.; Wright G. D. Combinations of antibiotics and nonantibiotic drugs enhance antimicrobial efficacy. *Nat. Chem. Biol.,* **2011**, *7*, 348-350.

67. Elasri, M. O., Thomas, J. R.; Skinner, R. A.; Blevins, J. S.; Beenken, K. E.; Nelson, C. L.; Smelter, M. S. *Staphylococcus aureus* collagen adhesin contributes to the pathogenesis of osteomyelitis. *Bone*, **2002**, *30*, 275–280.
68. Eleswarapu, S.V.; Responte, D.J.; Athanasiou, K.A. Tensile properties, collagen content, and crosslinks in connective tissues of the immature knee joint. *PLoS One* **2011**, *6*, e26178.
69. Epand, R. M.; Epand, R. F. Lipid domains in bacterial membranes and the action of antimicrobial agents. *Biochim. Biophys. Acta*, **2009**, *1788*, 289-294.
70. Everds, N.E. Evaluation of clinical pathology data: correlating changes with other study data. *Toxicol Pathol*., **2015**, *43*, 90–97.
71. Faig, A.; Arthur, T. D.; Fitzgerald, P. O.; Chikindas, M.; Mintzer, E.; Uhrich, K. E. Biscationic tartaric acid-based amphiphiles: charge location impacts antimicrobial activity. *Langmuir* **2015**, *31*, 11875−11885.
72. Fair, R. J., & Tor, Y. Antibiotics and bacterial resistance in the 21st century. *Perspect. Medicin. Chem.*, **2014,** 25–64.
73. Falagas, M. E.; Kasiakou S.K. Toxicity of polymyxins: A systematic review of the evidence from old and recent studies. *Crit. Care*., **2006**, *10*, R27.
74. Fernandez, L.; Hancock, R. E. Adaptive and mutational resistance: role of porins and efflux pumps in drug resistance. *Clin. Microbiol. Rev*. **2012**, *25*, 661-681.
75. Findlay, B.; Zhanel, G. G.; Schweizer, F. Cationic amphiphiles, a new generation of antimicrobials inspired by the natural antimicrobial peptide scaffold. *Antimicrob. Agents Chemother.*, **2010**, *54*, 4049–4058.
76. Fischbach M. A. Combination therapies for combating antimicrobial resistance. *Curr. Opin. Microbiol*., **2011**, *14*, 519-523.
77. Fischbach, M. A.; Walsh, C. T. Antibiotics for emerging pathogens, *Science* **2009**, *325*, 1089-1093.

78. Fischer D.; Li Y.; Ahlemeyer B.; Krieglstein J.; Kissel T. *In vitro* cytotoxicity testing of polycations: influence of polymer structure on cell viability and hemolysis. *Biomaterials*, **2003**, *24*, 1121-1131.

79. Flemming, H. C.; Wingender, J. The biofilm matrix. *Nat. Rev. Microbiol*. **2010**, *8*, 623-633.

80. Floyd, J. L.; Smith, K. P.; Kumar, S. H.; Floyd, J. T.; Varela, M. F. LmrS is a multidrug efflux pump of the major facilitator superfamily from *Staphylococcus aureus*. *Antimicrob. Agents Chemother.* **2010**, *54*, 5406-5412.

81. Foster, J. W. *Escherichia coli* acid resistance: tales of an amateur acidophile. *Nat. Rev. Microbiol*. **2004**, *2*, 898-907.

82. Foster, J. W. When protons attack: microbial strategies of acid adaptation. *Curr. Opin. Microbiol*. **1999**, *2*, 170-174.

83. French, S.; Puddephatt, D.; Habash, M.; Glasauer, S., The dynamic nature of bacterial surfaces: Implications for metal–membrane interaction. *Crit. Rev. Microbiol*., **2013**, *39*, 196-217.

84. Fuente-Nunez, C. D. L.; Reffuveille, F.; Fernandez, L.; Hancock, R. E. WW. Bacterial biofilm development as a multicellular adaptation: antibiotic resistance and new therapeutic strategies. Curr. Opin. Microbiol., **2013**, *16*, 580–589.

85. Fukushima K.; Tan J. P. K.; Korevaar P. A.; Yang Y. Y.; Pitera J.; Nelson A.; Maune H.; Coady D. J.; Frommer J. E.; Engler A. C.; Huang Y.; Xu K.; Ji Z.; Qiao Y.; Fan W.; Li L.; Wiradharma N.; Meijer E. W.; Hedrick J. L. Broad-spectrum antimicrobial supramolecular assemblies with distinctive size and shape. *ACS Nano*, **2012**, *6*, 9191-9199.

86. Fux, C. A.; Costerton, J. W.; Stewart, P. S.; Stoodley, P. Survival strategies of infectious biofilms. *Trends Microbiol*. **2005**, *13*, 34-40.

87. Geoghegan, J. A.; Corrigan, R. M.; Gruszka, D. T.; Speziale, P.; O'Gara, J. P.; Potts, J. R.; Foster, T. J. Role of surface protein SasG in biofilm formation by *Staphylococcus aureus*. *J. Bacteriol*. **2010**, *192*, 5663-5673.

88. Ghssein, G.; Brutesco, C.; Ouerdane, L.; Fojcik, C.; Izaute, A.; Wang, S.; Hajjar, C.; Lobinski, R.; Lemaire, D.; Richaud, P.; Voulhoux, R.; Espaillat, A.; Cava, F.; Pignol, D.; Borezée-Durant, E.; Arnoux, P. Biosynthesis of a broad-spectrum nicotianamine-like metallophore in *Staphylococcus aureus*. *Science* **2016**, *352*, 1105-1109.

89. Giacometti, A; Oscar C.; Maria S.; Del P.; Alessandra M.; Marcello M.; D. Errico; Giorgio S. Combination studies between polycationic peptides and clinically used antibiotics against gram-positive and gram-negative bacteria., *Peptides*, **2000**, *21*, 1155–1160.

90. Gokel, G. W.; Negin, S. Synthetic membrane active amphiphiles. *Adv. Drug Del. Rev.*, **2012**, *64*, 784–796.

91. Gootz, T. D. The global problem of antibiotic resistance. *Crit. Rev. Immun*. **2010**, *30*, 79-93.

92. Goswami, S.; Adhikari M.D.; Kar C.; Thiyagarajan D.; Das G.; Ramesh A. Synthetic amphiphiles as therapeutic antibacterials: Lessons on bactericidal efficacy and cytotoxicity and potential application as an adjuvant in antimicrobial chemotherapy. *Journal of Materials Chemistry B*, **2013**, *1*, 2612-2623.

93. Goswami, S.; Thiyagarajan, D.; Samanta, S.; Das, G.; Ramesh, A. A zinc complex of a neutral pyridine-based amphiphile: a highly efficient and potentially therapeutic bactericidal material. *J. Mater. Chem. B*, **2015**, *3*, 7068-7078.

94. Griffin, W C. Calculation of HLB values of non-ionic surfactants. *J. Soc. Cosmet. Chem*., **1954**, *5*, 249-256.

95. Griffin, W C. Classification of the surface-active agents by HLB. *J. Soc. Cosmet. Chem*., **1949**, *1*, 311-326.

96. Grim, K. P.; Francisco, B. S.; Radin, J. N.; Brazel, E. B.; Kelliher, J. L.; Solorzano, P. K. P.; Kim, P. C.; McDevitt, C. A.; Kehl-Fiea, T. E. The metallophore staphylopine enables *Staphylococcus aureus* to compete with the host for zinc and overcome nutritional immunity. *mBio,* **2017**, *8,* e01281-17.

97. Guo, Y.; Ramos, R. I.; Cho, J. S.; Donegan, N. P.; Cheung, A. L.; Miller, L. S. *In vivo* bioluminescence imaging to evaluate systemic and topical antibiotics against community-acquired methicillin-resistant *Staphylococcus aureus*-infected skin wounds in mice. *Antimicrob. Agents Chemother*. **2013**, *57*, 855–863.

98. Gutsmann, T.; Seydel, U. Impact of the glycostructure of amphiphilic membrane components on the function of the outer membrane of Gram-negative bacteria as a matrix for incorporated channels and a target for antimicrobial peptides or proteins. *Eur. J. Cell Biol*. **2010**, *89*, 11-23.

99. Habash, M; Reid G. Microbial biofilms: their development and significance for medical device-related infections. *J. Clin. Pharmacol.,* **1999**, *39*, 887–898.

100. Haldar, J.; Kondaiah, P.; Bhattacharya, S. Synthesis and antibacterial properties of novel hydrolyzable cationic amphiphiles. Incorporation of multiple head groups leads to impressive antibacterial activity. *J Med Chem*. **2005**, *48*, 3823-3831.

101. Hall, C.W.; Mah, T.F. Molecular mechanisms of biofilm-based antibiotic resistance and tolerance in pathogenic bacteria. *FEMS Microbiol. Rev*., **2017**, *41*, 276-301.

102. Hall-Stoodley, L; Costerton, J.W.; Stoodley, P; Bacterial biofilms: from the natural environment to infectious diseases. *Nat. Rev. Microbiol.* **2004**, *2*, 95–108.

103. Harris, T. L.; Worthington, R. J.; Melander, C. Potent small-molecule suppression of oxacillin resistance in methicillin-resistant *Staphylococcus aureus*. *Angew. Chemie - Int. Ed.*, **2012**, *51*, 11254–11257.

104. Hawkey, P. M.; Jones, A. M. The changing epidemiology of resistance. *J. Antimicrob. Chemother*. **2009**, *64 Suppl 1*, i3-10.

105. Hayden M. K.; Rezai K.; Hayes R.; Lolans K.; Quinn J. P.;Weinstein R. Development of daptomycin resistance *in Vivo* in methicillin-resistant *Staphylococcus aureus*. *J. Clin. Microbiol*., **2005**, *43*, 5285-5287.

106. Heilmann, C.; Hussain, M.; Peters, G.; Götz, F. Evidence for autolysin-mediated primary attachment of *Staphylococcus epidermidis* to a polystyrene surface. *Mol. Microbiol*. **1997**, *24*, 1013-1024.

107. Helander, I. M.; Mattila-Sandholm, T., Permeability barrier of the gram-negative bacterial outer membrane with special reference to nisin. *Int. J. Food Microbiol.*, **2000**, *60*, 153-161.

108. Herzog, I. M.; Fridman, M. Design and synthesis of membrane-targeting antibiotics: from peptides- to aminosugar-based antimicrobial cationic amphiphiles. *MedChemComm*, **2014**, *5*, 1014-1026.

109. Hess, D. J.; Henry-Stanley, M. J.; Wells, C. L. Antibacterial synergy of glycerol monolaurate and aminoglycosides in *Staphylococcus aureus* biofilms. *Antimicrob. Agents Chemother*. **2014,** 58, 6970–6973.

110. Hetrick, EM; Schoenfisch, M.H. Reducing implant-related infections: active release strategies. *Chem. Soc. Rev.*, **2006,** *35*, 780–789.

111. Hidron, A.; Edwards, J.; Patel, J.; Horan, T. Update: antimicrobial-resistant pathogens associated with healthcare-associated infections: annual summary of data reported to the National Healthcare. *Infec. Cont. Hosp. Epidem.*, **2008**, *29*, 996–1011.

112. Hoefel, D.; Grooby, W. L.; Monis, P. T.; Andrews, S.; Saint, C. P. A comparative study of carboxyfluorescein diacetate and carboxyfluorescein diacetate succinimidyl ester as indicators of bacterial activity. *J. Microbiol. Methods*, **2003**, *52*, 379-388.

113. Hoiby, N.; Bjarnsholt, T.; Givskovb, M.; Molin, S.; Ciofu, O. Antibiotic resistance of bacterial biofilms. *Int. J. Antimicrob. Agents* **2010**, *35*, 322-332.

114. Hood, M.I.; Skaar, E.P. Nutritional immunity: transition metals at the pathogen-host interface. *Nat. Rev. Microbiol*. **2012**, *10*, 525-537.

115. Hoque, J.; Akkapeddi, P.; Yarlagadda, V.; Uppu, D. S.; Kumar, P.; Haldar, J. Cleavable cationic antibacterial amphiphiles: synthesis, mechanism of action, and cytotoxicities, *Langmuir* **2012,** *28*, 12225-12234.

116. Horcas, I. et al. WSXM: A software for scanning probe microscopy and a tool for nanotechnology. *Rev. Sci. Instrum*. **2007**, *78*, 013705.

117. Houlihan H. H.; Mercier R. C.; Rybak M. J.; Pharmacodynamics of vancomycin alone and in combination with gentamicin at various dosing intervals against methicillin-resistant *Staphylococcus aureus* -Infected Fibrin- Platelet Clots in an *in vitro* infection model. *Antimicrob. Agents Chemother*., **1997**, *41*, 2497-2501.

118. Hu X.; Le X.; Li D.; Shao L.; Dong X.; He X. P.; Chen G. R.; Chen D., Triazole-linked glycolipids enhance the susceptibility of MRSA to β-Lactam antibiotics. *ACS Med. Chem. Lett.*, **2015**, *6*, 793-797.

119. Hubner, G.; Brauchle, M.; Smola, H.; Madlener, M.; Fässler, R.; Werner, S. Differential regulation of pro-inflammatory cytokines during wound healing in normal and glucocorticoid-treated mice. *Cytokine*, **1996**, *8*, 548–556.

120. Hurdle, J. G.; O'Neill, A. J.; Chopra, I.; Lee, R. E. Targeting bacterial membrane function: an underexploited mechanism for treating persistent infections. *Nat. Rev. Microbiol*. **2011**, *9*, 62-75.

121. Inoue, Y.; Hagi, A.; Nii, T.; Tsubotani, Y.; Nakata, H.; Iwata, K. Novel antiseptic compound OPB-2045G shows potent bactericidal activity against methicillin-resistant *Staphylococcus aureus* and vancomycin-resistant *Enterococcus* both *in vitro* and *in vivo*: a pilot study in animals. *J. Med. Microbiol*. **2015**, *64*, 32–36.

122. Ishikawaa, A. A.; Salazarb, J. V.; Salinasc, M.; Gaitania, C. M.; Nurkiewiczd, T.; Negretec, G. R.; Garciae, C. D. Self-assembled nanospheres for encapsulation and aerosolization of rifampicin. *RSC Adv*. **2016**, *6*, 12959–12963.

123. Ivanova, E. P.; Nguyen, S. H.; Guo, Y.; Baulin, V. A.; Webba, H. K.; Truong, V. K.; Wandiyanto, J. V.; Garvey, C. J.; Mahon, P. J.; Mainwaring, D. E.; Crawford, R. J. Bactericidal activity of self-assembled palmitic and stearic fatty acid crystals on highly ordered pyrolytic graphite. *Acta Biomater*. **2017**, *59*, 148–157.

124. Jennings, M. C.; Buttaro, B. A.; Minbiole, K. P. C.; Wuest, W. M. Bioorganic investigation of multicationic antimicrobials to combat qac-resistant *Staphylococcus aureus*. *ACS Infect. Dis*. **2015**, *1*, 304−309.

125. Jennings, M. C.; Minbiole, K. P. C.; Wuest, W. M. Quaternary ammonium compounds: an antimicrobial mainstay and platform for innovation to address bacterial resistance. *ACS Infect. Dis*. **2015**, *1*, 288−303.

126. Jiang, Z.; Vasil, A. I.; Hale, J. D.; Hancock, R. E.; Vasil, M. L.; Hodges, R. S. Effects of net charge and the number of positively charged residues on the biological activity of amphipathic alpha-helical cationic antimicrobial peptides. *Biopolymers*. **2008**, *90*, 369-383.

127. Jin, Y.; Shao, C.; Li, J.; Fan, H.; Bai, Y.; Wang, Y. Outbreak of multidrug resistant NDM-1-producing *Klebsiella pneumoniae* from a neonatal unit in Shandong Province, China, *PLoS One,* **2015,** *10*, e0119571.

128. Marafino, J. N.; Gallagher, T. M.; Barragan, J.; Volkers, B. L.; Ladow, J. E.; Bonifer, K.; Fitzgerald, G; Floyd, J.L.; McKenna, K; Minahan, N.T.; Walsh, B; Seifert, K; Caran, K. L; Colloidal and antibacterial properties of novel triple-headed, double-tailed amphiphiles: Exploring structure-activity relationships and synergistic mixtures. *Bioorganic and Medicinal Chemistry,* **2015,** *23*, 3566–3573.

129. Johnston, C. W.; Skinnider, M. A.; Dejong, C. A.; Rees, P. N.; Chen, G. M.; Walker, C. G.; French, S.; Brown, E. D.; Berdy, J.; Liu, D. Y.; Magarvey, N. A. Assembly and clustering of natural antibiotics guides target identification, *Nat. Chem. Biol.***2016,** *12*, 233-239.

130. Joo, H. S.; Cheung, G. Y; Otto, M. Antimicrobial activity of community-associated methicillin-resistant *Staphylococcus aureus* is caused by phenol-soluble modulin derivatives. *J. Biol. Chem*., **2011**, *286*, 8933–8940.

131. Joo, H.S.; Otto, M.; Molecular basis of *in vivo* biofilm formation by bacterial pathogens. *Chem. Biol*., **2012,** *19*, 1503-1513.

132. Kaatz, G. W.; McAleese, F.; Seo, S. M. Multidrug resistance in *Staphylococcus aureus* due to overexpression of a novel multidrug and toxin extrusion (MATE) transport protein. *Antimicrob. Agents Chemother.* **2005**, *49*, 1857-1864.

133. Kaatz, G. W.; Seo, S. M.; Ruble, C. A. Efflux-mediated fluoroquinolone resistance in *Staphylococcus aureus*. *Antimicrob. Agents Chemother.* **1993**, *37*, 1086-1094.

134. Kalhapure, R. S.; Jadhav, M.; Rambharose, S.; Mocktar, C.; Singh, S.; Renukuntla, J.; Govender, T. pH-responsive chitosan nanoparticles from a novel twin-chain anionic amphiphile for controlled and targeted delivery of vancomycin. *Colloids Surf. B: Biointerfaces*. **2017**, *158*, 650–657.

135. Kanazawa, A.; Ikeda, T.; Endo, T. Synthesis and antimicrobial activity of dimethyl- and trimethyl-substituted phosphonium salts with alkyl chains of various lengths. *Antimicrob Agents Chemother*. **1994**, *38*, 945-952.

136. Kapoor, V.; Rai, R.; Thiyagarajan, D.; Mukherjee, S.; Das, G.; Ramesh, A. A Nonbactericidal Zinc-Complexing Ligand as a Biofilm Inhibitor: Structure-Guided Contrasting Effects on Staphylococcus aureus Biofilm. *ChemBioChem*, **2017**, *18*, 1502–1509.

137. Katz S.; Izhar M.; Mirelman D. Bacterial adherence to surgical sutures. A possible factor in suture induced infection. *Ann. Surg*. **1981,** *194*, 35–41.

138. Kaye, K. S.; Kaye, D. Multidrug-resistant pathogens: mechanisms of resistance and epidemiology. *Curr. Infect. Dis. Rep*. **2000**, *2*, 391-398.

139. Kehl-Fie T.E.; Chitayat, S.; Hood, M.I.; Damo, S.; Restrepo, N.; Garcia, C.; Munro, K.A.; Chazin, W.J.; Skaar, E.P. Nutrient metal sequestration by calprotectin inhibits bacterial superoxide defense, enhancing neutrophil killing of *Staphylococcus aureus*. *Cell Host Microbe* **2011**, *10*, 158-164.

140. Khondker, A.; Dhaliwal A. K.; Saem S.; Mahmood A.; Fradin C; Moran-Mirabal J.; Rheinstädter M.C. Membrane charge and lipid packing determine polymyxin-induced membrane damage. *Commun. Biol.*, **2019**, *67*, 1–11.

141. Klein, J.S.; Lewinson, O. Bacterial ATP-driven transporters of transition metals: physiological roles, mechanisms of action, and roles in bacterial virulence. *Metallomics* **2011**, *3*, 1098-1108.

142. Kohanski, M. A.; Dwyer, D. J.; Collins, J. J. How antibiotics kill bacteria: from targets to networks. *Nat. Rev. Microbiol*. **2010**, *8*, 423-435.

143. Kohler, T.; Weidenmaier, C.; Peschel, A. Wall teichoic acid protects *Staphylococcus aureus* against antimicrobial fatty acids from human skin. *J. Bacteriol*. **2009**, *191*, 4482-4484.

144. Konai, M. M.; Haldar, J. Lysine-based small molecules that disrupt biofilms and kill both actively growing planktonic and nondividing stationary phase bacteria, *ACS. Infect. Dis.* **2015,** *1*, 469-478.

145. Kontos, R. C.; Schallenhammer, S. A.; Bentley, B. S.; Morrison, K. R.; Feliciano, J. A.; Tasca, J. A.; Kaplan, A. R. Bezpalko, M. W.; Kassel, W. S.; Wuest, W. M.; Minbiole, K. P. C. An investigation into rigidity–activity relationships in bisqac amphiphilic antiseptics. *ChemMedChem* **2019**, *14*, 83-87.

146. Kostakioti, M.; Hadjifrangiskou, M.; Hultgren, S. J. Bacterial biofilms: development, dispersal, and therapeutic strategies in the dawn of the postantibiotic era. *Cold Spring Harb. Perspect. Med*. **2013**, *3*, a010306.

147. Kouidhi, B.; Zmantar, T.; Hentati, H.; Bakhrouf, A. Cell surface hydrophobicity, biofilm formation, adhesives properties and molecular detection of adhesins genes in *Staphylococcus aureus* associated to dental caries. *Microb. Pathog.*, **2010**, *49*, 14–22.

148. Kugelberg, E.; Norstrom, T.; Petersen, T. K.; Duvold, T.; Andersson, D. I.; Hughes, D. Establishment of a Superficial Skin Infection Model in Mice by Using *Staphylococcus aureus* and *Streptococcus pyogenes*. *Antimicrob. Agents Chemother*., **2005**, *49*, 3435-3441.

149. Kugelberg, E.; Norstrom, T.; Petersen, T. K.; Duvold, T.; Andersson, D. I.; Hughes, D. Establishment of a superficial skin infection model in mice by using *Staphylococcus aureus* and *Streptococcus pyogenes*. *Antimicrob. Agents Chemother*. **2005**, *49*, 3435-3441.

150. Kulkarni, R.; Antala, S.; Wang, A.; Amaral, F. E.; Rampersaud, R.; LaRussa, S. J.; Plant, P. ; Ratner, A. J. Cigarette smoke increases *Staphylococcus aureus* biofilm formation via oxidative stress. *Infect. Immun.*, **2012**, *80*, 3804–3811.

151. Kumar, S.; Varela, M. F. Molecular mechanisms of bacterial resistance to antimicrobial agents. *Chemotherapy* **2013**, *14*, 18.

152. Kuroda, K.; DeGrado, W. F. Amphiphilic polymethacrylate derivatives as antimicrobial agents. *J Am Chem Soc*. **2005**, *127*, 4128-4129.

153. LaDow, J. E.; Warnock, D. C.; Hamill, K. M.; Simmons, K. L.; Davis, R. W.; Schwantes, C. R.; Flaherty, D. C.; Willcox, J. A.; Wilson-Henjum, K.; Caran, K. L.; Minbiole, K. P.; Seifert, K. Bicephalic amphiphile architecture affects antibacterial activity. *Eur. J. Med. Chem*. **2011**, *46*, 4219-4226.

154. Lambert, P.A. Mechanisms of antibiotic resistance in *Pseudomonas aeruginosa*. *J. Roy. Soc. Med.* **2002**, *95 (suppl 41)*, 22-26.

155. Lamp, K. C.; Rybak, M. J.; Bailey, E. M.; Kaatz, G. W. *In vitro* pharmacodynamic effects of concentration, pH, and growth phase on serum bactericidal activities of daptomycin and vancomycin. *Antimicrob. Agents Chemother*. **1992**, *36*, 2709-2714

156. Lange, R. P.; Locher, H. H.; Wyss, P. C.; Then, R. L. The targets of currently used antibacterial agents: lessons for drug discovery. *Curr Pharm Des*. **2007**, *13*, 3140-3154.

157. LaPlante, K. L.; Woodmansee, S. Activities of daptomycin and vancomycin alone and in combination with rifampin and gentamicin against biofilm-forming methicillin-resistant *Staphylococcus aureus* isolates in an experimental model of endocarditis. *Antimicrob. Agents Chemother.*, **2009,** *53*, 3880–3886.

158. Lee, A. S.; Lencastre, H. D.; Garau, Javier.; Kluytmans, J.; Malhotra-kumar, S.; Peschel, A.; Harbarth, S. Methicillin-resistant *Staphylococcus aureus*. *Nat. Rev. Dis. Primer* **2018**, *4*, 18033.

159. Lenz, A. P.; Williamson, K. S.; Pitts, B.; Stewart, P. S.; Franklin, M. J. Localized gene expression in *Pseudomonas aeruginosa* biofilms. *Appl. Environ. Microbiol*. **2008**, *74*, 4463-4471.

160. Lewis, K. Multidrug tolerance of biofilms and persister cells. *Curr. Top. Microbiol. Immunol*. **2008**, *322*, 107-131.

161. Lewis, K. Platforms for antibiotic discovery. *Nat. Rev. Drug. Discov*. **2013**, *12*, 371-387.

162. Li Y.; Kumar K. N.; Dabkowski J. M.; Corrigan M.; Scott R. W.; Nu¨sslein K.; Tew G. N. New bactericidal surgical suture coating. *Langmuir*, **2012**, *28*, 12134-12139.

163. Li, X. Z.; Nikaido, H. Efflux-mediated drug resistance in bacteria: an update. *Drugs* **2009**, *69*, 1555-1623.

164. Lin, S.; Koh, J-J.; Aung, T. T.; Lim, F.; Li, J.; Zou, H.; Wang, L.; Lakshminarayanan, R.; Verma, C.; Wang, Y.; Tan, D. T. H.; Cao, D.; Beuerman, R. W.; Ren, L.; Liu, S. Symmetrically substituted xanthone amphiphiles combat Gram-positive bacterial resistance with enhanced membrane selectivity. *J. Med. Chem*. **2017**, *60*, 1362−1378.

165. Liu S. Q.; Venkataraman S.; Ong Z. Y.; Chan J. M. W.; Yang C.; Hedrick J. L.; Yang Y. Y. Overcoming multidrug resistance in microbials using nanostructures self-assembled from cationic bent-core oligomers. *Small*, **2014**, *10*, 4130-4135.

166. Liu, C.; Krishnan, J.; Xu, X. Y. Intrinsic and induced drug resistance mechanisms: *in silico* investigations at the cellular and tissue scales. *Integrative Biology*, **2015**, *7*, 1044–1060.

167. Livak, K.J.; Schmittgen, T.D. Analysis of relative gene expression data using real-time quantitative PCR and the 2(-Delta Delta C(T)) Method. *Methods* **2001**, *25*, 402-408.

168. Lowy, F.D. *Staphylococcus aureus* infections. *N. Engl. J. Med*., **1998**, *339*, 520-532.

169. Luo, X.; Miao, W.; Wu, S.; Liang, Y. Spontaneous Formation of Vesicles from Octadecylamine in Dilute Aqueous Solution Induced by Ag(I) Ion, *Langmuir*, **2002**, *18*, 9611-9612.

170. Luo, X.; Wu, S.; Liang, Y. Vesicle formation induced by metal ions from micelle-forming sodium hexadecylimino diacetate in dilute aqueous solution, *Chem. Commun.* **2002**, *5*, 492-493.

171. Ma, Z.; Yang, J.; Han, J.; Gao, L.; Liu, H.; Lu, Z.; Zhao, H.; Bie, X. Insights into the antimicrobial activity and cytotoxicity of engineered α-helical peptide amphiphiles, *J. Med. Chem.* **2016,** *59*, 10946-10962.

172. Madani, A.; Garakani, K.; Mofrad, M. R. K. Molecular mechanics of *Staphylococcus aureus* adhesin, CNA, and the inhibition of bacterial adhesion by stretching collagen. *PLoS One*, **2017**, *12*, e0179601.

173. Maeda H. Macromolecular therapeutics in cancer treatment: The EPR effect and beyond. *J. Control. Release*, **2012**, *164*, 138–144.

174. Marques, M. R. C.; Loebenberg, R.; Almukainzi, M. Simulated biological fluids with possible application in dissolution testing. *Dissolution Technologies*, **2011**, 15–28.

175. Marr, A. K.; Gooderham, W. J.;Hancock, R. E. W. Antibacterial peptides for therapeutic use : obstacles and realistic outlook. *Curr. Opin. Pharmacol.*, **2006**, 468–472.

176. Marra, A. Animal models in drug development for MRSA, In *Methicillin-Resistant Staphylococcus aureus (MRSA) Protocols*. 2nd Edition, Yinduo, J., Ed.; Humana Press; Springer Science 2014; pp 333-345.

177. Martinez, J. S.; Carter-Franklin, J. N.; Mann, E. L.; Martin, J. D.; Haygood, M. G.; Butler, A. Structure and membrane affinity of a suite of amphiphilic siderophores produced by a marine bacterium. *Proc. Natl. Acad. Sci. U.S.A.*, **2003**, *100*, 3754-3759.

178. Marty F. M.; Yeh W., Wennersten C. B.; Venkataraman L.; Albano E.; Alyea E. P.; Gold H. S.; Baden L. R.; Pillai S. K. Emergence of a clinical daptomycin resistant *Staphylococcus aureus* isolate during treatment of methicillin resistant *Staphylococcus aureus* bacteremia and osteomyelitis. *J. Clin. Microbiol*., **2006**, *44*, 595-597.

179. Mather, A. E.; Reid, S. W.; Maskell, D. J.; Parkhill, J.; Fookes, M. C.; Harris, S. R.; Brown, D. J.; Coia, J. E.; Mulvey, M. R.; Gilmour, M. W.; Petrovska, L.; de Pinna, E.; Kuroda, M.; Akiba, M.; Izumiya, H.; Connor, T. R.; Suchard, M. A.; Lemey, P.; Mellor, D. J.; Haydon, D. T.; Thomson, N. R. Distinguishable epidemics of multidrug-resistant *Salmonella Typhimurium* DT104 in different hosts. *Science* **2013**, *341*, 1514-1517.

180. McCarthy H.; Rudkin J. K.; Black N. S.; Gallagher L.; O'Neill E.;O'Gara J. P. Methicillin resistance and the biofilm phenotype in *Staphylococcus aureus. Front. Cell. Infect. Microbiol*., **2015**, *5*, 1-9.

181. McCoy, L. S.; Xie, Y.; Tor, Y. Antibiotics that target protein synthesis. *Wiley Interdiscip. Rev. RNA*. **2011**, *2*, 209-232.

182. McInnes, E. (Ed.) Pathology for Toxicologists: Principles and Practices of Laboratory Animal Pathology for Study Personnel, *Wiley-Blackwell* **2017**, 1-216.

183. Menzies, B.E. The role of fibronectin binding proteins in the pathogenesis of *Staphylococcus aureus* infections. *Curr. Opin. Infect. Dis*., **2003**, *16*, 225–229.

184. Mercier, R. C.; Stumpo, C.; Rybak, M. J. Effect of growth phase and pH on the *in vitro* activity of a new glycopeptide, oritavancin (LY333328), against *Staphylococcus aureus* and *Enterococcus faecium*. *J. Antimicrob Chemother*. **2002**, *50*, 19-24.

185. Merrell, D. S.; Camilli, A. Acid tolerance of gastrointestinal pathogens. *Curr. Opin. Microbiol.,* **2002**, *5*, 51-55.

186. Miller R.P; Laehnemann D.; Jansen G.; Fuentes-Hernandez A.; Rosenstiel P.; Schulenburg H.; Beardmore R. When the most potent combination of antibiotics selects for the greatest bacterial load: the smile-frown transition. *PLoS Biology*, **2013**, *11*, e1001540.

187. Mingeot-Leclercq, M-P.; Jean-Luc, D. Bacterial lipid membranes as promising targets to fight antimicrobial resistance, molecular foundations and illustration through the renewal of aminoglycoside antibiotics and emergence of amphiphilic aminoglycosides. *Med. Chem. Commun*. **2016**, *7*, 586-611.

188. Mintzer, M. A.; Dane, E. L.; O'Toole, G. A.; Grinstaff, M. W. Exploiting Dendrimer multivalency to combat emerging and re-emerging infectious diseases. *Mol. Pharmaceutics* **2012**, *9*, 342-354.

189. Mitra, M.; Asad, M.; Kumar, S;, Yadav, K.; Chaudhary, S.; Bhavesh, N. S.; Khalid,S; Thukral,L; Bajaj, A. Distinct intramolecular hydrogen bonding dictates antimicrobial action of membrane-targeting amphiphiles. *J. Phy. Chem. Lett.*, **2019**, *10*, 754–760.

190. Mitra, R. N.; Shome, A.; Paul, P.; Das, P. K. Antimicrobial activity, biocompatibility and hydrogelation ability of dipeptide-based amphiphiles. *Org. Biomol. Chem*. **2009**, *7*, 94-102.

191. Mitra, R. N.; Shome, A.; Paul, P.; Das, P. K. Antimicrobial activity, biocompatibility and hydrogelation ability of dipeptide-based amphiphiles. *Org Biomol Chem*. **2009**, *7*, 94-102.

192. Mohammed, Y. H. E.; Manukumar, H. M.; Rakesh, K. P.; Karthik, C. S.; Mallu, P.; Qin, H. L. Vision for medicine: *Staphylococcus aureus* biofilm war and unlocking key's for anti-biofilm drug development. *Microb. Pathog.*, **2018,** *123*, 339–347.

193. Molin, S.; Tolker-Nielsen, T. Gene transfer occurs with enhanced efficiency in biofilms and induces enhanced stabilisation of the biofilm structure. *Curr. Opin. Biotechnol*. **2003**, *14*, 255-261.

194. Monds, R. D.; O'Toole, G. A. The developmental model of microbial biofilms: Ten years of a paradigm up for review. *Trends Microbiol*. **2009**, *17*, 73-87.

195. Moretti, A.; Weeks, R. M.; Chikindas, M.; Uhrich, K. E. Cationic amphiphiles with specificity against Gram-positive and Gram-negative bacteria: chemical composition and architecture combat bacterial membranes. *Langmuir* **2019**, *35*, 5557−5567.

196. Mueller, M.; de la Pena, A.; Derendorf, H. Issues in pharmacokinetics and pharmacodynamics of anti-infective agents: kill curves versus MIC. *Antimicrob. Agents Chemother*. **2004**, *48*, 369-377.

197. Muller P.; Alber D. G.; Turnbull L.; Schlothauer R. C.; Carter D. A.; Whitchurch C. B.; Harry E. J.; Synergism between medihoney and rifampicin against methicillin-resistant *Staphylococcus aureus* (MRSA). *PLoS One*, **2013**, *8*, 1-9.

198. Murthy, S.; Gautam, M. K.; Goel, S.; Purohit, .; Sharma, H.; Goel, R. K. Evaluation of *In Vivo* Wound Healing Activity of *Bacopa monniera* on Different Wound Model in Rats. BioMed Res. Int., **2013**, *2013*, Article ID 972028.

199. Nair, A.K.; Gautieri, A.; Buehler, M.J. Role of intrafibrillar collagen mineralization in defining the compressive properties of nascent bone. *Biomacromolecules*, **2014**, *15*, 2494-2500.

200. Negm, N. A.; Zaki, M. F. Structural and biological behaviors of some nonionic Schiff-base amphiphiles and their Cu(II) and Fe(III) metal complexes. *Colloids and Surfaces B: Biointerfaces*, **2008**, *64*, 179–183.

201. Nepal, M.; Mohamed, M. F.; Blade, R.; Eldesouky, H. E.; Anderson, T. N.; Seleem, M. N.; Chmielewski, J. A library approach to cationic amphiphilic polyproline helices that target intracellular pathogenic bacteria. *ACS Infect. Dis*. **2018**, *4*, 1300−1305.

202. Nichols, J. W.; Bae, Y. H. EPR: Evidence and Fallacy. *J. Control. Release*, **2014,** *190*,451–464.

203. Nikaido, H. Molecular basis of bacterial outer membrane permeability revisited.*Microbiol. Mol. Biol. Rev*., **2003**, *67*, 593-656

204. Nikaido, H. Multidrug resistance in bacteria. *Annu. Rev. Biochem.*, **2010**, *78*, 119–146.

205. Nordmann, P.; Poirel, L.; Walsh, T. R.; Livermore, D. M. The emerging NDM carbapenemases. *Trends Microbiol.* **2011**, *19*, 588-595.

206. O'Neill, E.; Pozzi, C.; Houston, P.; Humphreys, H.; Robinson, D.A.; Loughman, A.; Foster, T.J.; O'Gara, J.P. A novel *Staphylococcus aureus* biofilm phenotype mediated by the fibronectin binding proteins, FnBPA and FnBPB. *J. Bacteriol.* **2008**, *190*, 3835-3850.

207. O'Toole, G.; Kaplan, H.B.; Kolter, R. Biofilm formation as microbial development. *Annu*. *Rev*. *Microbiol*. **2000**, *54*, 49-79.

208. Obermeier A.; Schneider J.; Wehner S.; Matl F.D.; Schieker M.; Rothe R.; Stemberger A; Burgkart R. Novel high efficient coatings for anti-microbial surgical sutures using chlorhexidine in fatty acid slow-release carrier systems. *PLoS One*, **2014,** *9*, e101426.

209. Obermeier, A.; Schneider J.; Föhr1 P.; Wehner S.; Kühn K.-D.; Stemberger A; Schieker M.; Burgkart R. *In vitro* evaluation of novel antimicrobial coatings for surgical sutures using octenidine. *BMC Microbiol*., **2015,** *15*, 186.

210. Oda Y.; Kanaoka S.; Sato T.; Aoshima S.; Kuroda K. Block versus random amphiphilic copolymers as antibacterial agents. *Biomacromolecules*, **2011**, *12*, 3581-3591.

211. Oliveira, W.F.; Silva, P.M.S.; Silva, R.C.S.; Silva, G.M.M.; Machado, G.; Coelho, L.; Correia, M.T.S. *Staphylococcus aureus* and *Staphylococcus epidermidis* infections on implants. *J. Hosp. Infect.* **2018**, *98*, 111-117.

212. Onufrak, N. J.; Forrest, A.; Gonzalez, D. Pharmacokinetic and pharmacodynamic principles of anti-infective dosing, *Clin. Ther.* **2016,** *38*, 1930-1947.

213. Otto, M. Staphylococcal biofilms. *Curr. Top. Microbiol. Immunol*. **2008**, *322*, 207-228.

214. Owen, T.; Pynn, R.; Martinez, J. S.; Butler, A. Micelle-to-vesicle transition of an iron-chelating microbial surfactant, marinobactin E, *Langmuir*, **2005**, *21*, 12109-12114.

215. Owen, T; Pynn, R; Hammouda, B; Butler, A. Metal-dependent self-assembly of a microbial surfactant, *Langmuir*, **2007** ,*23*, 9393-400.

216. Owens C. D.; Stoessel K. Surgical site infections: epidemiology, microbiology and prevention. *J. Hosp. Infect*. **2008,** *70*, 3–10.

217. Pagès, J. M.; Kascàkovà, S.; Maigre, L.; Allam, A.; Alimi, M.; Chevalier, J.;Artaud, I. New peptide-based antimicrobials for tackling drug resistance in bacteria: single-cell fluorescence imaging. *ACS Med. Chem. Lett.*, **2013**, *4*, 556–559.

218. Palermo E. F.; Kuroda K.; Chemical structure of cationic groups in amphiphilic polymethacrylates modulates the antimicrobial and hemolytic activities. *Biomacromolecules*, **2009**, *10*, 1416-1428.

219. Palermo, E. F.; Sovadinova, I.; Kuroda, K. Structural determinants of antimicrobial activity and biocompatibility in membrane-disrupting methacrylamide random copolymers. *Biomacromolecules*. **2009**, *10*, 3098-3107.

220. Palermo, E. F.; Vemparala, S.; Kuroda, K. Cationic spacer arm design strategy for control of antimicrobial activity and conformation of amphiphilic methacrylate random copolymers. *Biomacromolecules,* **2012**, *13*, 1632-1641.

221. Palmer, A. C.; Kishony, R. Opposing effects of target overexpression reveal drug mechanisms. *Nat. Commun*. **2014**, *5*, 4296.

222. Parsek, M. R.; Singh, P. K. Bactrial biofilms: An emerging link to disease pathogenesis. *Annu. Rev. Microbiol*., **2003**. *57*, 677-701.

223. Patel, M. B.; Garrad, E.; Meisel, . W.; Negin, S. Gokela, M. R.; Gokel, G. W. Synthetic ionophores as non-resistant antibiotic adjuvants. *RSC Adv*., **2019**, *9*, 2217–2222.

224. Patti J.M.; Bremell, T.; Krajewska-Pietrasik, D.; Abdelnour, A.; Tarkowski, A.; Ryden, C.; Hook, M. The *Staphylococcus aureus* collagen adhesin is a virulence determinant in experimental septic arthritis. *Infect. Immun.*, **1994**, *62*,152-161.

225. Patti, J.M.; Allen, B.L.; McGavin, M.J.; Hook, M. MSCRAMM-mediated adherence of microorganisms to host tissues. *Annu. Rev. Microbiol*. **1994**, *48*, 585-617.

226. Peng, G.; Hou, X.; Zhang, W.; Song, M.; Yin, M.; Wang, J.; Li, J.; Liu, Y.; Zhang, Y.; Zhou, W.; Li, X.; Li, G. Alkyl rhamnosides, a series of amphiphilic materials exerting broad-spectrum anti-biofilm activity against pathogenic bacteria via multiple mechanisms. *Artif. Cells Nanomed. Biotechnol.,***2018**, *46:sup3*, S217-S232.

227. Periasamy, S.; Joo, H. S.; Duong, A. C.; Bach, T. H. L.; Tan, V. Y. Chatterjee, S. S.; Cheung, G. Y. C.; Otto, M. How *Staphylococcus aureus* biofilms develop their characteristic structure. *Proc. Natl. Acad. Sci*., **2012**, *109*, 1281–1286.

228. Perlroth, J.; Kuo, M.; Tan, J.; Bayer, A. S.; Miller, L. G. Adjunctive Use of Rifampin for the Treatment of *Staphylococcus aureus* Infections. *Arch. Intern. Med*., **2008**, *168*, 805-819.

229. Peschel, A.; Otto, M. Phenol-soluble modulins and staphylococcal infection. *Nat. Rev. Microbiol*., **2013**, *11*, 667–673.

230. Petchiappan, A.; Chatterji, D. Antibiotic resistance: current perspectives. *ACS Omega* **2017**, *2*, 7400-7409.

231. Peterson, E.; Kaur, P. Antibiotic resistance mechanisms in bacteria: relationships between resistance determinants of antibiotic producers, environmental bacteria, and clinical pathogens. *Front. Microbiol*., **2018**, *9*, 2928.

232. Petkau-Milroy K.; Brunsveld L., Supramolecular chemical biology; bioactive synthetic self-assemblies. *Org. Biomol. Chem*., **2013**, *11*, 219-232.

233. Piletska, E. V.; Stavroulakis, G.; Larcombe, L. D.; Whitcombe, M. J.; Sharma, A.; Primrose, S.; Robinson, G. ; Piletsky, S. A. Passive control of quorum sensing: prevention of *Pseudomonas aeruginosa* biofilm formation by imprinted polymers. *Biomacromolecules* **2011**, *12*, 1067-1071.

234. Poirel L.; Jayol A.; Nordmann P.; Polymyxins: Antibacterial activity, susceptibility testing, and resistance mechanisms encoded by plasmids or chromosomes, *Clin. Microbiol. Rev*., **2017**, *30*, 557–596.

235. Price, B. L.; Lovering, A. M.; Bowling, F. L.; Dobson, C. B. Development of a novel collagen wound model to simulate the activity and distribution of antimicrobials in soft tissue during diabetic foot infection. *Antimicrob. Agents Chemother*., **2016**, *60*, 6880–6889.

236. Qiao Y.; Yang C.; Coady D. J.; Ong Z. Y.; Hedrick J. L.; Yang Y. Y. Highly dynamic biodegradable micelles capable of lysing Gram-positive and Gram-negative bacterial membrane. *Biomaterials*, **2012**, *33*, 1146-1153.

237. Rahman, A.; Bam, M.; Luat, E.; Jui, M. S.; Ganewatta, M. S.; Shokfai, T.; Nagarkatti, M.; Decho, A. W.; Tang, C. Macromolecular-clustered facial amphiphilic antimicrobials. *Nat. Commun*. **2018**, *9*, 5231.

238. Rand, R. P.; Sengupta, S. Cardiolipin forms hexagonal structures with divalent cations *Biochim. Biophys. Acta*, **1972**, *255*, 484-492.

239. Rawlinson, L. A.; Ryan, S. M.; Mantovani, G.; Syrett, J. A.; Haddleton, D. M.; Brayden, D. J., Antibacterial effects of poly (2- (dimethylamino ethyl) methacrylate) against selected gram-positive and gram-negative bacteria. *Biomacromolecules*, **2010**, *11*, 443-53.

240. Reddy, G. K., Enwemeka, C. S. A simplified method for the analysis of hydroxyproline in biological tissues. *Clin. Biochem.*, **1996**, *29*, 225–229.

241. Rehm S. J.; Tice A. *Staphylococcus Aureus:* Methicillin-susceptible *S. aureus* to methicillin-resistant *S. aureus* and vancomycin-resistant *S. aureus*. *Clin. Infect. Dis*., **2010**, *51*, S176-S182.

242. Remy, L.; Carriere, M.; Bobillot, A. D.; Martini, C.; Sanguinetti, M.; Durant, E. B. The *Staphylococcus aureus* Opp1 ABC transporter imports nickel and cobalt in zinc-depleted conditions and contributes to virulence. *Mol. Microbiol*. **2013**, *87*, 730-743.

243. Ribeiro, M.; Monteiro, F.J.; Ferraz, M.P. Infection of orthopedic implants with emphasis on bacterial adhesion process and techniques used in studying bacterial-material interactions. *Biomaterials* **2012**, *2*, 176-194.

244. Richard, H.; Foster, J. W. *Escherichia coli* glutamate- and arginine-dependent acid resistance systems increase internal pH and reverse transmembrane potential. *J. Bacteriol*. **2004**, *186*, 6032-6041.

245. Rigozzi, S.; Muller, R.; Stemmer, A.; Snedeker, J.G. Tendon glycosaminoglycan proteoglycan sidechains promote collagen fibril sliding-AFM observations at the nanoscale. *J. Biomech*., **2013**, *46*, 813-818.

246. Rodrigues, L.R.; Linke, D.; Goldman, A. (Eds.), Inhibition of Bacterial Adhesion on Medical Devices. In: *Bacterial Adhesion. Advances in Experimental Medicine and Biology, Springer, Dordrecht***, 2011**, 1-715.

247. Rodvold, K. A.; Mcconeghy, K. W. Methicillin-resistant staphylococcus aureus therapy: Past, present, and future. *Clin. Infect. Dis*., **2014,** *58*, 20–27.

248. Saha, S.; Savage, P. B.; Bal, M. Enhancement of the efficacy of erythromycin in multiple antibiotic-resistant gram-negative bacterial pathogens. *J. Appl. Microbiol*.**2008**, *105*, 822-828.

249. Salta, J.; Benhamou, R. I.; Herzog, I. M.; Fridman, M. Tuning the effects of bacterial membrane permeability through photo-isomerization of antimicrobial cationic amphiphiles. *Chem. Eur. J.*, **2017**, *23*, 12724–12728.

250. Sande L.; Sanchez M.; Montes J.; Wolf A. J.; Morgan M.; Omri A.; Liu G. Y. J. Liposomal encapsulation of vancomycin improves killing of methicillin-resistant *Staphylococcus aureus* in a murine infection model. *Antimicrob. Chemother*., **2012**, *67*, 2191-2194.

251. Schneewind, O.; Missiakas, D. Lipoteichoic acids, phosphate-containing polymers in the envelope of Gram-positive bacteria. *J. Bacteriol*. **2014**, *196*, 1133-1142.

252. Scozzafana, A.; Supuran, C.T. Carbonic anhydrase and matrix metallo- proteinase inhibitors: sulfonylated amino acid hydroxamates with MMP inhibitory properties

act as efficient inhibitors of CA isozymes I, II, and IV, and N-hydroxysulfonamides inhibit both these zinc enzymes, *J. Med. Chem.* **2000,** 43, 3677–3687.

253. Scozzafava, A.; Menabuoni, L.; Mincione, F.; Briganti, F; Mincione, G; Supuran, CT. Carbonic anhydrase inhibitors: synthesis of sulfonamides incorporating DTPA tails and of their zinc complexes with powerful topical antiglaucoma properties, *Bioorg. Med. Chem. Lett.* **2001**, *11*, 575–582.

254. Seo, Y. S.; Lee, D. Y.; Rayamahji, N.; Kang, M. L.; Yoo, H. S. Biofilm-forming associated genotypic and phenotypic characteristics of *Staphylococcus* spp. isolated from animals and air. *Res. Vet. Sci.*, **2008**, *85*, 433–438.

255. Shah, S.R.; Tatara, A.M.; D'Souza, R.N.; Mikos, A.G.; Kasper, F.K. Evolving strategies for preventing biofilm on implantable materials, *Mater. Today*, **2013**, *16*, 177-182.

256. Silver, L. L. Challenges of antibacterial discovery. *Clin Microbiol Rev*. **2011**, *24*, 71-109.

257. Simonetti, O.; Lucarini, G.; Orlando, F.; Pierpaoli, E.; Ghiselli, R.; Provinciali, M.; Castelli, P.; Guerrieri, M.; Primio, R. D.; Offidani, A.; Giacometti, A.; Cirionie, O. Role of Daptomycin on Burn Wound Healing in an Animal Methicillin-Resistant *Staphylococcus aureus* Infection Model. *Antimicrob. Agents Chemother*., **2017**, *61*, e00606- e00617.

258. Singh, A. K.; Mukherjee, S.; Adhikari, M. D.; Ramesh, A. Fluorescence-based comparative evaluation of bactericidal potency and food application potential of anti-listerial bacteriocin produced by lactic acid bacteria isolated from indigenous samples. *Prob. Antimicrob. Proteins*., **2012**, *4*, 122-132.

259. Singh, P. K.; Schaefer, A. L.; Parsek, M. R.; Moninger, T. O.; Welsh, M. J.; Greenberg, E. P. Quorum-sensing signals indicate that cystic fibrosis lungs are infected with bacterial biofilms. *Nature*. **2000**, *407*, 762-764.

260. Song, A.; Walker, S. G.; Parker, K. A.; Sampson, N. S. Antibacterial studies of cationic polymers with alternating, random, and uniform backbones. *ACS Chem. Biol*., **2011**, *6*, 590-599.

261. Sorrenti A.; Illa O.; Ortuño R. M. Amphiphiles in aqueous solution: well beyond a soap bubble. *Chem. Soc. Rev*., **2013**, *42*, 8200-8219.

262. Speziale, P.; Pietrocola, G.; Rindi, S.; Provenzano, M.; Provenza, G.; Di Poto, A.; Visai, L.; Aricola, C. R. Structural and functional role of *Staphylococcus aureus* surface components recognizing adhesive matrix molecules of the host. *Future Microbiol* **2009**, *4*, 1337-1352.

263. Steinbuch, K. B.; Fridman, M. Mechanisms of resistance to membrane-disrupting antibiotics in gram-positive and gram-negative bacteria. *Med. Chem. Commun.*, **2016,** *7*, 86–102.

264. Stewart, P. S.; Costerton, J. W. Antibiotic resistance of bacteria in biofilms. *Lancet*. **2001**, *358*, 135-138.

265. Stoodley, P; Ehrlich, G.D.; Sedghizadehc, P.P.; Hall-Stoodley, L; Baratze, M. E.; Altmane, D.T.; Sotereanose, N.G.; Costertone, J.W.; DeMeoe, P. Orthopaedic biofilm infections, *Curr. Orthop. Pract*., **2011**, *22*, 558–563.

266. Stryjewski M. E. and Corey G. R., Methicillin-Resistant *Staphylococcus aureus*: An evolving pathogen. *Clin. Infect. Dis*., **2014**, *58*, 10–19.

267. Suarez, D. F.; Consuegra, J.; Trajano, V. C.; Gontijo, S. M. L.; Guimaraes, P. P. G.; Cortes, M. E.; Denadai, A. L.; Sinisterra, R. D. Structural and thermodynamic characterization of doxycycline/ β-cyclodextrin supramolecular complex and its bacterial membrane interactions. *Colloids Surf., B*, **2014**, *118*, 194-201.

268. Suresh, M. K.; Biswas, R.; Biswas, L. An update on recent developments in the prevention and treatment of *Staphylococcus aureus* biofilms. *Int. J.Med.Microbiol.,* **2019**, *309*, 1-12.

269. Tacconelli, E.; Carrara, E.; Savoldi, A.; Harbarth, S.; Mendelson, M.; Monnet, D. L.; Pulcini, C.; Kahlmeter, G.; Kluytmans, J.; Carmeli, Y.; Ouellette, M.; Outterson, K.; Patel, J.; Cavaleri, M.; Cox, E. M.; Houchens, C. R.; Grayson, M. L.; Hansen, P.; Singh, N.; Theuretzbacher, U.; Magrini, N.; the WHO Pathogens Priority List Working Group; Discovery, research, and development of new antibiotics: the WHO priority list of antibiotic-resistant bacteria and tuberculosis *Lancet Infect. Dis*., **2017**, *18,* 318-324.

270. Tamplin, M. L. Inactivation of *Escherichia coli* O157:H7 in simulated human gastric fluid. *Appl Environ Microbiol*. **2005**, *71*, 320-325.

271. Tang, H.; Doerksen, R. J.; Jones, T. V.; Klein, M. L.; Tew, G. N. Biomimetic facially amphiphilic antibacterial oligomers with conformationally stiff backbones. *Chem Biol*. **2006**, *13*, 427-435.

272. Thangamani S.; Mohammad H.; Abushahba M. F. N.; Sobreira T. J. P.; Hedrick V. E.; Paul L. N.; Seleem M. N.; Antibacterial activity and mechanism of action of auranofin against multi-drug resistant bacterial pathogens, *Sci. Rep*., **2016**, *6*, 22571.

273. Thangamani S.; Mohammad H.; Abushahba M. F. N.; Sobreira T. J. P. and Seleem M. N. Repurposing auranofin for the treatment of cutaneous staphylococcal infections. *Int. J. Antimicrob. Agents*, **2016**, *47*, 195-201.

274. Thiyagarajan D.; Das G.; Ramesh A., Amphiphilic cargo-loaded nanocarrier enhances antibiotic uptake and perturbs efflux: effective synergy for mitigation of methicillin-resistant *Staphylococcus aureus*. *ChemMedChem,* **2017**, *12*, 1125-1132.

275. Thiyagarajan, D.; Das G.; Ramesh A. Extracellular-DNA-targeting nanomaterial for effective elimination of biofilm. *ChemNanoMat*, **2016,** *2*, 879–87.

276. Thiyagarajan, D.; Goswami, S.; Kar, C.; Das, G.;Ramesh, A. A prospective antibacterial for drug-resistant pathogens: a dual warhead amphiphile designed to track interactions and kill pathogenic bacteria by membrane damage and cellular DNA cleavage. *Chem. Commun.,* **2014**, *50*, 7434–7436.

277. Thompson, R. J.; Bobay, B. G.; Stowe, S. D.; Olson, A.L.; Peng, L.; Su, Z.; Actis, L.A.; Melander, C.; Cavanagh, J. Identification of BfmR, a response regulator involved in biofilm development, as a target for 2-Aminoimidazole-based antibiofilm agent. *Biochemistry* **2012**, *51*, 9776-9778.

278. Tong, S.Y.C.; Davis, J.S.; Eichenberger, E.; Holland, T.L.; Fowler, V.G., Jr. *Staphylococcus aureus* infections: epidemiology, pathophysiology, clinical manifestations, and management. *Clin. Microbiol. Rev*., **2015**, *28*, 603-661.

279. Toprak, E.; Veres, A.; Michel, J. B.; Chait, R.; Hartl, D. L.; Kishony, R. Evolutionary paths to antibiotic resistance under dynamically sustained drug selection. *Nat. Genet*. **2012**, *44*, 101-105.

280. Trotonda, M. P.; Manna, A. C.; Cheung, A. L.; Lasa, I.; Penades, J. R. SarA positively controls bap-dependent biofilm formation in *Staphylococcus aureus*. *J. Bacteriol*. **2005**, *187*, 5790-5798.

281. Tsuji B. T.; Rybak M. J.; Short-course gentamicin in combination with daptomycin or vancomycin against *Staphylococcus aureus* in an *in vitro* pharmacodynamic model with simulated endocardial vegetations. *Antimicrob. Agents Chemother*., **2005**, *49*, 2735-2745.

282. Tyuleva, S. N.; Allen, N.; White, L. J.; Pepes, A.; Shepherd, H. J.; Saines, P. J.; Ellaby, R. J.; Mulvihill, D. P.; Hiscock, J. R. A symbiotic supramolecular approach to the design of novel amphiphiles with antibacterial properties against MSRA. *Chem. Commun*., **2019**, *55*, 95-98.

283. Uday, P. S.; Thiyagarajan, D.; Goswami, S.; Adhikari, M. D.; Das, G.; Ramesh, A. Amphiphile-mediated enhanced antibiotic efficacy and development of a payload nanocarrier for effective killing of pathogenic bacteria. *J. Mater. Chem. B.* **2014**, *2*, 5818-5827.

284. Ukong, S.; Ampawong, S.; Kengkoom, K. Collagen Measurement and Staining Pattern of Wound Healing Comparison with Fixations and Stains. *J. Micros. Soc. Thailand*, 2008, *22*, 37–41.

285. Ulvatne, H.; Karoliussen, S.; Stiberg, T.; Rekdal, O.; Svendsen, J. S. Short antibacterial peptides and erythromycin act synergically against *Escherichia coli*. *J. Antimicrob. Chemother*., **2001**, *48*, 203-208.

286. Vaara, M. Polymyxins and their novel derivatives. *Curr Opin Microbiol*. **2010**, *13*, 574-581.

287. Vail, W. J.; Stollery, J. G. Phase changes of cardiolipin vesicles mediated by divalent cations. *Biochim. Biophys. Acta* ,**1979**, *551*,74-84.

288. van Bambeke, F.; Mingeot-Leclercq, M. P.; Struelens, M. J.; Tulkens, P. M. The bacterial envelope as a target for novel anti-MRSA antibiotics. *Trends Pharmacol. Sci*. **2008**, *29*, 124-134.

289. Vasilenko, I.; De Kruijff, B.; Verkleij, A. J. Polymorphic phase behaviour of cardiolipin from bovine heart and from *Bacillus subtilis* as detected by ^{31}P-NMR and freeze-fracture techniques: Effects of Ca2+, Mg2+, Ba2+ and temperature *Biochim. Biophys. Acta* ,**1982**, *684*, 282-286.

290. Veenstra, D,L.; Saint, S.; Saha, S.; Lumley, T.; Sullivan, S.D. Efficacy of antiseptic-impregnated central venous catheters in preventing catheter-related bloodstream infection: a meta-analysis. *JAMA*, **1999**, *281*, 261–267.

291. Velkov T.; Roberts K.D.; Nation R.L.; Thompson P.E.; Li.J. Pharmacology of polymyxins: new insights into an 'old' class of antibiotics. *Future Microbiol*. **2013**, *8*, 10.2217.

292. Vergara-Irigaray, M.; Valle, J.; Merino, N.; Latasa, C.; García, B.; de los Mozos, I. R.; Solano, C.; Toledo-Arana, A.; Penades, J. R.; Lasa, I. Relevant role of fibronectin-binding proteins in *Staphylococcus aureus* biofilm-associated foreign-body infections. *Infect. Immun*., **2009**, *77*, 3978–3991.

293. Virto, R.; Manas, P.; Alvarez, I.; Condon, S.; Raso, J. Membrane damage and microbial inactivation by chlorine in the absence and presence of a chlorine demanding substrate. *Appl. Environ. Microbiol*., **2005**, *71*, 5022-5028.

294. Vudumula, U.; Adhikari, M. D.; Ojha, B.; Goswami, S.; Das, G.; Ramesh, A. Tuning the bactericidal repertoire and potency of quinoline-based amphiphiles for enhanced killing of pathogenic bacteria, *RSC Adv*., **2012**, *2*, 3864-3871.

295. Vuong, C.; Saenz, H.L.; Gotz, F.; Otto, M. Impact of the agr quorum-sensing system on adherence to polystyrene in *Staphylococcus aureus*. *J. Infect. Dis*. **2000**, *182*, 1688-1693.

296. Walker, U.A.; Warnatz, K. Idiopathic CD4 lymphocytopenia. *Curr. Opin. Rheumat.*, **2006**, *18*, 389-395.

297. Watkins, R. R.; David, M. Z.; Salata, R. A. Current concepts on the virulence mechanisms of meticillin-resistant *Staphylococcus aureus*. *J. Med. Microbiol*., **2012**, *61*, 1179–1193.

298. Weidenmaier, C.; Peschel, A. Teichoic acids and related cell-wall glycopolymersin gram-positive physiology and host interactions. *Nat. Rev. Microbiol*.,**2008**,*6*,276-287.

299. Werner, S.; Grose, R. Regulation of wound healing by growth factors and cytokines. *Physiol. Rev*., **2003**, *83*, 835–870.

300. Wilson, D. N. Ribosome-targeting antibiotics and mechanisms of bacterial resistance. *Nat. Rev. Microbiol*. **2014**, *12*, 35-48.

301. Wimley, W.; Hristova, K. Antimicrobial peptides: successes, challenges and unanswered questions. *J. Membr. Biol.*, **2011,** *239*, 27–34.

302. Wiseman, T.; Williston, S.; Brandts, J. F.; Lin, L-N. Rapid measurement of binding constants and heats of binding using a new titration calorimeter. *Anal. Biochem.* **1989**, *179*, 131-137.

303. Wispelwey, B. Clinical implications of pharmacokinetics and pharmacodynamics of fluoroquinolones. *Clin Infect Dis*. **2005**, *41 Suppl 2*, S127-135.

304. World Health Organization (WHO). Antimicrobial resistance: Global report on surveillance (2014). Available from: http://www.who.int/drugresistance/documents/surveillancereport/en/

305. Worthington, R.; Melander, C. Combination approaches to combat multidrug-resistant bacteria. *Trends Biotechnol.* **2013**, *31*, 177-184.

306. Wright, G. D. Bacterial resistance to antibiotics: enzymatic degradation and modification. *Adv Drug Deliv. Rev*. **2005**, *57*, 1451-1470.

307. Wright, G. D. Molecular mechanisms of antibiotic resistance. *Chem. Commun.*, **2011,** *47*, 4055-4061.

308. Wright, P. M.; Seiple, I. B.; Myers, A. G. The evolving role of chemical synthesis in antibacterial drug discovery. *Angew. Chem. Int. Ed*. **2014**, *53*, 8840-8869.

309. Xu, H. V.; Zheng, X. T.; Wang, C.; Zhao, Y.; Ta, Y. N. Bioinspired antimicrobial nanodots with amphiphilic and zwitterionic-like characteristics for combating multidrug-resistant bacteria and biofilm removal. *ACS Appl. Nano Mater*. **2018**, *1*, 2062−2068.

310. Yao D.; Li S.; Zhu X.; Wu J.; Tian H. Tumor-cell targeting polydiacetylene micelles encapsulated with an antitumor drug for the treatment of ovarian cancer. *Chem. Commun.*, **2017**, *53*, 1233-1236.

311. Yeaman, M. R.; Yount, N. Y. Mechanisms of antimicrobial peptide action and resistance. *Pharmacol. Rev.*, **2003,** *55*, 27–55.

312. Zasloff, M. Antimicrobial peptides of multicellular organisms. *Nature*. **2002**, *415*, 389-395.

313. Zavascki, A. P.; Goldani, L. Z.; Li, J.; Nation, R. L. Polymyxin B for the treatment of multidrug-resistant pathogens: a critical review. *J. Antimicrob. Chemother*. **2007**, *60*, 1206-1215.f

314. Zhang, Y.; Algburib, A.; Wang, N.; Kholodovych, V.; Ohf, D. O.; Chikindas, M.; Uhrich, K. E. Self-assembled cationic amphiphiles as antimicrobial peptides mimics: role of hydrophobicity, linkage type, and assembly state. *Nanomedicine: NBM*., **2017**, *13*, 343-352.

315. Zhang, E.; Bai, P-Y.; Cui, D-Y.; Chu, W-C.; Hua, Y-G.; Liu, Q.; Yin, H-Y.; Zhang, Y-J.; Qin, S.; Liu, H-M. Synthesis and bioactivities study of new antibacterial peptide mimics: The dialkyl cationic amphiphiles. *Eur. J. Med. Chem*. **2018**, *143*, 1489-1509.

316. Zhang, S.; Ding, S.; Yu, J.; Chen, X.; Lei, Q.; Fang, W. Antibacterial activity, in vitro cytotoxicity, and cell cycle arrest of gemini quaternary ammonium surfactants. *Langmuir* **2015**, *31*, 12161−12169.

317. Zhang, Y.; Huo, M.; Zhou, J.; Yu, D.; Wu, Y. Potential of amphiphilically modified low molecular weight chitosan as a novel carrier for hydrophobic anticancer drug: Synthesis, characterization, micellization and cytotoxicity evaluation. *Carb. Pol*., **2009**, *77*, 231–238

318. Zheng, H.; Gao, C.; Peng, B.; Shu, M.; Che, S. pH-responsive drug delivery system based on coordination bonding in a mesostructured surfactant/silica hybrid. *J. Phys. Chem. C* **2011**, *115*, 7230–7237.

319. Zilberman, M; Elsner, J.J. Antibiotic-eluting medical devices for various applications. *J. Control. Release*, **2008,** *130*, 202–215.

320. Zimmermann, L.; Das, I.; Desire, J.; Sautrey, G.; Barros, R. S. V.; El Khoury, M.; Mingeot-Leclercq, M. P.; Decout, J. L. New broad-spectrum antibacterial amphiphilic aminoglycosides active against resistant bacteria: from neamine derivatives to smaller neosamine analogues, *J. Med. Chem.* **2016,** *59*, 9350-9369.

321. Zimmermann, L.; Kempf, J.; Briee, F.; Swain, J.; Mingeot-Leclercq, M-P.; Decout, J-L. Broad-spectrum antibacterial amphiphilic aminoglycosides: a new focus on the structure of the lipophilic groups extends the series of active dialkyl neamines. *Eur. J. Med. Chem*. **2018**, *157*, 1512-1525.

322. Zwietering, M. H.; Jongenburger, I.; Rombouts, F. M.; Riet, K. Van't. Modeling of the bacterial growth curve. *Appl. Env. Microbiol*. **1990**, *56*, 1875-1881.

APPENDIX

APPENDIX

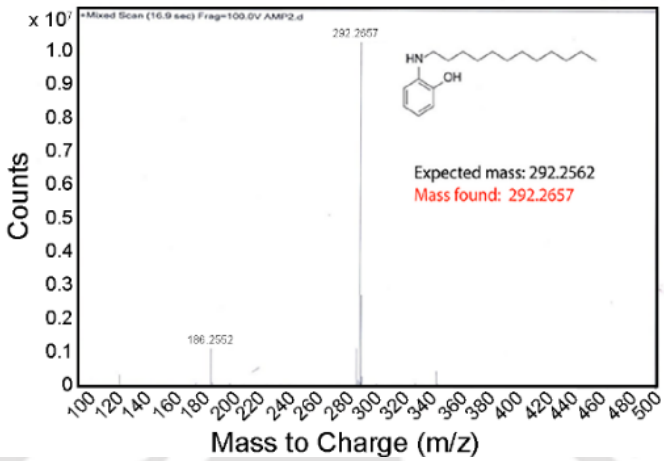

Figure A2.1. ESI-MS of C1 performed in positive mode.

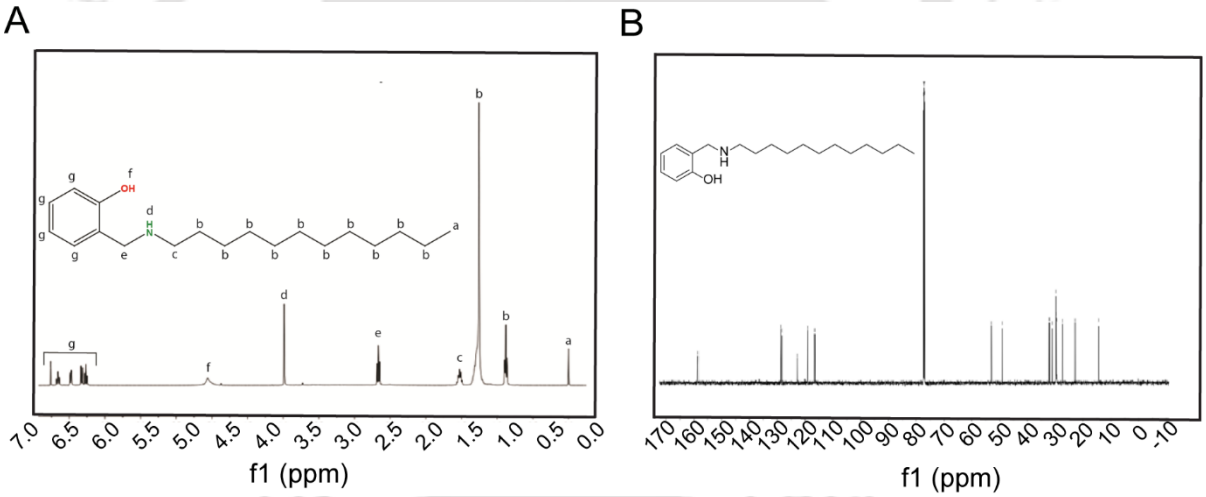

Figure A2.2. (A) ^{1}H NMR spectra of C1 in $CDCl_3$ solution. (B) ^{13}C NMR spectra of C1 in $CDCl_3$ solution.

^{1}H NMR [400 MHz, Chloroform-d1, TMS, J (Hz), δ (ppm)]: 7.26 - 6.76 (4H, m), 5.06 (1H, broad s), 3.99 (1H, s), 2.66 (2H, t), 1.53 (2H, m), 1.37 - 1.21 (20H, m), 0.88 (3H, t), ^{13}C NMR [150 MHz, Chloroform-d1, TMS, δ (ppm)]: 158.58, 128.80, 128.37, 122.83, 119.07, 116.54, 52.94, 42.97, 32.11, 31.12, 29.82, 29.78, 29.74, 29.66, 20.34, 27.34, 22.88, 14.31. ESI-MS (positive mode, *m/z*) Calculated for $C_{19}H_{33}NO$: 292.2562. Found: 292.2657 [(M + H+)].

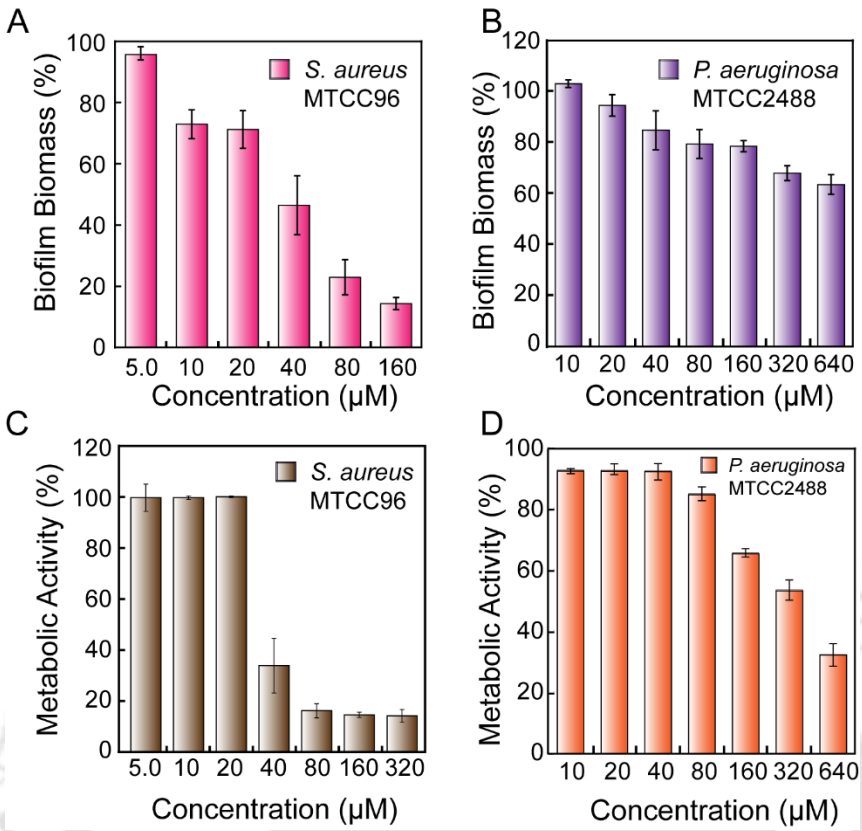

Figure A2.3. (A-B) Determination of biofilm biomass by CV assay and (C-D) metabolic activity by MTT assay to ascertain inhibition of (A and C) *S. aureus* MTCC 96 and (B and D) *P. aeruginosa* MTCC 2488 biofilm by C1.

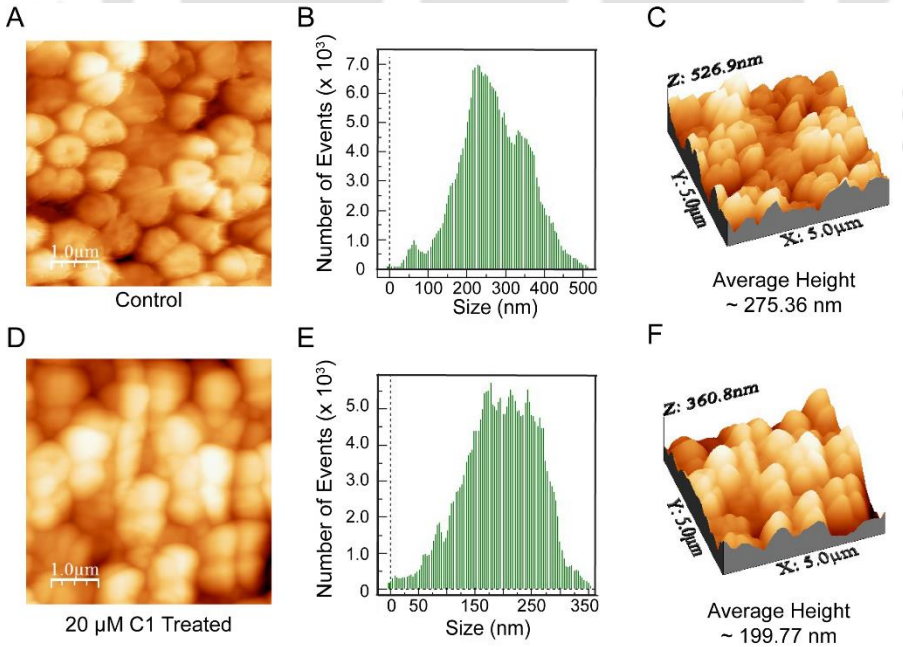

Figure A2.4. AFM analysis to study eradication of *S. aureus* MTCC 96 biofilm by C1.

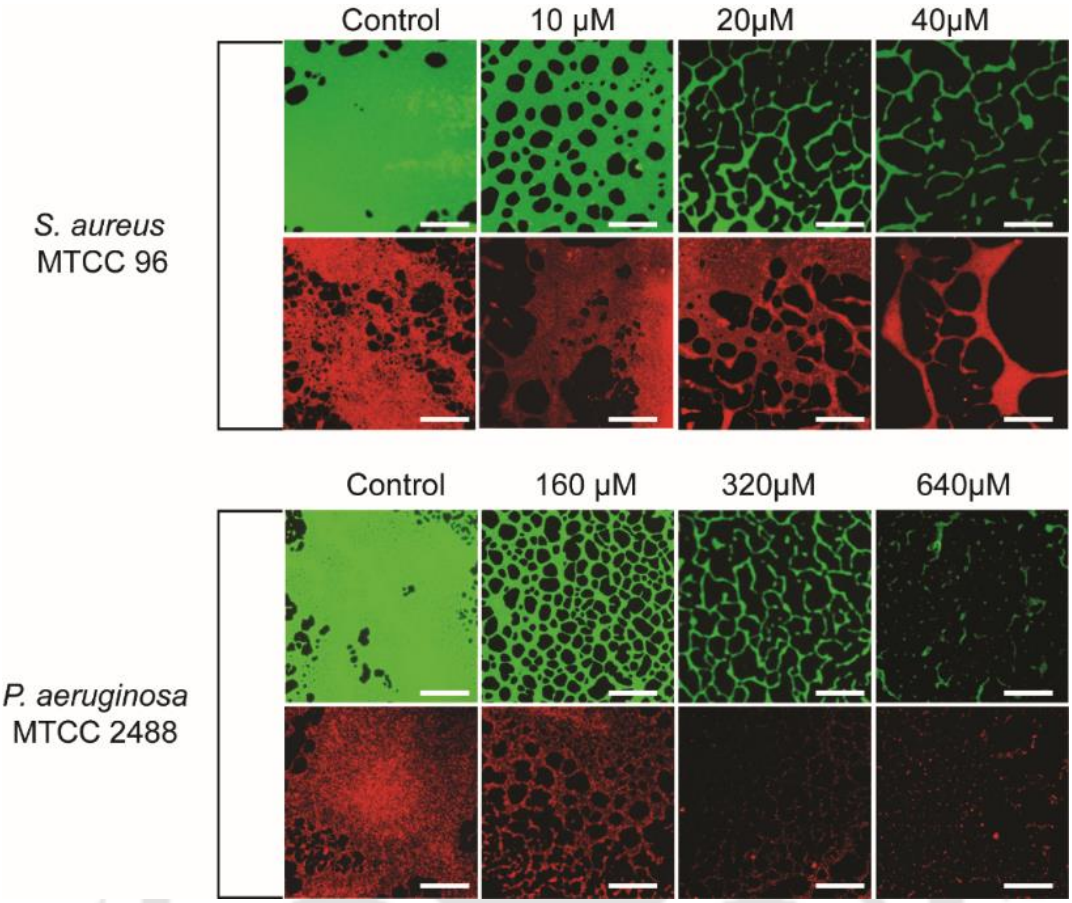

Figure A2.5. cFDA-SE and congo red based fluorescence microscopy analysis to ascertain inhibition potential of C1 against *S. aureus* MTCC96 and *P. aeruginosa* MTCC 2488 biofilm.

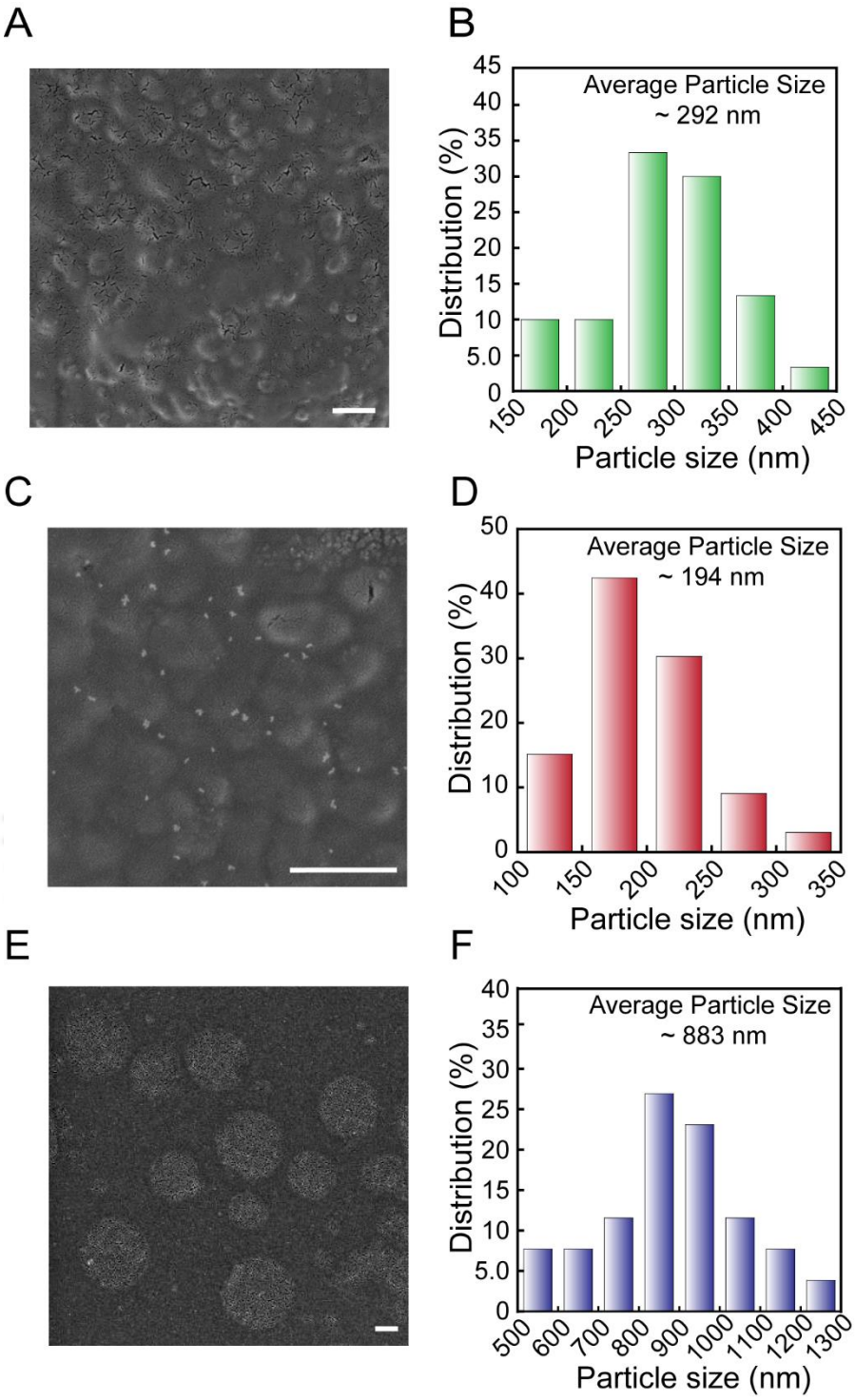

Figure A3.1. FESEM image of (A) $C1_M$, (C) $C1_M$-R and (E) $C1_M$-V. Scale bar for the images is 500 nm. Particle size distribution of (B) $C1_M$, (D) $C1_M$-R and (F) $C1_M$-V. Particle size distribution was determined by ImageJ software.

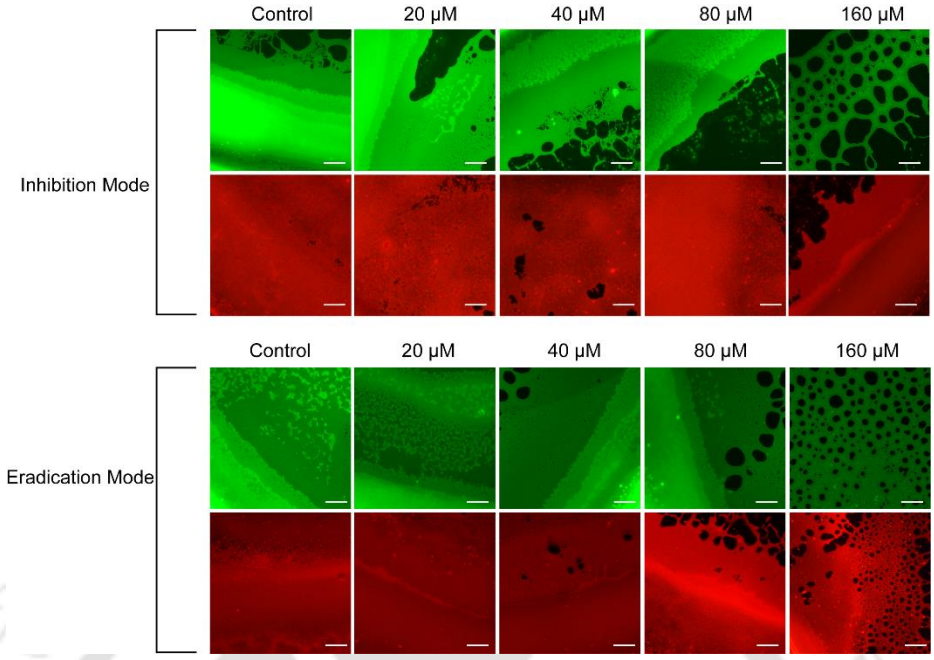

Figure A3.2. cFDA-SE and congo red based fluorescence microscopy analysis to ascertain inhibition and eradication potential of $C1_M$ against *S. aureus* MRSA 100 biofilm.

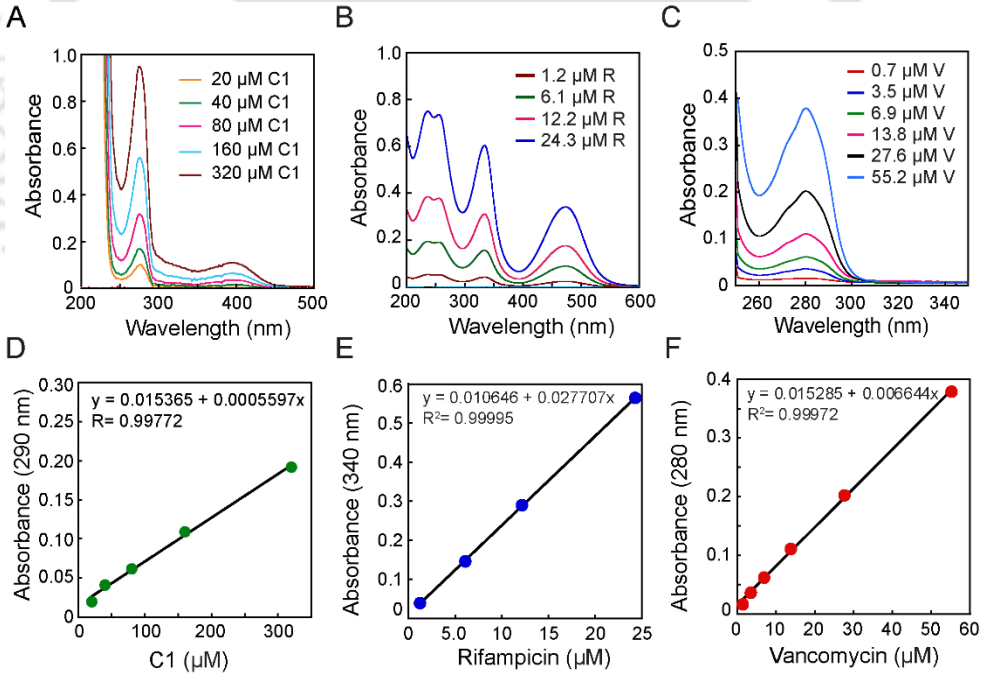

Figure A3.3. UV-visible absorption spectra of varying concentrations of (A) C1, (B) rifampicin (R) and (C) vancomycin (V). Calibration plots for (D) C1, (E) rifampicin and (F) vancomycin generated by plotting the respective absorbance maxima against concentration.

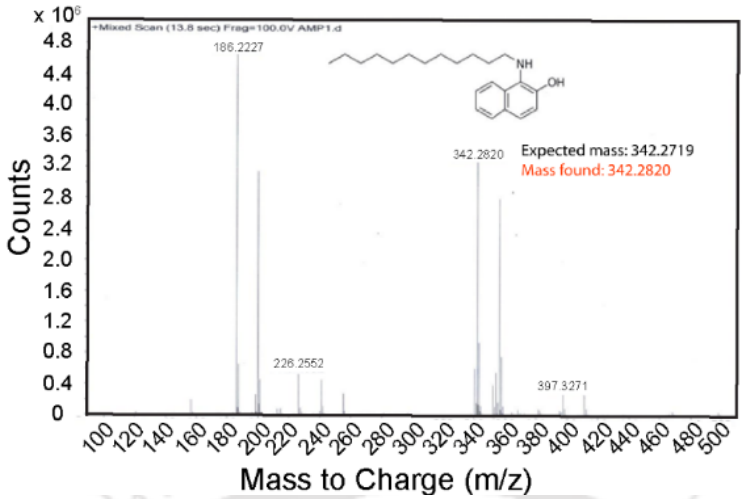

Figure A4.1. ESI-MS of C2 in positive mode.

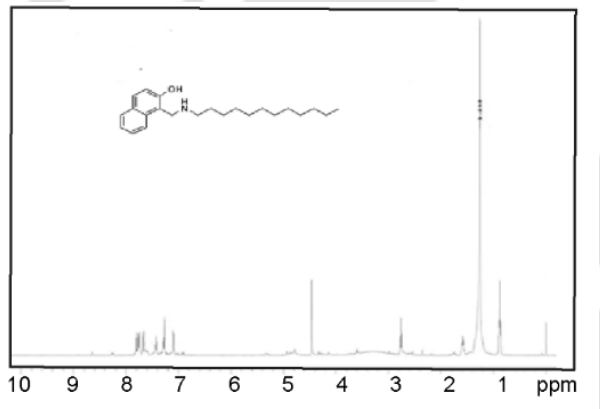

Figure A4.2. ^{1}H NMR spectra of C2 in $CDCl_3$ solution.

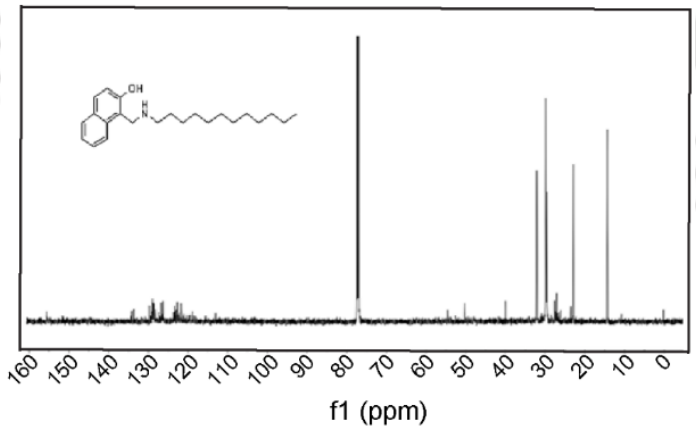

Figure A4.3. ^{13}C NMR spectra of C2 in $CDCl_3$ solution.

^{1}H NMR [600 MHz, Chloroform-d_1, TMS, J (Hz), δ (ppm)]: 7.08-780(6H, m), 4.46(1H, s), 2.76(2H, t), 1.25-1.68(18H, m). ESI-MS (positive mode, m/z) Calculated for $C_{19}H_{33}NO$: 342.2719. Found: 342.2820 [(M + H+)].

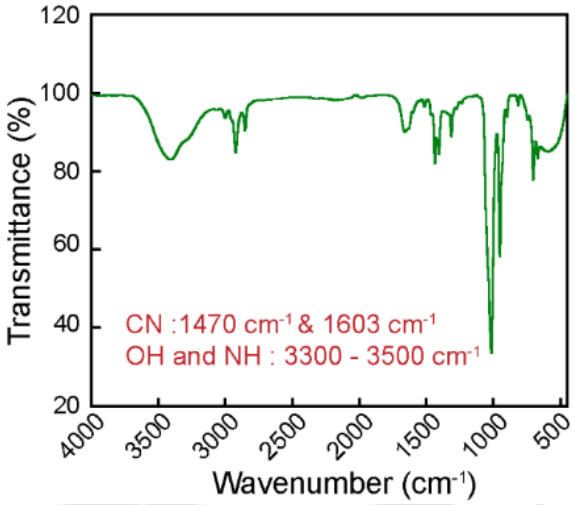

Figure A4.4. FTIR spectra of C2.

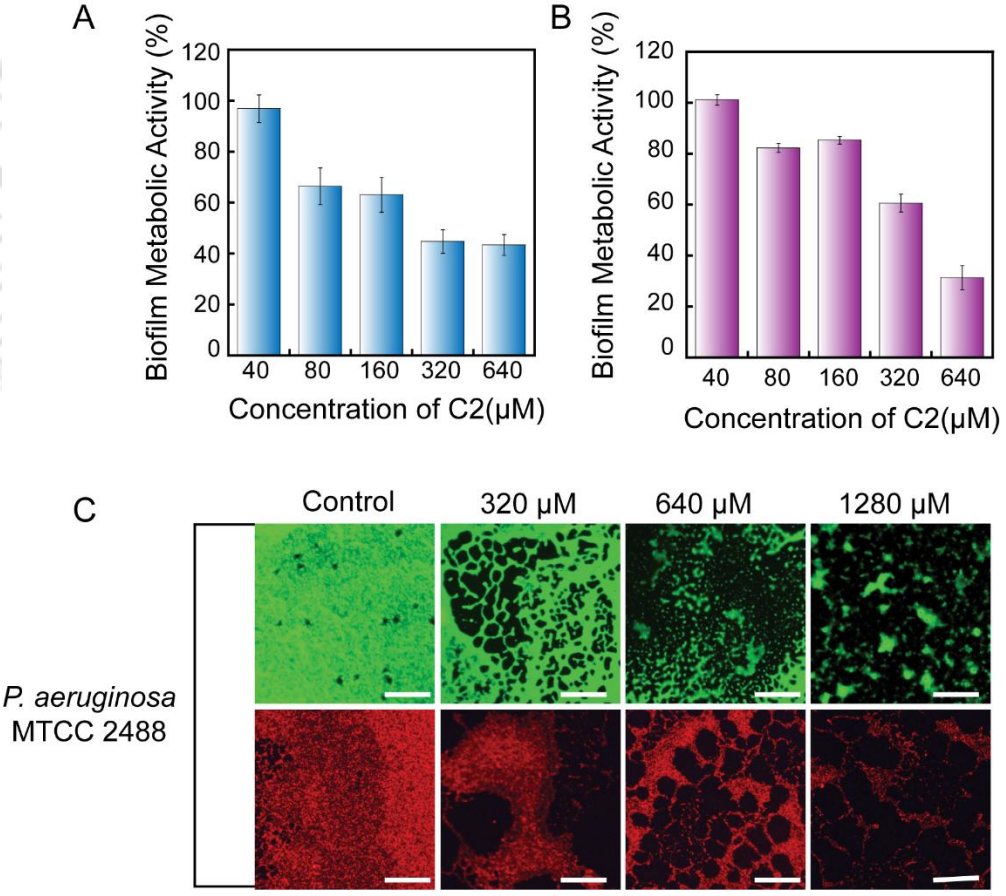

Figure A4.5. (A) Inhibition and (B) Eradication of *S. aureus* MRSA 100 biofilm by C2 determined by MTT assay. (C) Fluorescence microscopic analysis to study inhibition of *P. aeruginosa* MTCC 2488 biofilm growth in the presence of C2.

Table A4.1. Therapeutic index of C2.

Sl. No.	Target Bacteria	MIC (µM)	Therapeutic Index (IC_{50} / MIC)*		
			HEK 293	HT-29	HeLa
1.	*S. aureus* MTCC 96	160	2.625	0.725	0.768
2.	*L. monocytogenes* Scott A	320	1.312	0.362	0.384
3.	*P. aeruginosa* MTCC 2488	640	0.656	0.1812	0.192
4.	*E. coli* MTCC 433	640	0.656	0.1812	0.192
5.	*S. aureus* MRSA 100	320	1.312	0.362	0.384
6.	*S. aureus* MSSA-104	320	1.312	0.362	0.384

*IC_{50} against HEK 293 cells = 420 µM, HT 29 cells = 116 µM and HeLa cells = 123 µM

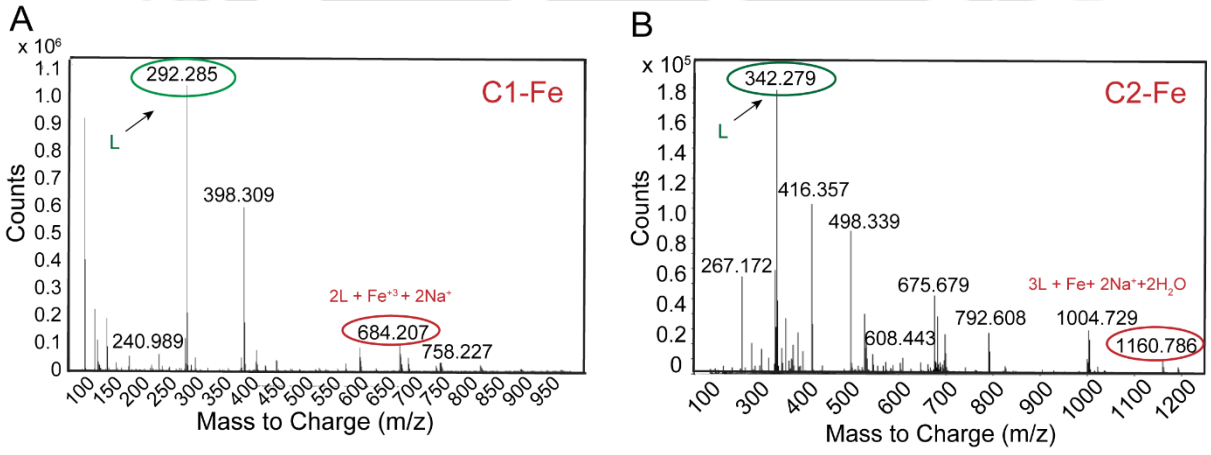

Figure A5.1. (A) ESI-MS of C1-Fe and C2-Fe performed in positive mode.

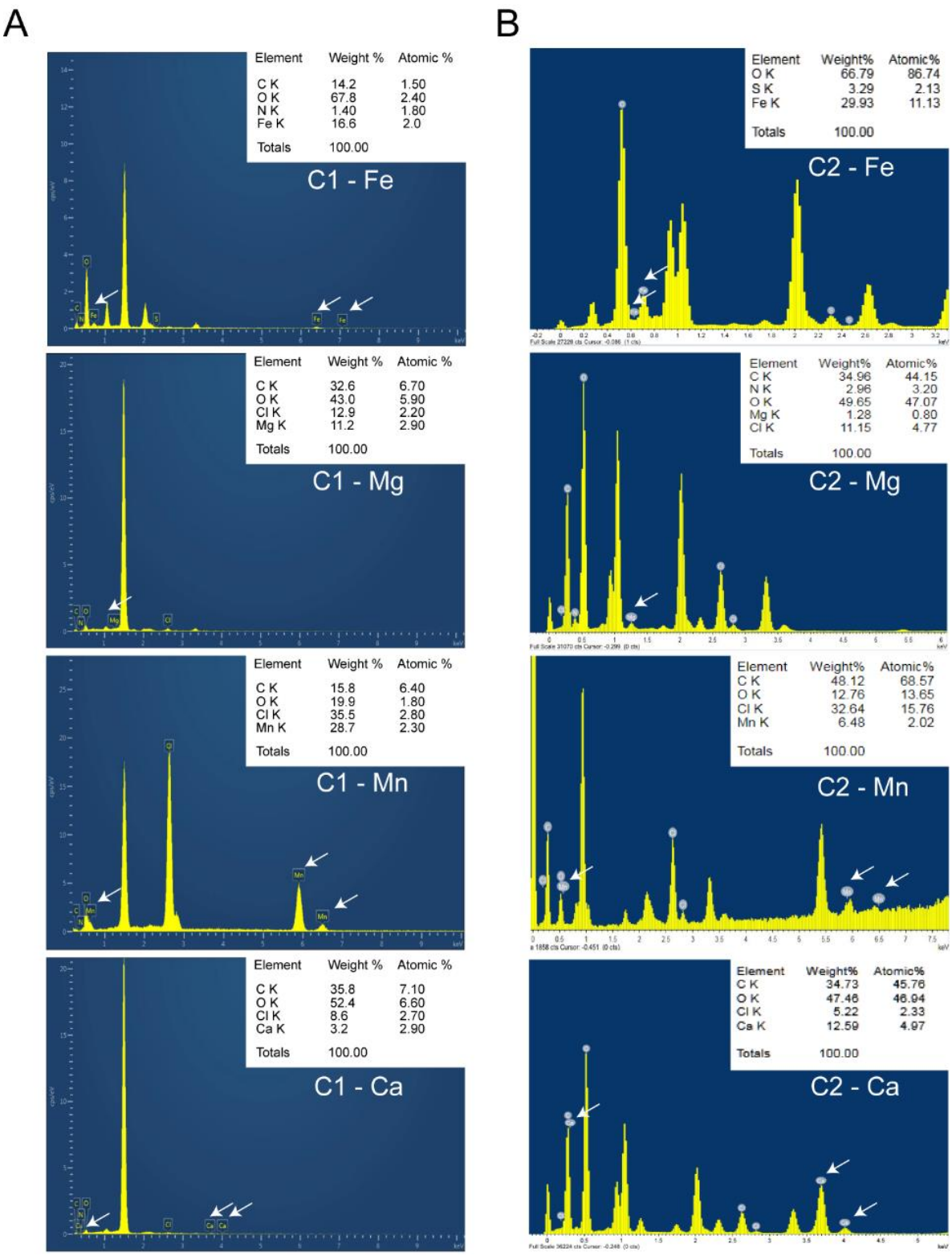

Figure A5.2. Evidence for metal complexation of (A) C1 and (B) C2 against various metals acquired by EDX analysis.

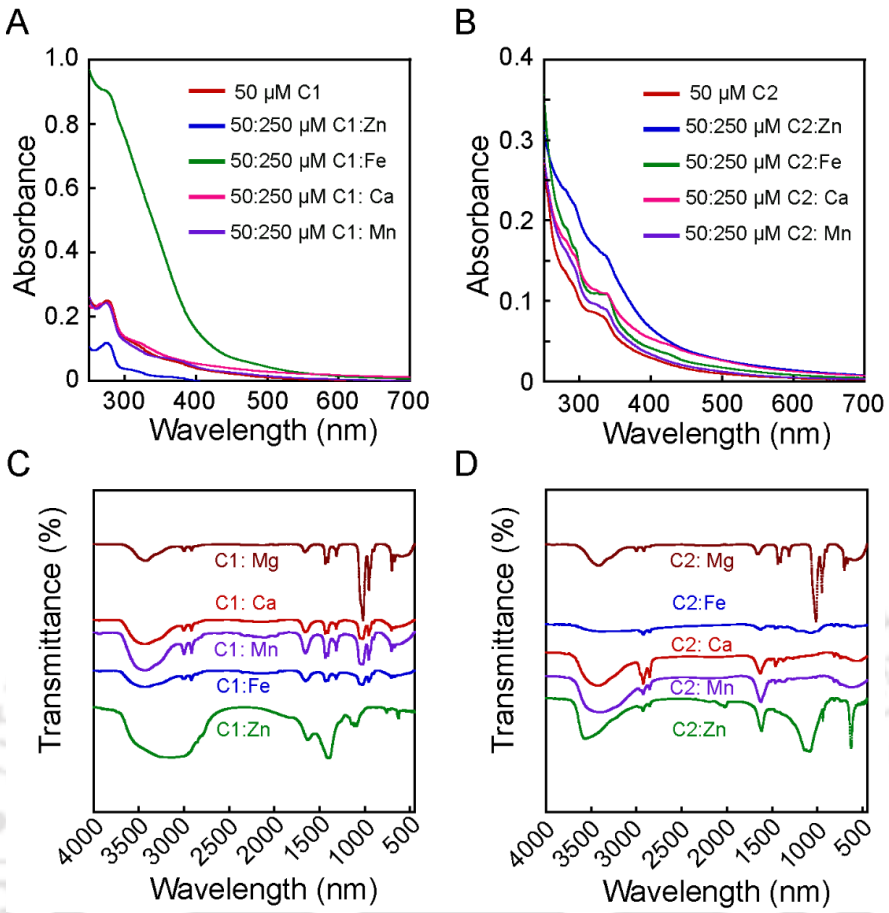

Figure A5.3. UV-visible spectra of metal complexes of (A) C1 and (B) C2. FTIR spectra of metal complexes of (C) C1 and (D) C2.

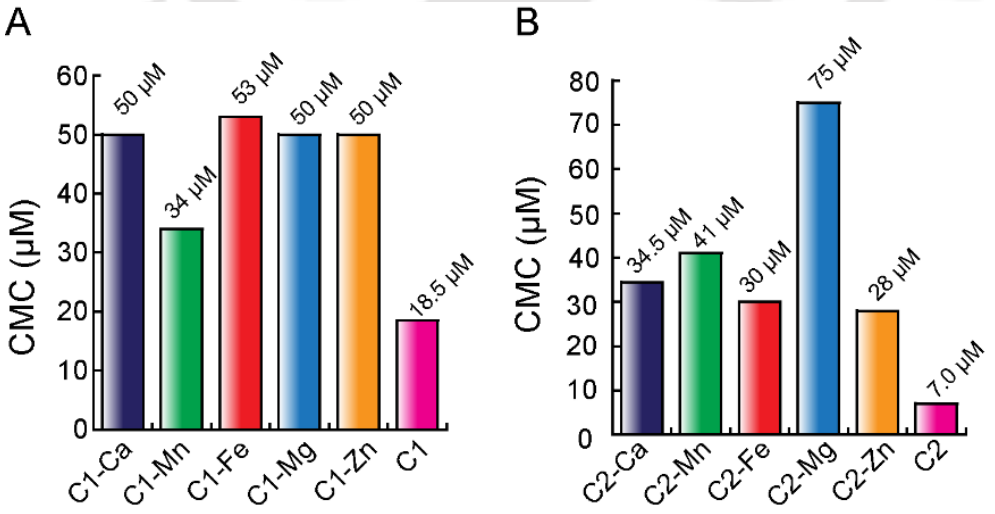

Figure A5.4. Determination of the CMC values for C1- and C2-metal complexes.

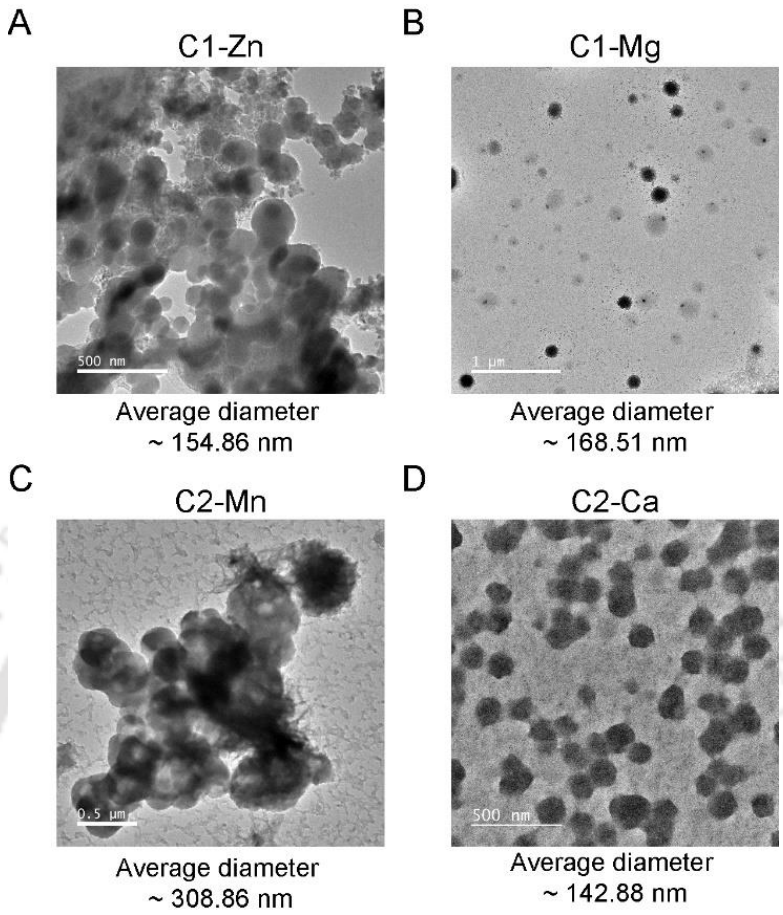

Figure A5.5. FETEM analysis of C1- and C2-metal complexes.

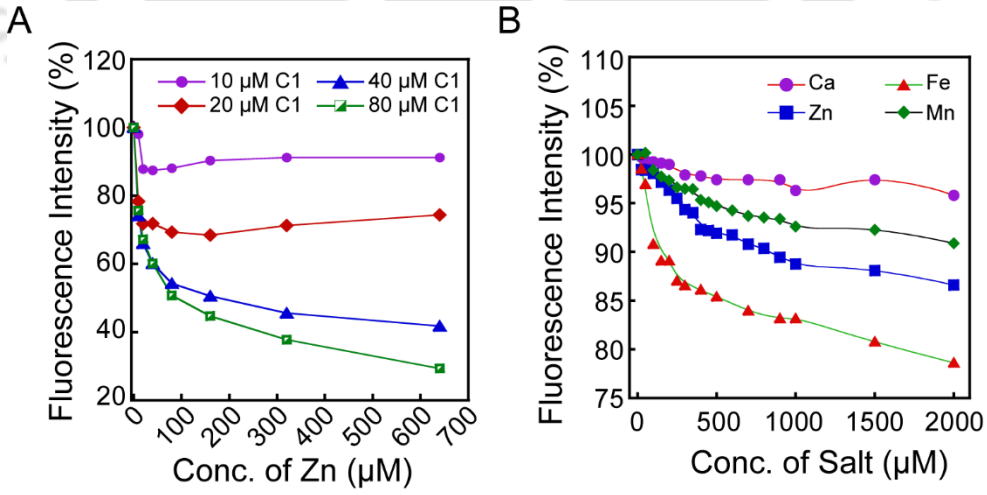

Figure A5.6. Changes in the fluorescence intensity of ANS (3.0 µM) entrapped in (A) Varying concentrations of C1 micelle in presence of varying concentrations of Zn (B) C2 micelle (80 µM) in presence of varying concentrations of metal salts.

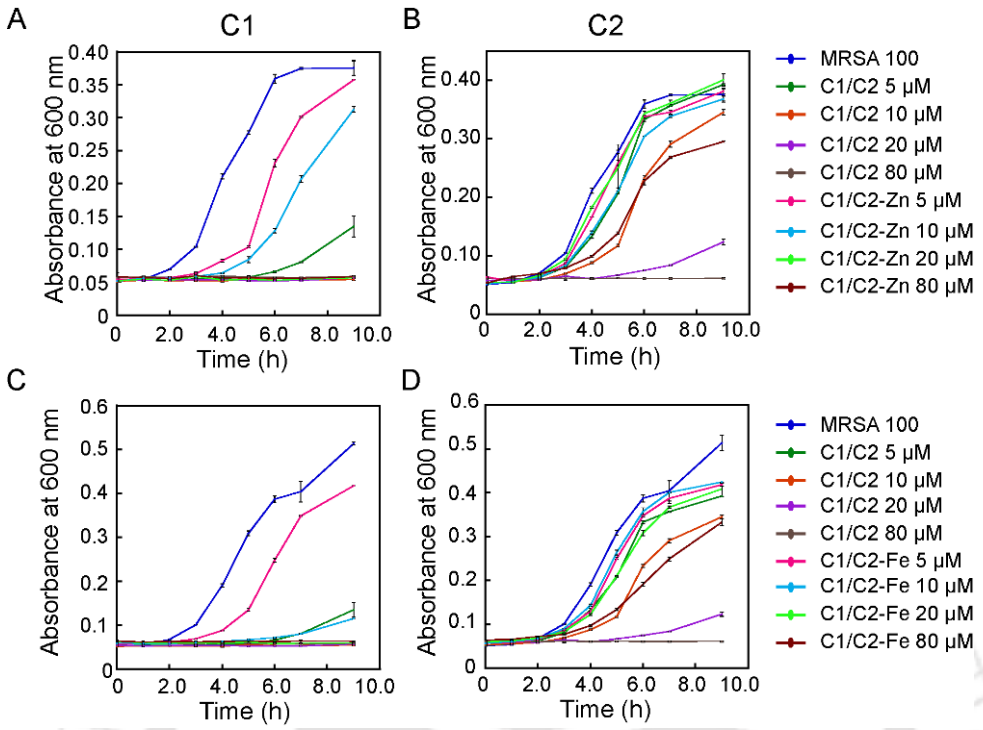

Figure A5.7. Effect of C1and C2-metal complexes on the growth of *S. aureus* MRSA 100 in BHI media.

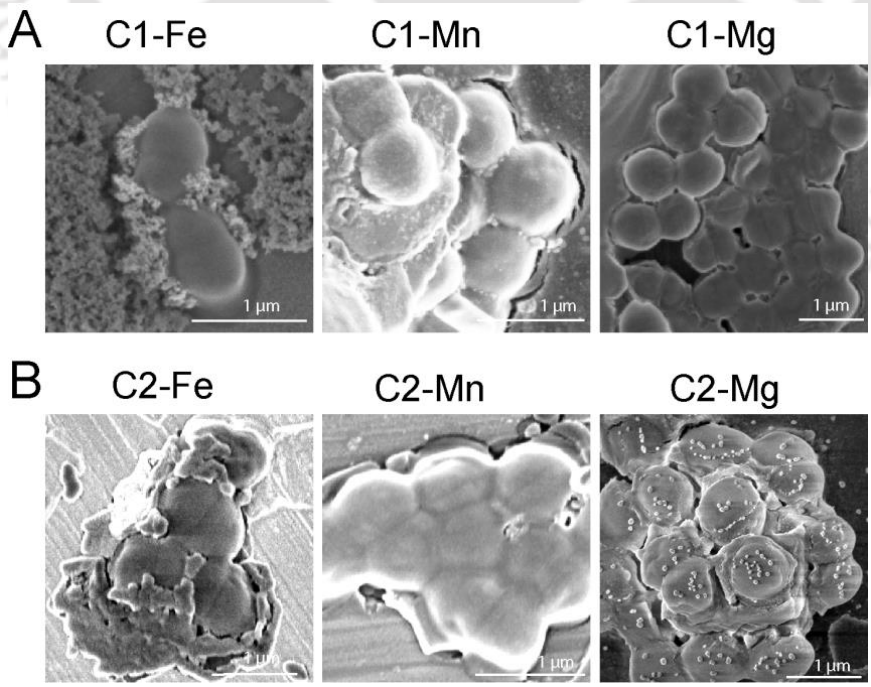

Figure A5.8. FESEM image of *S. aureus* MRSA 100 cells treated with (A) C1-metal complexes and (B) C2-metal complexes.

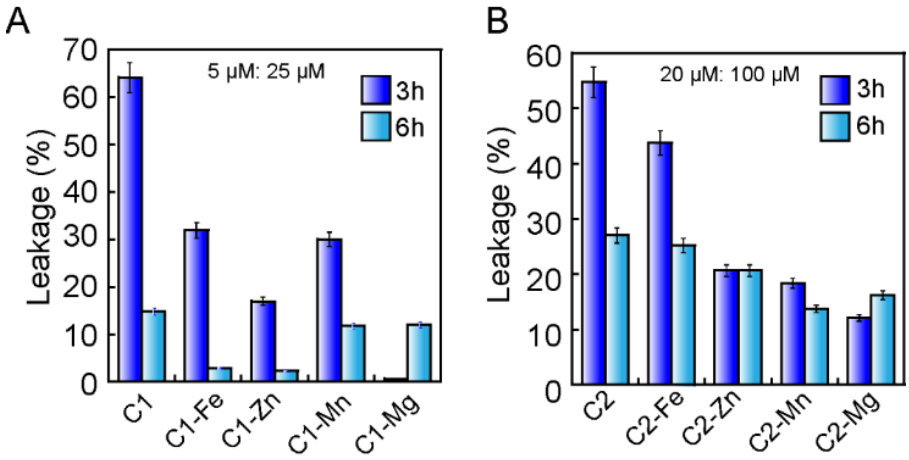

Figure A5.9. Assessment of membrane-directed activity of (A) C1- and (B) C2-metal complexes against *S. aureus* MRSA 100 by cFDA-SE leakage assay.

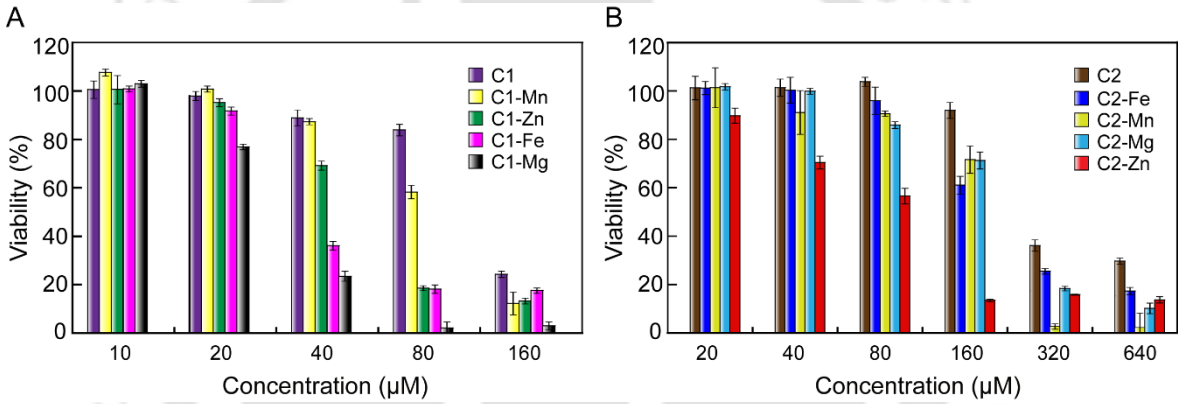

Figure A5.10. MTT assay to ascertain the *in vitro* cytotoxic effect of varying concentrations of (A) C1 and (B) C2 along with their metal complexes on HEK 293 cells.

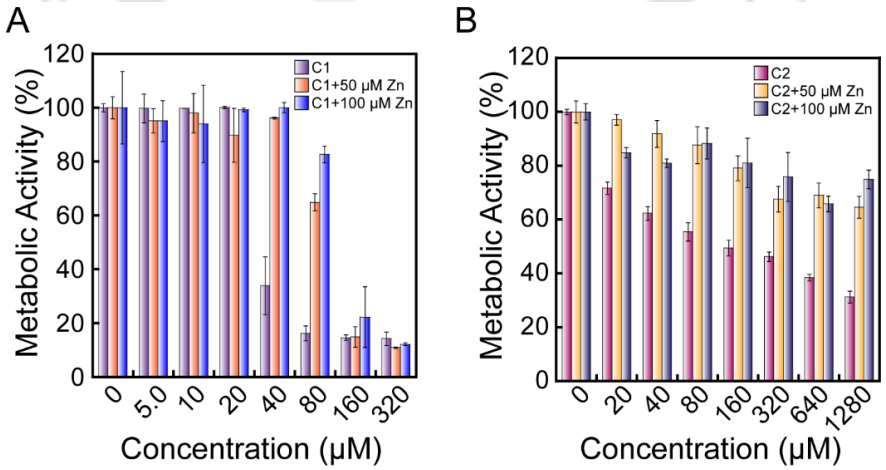

Figure A5.11. Effect of zinc supplementation on the metabolic activity of (A) C1 and (B) C2 treated biofilm of *S. aureus* MTCC 96.

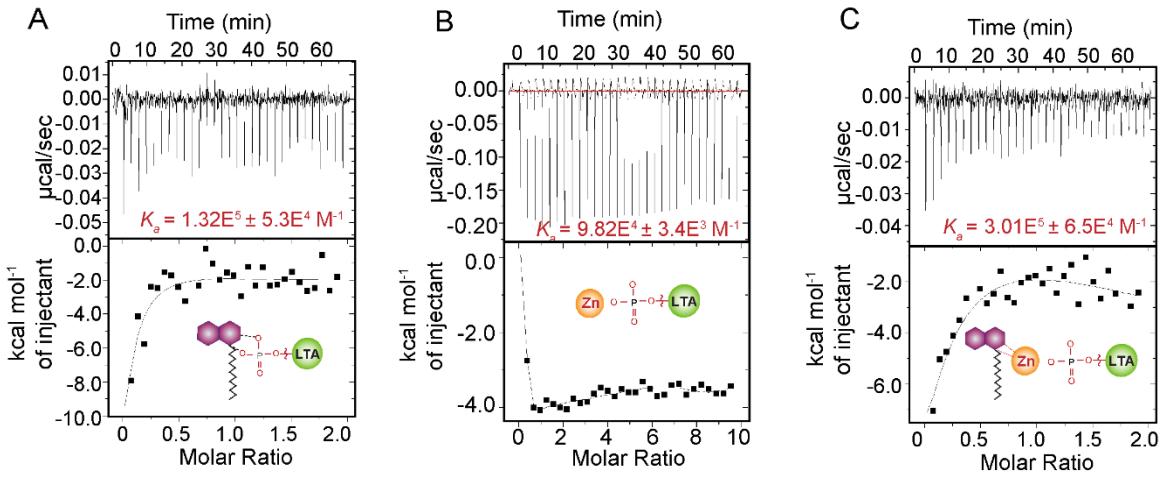

Figure A5.12. ITC analysis to study the interaction between (A) C2 and LTA (B) Zn and LTA and (C) C2-Zn complex and LTA.

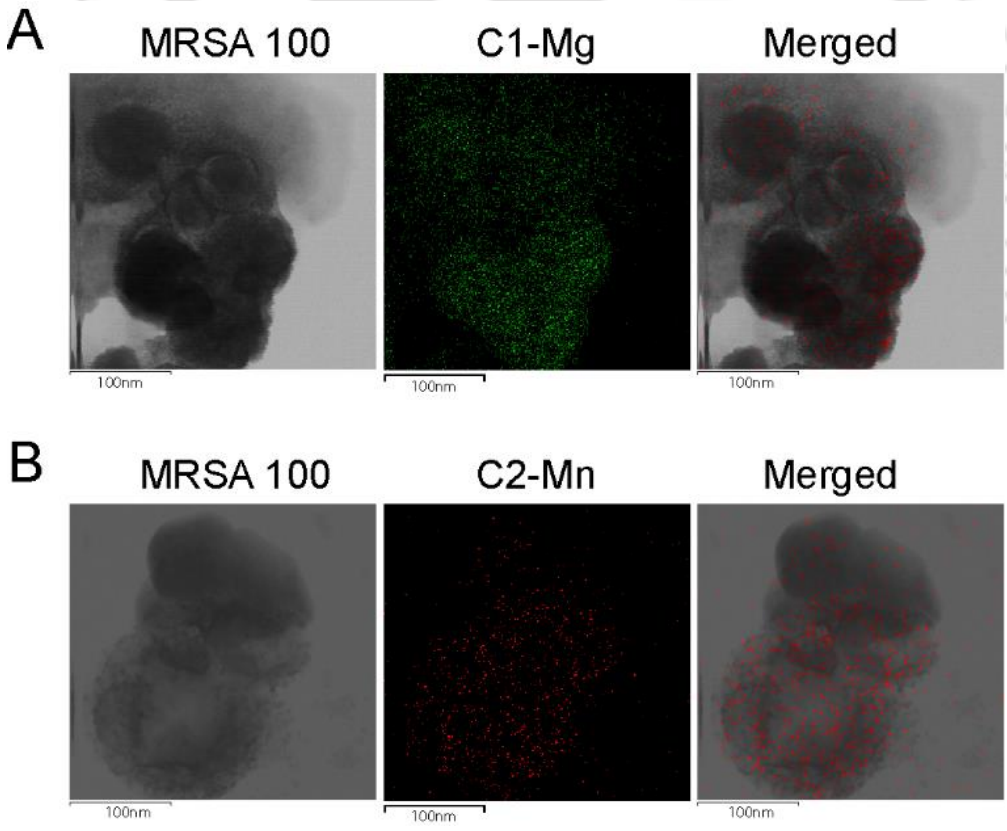

Figure A5.13. FETEM-based mapping analysis indicating the presence of (A) cell associated C1-$MgCl_2$ complex and (B) cell associated C2-$MnCl_2$ complex.

Table A6.1 Body Weight measurements for sighting studies (300 mg/kg dose of C1)

Day	Male	Female
1	28.35	24.51
2	28.31	24.50
3	28.05	24.74
4	28.17	25.06
5	28.14	25.23

Table A6.2 Body Weight measurements for sighting studies (1000 mg/kg dose of C1)

Day	Male	Female
1	27.3	26.3
2	26.2	25.5
3	26.1	25.1
4	26.4	25.0
5	26.5	25.4
6.	26.7	25.6
7.	27.1	25.9
8.	27.5	26.5

Table A6.3. Haematological Screening in 1000mg/kg treated male BALB/c mice for sighting study.

Sl.No.	Parameter	Estimated Values	Reference Values
1.	Platelets (x 10^3 cells/µL)	626.00	325 - 888
2.	RBC (x 10^6 cells/µL)	9.44	7.1 -9.5
3.	Haemoglobin (g/dL)	21.40	11.6 – 15.8
4.	Hematocrit (%)	49.80	37.4 – 51.7
5.	Mean Corpuscular Volume (fL)	52.70	41.5 – 57.4
6.	Mean Corpuscular Haemoglobin (pg)	22.70	14.1 – 18.4
7.	Neutrophil (%)	10.40	11 - 29
8.	Lymphocytes (%)	75.50	65 - 87
9.	Monocytes (%)	2.30	0 – 6.0
10.	WBC (x 10^3 cells/µL)	8.44	3.48 - 14.03
11.	Eosinophils (%)	9.40	0 – 5.0
12.	Basophils (%)	0.10	0 – 1.0
13.	Leucocytes (%)	2.30	0 – 3.2

Table A6.4. Haematological Screening in 1000 mg/kg treated female BALB/c mice for sighting study.

Sl.No.	Parameter	Estimated Values	Reference Values
1.	Platelets (x 10^3 cells/µL)	943.00	766 - 1657
2.	RBC (x 10^6 cells/µL)	9.77	7.0 -10.1
3.	Haemoglobin (g/dL)	22.00	11.8 – 14.9
4.	Hematocrit (%)	49.90	36.7 – 46.8
5.	Mean Corpuscular Volume (fL)	51.10	42.2 – 59.2
6.	Mean Corpuscular Haemoglobin (pg)	22.50	13.8 – 18.5
7.	Neutrophil (%)	12.70	6.8 - 31.1
8.	Lymphocytes (%)	82.60	60.2 – 95.0
9.	Monocytes (%)	1.10	0 – 4.3
10.	WBC (x 10^3 cells/µL)	5.37	3.2 – 12.7
11.	Eosinophils (%)	1.80	0.2 – 5.9
12.	Basophils (%)	0.20	0 – 1.0
13.	Leucocytes (%)	1.50	0 - 3.2

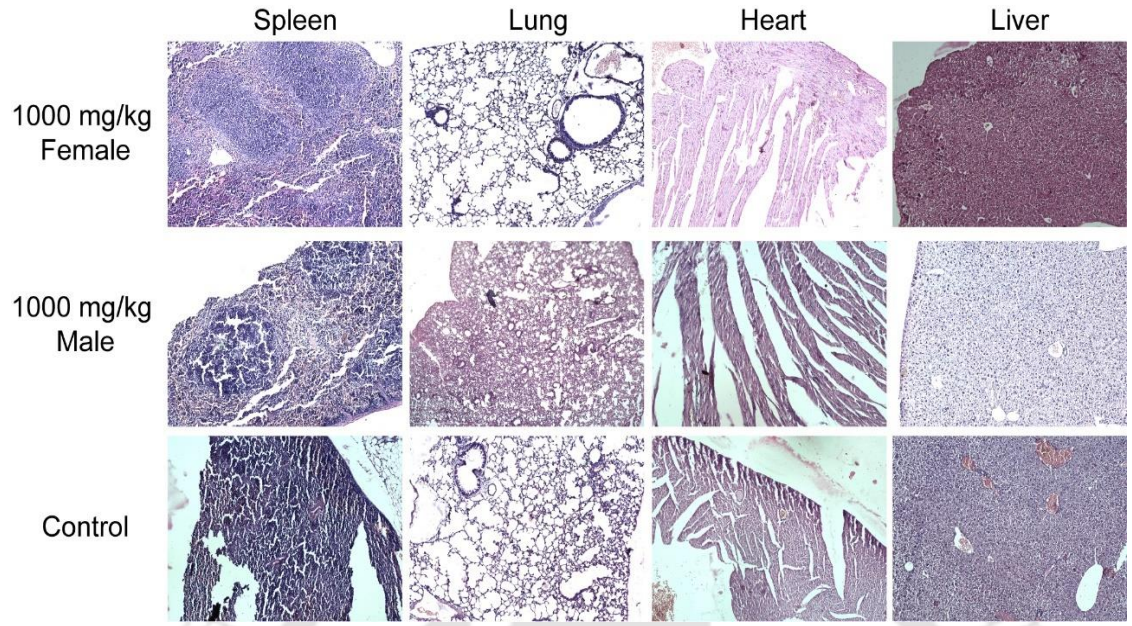

Figure A6.1. Histopathology analysis for studies sighting study of 1000 mg/kg treated BAlb/c mice.

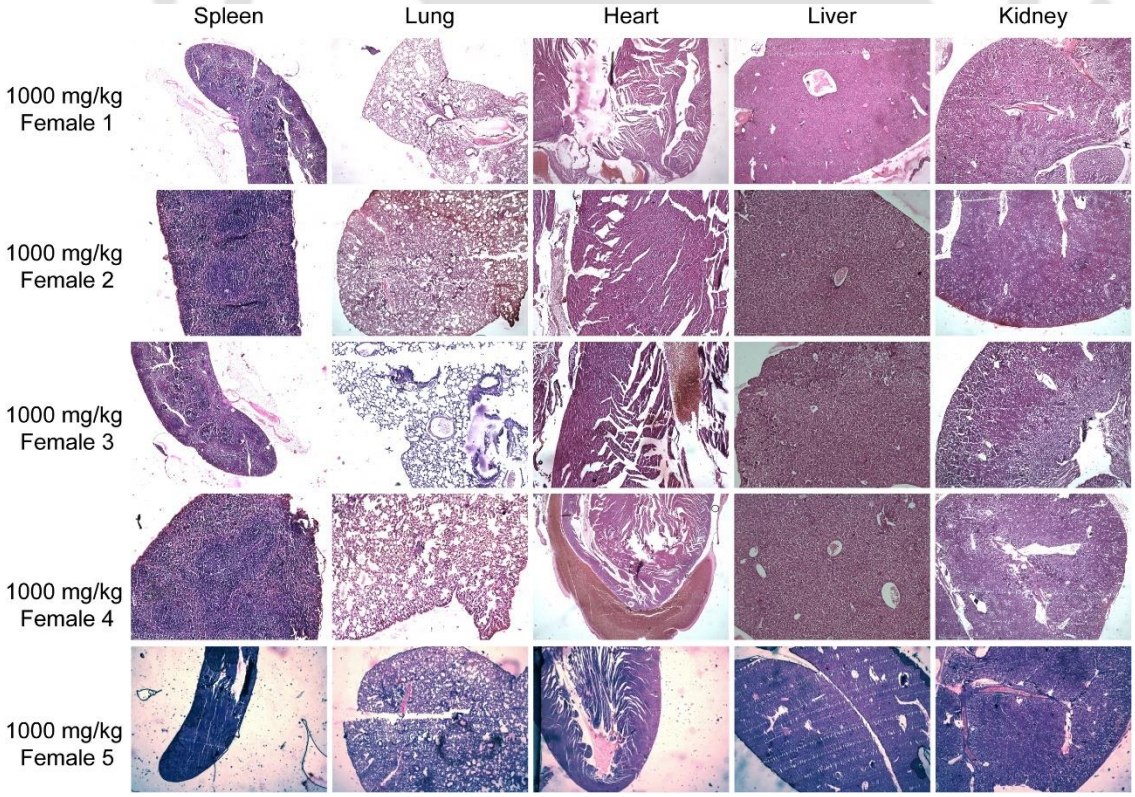

Figure A6.2. Histopathology analysis for acute toxicity of 1000 mg/kg treated female BAlb/c mice.

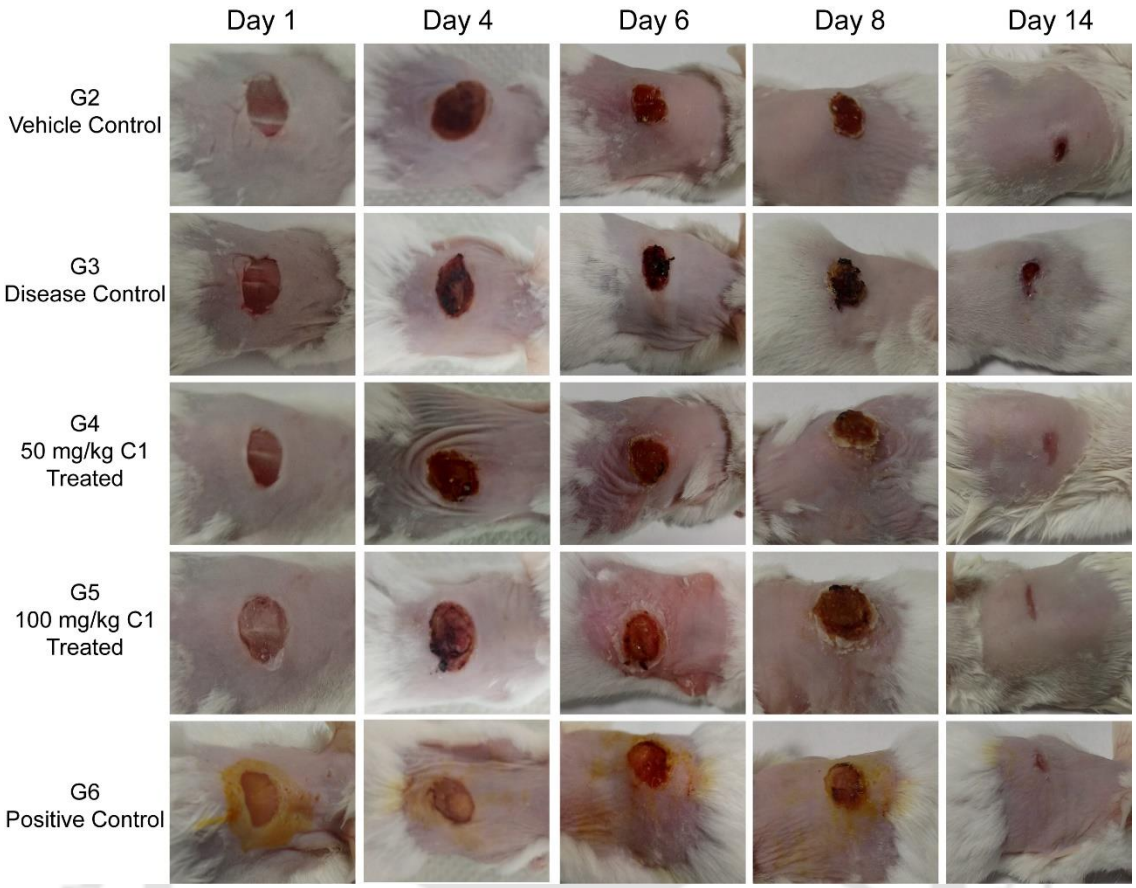

Figure A6.3. Visualization of the wound closure over the duration of the study.

LIST OF PUBLICATIONS

List of Publications

Publications from Ph.D. Thesis Work:

(A) Journal Publications:

1. **Dey, P.**, Mukherjee, S., Das, G., Ramesh, A. (**2018**). Micellar chemotherapeutic platform based on a bifunctional salicaldehyde amphiphile delivers a "combo-effect" for heightened killing of MRSA. *Journal of Materials Chemistry B*, 6, 2116-2125.

2. **Dey, P**., Das, G. and Ramesh, A. (**2020**). Interplay between supramolecular and coordination interactions in synthetic amphiphiles: Triggering metal starvation and anchorage onto MRSA cell surface. *Langmuir*, 36, 2110−2119.

3. **Dey, P**., Eshwar, P., Naidu, V. G. M., Das, G. and Ramesh, A. (**2020**). Multifunctional synthetic amphiphile for niche therapeutic applications: Mitigation of MRSA biofilm and potential in wound healing **(Manuscript under preparation).**

(B) Conference Presentations:

1. **Dey, P.,** Boral, M., Das, G. and Ramesh, A. (**2015**). Salicyaldehyde-based amphiphile as a potent bactericidal agent. Abstract MEDM56. Presented in the *56th Annual Conference of Association of Microbiologists of India* (AMI), JNU, New Delhi, India, 7-10 December 2015.

2. **Dey, P.,** Mukherjee, S., Das, G. and Ramesh, A (**2018**). Synthetic amphiphilic arsenal to combat MRSA biofilm: Exploring metal complexation and self-assembling attribute. Presented in the *8th ASM Conference on Biofilms*, Washington, DC, USA, 7-11 October 2018.

3. Saha, D., **Dey, P**., Das, G. and Ramesh, (**2018**) A. Pyrene-tethered small amphiphilic ligand for heavy metal sensing: Solution-based and cell interaction studies. Presented in *Frontier in Chemical Science* (FICS), IIT Guwahati, 6-8 December 2018.

(C) Publications from Other Research Projects:

1. Samanta, S., **Dey, P**., Ramesh, A. and Das, G. (**2016**). A solo fluorogenic probe for real-time sensing of SO_3^{2-} and SO_4^{2-}/HSO_4^- in aqueous medium and live cells by distinct turn-on emission signals. *Chemical Communications*, 52, 10381-10384.

2. Samanta, S., Halder, S., **Dey, P**., Manna, U., Ramesh, A. and Das, G. (**2018**). A ratiometric fluorogenic probe for real-time sensing of SO32- in aqueous medium: Application in cellulose paper-based device and potential to sense SO_3^{2-} in mitochondria. *Analyst*, 143, 250-257.

3. Chauhan, P., **Dey, P**., Mukherjee, S., Manna, U., Das, G and Ramesh, A. (**2018**). A cytocompatible zinc oxide nanocomposite loaded with an amphiphilic arsenal for alleviation of staphylococcus biofilm. *Chemistry Select*, 3, 2492-2497.

4. Sahareen, T., **Dey, P**., Mukherjee, S., Das, G and Ramesh, A. (**2018**). Potential of pyridine amphiphiles as staphylococcal nuclease inhibitor. *ChemBioChem*, 19, 1400-1408.